



**HAL**  
open science

# Integration of graphene on micro-acoustic radiofrequency components

Mario Costanza

► **To cite this version:**

Mario Costanza. Integration of graphene on micro-acoustic radiofrequency components. Micro and nanotechnologies/Microelectronics. Université Bourgogne Franche-Comté, 2023. English. NNT : 2023UBFCD057 . tel-04517386

**HAL Id: tel-04517386**

**<https://theses.hal.science/tel-04517386>**

Submitted on 22 Mar 2024

**HAL** is a multi-disciplinary open access archive for the deposit and dissemination of scientific research documents, whether they are published or not. The documents may come from teaching and research institutions in France or abroad, or from public or private research centers.

L'archive ouverte pluridisciplinaire **HAL**, est destinée au dépôt et à la diffusion de documents scientifiques de niveau recherche, publiés ou non, émanant des établissements d'enseignement et de recherche français ou étrangers, des laboratoires publics ou privés.

**THESE DE DOCTORAT DE L'ETABLISSEMENT UNIVERSITE BOURGOGNE FRANCHE-COMTE  
PREPAREE A L'UNIVERSITE DE FRANCHE-COMTE**

Ecole doctorale n°37

Ecole Doctorale de Sciences Physiques pour l'Ingénieur et Microtechniques

Doctorat de Microtechniques

Par

COSTANZA Mario

**Integration of graphene on micro-acoustic radiofrequency components**

*Intégration du graphène sur composants micro-acoustiques radiofréquences*

Thèse présentée et soutenue à Besançon, le 05/12/2023

**Composition du Jury :**

|                      |   |                    |
|----------------------|---|--------------------|
| M. Kersalé Yann      | Pr Université Bourgogne Franche-Comté, Besançon (FR)                        | Président          |
| M. Stivala Salvatore | Università degli Studi di Palermo (IT)                                      | Rapporteur         |
| M. Winkemann Clemens | MCF Grenoble INP, Institut Néel (FR)  | Rapporteur         |
| M. Santos Paulo V.   | Dir. de Recherche Paul-Drude-Institut für Festkörperelektronik, Berlin (DE) | Examineur          |
| M. Devel Michel      | Pr Université Bourgogne Franche-Comté, Besançon (FR)                        | Examineur          |
| M. Margueron Samuel  | MCF Université Bourgogne Franche-Comté, Besançon (FR)                       | Directeur de Thèse |
| M. Dumont Yves       | Pr Université Versailles St-Quentin-en-Yvelines, GeMAC (FR)                 | Invité             |



*To whom could not be here for this very moment, and to my beloved family and friends, who supported me in my years of Ph.D. and before,*

*I thank you from the bottom of my heart.*



## Introduction

Piezoelectric devices use the ability of a certain family of materials to couple electrical and mechanical energy due to a strain-induced electric polarization. The advantage of piezoelectric devices is the possibility of using the **slow-propagating** displacement field, which allows to greatly reduce the size of devices, to insulate electrically inputs and outputs, to fine-tune the frequency response of through standard lithographic means.

Acoustoelectronic devices belong to a small family of piezoelectric devices that **non-linearly** couples acoustic waves (strain) to the free carriers in a semiconductor through a perturbation of their conduction/valence bands. This coupling phenomenon has been treated in solid-state physics books for a long time and is explained by means of electron-phonon interactions which causes the generation of a continuous electrical current transported by an acoustic wave. The electron-phonon interactions are responsible, for instance, for the electrical resistivity of metal in temperature (Wiedemann–Franz’s law).

The use of the piezoelectric effect in combination with non-linearity has been used in devices, starting between the 60s and the 70s, with the objective of developing microacoustic convolvers, correlators and amplifiers for applications in radars and telecommunications.

The **convolver** is a device capable of performing a fully-analog **time-domain convolution** between two contra-propagating acoustic signals under a conductive, nonlinear medium. The signal is integrated on the nonlinear medium length via the electric response, generating a convolution output signal at twice the input frequency. These devices were limited to frequencies of few hundreds of MHz (due to strong absorption) and they almost disappeared with the digital processing era. Recently, there has been an increasing interest in convolvers and acoustoelectronic devices, as they represent a very strong way to improve the performances of existing microacoustic devices and to accurately manipulate charges. One can note the manipulation of quantum emitters by the group of *Paulo V. Santos* in Berlin, the spin transport in quantum wells by *Christopher Baueker* in Grenoble, the application in charge metrology. Most of this work has been concentrated to acousto-electronic interactions in piezo-semiconductor and piezo-dielectric/semiconductor heterostructures.

Meanwhile, the goal of my PhD was the development of a **convolver device that could work in the range of GHz frequencies**. The final goal would be to treat analogically massive data at a rate of GHz. For instance, this could be applied to perform the correlation or

convolution of photoluminescent emitters originated from nitrogen vacancy centers in diamond at 2.8-2.9 GHz.

With this purpose, this work combines surface acoustic devices that can be concentrated on a small, high-energy, self-guided Rayleigh waves at GHz frequencies and ‘massless’ graphene. Graphene is a 2D material which possesses exceptional properties, which severely reduce the mechanical damping of acoustic waves in respect to ‘classic’ devices.

Then, to follow the objective of my PhD, I will present the methodology in the development of my thesis during my three years at FEMTO-ST under the supervision of Dr. Samuel Margueron. The work I did at the Renatech network of clean room facilities (MIMENTO) with the help of numerous engineers, in particular Dr. Djaffar Belharet. I wish to thank Professors Yves Dumont and Joseph Scola, at laboratory GEMaC (Groupe d’Étude de la Matière Condensée) of the Université de Versailles Saint-Quentin-en-Yvelines with. Finally, I cannot underestimate the help of Dr. Arthur De Sousa Lopes Moreira, Léa La Spina, Professor Ausrine Bartasyte, as well as the researchers and engineers at the time&frequency department, in particular, Jean-Michelle Friedt, Clément Lacroûte, Boudot, Yannick Gruson, David Vernier, Professor Enrico Rubiola, Philippe Abbé.

This PhD is organized as follows:

- In Chapter 1, I present a review of the piezoelectric and acoustoelectronic effect, alongside with the acousto-electronic devices present in the literature. In particular, a special attention is given to the different strategies, which made possible to attain a convolver in the GHz frequencies by the use of 2D material such as graphene.
- In Chapter 2, I expose the experimental work I develop in cleanroom to transfer and process graphene on LiNbO<sub>3</sub> (GoL).
- In Chapter 3, I made an extensive characterization by Raman scattering of the processed GoL devices. In addition, a study on the effect of spontaneous polarization in LiNbO<sub>3</sub> and doping the sources of defects at electrode contacts.
- In Chapter 4, I present an electrical characterization for measuring the resistivity, contact resistance and mobility of GoL.
- In Chapter 5, I present the first AE current measurement under the frequency range 2.0 GHz – 3.0 GHz,
- In Chapter 6, I present the preliminary results on GoL convolver.
- Finally, I conclude and give some perspective to this work.

# Glossary

We present a table of the most significant abbreviations throughout the thesis:

|                    |   |
|--------------------|---|
| LiNbO <sub>3</sub> | Lithium Niobate                           |
| GoLN               | Graphene-on-Lithium Niobate               |
| SAW                | Surface Acoustic Wave                     |
| BAW                | Bulk Acoustic Wave                        |
| PPLN               | Periodically-Poled Lithium Niobate        |
| DC                 | Direct Current (time-independent)         |
| AE                 | Acousto-Electric                          |
| RF                 | Radio-Frequency                           |
| TLM                | Transmission Line Model                   |
| PLC                | Power Line Cycle                          |
| IDT                | Inter-Digital Transducer                  |
| CMA                | Combined-Medium Amplifier                 |
| SMA                | Separated-Medium Amplifier                |
| GFET               | Graphene Field-Effect Transistor          |
| DAGSF              | Degenerate Air-Gapped Semiconductive Film |
| CVD                | Chemical Vapor Deposition                 |
| RIE                | Reactive Ion Etching                      |
| D/2D Raman modes   | First and second order process of D modes |
| G/2G Raman modes   | First and second order process of G modes |
| 2D                 | Two dimensions (materials)                |
| 3D                 | Three dimensions (plot)                   |
| CHE and QHE        | Classical/Quantum Hall Effect             |
| ASK                | Amplitude-Shift Keying                    |

# Table of contents

|   |    |
|---|----|
| 1 State of the Art.....   | 6  |
| 1.1 Acoustic Waves in Solids.....                                   | 6  |
| 1.1.1 Linear strain and stress.....                                 | 6  |
| 1.1.2 Nonlinear strain.....   | 8  |
| 1.1.3 Equation of Motion of Acoustic Waves.....                     | 8  |
| 1.1.4 Piezoelectric effect.....                                     | 10 |
| 1.1.4.1 Electrical and mass loading of a piezoelectric surface..... | 13 |
| 1.1.5 Pyroelectric effect.....                                      | 14 |
| 1.2 Graphene on Piezoelectric Substrates.....                       | 15 |
| 1.2.1 Graphene.....   | 15 |
| 1.2.2 Production of Graphene.....                                   | 17 |
| 1.3 Acoustoelectronic devices.....                                  | 17 |
| 1.3.1 Reports on AE current.....                                    | 18 |
| 1.3.1.1 Graphene devices.....                                       | 22 |
| 1.4 Surface acoustic wave devices.....                              | 24 |
| 1.4.1 Linear SAW filters.....                                       | 25 |
| 1.4.2 Nonlinear devices.....  | 27 |
| 1.4.2.1 AE Amplifiers.....  | 28 |
| 1.4.2.2 Acoustoelectronic convolvers.....                           | 33 |
| 1.5 References.....   | 40 |
| 2 GoL : Graphene on LiNbO <sub>3</sub> .....                        | 52 |
| 2.1 Graphene processing.....  | 52 |
| 2.1.1 Graphene on Si/SiO <sub>2</sub> .....                         | 53 |
| 2.1.2 Challenges for LiNbO <sub>3</sub> .....                       | 53 |
| 2.1.3 Metal-graphene contacts.....                                  | 54 |
| 2.2 Description of the Process.....                                 | 56 |
| 2.2.1 Wafer cutting and substrate cleaning.....                     | 57 |

|         |   |     |
|---------|---|-----|
| 2.2.2   | Lithographic process.....                               | 59  |
| 2.2.2.1 | UV Lithographic process for Liffoff.....                | 60  |
| 2.2.2.2 | UV Lithographic process for Patterning.....             | 62  |
| 2.2.2.3 | Electron Beam Lithographic process for Liffoff.....     | 63  |
| 2.2.3   | Metal Deposition and Liffoff.....                       | 65  |
| 2.2.3.1 | Liffoff.....  | 65  |
| 2.2.3.2 | Backside electrode.....                                 | 68  |
| 2.2.4   | Graphene Transfer.....                                  | 68  |
| 2.2.4.1 | Process with the “easy transfer kit”.....               | 69  |
| 2.2.4.2 | Process With CVD Graphene on Cu Substrates.....         | 72  |
| 2.2.5   | Graphene Annealing.....                                 | 76  |
| 2.2.6   | Graphene Patterning.....                                | 78  |
| 2.3     | Description of Other Methods.....                       | 78  |
| 2.4     | Visible-light microscopy.....                           | 81  |
| 2.5     | Improvements of the process.....                        | 82  |
| 2.6     | References.....   | 83  |
| 3       | Raman spectroscopy of GoL.....                          | 92  |
| 3.1     | Elements of Theory.....                                 | 92  |
| 3.2     | Graphene.....   | 93  |
| 3.2.1   | Estimation of layer number and defects.....             | 95  |
| 3.3     | Description of the Experiments.....                     | 99  |
| 3.3.1   | Analysis of the uniformity of the Hall bar devices..... | 108 |
| 3.3.2   | Results for graphene on PPLN.....                       | 110 |
| 3.4     | References.....   | 116 |
| 4       | DC electrical analysis.....                             | 120 |
| 4.1     | DC Resistivity of Graphene and Contacts.....            | 120 |
| 4.1.1   | Theory.....   | 120 |
| 4.1.2   | State-of-the-art graphene.....                          | 123 |
| 4.1.3   | Design of the characterization devices.....             | 123 |

|         |   |     |
|---------|---|-----|
| 4.1.4   | Description of the experiments.....   | 124 |
| 4.2     | Hall effect.....  | 129 |
| 4.2.1   | Hall effect Theory.....   | 130 |
| 4.2.1.1 | Classical Hall effect.....  | 130 |
| 4.2.1.2 | Quantum Hall effect.....  | 132 |
| 4.2.1.3 | Quantum Hall effect in graphene.....  | 134 |
| 4.2.2   | Description of the experiment.....  | 135 |
| 4.3     | Discussion of the results.....  | 148 |
| 4.4     | References.....   | 149 |
| 5       | Acousto-Electric current measurements.....  | 154 |
| 5.1     | Introduction.....   | 154 |
| 5.2     | Paper : Acousto-electric measurements at 2.5 GHz on graphene transferred onto YX128°-LiNbO <sub>3</sub> ..... | 154 |
| 5.2.1   | Abstract.....   | 154 |
| 5.2.2   | Introduction.....   | 155 |
| 5.2.3   | Microfabrication.....   | 156 |
| 5.2.4   | Results.....  | 159 |
| 5.2.5   | Discussion and concluding remarks.....  | 163 |
| 5.3     | Follow-up on AE Characterization.....   | 167 |
| 5.3.1   | Characterization at 2.0 GHz and 3 GHz.....  | 168 |
| 5.3.2   | Saturation power and breakdown of the IDTs.....   | 172 |
| 5.3.3   | Automation of the setup.....  | 175 |
| 5.4     | Conclusion.....   | 177 |
| 5.5     | References.....   | 177 |
| 6       | Preliminary results on acoustoelectronic convolvers.....  | 184 |
| 6.1     | Convolver.....  | 184 |
| 6.2     | Numerical simulation of the devices.....  | 186 |
| 6.2.1   | Description of the algorithm.....   | 186 |
| 6.2.2   | Simulated results.....  | 188 |

|       |   |     |
|-------|---|-----|
| 6.2.3 | Description of the experiments.....                 | 190 |
| 6.2.4 | Difference between batches variations.....          | 199 |
| 6.2.5 | Explanation of the optimized current.....           | 200 |
| 6.3   | AE GoL SAW amplifiers.....                          | 201 |
| 6.4   | Conclusions.....                                    | 202 |
| 6.5   | References.....                                     | 203 |
| 7     | General conclusion.....                             | 205 |
| 8     | Summary of my research and teaching activities..... | 207 |
| 8.1   | List of presentations and publications .....        | 207 |
| 8.2   | Teaching activities.....                            | 211 |

# Contents of the chapter:

- 1 State of the Art.....6
  - 1.1 Acoustic Waves in Solids..... 6
    - 1.1.1 Linear strain and stress.....6
    - 1.1.2 Nonlinear strain..... 8
    - 1.1.3 Equation of Motion of Acoustic Waves.....8
    - 1.1.4 Piezoelectric effect..... 10
      - 1.1.4.1 Electrical and mass loading of a piezoelectric surface ..... 13
    - 1.1.5 Pyroelectric effect.....14
  - 1.2 Graphene on Piezoelectric Substrates..... 15
    - 1.2.1 Graphene.....15
    - 1.2.2 Production of Graphene.....17
  - 1.3 Acoustoelectronic devices.....17
    - 1.3.1 Reports on AE current..... 18
      - 1.3.1.1 Graphene devices.....22
  - 1.4 Surface acoustic wave devices.....24
    - 1.4.1 Linear SAW filters ..... 25
    - 1.4.2 Nonlinear devices.....27
      - 1.4.2.1 AE Amplifiers.....28
      - 1.4.2.2 Acoustoelectronic convolvers.....33
  - 1.5 References.....40

# 1 State of the Art

To develop high frequency acoustoelectronic devices, this chapter presents the basis of surface acoustic devices (Section 1.1) and graphene (Section 1.2). At the end of the chapter, I provide a review the acoustoelectronic devices available in literature. Particularly, I will discuss the different strategies usable to develop a graphene-based acoustoelectronic convolver in the GHz range (Section 1.3).

## 1.1 Acoustic Waves in Solids

Acoustic waves are represented by periodic fluctuations in the positions of atoms in a material caused by a mechanical excitation. The objective of the first sections is to provide some basic mathematical tools to understand the propagation of mechanical waves in standard nonpiezoelectric materials by introducing the mechanical fields of displacement, stress and strain, then proceeding in the description of the piezoelectric effect. In this explanation, for the ease of notation, the  $x$ ,  $y$ , and  $z$  axes will be respectively referred via the set  $e_1$ ,  $e_2$  and  $e_3$  and Einstein's summation convention is used unless specified otherwise.

### 1.1.1 Linear strain and stress

When a force is applied to an elastic body, it deforms, as shown in Figure 1.1, this is mathematically represented as a certain transformation  $\psi$  from a generic point  $X = (x_1, x_2, x_3)$ , in the undeformed space  $\Omega_0$ , to a point  $X' = (x'_1, x'_2, x'_3)$ , in the deformed space  $\Omega_1$ :

$$X \rightarrow X' = \psi(X, t). \quad (1.1)$$

The displacement field is represented by a vector quantity  $U = (u_1, u_2, u_3)$ , equal to the difference between the undisturbed  $X$  and the transformed point  $X'$ :

$$U = X' - X. \quad (1.2)$$

The usage of the displacement  $U$ , rather than  $X$  or  $X'$  allows defining the other mechanical quantities using the frame of reference of the object, meaning that they are invariant to its movement and rotation.

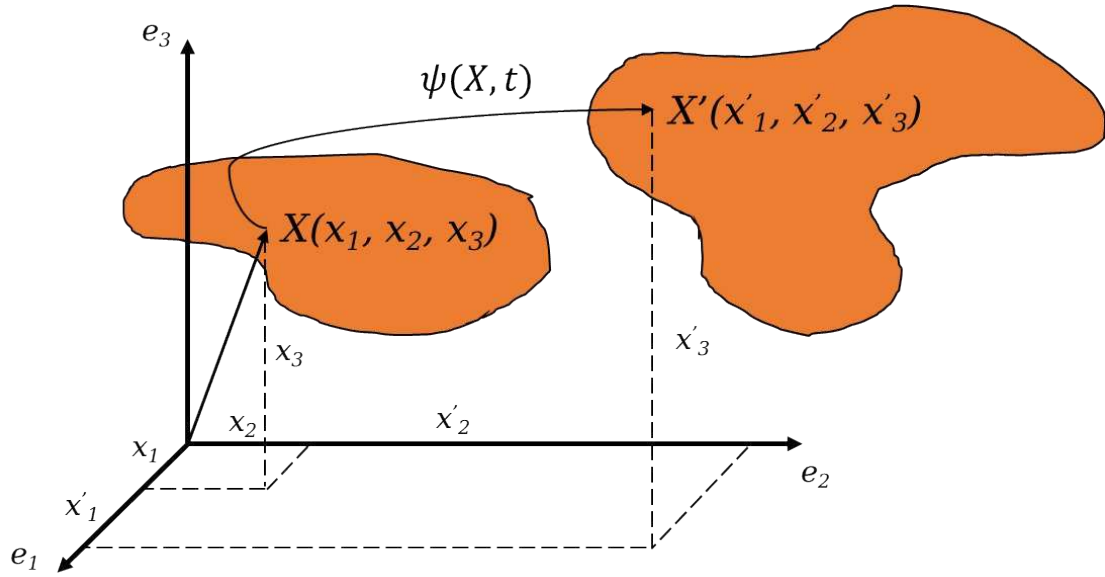


**Figure 1.1: The deformation of a point  $X$  in  $\Omega_0$  to  $X'$  in  $\Omega_1$ .**

Strain is defined as the gradient displacement with respect to the undistorted coordinate system. As the mechanical properties of a body are a function of the interatomic distances, it is a nonlinear quantity, which is better discussed in Section 1.1.2. However, for the sake of simplicity, this short introduction, we use the small-amplitude approximation for the displacement, which describes the strain  $S$  as:

$$S_{ij} = \frac{1}{2} \cdot \left( \frac{\partial u_i}{\partial x_j} + \frac{\partial u_j}{\partial x_i} \right). \quad (1.3)$$

This is a symmetrical second-rank tensor, therefore, with 6 independent components, and of physical dimensions of strain is in m/m. The variation of the lengths within the lattice caused by a displacement field causes a variation on the interatomic electrostatic potential energy and force.

The force between the interatomic planes is represented by the mechanical stress  $T$ , dimensionally expressed as  $\text{N/m}^2$ , can be either caused by defects or an applied strain, through the stiffness tensor  $c$ :

$$T_{ij} = c_{ijkl} S_{kl}. \quad (1.4)$$

The stiffness tensor is a large 4th rank tensor, with 81 elements, however, it can be demonstrated that the stress tensor is also symmetric, which, together with the symmetric nature of  $S$  reduces the independent values to 21. The inverse relation of (1.4) similarly defines the compliance tensor  $K$  as:

$$S_{ij} = K_{ijkl} T_{kl}. \quad (1.5)$$

### 1.1.2 Nonlinear strain

In the case of large oscillations, the linear approximation of strain in Equation (1.3) is no longer valid. In fact, the strain defined in Equation (1.3) is a special case of the more general strain Green-Lagrangian strain tensor [1]–[3]:

$$S_{ij} = \frac{1}{2} \cdot \left( \frac{\partial u_i}{\partial x_j} + \frac{\partial u_j}{\partial x_i} + \frac{\partial u_k}{\partial x_i} \cdot \frac{\partial u_k}{\partial x_j} \right). \quad (1.6)$$

In practice, for large displacement amplitudes, the nonlinearity of the strain is integrated in higher order stiffness tensors [4]. This effect is not the source of Acousto-Electric effect, but it is also a source of higher-order harmonics of propagating acoustic modes.

### 1.1.3 Equation of Motion of Acoustic Waves

The Equation of motion for acoustic waves is computed by considering the total force applied to an infinitesimal mass inside the object. For the sake of brevity, we assume it to be dimensionally equivalent to a small rigid cube, of mass  $dm$ , position  $X = (x_1, x_2, x_3)$  and edges long  $dx$  (the same can be demonstrated in different shapes). This small cube is pulled on each of its 6 faces, all of the area  $dx^2$  and position  $(x_1 \pm dx/2, x_2, x_3)$ ,  $(x_1, x_2 \pm dx/2, x_3)$  or  $(x_1, x_2, x_3 \pm dx/2)$ , from the stress, so that the total force operating on a single face of the object is found as:

$$F_i(x_i \pm dx/2) = dx^2 \delta_{ij} T_{ij}, \quad (1.7)$$

where the  $\delta_{ij}$  is the *Kronecker delta*, and  $x_i \pm dx/2$  subintends that the  $dx$  variation is only on the  $i$  axis. Considering the total volume, the total force applied to the cube is:

$$F_i(X) = dx^3 \frac{\partial T_{ij}}{\partial x_j}. \quad (1.8)$$

Now, by considering  $F_i = dm \cdot (\partial^2 u_i) / (\partial t^2)$ :

$$dm \frac{\partial^2 u_i}{\partial t^2} = dx^3 \frac{\partial T_{ij}}{\partial x_j}. \quad (1.9)$$

Finally, by considering the mass density  $\rho_{Mass} = dm/dx^3$  and the definition of the stiffness tensor (1.4), we find the displacement wave equation [5]:

$$\rho_{Mass} \frac{\partial^2 u_i}{\partial t^2} = \frac{\partial T_{ij}}{\partial x_j} = c_{ijkl} \frac{\partial^2 u_k}{\partial x_j \partial x_l}. \quad (1.10)$$

The solutions of the Equation (1.10) describe a multitude of possible waves that can propagate in the body. The velocity of propagation of the wave is strongly dependent on the stiffness factors of the crystal, in the special case of an isotropic medium, where each component  $c_{ij} = c$  we find:

$$v = \sqrt{\frac{c}{\rho_{Mass}}}. \quad (1.11)$$

Depending on the direction of propagation, we distinguish different propagating modes in surface acoustic waves (SAWs) and bulk acoustic waves (BAWs); both of which can be further differentiated in different modes, depending on the wave polarization, as shown in Figure 1.2 and described as:

- Pressure waves are represented by compression/relaxation in the propagation direction.
- Shear waves are a type of mechanical wave, where the displacement is transverse to the direction of propagation.
- Love waves, named after Augustus Edward Hough Love, are a surface shear wave with the direction of the displacement in the plane.
- Rayleigh waves, named after Lord Rayleigh, are a category of self-guided nondispersive surface waves, composed of a partial pressure and shear wave and propagating velocity similar to the latter.

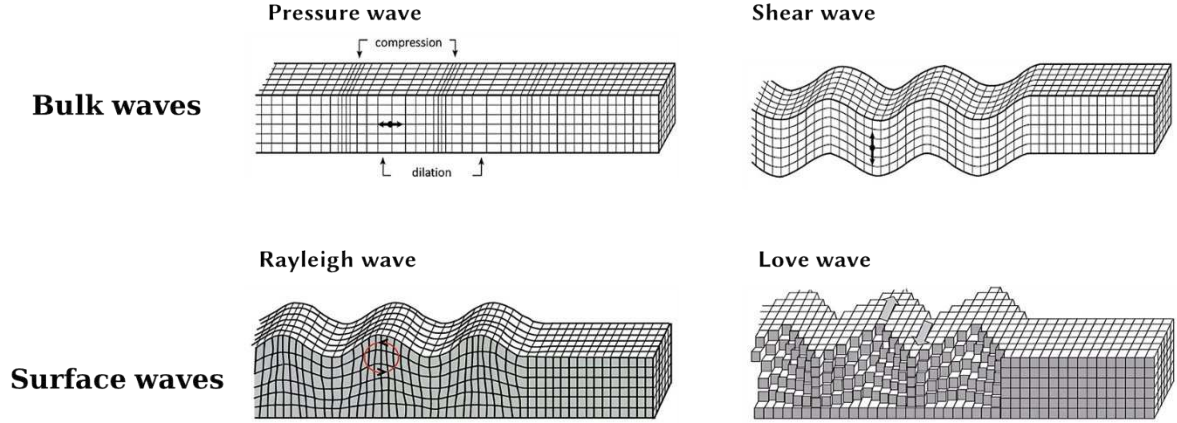


*Figure 1.2: Representation of the Bulk pressure and shear waves and of surface Rayleigh and Love waves (modified from [6]).*

### 1.1.4 Piezoelectric effect

The piezoelectric effect [5], [7], [8] is a physical property of certain materials where the application of certain mechanical stress causes a charge imbalance, which creates an electric field, as visualized in Figure 1.3. This effect is present in many organic molecular chains [9] and non-centrosymmetric inorganic crystals, like the dielectric  $\text{LiNbO}_3$  [4],  $\text{LiTaO}_3$  [4], quartz [10]–[12], but also various semiconductors such as GaAs [13]–[15], GaN [15], SiC [15], Ge [16]. Some examples of organic piezoelectric materials are the poly-L-lactic acids (PLLA) [17], the polyvinylidene fluorides (PVDF) [18] and various amino-acids [19].

Mathematically, the piezoelectric effect is described via the piezoelectric tensor, which is a rank-3 tensor which can be defined as coupling the electric field  $E$  with either the strain  $S$  or the stress  $T$ , by virtue of Equation (1.4).

The strain definition of the piezoelectric tensor  $e$  modifies (1.4) as:

$$T_{ij} = c_{ijkl}^E S_{kl} - e_{kij} E_k, \quad (1.12)$$

where the  $E$  superscript denotes stiffness taken when the electric field is constant. Similarly, the stress definition of piezoelectricity modifies (1.5) as:

$$S_{ij} = K_{ijkl}^E T_{kl} + d_{kij} E_k. \quad (1.13)$$

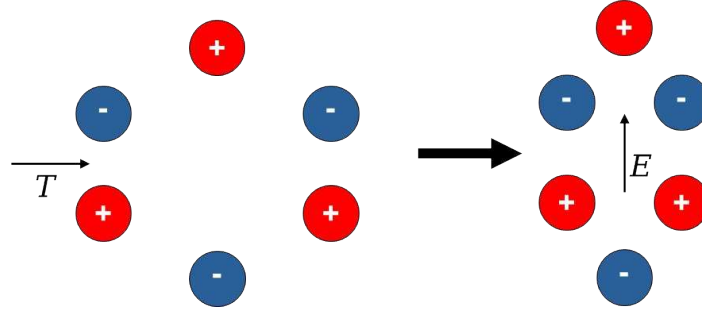


**Figure 1.3: Representation of the piezoelectric effect in a non-centrosymmetric crystal.**

As for the electric field, piezoelectricity modifies the definition of the electric displacement  $D$  in the piezoelectric as (1.14), for the strain-defined tensor, and (1.15) for the stress-defined tensor, where the  $S$  and  $T$  superscripts denote the values taken under a constant strain and stress respectively, and  $\varepsilon_{ij}$  are the components of the dielectric tensor of the piezoelectric.

$$D_i = \varepsilon_{ij}^S E_j + e_{ijk} S_{jk}. \quad (1.14)$$

$$D_i = \varepsilon_{ij}^T E_j + d_{ijk} T_{jk}. \quad (1.15)$$

This lets to rewrite the rest of the Maxwell equations for a piezoelectric as:

$$\nabla \cdot D = \frac{\partial D_i}{\partial x_i} = \rho_{Charge} + e_{ijkl} \frac{\partial S_{jk}}{\partial x_i} = \rho_{Charge} + e_{ijk} \frac{\partial^2 u_j}{\partial x_i \partial x_k}. \quad (1.16)$$

$$\nabla \cdot B = \frac{\partial B_i}{\partial x_i} = 0. \quad (1.17)$$

$$\nabla \times H = J + \frac{\partial D}{\partial t}. \quad (1.18)$$

$$\nabla \times E = -\frac{\partial B}{\partial t}. \quad (1.19)$$

The Equation (1.12) enables to modify the displacement wave Equation (1.10), by expressing the electric field as the gradient of the electrostatic potential  $V$  ( $E_i = -\partial V / \partial x_i$ ):

$$\rho_{Mass} \frac{\partial^2 u_i}{\partial t^2} = \frac{\partial}{\partial x_j} \left( c_{ijkl}^E S_{kl} - e_{kij} E_k \right) = c_{ijkl}^E \frac{\partial^2 u_k}{\partial x_j \partial x_l} - e_{kij} \frac{\partial^2 V}{\partial x_j \partial x_k}. \quad (1.20)$$

Equation (1.16) can also be rewritten in a similar manner as:

$$\varepsilon_{ij}^S \frac{\partial^2 V}{\partial x_i \partial x_j} + \rho_{Charge} - e_{ijk} \frac{\partial^2 u_j}{\partial x_i \partial x_k} = 0. \quad (1.21)$$

Finally, when computing piezoelectric-based effects, in non-magnetic materials, the magnetic portion of the wave can usually be approximated to 0 [5], [7]. This quasi-static approximation comes in virtue of the fact that the propagation velocity of the acoustic wave in piezoelectrics, in the order of magnitude of  $10^3$  m/s, is much lower than the electromagnetic wave, in the order of magnitude of  $10^7$  m/s ( $\partial D/\partial t|_{EM} \gg \partial D/\partial t|_{piezo}$ ).

Starting from Equations (1.14 – 1.21), it is possible to find the effective coupling coefficient between the electrical and mechanical energies  $K_{eff}$ , which is mathematically defined as a function of the stiffness tensor, the piezoelectric tensor  $e$  and the dielectric tensor [21]. In the case of an isotropic medium, we find:

$$K_{eff}^2 = \frac{e^2}{c\epsilon}. \quad (1.22)$$

**Table 1-1: SAW velocity and coupling coefficients for most common piezoelectric substrates with crystal cuts and propagating direction [7], [20].**

| <i>Material</i>                    | <i>Crystal cut</i> | <i>SAW axis</i> | <i>SAW velocity [m/s]</i> | $K_{eff}^2$<br>[%] |
|------------------------------------|--------------------|-----------------|---------------------------|--------------------|
| Quartz                             | ST                 | X               | 3158                      | 0.11               |
| LiNbO <sub>3</sub>                 | Y                  | W               | 3488                      | 4.5                |
| LiNbO <sub>3</sub>                 | YX-128°            | X               | 3992                      | 5.3                |
| Bi <sub>12</sub> GeO <sub>20</sub> | 110                | 1               | 1681                      | 1.4                |
| LiTaO <sub>3</sub>                 | Y                  | W               | 3230                      | 0.72               |
| LiTaO <sub>3</sub>                 | 36°-Y              | X               | 4160                      | 5.0                |
| h-SiC                              | 0001               | 0001            | 6832                      | 0.01               |
| GaAs                               | 1                  | 110             | <2841                     | 0.06               |
| h-ZnO                              | 0001               | 0001            | 2691                      | 1.12               |

Table 1-1 presents the electromechanical coefficient and SAW velocity of most common piezoelectric materials with the most commonly used crystal cut and wave direction [7], [20]. The data show an overall stronger coupling for piezo-dielectric material rather than for piezo-semiconductors.

### 1.1.4.1 Electrical and mass loading of a piezoelectric surface

When loading a piezoelectric substrate with a certain film, as represented in Figure 1.4, two important effects are applied on the propagating wave:

1. the discontinuity causes some of the wave's power to be either reflected back, or dispersed in the crystal as BAWs,
2. the propagation parameters of the wave change due to a local variation in the electric and mechanical properties.

The total change is a sum of both an electrically based effect, the electrical loading, and of a mechanically based effect, the mass loading. Both effects are well represented through a perturbation theory on the energy the wave [7], [22]:

$$\frac{v_f - v_0}{v_0} = \frac{\Delta v}{v_0} = \frac{\Delta W \cdot v_0}{2P}, \quad (1.23)$$

where  $\Delta W$ , expressed in  $J/m^2$ , represents the perturbation of the surface energy density in the elastic wave from the loading,  $v_0$  is the unperturbed propagation velocity of the acoustic wave,  $v_f$  is the final velocity after the application of the film and  $\Delta v = v_f - v_0$ .

Through mass loading, the wave propagation is shared between the piezoelectric and the film, meaning that the final wave velocity  $v_f$  and the propagation loss factor  $a_f$  are in between the two materials. The change in velocity for a homogeneous amorphous film with a defined thickness  $h$ , mass density  $\rho_f$ , shear modulus  $\mu'$  and first Lamé constant  $\lambda'$ , is found as [22]:

$$\frac{v_f - v_0}{v_0} = \frac{\Delta v}{v_0} = -\frac{\omega h \beta_0}{4P} \cdot (\rho_f v_0^2 |u_i|^2 - a_f |u_1|^2 - \mu' |u_3|^2), \quad (1.24)$$

where  $a_f = 4\mu' \cdot (\lambda' + \mu') / (\lambda' + 2\mu')$ .

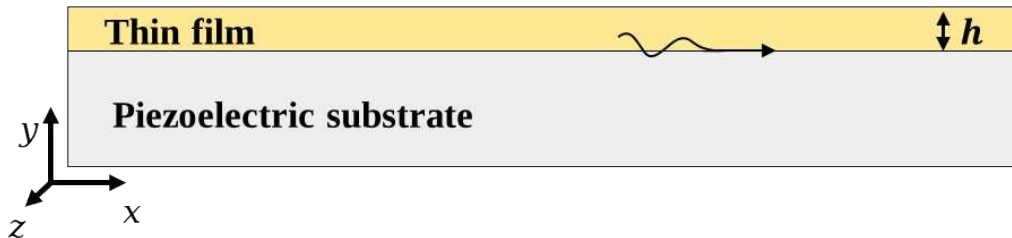


*Figure 1.4: A thin film of thickness  $h$  deposited on a piezoelectric substrate.*

As for the electrical loading, the application of a conductive film of homogeneous sheet resistivity  $\rho_{\square}$ , the electric field component of the piezoelectric gets partially short-circuited, causing an increase in damping and a relative decrease in the propagation velocity  $\Delta v/v_0$  (piezoelectric stiffening). It can be demonstrated that, for a quasi-2D electron gas, both the relative velocity variations  $\Delta v/v_0$  and the added damping  $\alpha$  are related to the electromechanics coupling coefficient  $K_{eff}^2$ , the resistivity  $\rho_{\square}$  and a factor  $\rho_M$  which depends on the unperturbed velocity  $v_0$  and the local dielectric constants, as Equations (1.25) and (1.26) [5], [7], [21], [23]:

$$\frac{v_f - v_0}{v_0} = \frac{\Delta v}{v_0} = -\frac{K_{eff}^2}{2} \cdot \frac{1}{1 + (\rho_M/\rho_{\square})^2} \quad (1.25)$$

$$\alpha = \beta_0 \cdot \frac{K_{eff}^2}{2} \cdot \frac{\rho_M/\rho_{\square}}{1 + (\rho_M/\rho_{\square})^2}. \quad (1.26)$$

Interestingly, for low resistivity values, the added damping is null and the relative velocity variation is purely dependent to  $K_{eff}$ :

$$\frac{\Delta v}{v_0} (\rho_{\square} = 0) = -\frac{K_{eff}^2}{2}. \quad (1.27)$$

### 1.1.5 Pyroelectric effect

The pyroelectric effect is a secondary effect of piezoelectricity, which appears in some piezoelectric materials [15], [24]. This effect is similar to piezoelectricity, in the way that it causes an electric polarization to arise due to temperature [25]–[28]. Differently than the thermoelectric effect, pyroelectricity depends on the absolute temperature variation rather than a thermal gradient, and is defined via the pyroelectric 1<sup>st</sup> rank tensor  $p$  so that the pyroelectric-caused electric displacement field  $D$  is:

$$D_i = p_i \cdot (T - T_0), \quad (1.28)$$

where  $T$  is the current temperature in  $K$  and  $T_0$  is the initial temperature.

Most physical discussions in this work follow a constant or quasi-constant temperature approximation, so that the pyroelectric electric is negligible. However, pyroelectricity must be taken into account and will be discussed in the device processing section, Chapter 2, and in the study of quantum Hall effect, because of the low temperatures required, Chapter 4.

## 1.2 Graphene on Piezoelectric Substrates

Since its discovery, graphene and other 2D materials have been seen as a significant opportunity to improve performances in AE-based devices because of its unique electrical and mechanical properties [20], [29]. In fact, the **low mass density and small thickness disturbs only slightly wave propagation** (1.24) and the exceptional electric properties can be used to greatly improve the performances of micro-acoustic devices [20].

### 1.2.1 Graphene

Graphene is a carbon allotrope where each atom is tightly bound to the nearest three in a  $120^\circ$  angles, forming a monolayer of carbon atoms arranged in a 2D hexagonal lattice, shown in Figure 1.5(d), which gives it exceptional electric, mechanical and thermal properties [30]–[33].

The C-C interactions in graphene are represented in Figure 1.5. Each carbon atom, Figure 1.5(a), is bound to each other via interatomic  $\sigma$  bonds, Figure 1.5(e), which derives from the  $sp^2$  hybridization of the  $2s$  and  $2p$  orbitals, Figure 1.5(b) and (c), leaving one free electron in the  $2p_z$   $\pi$  orbitals outside the plane, similarly to materials like cycloalkanes, which is free to move and one of the principal causes of its electrical properties [30], [34].

A precise explanation of the properties of graphene is found by applying the tight-binding approximation which, for this specific lattice, results in the electron band structure shown in Figure 1.6(a) that, in the proximity of the defined  $K$  and  $K'$  points, creates the linearly dispersive Dirac cones Figure 1.6(b), with the Fermi energy level in the middle [30], [33]. The specific Dirac cones make so that graphene is a semimetal with giant velocity for both electron and hole charges, of  $1/300$  the speed of light, in pristine graphene [30], [31], [33]. The 0 eV bandgap of pristine graphene makes it quite challenging to develop high-performance low-power CMOS-like structures, however, it must be noted that some nanostructures of graphene, like carbon nanotubes and some nanoribbons, can be engineered to create a small bandgap [33], [35].

Overall, the properties of graphene have enabled several breakthroughs in quantum research and in the development of high-speed electronics. For instance, the linear electron dispersion near the  $K$  and  $K'$  points is the cause of a **unique half-integer quantum hall** effect [36]–[38], and twisted multi-layer structures possess **unique superconductivity** [39], [40].

The 2D structure makes graphene extremely flexible and compatible with a variety of surfaces [41], [42] and the high ambipolar charge mobility enables the high-performance nanoelectronic devices [43]–[45].

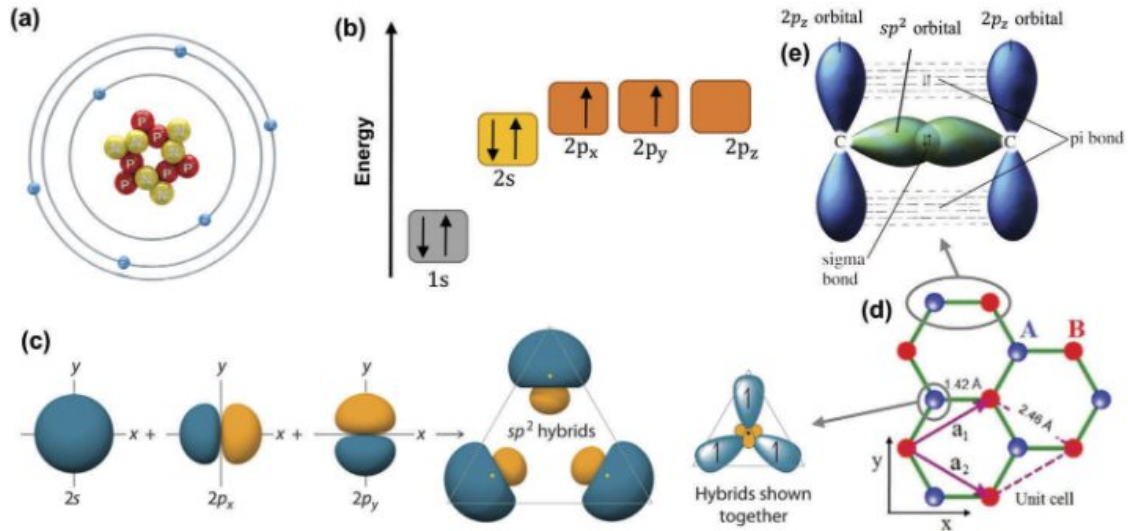


*Figure 1.5: (a) Atomic structure of a carbon atom. (b) Energy levels of outer electrons in carbon atoms. (c) The formation of  $sp^2$  hybrids. (d) The crystal lattice of graphene, where  $A$  and  $B$  are carbon atoms belonging to different sub-lattices,  $a_1$  and  $a_2$  are the unit-cell vectors. (e) The  $\sigma$  bond and  $\pi$  bond formed by  $sp^2$  hybridization [34].*

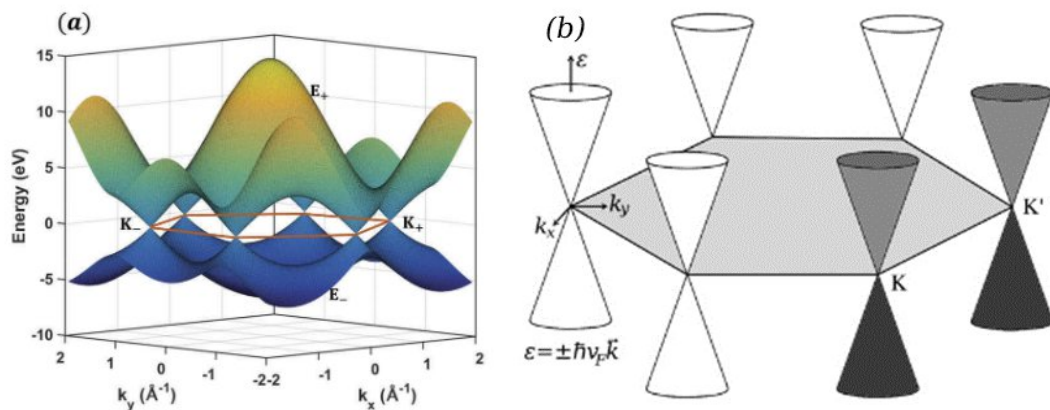


*Figure 1.6: (a) The band structure of graphene calculated via the tight-binding model, highlighting the Dirac cones at the  $K$  and  $K'$  points [34]. (b) The  $K$  and  $K'$  points in the reciprocal space [30].*

## 1.2.2 Production of Graphene

One of the challenges of graphene is its production and processing. Large-scale devices are usually produced via Chemical Vapor Deposition (CVD) [46]–[48] and need to be transferred, patterned, contacted via metal, etc. [49]. Depending on the substrate of destination, the various processing steps need to be tuned specifically. In particular, the piezoelectric and pyroelectric properties of substrates like LiNbO<sub>3</sub> require extra care. For this reason, the state of the art of production and characterization has been moved to the respective parts in Chapter 2, Chapter 3 and Chapter 4, in order to better explain the reasoning for the steps taken.

## 1.3 Acoustoelectronic devices

Acoustoelectronic devices make use of the nonlinear coupling between electric charges and acoustic waves inside a piezoelectric material. The strength of interaction is measurable via the Acousto-Electric (AE) effect, which is the **physical phenomenon of the generation of a small DC current in a piezoelectric semiconductor** or a semiconductor/piezo-dielectric heterostructure caused by the propagation of a mechanical displacement wave [8], [50].

Microscopically, the slow-moving piezoelectrically generated electric field couples with the charges possessing a similar wave vector component in the direction of the acoustic waves, as represented in Figure 1.7, generating a net current flow  $I_{AE}$ . Mathematically, the generated AE current depends linearly on the acoustic power  $P_A$ , a coupling factor  $\alpha_{AE}$ , the charge mobility  $\mu$  and the acoustic velocity  $v_0$  [51], [52]:

$$I_{AE} \cong \mu \cdot P_A \cdot \alpha_{AE} / v_0. \quad (1.29)$$

By defining an AE coupling figure of merit  $FOM_{AE} = v_0 \cdot I_{AE} / P_A = \alpha_{AE} \cdot \mu$ , the Equation (1.29) can be rewritten as:

$$I_{AE} \cong FOM_{AE} \cdot P_A / v_0. \quad (1.30)$$

The sign of the measured current depends on the propagating direction of the propagation direction of the major charge carriers, indicating the possibility of using this effect to **analyze the doping type** and the charge carrier mobility.

The inverse effect enables to amplify the acoustic wave through a DC current [8], [53]–[55], which causes a **distributed amplification process** that is the piezoelectric

equivalent to traveling wave tube (TWT) amplifiers and a complete theory of the phenomenon is similarly explained [54]. A simplified model has also been developed, that shows the dependency of the amplification on the drift velocity of the charge carriers  $v_d$  relative to the acoustic propagation speed  $v_0$  [19], [53]:

$$\alpha_{AE} = \beta_0 \cdot \frac{K_{eff}^2}{2} \cdot \frac{\gamma \rho_M / \rho_{\square}}{1 + (\gamma \rho_M / \rho_{\square})^2}, \quad (1.31)$$

where  $\beta_0 = \omega_0 / v_0$  is the wavenumber of the acoustic wave,  $\gamma$  is a factor which depends on the acoustic velocity  $v_0$  and the charges drift speed  $v_d$ :

$$\gamma = \frac{v_0 - v_d}{v_0}. \quad (1.32)$$

Equation (1.32) reveals that the AE interaction is maximized when  $v_0 \approx v_d$ . Interestingly, for some piezoelectric semiconductors, the AE coupling has been shown to explain the unusual ohmic response, where the phonons generated through shot noise under high electric fields couple with the moving charges causing a sharp variation in the IV curve [21], [56], [57].

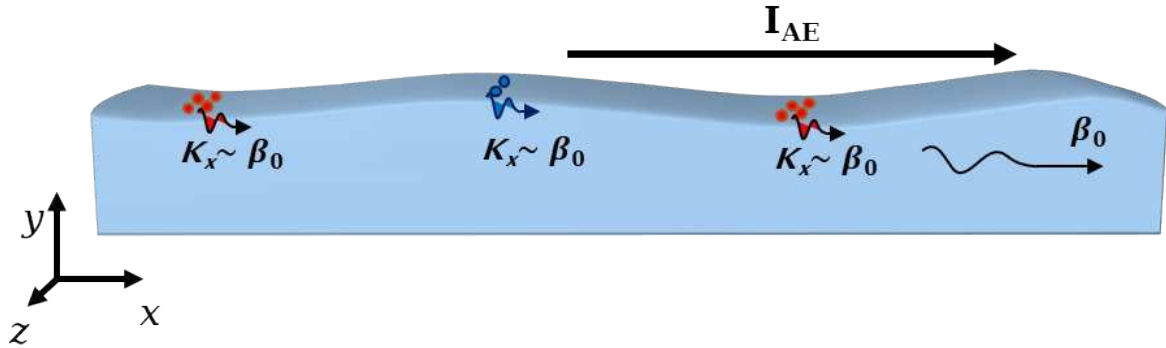


**Figure 1.7: Representation acoustoelectronically coupled electrons (blue) and holes (red) in a piezo-semiconductor, generating an Acousto-Electric current  $I_{AE}$ .**

### 1.3.1 Reports on AE current

The usage of semiconductive piezoelectric substrates for acoustoelectronic applications has the advantage that the designs can be manufactured without adding extra thin films of materials, avoiding phonon scattering due to discontinuities and mass loading effects. In principle, this would cause lower acoustic damping and simpler processing. However, the low

electromechanical coupling coefficient of piezo-semiconductors, as displayed in Table 1-1, makes them overall unattractive for these kinds of applications. In fact, only few reports have been performed in exploring the AE effect via the AE current  $I_{AE}$  in pure piezoelectric semiconductors such as CdS [56] and Ge [16], [58], [59]. Instead, piezo-dielectrics show considerably stronger electromechanical coupling coefficient  $K_{eff}$  [5], [7], which enables engineering of heterostructures possessing far higher AE performances.

Several studies have been performed on acoustoelectrically generated current for semiconductor/piezodielectric heterostructures on a variety of substrates like LiNbO<sub>3</sub> [52], AlGaAs [51], quartz [60]. The best results achieved for each substrate type are reported.

- *Ingebrigtsen* demonstrated a AE current of  $\sim 5 \mu\text{A}$  in a CdS thin-film on Y-cut quartz [60] using for a 40 MHz SAW excitation and input power 1 W, as shown in Figure 1.8.
- As shown in Figure 1.9, *Rotter et al.* reported a strong AE current  $\sim 20 \mu\text{A}$  in a top-gated GaAs/LiNbO<sub>3</sub> heterostructures at an optimized gate voltage for a SAW signal of 10 dBm and frequency 344 MHz [52].

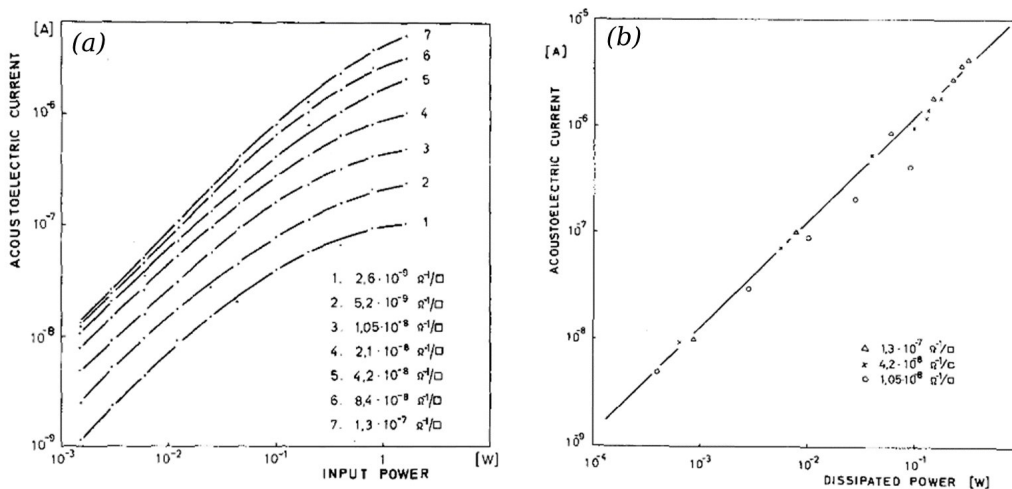


**Figure 1.8: Characterization of  $I_{AE}$  vs (a) input power at 40 MHz for CdS/quartz (y-cut) heterostructure for different doping values and (b) with the power dissipated from the unperturbed propagation extracted [60].**

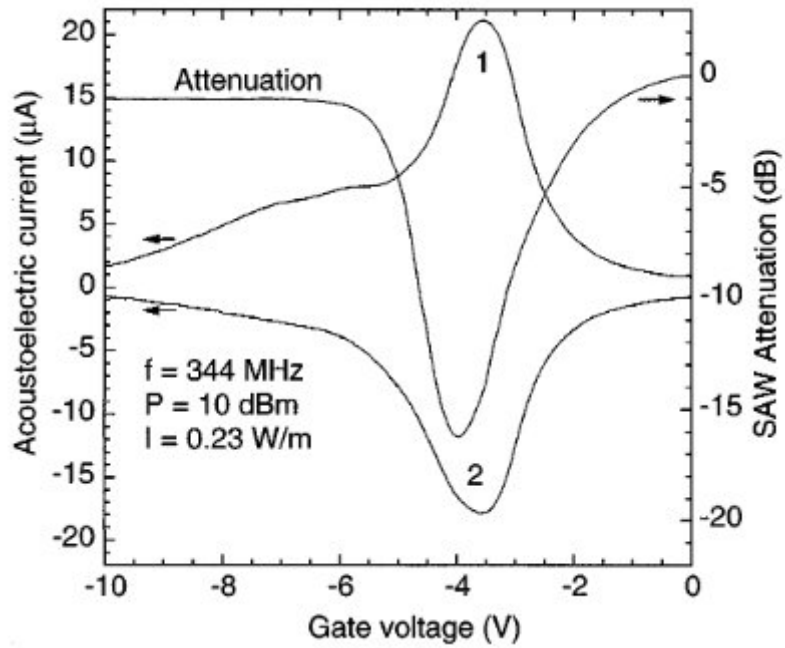


*Figure 1.9: SAW attenuation and  $I_{AE}$  vs gate bias for a top-gated GaAs/LiNbO<sub>3</sub> heterostructure, for input SAW signal at frequency 344 MHz and power +10 dBm. Curves 1 and 2 correspond to opposite directions of SAW propagation [52].*

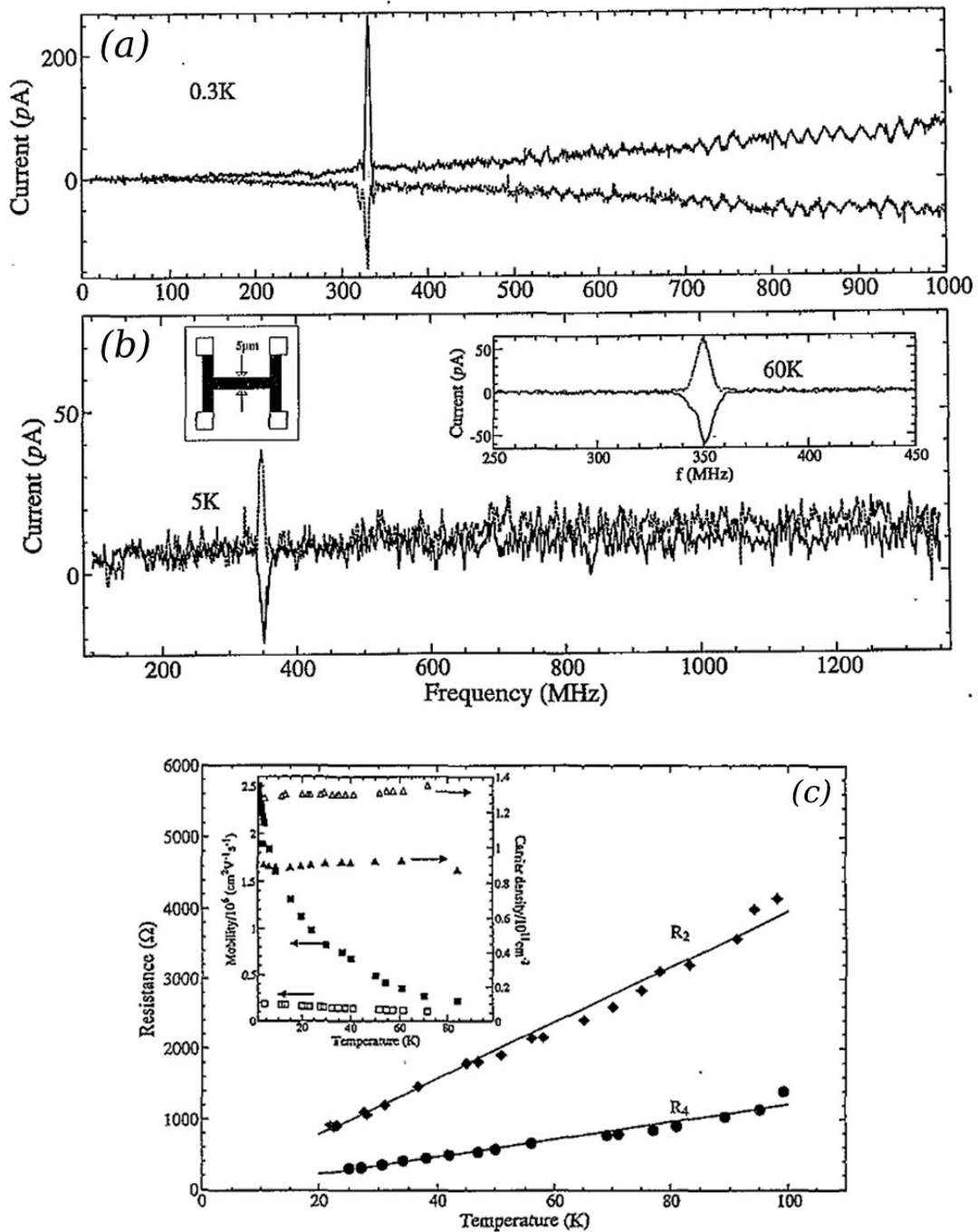


**Figure 1.10:**  $I_{AE}$  vs input frequency for an GaAs/AlGaAs heterostructure and a SAW signal between -18 dBm and -10 dBm input propagating in either positive and negative direction. The data in (a) 0.3 K, (b) 5 K and 60 K show a temperature dependency in part due to variations in (c) resistivity and mobility [51].

- Shilton *et al.* (Figure 1.10) performed a characterization of AE current on a GaAs/AlGaAs heterostructure, they explored the variance of AE current at different temperatures via

a hybrid Hall bar geometry and found  $I_{AE} \approx 250$  pA for a SAW frequency of 330 MHz and input power between -18 dBm and -10 dBm [51].

The results shown demonstrate good coupling between piezoelectrics and semiconductors, which is partially limited by **mass loading**.

### 1.3.1.1 Graphene devices

The extremely light nature of graphene monolayers, along with its exceptional electric parameters, allows for graphene-piezoelectric heterostructures to possess the advantage of low disturbance of the mechanical field present in air-gapped heterostructures, together with a simpler production process [20]. In virtue of this, a fair amount of research has been dedicated in exploring the AE coupling of graphene/piezoelectric heterostructures.

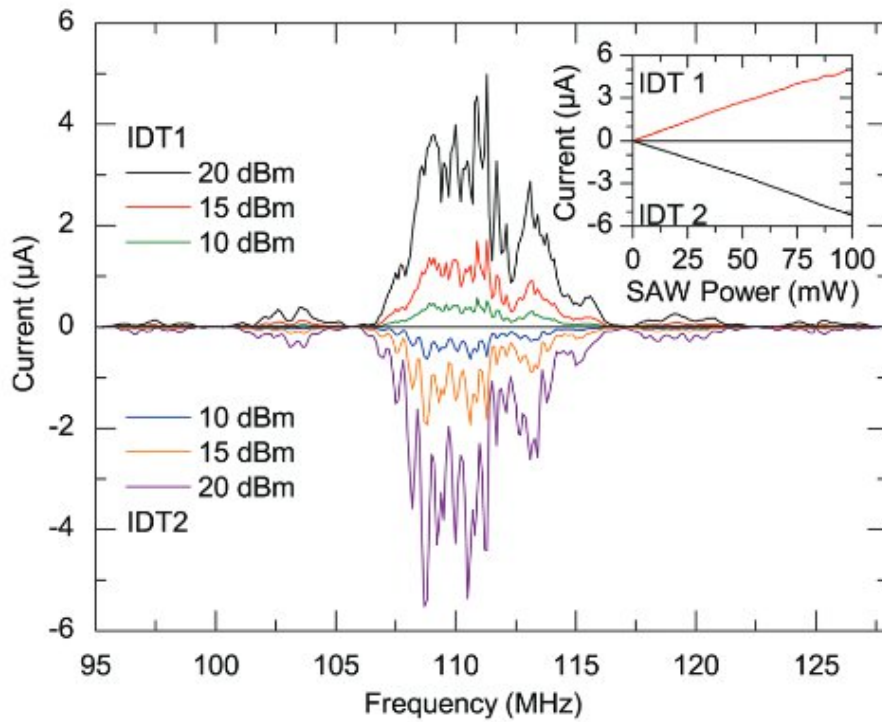


**Figure 1.11:**  $I_{AE}$  vs SAW frequency as applied to each input Inter-Digital Transducer (IDT) for graphene on  $YX-128^\circ$   $LiNbO_3$ . Inset: Peak AE current as a function of applied power to the two IDTs [29].

The first studies of AE current on graphene have been performed for CVD graphene transferred on a  $YX-128^\circ$   $LiNbO_3$  by *Miseikis et al.* (Figure 1.11) where they managed to extract a peak current of 5  $\mu$ A for  $P_A=20$  dBm [29]. Other studies using a variety of substrates

such as LiNbO<sub>3</sub> [29], [37], [61]–[65], LiTaO<sub>3</sub> [66], SiC [67] and Ca<sub>3</sub>NbGa<sub>3</sub>Si<sub>2</sub>O<sub>14</sub> (CNGS) [68].

All of the reported AE coupling experiments with graphene are reported in Table 1-2, alongside with the substrate crystal type and cut, resistivity of the graphene  $\rho_{\square}$ , the extracted mobility  $\mu$  and the quality factor of the AE coupling  $FOM_{AE}$ .

The data show an **effective charge mobility for AE-generated currents considerably lower than the values found via the Hall-effect characterization**, possibly demonstrating an incomplete understanding of AE effect on graphene heterostructures.

Unsurprisingly, the best coupling has been reported for graphene on YX-128° LiNbO<sub>3</sub> substrates, due to the higher  $K_{eff}^2$ , although not much has been reported for other substrates. For example, one would expect similar results of YX-36° LiTaO<sub>3</sub>, to YX-128° LiNbO<sub>3</sub> in virtue of the parameters shown in Table 1-1, however, *Okuda et al.* [66] demonstrated a much lower  $FOM_{AE}$ , probably due to the graphitic source or the process. Another important observation is that the data available to demonstrate a trend between  $\rho_{\square}$  and the SAW frequency, in agreement with Equation (1.31). In fact, to improve AE coupling, two strategies can be adopted:

1. increase the resistivity  $\rho_{\square}$  to the optimal  $\rho_{\square}$  of the substrate ( $\sim 800 \text{ k}\Omega/\square$  for YX-128° LiNbO<sub>3</sub>),
2. increase the SAW frequency.

The resistivity increase has been achieved either by removing dopant gases through vacuum [61], [69], cooling down the devices [37], [69] or doping through electric field through a top-gated [63], [67] or a back-gated [37].

Gated structures show a tunability of the AE effect, however, they possess some notable disadvantages. Indeed, the added complexity of a top-gate negates most of the advantages of using graphene for the added mass loading, while the usage of bottom-gate has the secondary effect of modifying the mechanical properties of the piezoelectric. The best results have been achieved for **graphene in vacuum** by *Bandhu et al.*, which reported a coupling factor of 23280 cm<sup>2</sup>/Vsm for the highest resistivity of 154 k $\Omega/\square$  for excitation frequency of 356 MHz [61].

Still, both approaches would be essentially unusable in a real commercial device. In order to achieve significant results, a more effective strategy would instead be the **tuning of the resistivity** directly in the production process and the **usage of higher SAW frequencies**.

*Table 1-2: Comparison of values of  $\alpha$  and  $\mu$ . Values marked ‘-’ were not available from the authors, values marked ‘\*’ were computed from the data, values marked ‘\*\*’ were estimated assuming a SAW propagation velocity from available data regarding various crystal cuts.*

| Ref           | Substrate                                      | Cut     | $\rho_{\square}$<br>[k $\Omega$ / $\square$ ] | $\alpha_{AE}$<br>[m <sup>-1</sup> ] | $\mu$<br>[cm <sup>2</sup> /Vs] | $FOM_{AE}$<br>[cm <sup>2</sup> /Vsm] | Freq.<br>[MHz]       |
|---------------|--|---------|---|-------------------------------------|--------------------------------|--------------------------------------|----------------------|
| [29]          | LiNbO <sub>3</sub>                             | YX-128° | 4.8   | 29*                                 | 68*                            | 2001*                                | 110                  |
| [61]          | LiNbO <sub>3</sub>                             | YX-128° | 154<br>(vac.)                                 | 2910*                               | 8                              | 23280                                | 11,32,<br>97,18, 356 |
| [69]          | LiNbO <sub>3</sub>                             | YX-128° | 77*<br>(vac.)                                 | 1100                                | 15                             | 16500                                | 11,32, 269           |
| [62]          | LiNbO <sub>3</sub>                             | YX-128° | -   | 150                                 | 5                              | 750                                  | 332                  |
| [65]          | LiNbO <sub>3</sub>                             | YX-128° | 10.5  | 205                                 | 10                             | 2060*                                | 356                  |
| [63]          | LiNbO <sub>3</sub>                             | YX-128° | -(gate)                                       | -                                   | -                              | 38.7*                                | 337                  |
| [70],<br>[71] | LiNbO <sub>3</sub>                             | YX-128° | 0.9-1.5<br>(gate)                             | -                                   | -                              | -                                    | 331                  |
| [64]          | LiNbO <sub>3</sub>                             | YZ      | -   | -                                   | -                              | 6.16· 10 <sup>-9</sup> *             | 114.5                |
| [37]          | LiNbO <sub>3</sub> /<br>SiO <sub>2</sub> /p-Si | -       | -(gate,<br>4.2K)                              | -                                   | -                              | 300-350**                            | 1878                 |
| [67]          | SiC  | -       | -(gate)                                       | -                                   | -                              | 30**                                 | 1990                 |
| [66]          | LiTaO <sub>3</sub>                             | YX-36°  | -   | -                                   | -                              | 22                                   | 174                  |
| [68]          | CNGS   | Y       | -   | -                                   | 4                              | -                                    | 710                  |

## 1.4 Surface acoustic wave devices

The coupling of mechanical and electromagnetic waves in piezoelectric solids has enabled the development of several groundbreaking technologies that are at the heart of high-end telecom systems [5], [7], [72]. By the transduction of the electromagnetic waves into mechanical waves, it has been possible to greatly reduce the size of filters due to the much lower

propagation velocity ( $\approx 4000$  m/s vs  $\approx 3 \cdot 10^8$  m/s), moreover, the interaction between the coupled displacement-electric field and a separate conductor has been used in developing nonlinear devices for signal processing [72], [73].

### 1.4.1 Linear SAW filters

For SAW-based devices, the transduction of energy between the electromagnetic and mechanical fields is performed via specifically engineered mechanically resonating structures called **Inter Digital Transducers** (IDTs). It can be demonstrated that the frequency response of an IDT depends on the period of the structure  $\lambda$  and the aperture  $A$ , defined as the overlap between fingers [5], [7], [74]. In particular, IDTs with periodically spaced fingers transmit power around the frequency  $f = v_0/\lambda$  and the transfer function  $H(f)$  is geometrically determined by the space distribution of the aperture [7], [74]–[81].

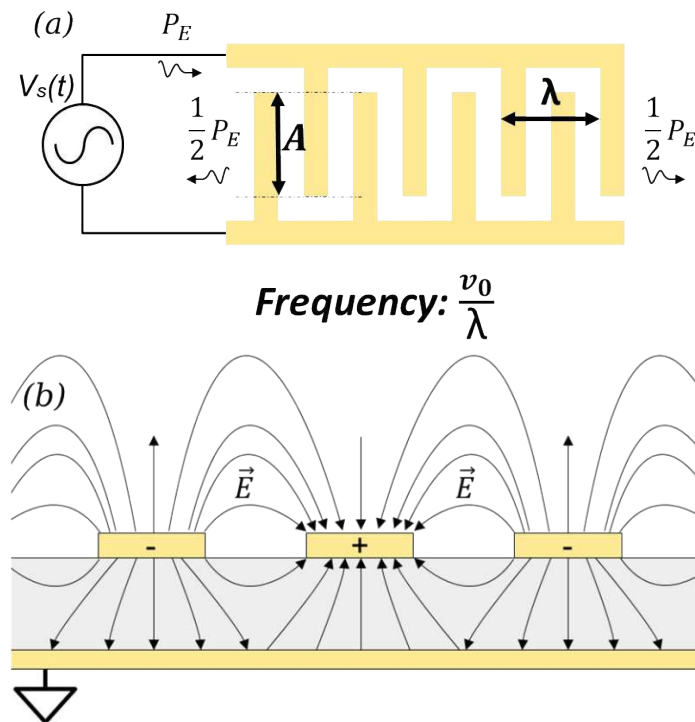


*Figure 1.12: Representation of (a) a symmetrical IDT with constant aperture  $A$  and equally spaced fingers with period  $\lambda$ . (b) Representation of the electric field in an IDT.*

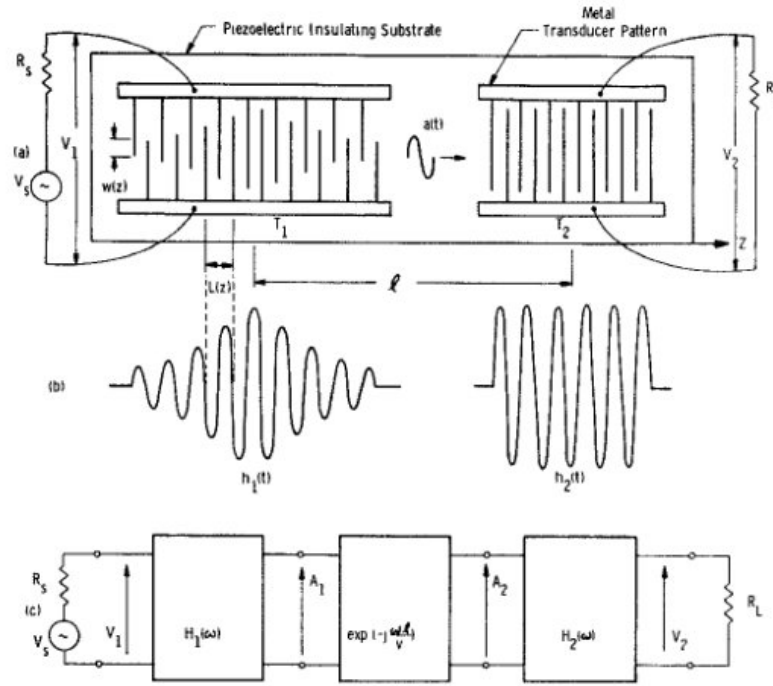


**Figure 1.13:** A surface-wave band-pass filter. (a) Representative device geometry. (b) Effective impulse response. (c) Representation for linear filter theory. [76].

Two IDTs can be placed in front of each other, as shown in Figure 1.13, creating a **SAW delay line** [74], [76], [78], [81]–[83]. This can be used as a frequency filter with an high electrical input-output insulation and a fixed response [7]:

$$H_{tot}(f) = H_1(f) \cdot H_2^*(f) \cdot e^{-f \cdot T}. \quad (1.33)$$

where  $H_1(f)$  and  $H_2(f)$  are the frequency response of the sender and receiver IDT, and  $T$  is the propagation delay.

Another interesting design possibility of using IDTs is that, as it is possible to choose their exact response through their geometries, it is possible to use a delay line as a fixed frequency SAW convolver, to extract a specific phase or frequency encoded features from the input [5], [7], [84], one example is reported in Figure 1.14, where the spacing in a receiver transducer is hard-coded to receive a chirp-modulated input [5].

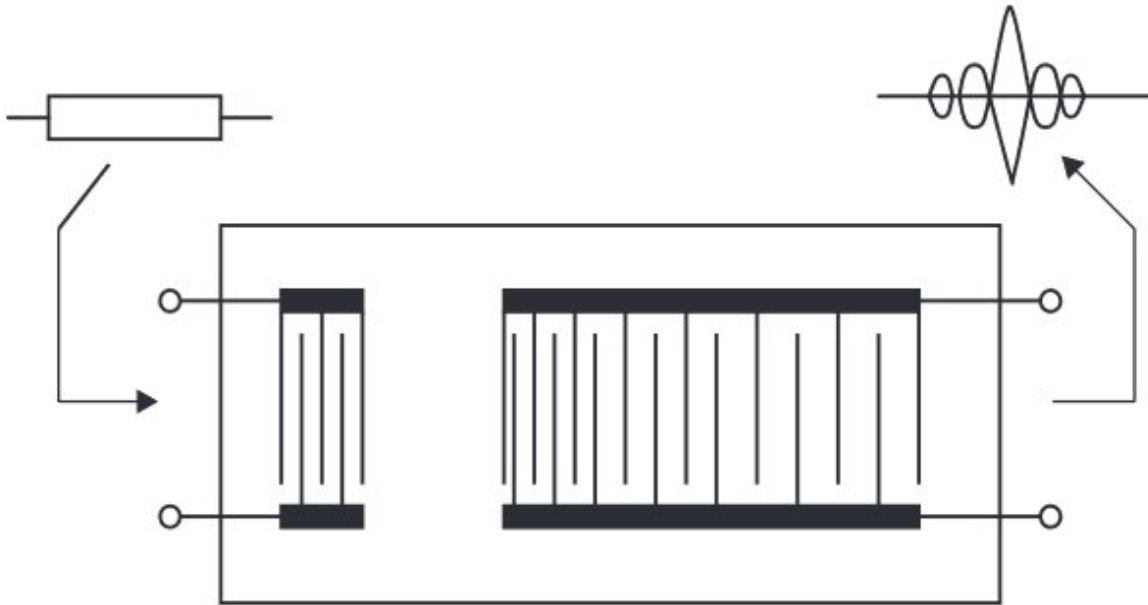


**Figure 1.14:** A SAW delay line with a chirp-encoded receiver IDT [5].

As represented in Figure 1.12, IDTs are composed of several conductive fingers. As the device is symmetric, IDT designs are usually a-directional, meaning that both converted electromagnetic and mechanical waves are split equally in both propagating directions, as is represented in Figure 1.12(a), meaning that delay lines using bidirectional IDTs possess an insertion loss  $> 6$  dB [5].

More complex designs can be used to achieve the unidirectionality of IDTs, mainly by reflecting back the power from one side using a SAW reflector [5], [7], [85]. However, depending on the coupling of the substrate, efficient SAW reflectors need to be quite large and there is a cost in the dynamic response of the transducer [5].

## 1.4.2 Nonlinear devices

Nonlinear SAW devices either use a nonlinear mechanical response caused by a deposited metal film [5], [7], [73], [86], [87] or the nonlinear interaction of the electric field component of the piezoelectric wave with a semiconductor [54], [83], [88]–[90].

### 1.4.2.1 AE Amplifiers

Non-reciprocal amplification of acoustic waves is achieved via the indirect AE effect described in Section 1.3 and can be performed for BAW waves in piezoelectric semiconductors, like CdS [91]–[93] or GaN [94], or SAW waves through both piezo-semiconductors [93] or piezo-dielectric/semiconductor heterostructures [55], [95]–[97]. Many types of SAW AE amplifiers are possible, which can be integrated into more complex designs like SAW isolator and gyrators [95].

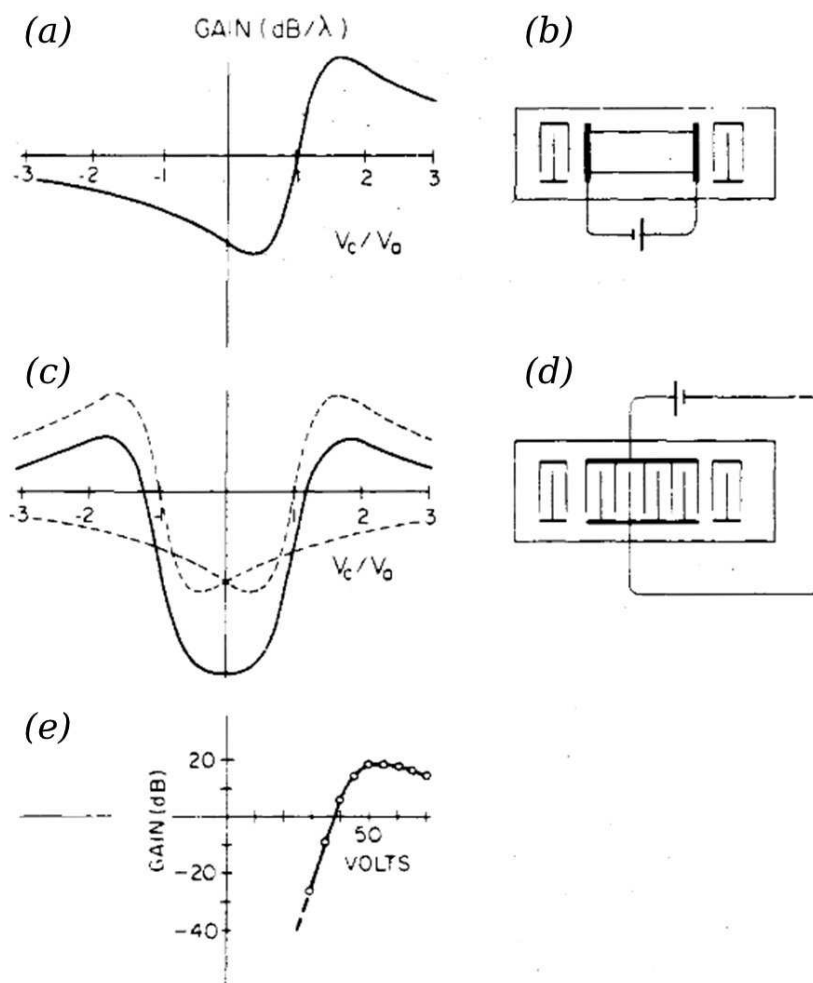


**Figure 1.15: Typical gain vs  $v_d/v_0$  and schematic representation for (a), (b) a mono-directional AE amplifier and (c), (d) a bi-directional AE amplifier. (e) Bi-directional amplification for a CdSe/LiNbO<sub>3</sub> heterostructure [90], [99].**

The simplest design is the non-reciprocal combined medium amplifier (CMA) shown in Figure 1.15(b), which is based on a delay line and amplifies or attenuates SAW waves depending on the direction of propagation of it and the electric current. With this design,

researchers have achieved strong acoustic gain, for instance, as shown in Figure 1.16, *Lemanov et al.* demonstrated a gain of  $\sim 70$  dB/cm using a pure CdS substrate [8], or *Hackett et al.* found a gain of  $\sim 1100$  dB/cm, as shown in Figure 1.17, for a device of InGaAs/LiNbO<sub>3</sub> cut YX-41° [95].

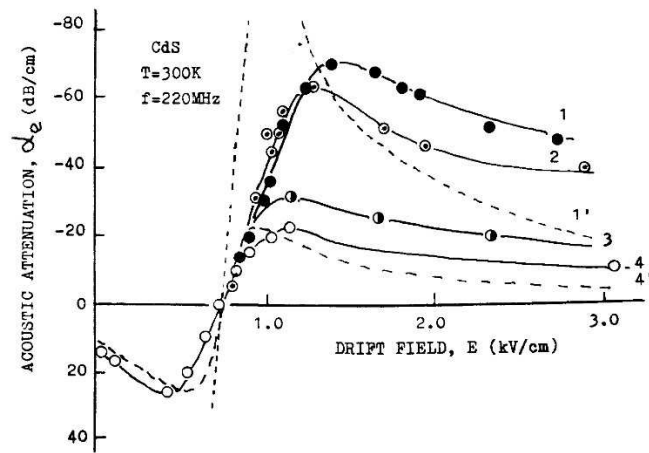


**Figure 1.16:** Amplification of the acoustic field through AE coupling for a CdS substrate at 220 MHz [8].

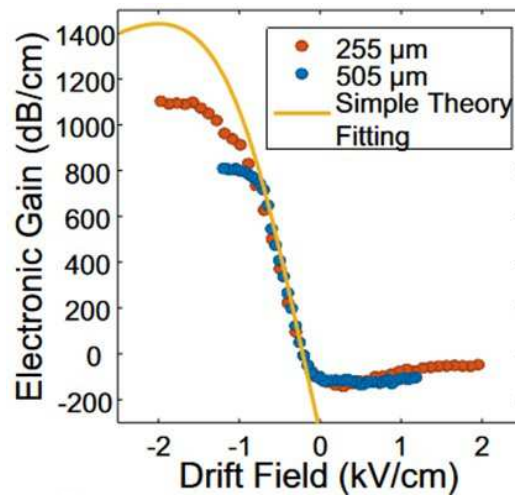


**Figure 1.17:** AE amplification from a InGaAs/LiNbO<sub>3</sub> heterostructure (YX-41° cut) [95].

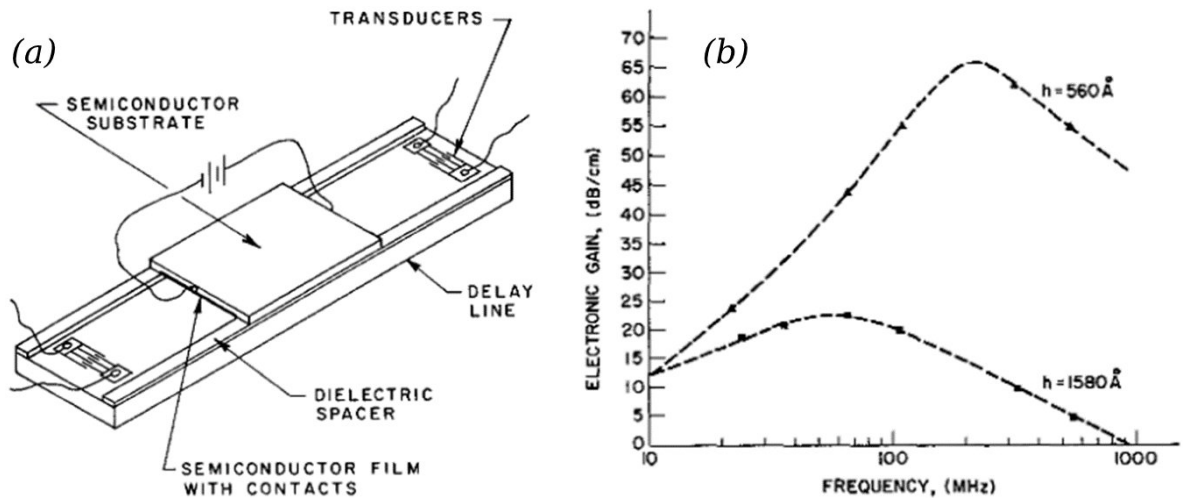


**Figure 1.18:** (a) An air-gapped 15.2 mm Si/gap/LiNbO<sub>3</sub> YZ cut SAW amplifier and (b) results for two different Si-LiNbO<sub>3</sub> distances  $h$  [98].

The separated medium amplifier (SMA), shown in Figure 1.18(a), is a modification of the simple non-reciprocal design where the semiconductor and piezoelectric are not in direct contact, but kept distant through a small air gap, to couple only with the electric field, avoiding power loss caused by mass loading [55], [88], [98]. However, the process of transferring a semiconductor on the piezoelectric is more challenging than for a standard CMA and the coupling can be somewhat limited by the distance. Notably, as shown in Figure 1.18(b), *Lakin et al.* managed to achieve a gain of  $\sim 65$  dB/cm at  $\sim 300$  MHz for a  $560 \text{ \AA}$  gapped Si//LiNbO<sub>3</sub> heterostructure [98].

Another possible design is a bi-directional amplifier, shown in Figure 1.15(d), which uses the fact that the AE amplification is usually stronger than AE attenuation (Figure 1.15(c)) [89]. This design was first shown by *Soile et al.* which reported a maximum gain of  $\sim 20$  dB, as shown in Figure 1.15(e) [90], [99].

#### 1.4.2.1.1 Graphene-based AE amplifiers

Very few research efforts have been given to AE amplifiers using a graphene/piezoelectric architecture. As of the time of writing, the literature available is divided into one theoretical analysis by *Nunes* [100] for a graphene/GaN architecture, and some experimental analysis by the groups of *Insepol et al.* [101], [102] and *Malocha et al.* [70], [71], using completely different designs and analysis process. In particular, *Malocha et al.* proposed an interesting architecture, shown in Figure 1.19, which was based on an array of  $127 \text{ \mu m}$ -long and  $300 \text{ \mu m}$ -wide graphene field-effect transistors (GFET) on a YX-128° LiNbO<sub>3</sub> substrate.

They generated and measured the acoustic signals via IDTs operating at 311 MHz and achieved a gain of  $\sim 0.4$  dB for an applied  $V_{DS}$  of 2 V and an average resistivity of their processed graphene of  $975 \Omega/\square$  from a  $V_{GS}$  of 0 V.

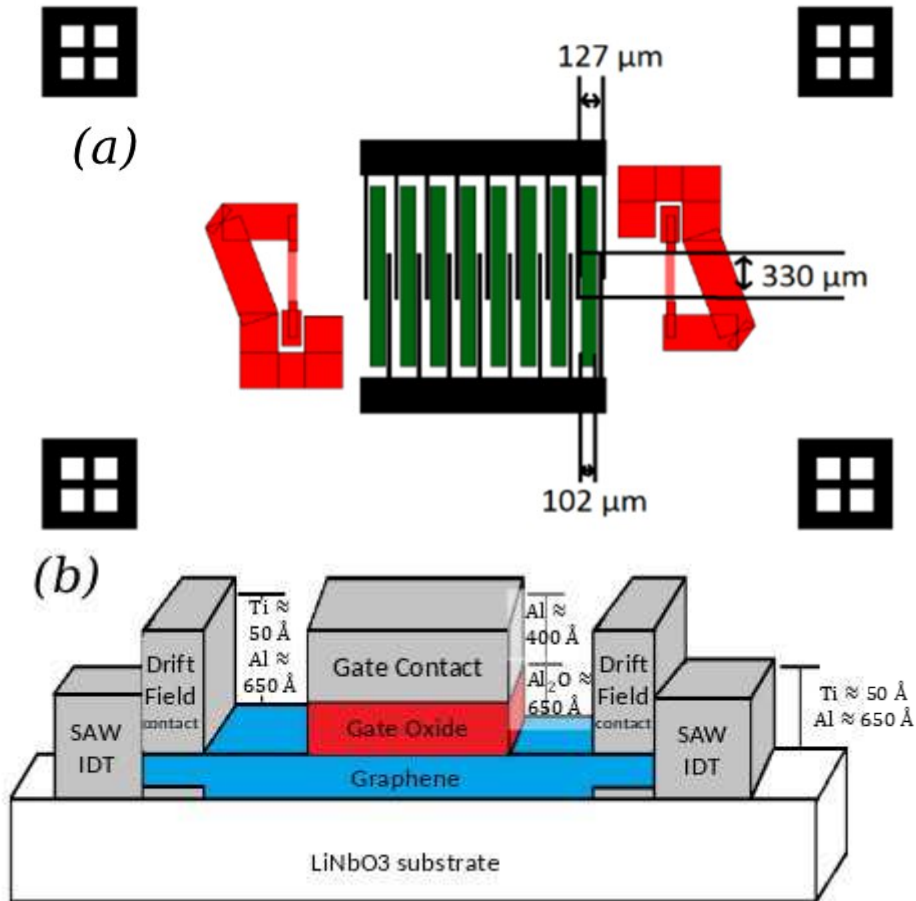


**Figure 1.19:** (a) The graphene/LiNbO<sub>3</sub> amplifier architecture proposed by Malocha *et al.* and (b) the representation of the structure of the GFET used [70], [71].

The design proposed by Insepol *et al.* is much simpler, as shown in Figure 1.20(a), their device is composed of a delay line operating at 471 MHz using a Ca<sub>3</sub>TaGa<sub>3</sub>Si<sub>2</sub>O<sub>14</sub> (CTGS) substrate, a wide graphene sheet with contacted with 10  $\mu\text{m}$ -wide Al contacts at a distance of 300  $\mu\text{m}$ . Differently from the other reports, they measured the amplitude of the amplified wave through an X-ray diffractometer, by looking at the variation in the rocking curves, in Figure 1.20(b), and reported an amplification of  $\sim 33$  dB/cm, which was confronted with older reports of [88], [92], [96].

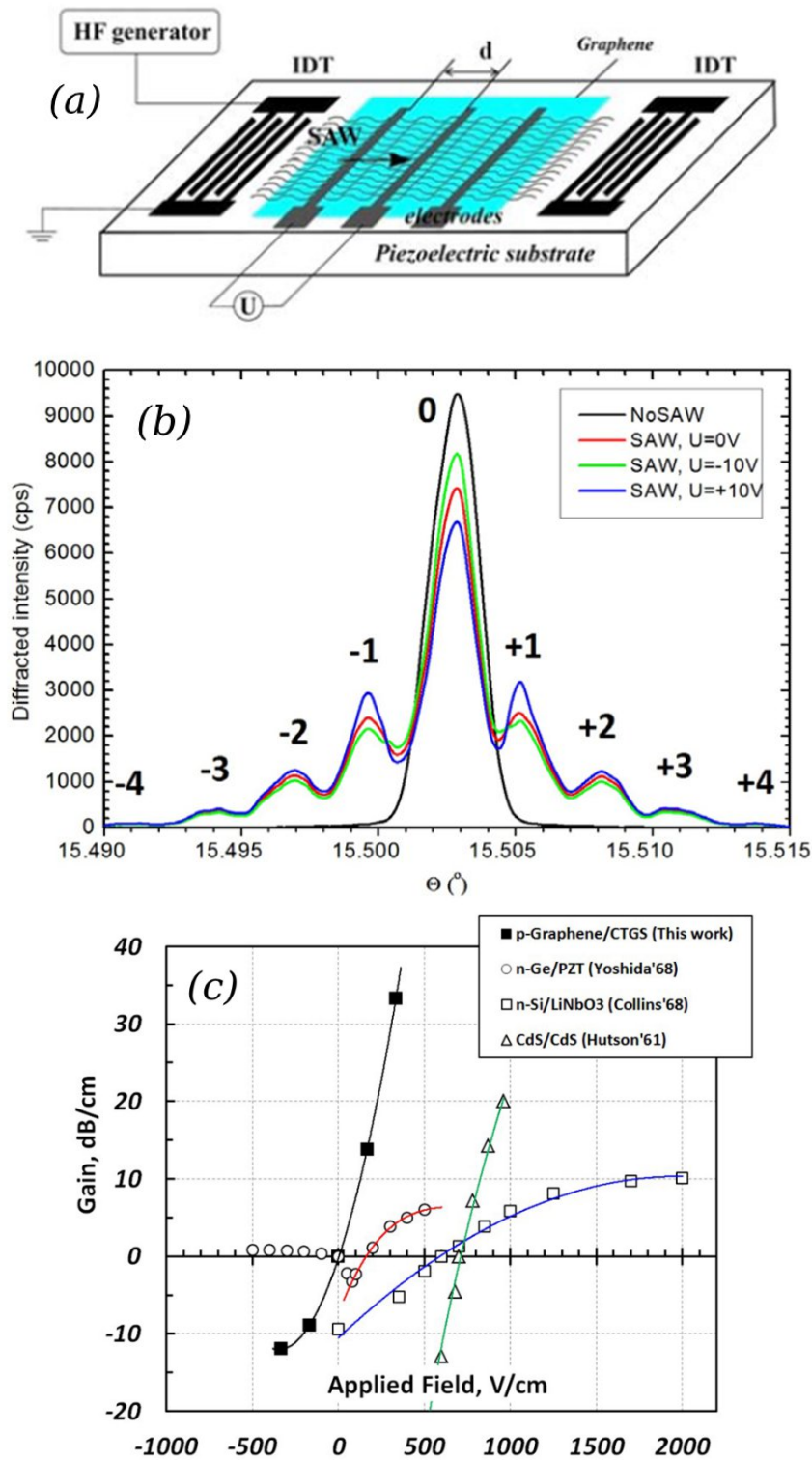


**Figure 1.20:** (a) The graphene/CTGS amplifier reported by Insepol et al. and their results (b) in the form of the rocking curves from X-ray analysis and (c) as dB/cm vs other results from Yoshida et al., Collins et al. and Hutson et al. [88], [92], [96].

Overall, currently available results did not show a significant improvement of AE amplification using graphene-based heterostructures. However, as shown in Section 1.3.1 and

Section 1.3.1.1, results of AE coupling of graphene/piezoelectric heterostructures has been shown to be at least in the range of other semiconductors, which indicates that there is a fair room for improvements.

### 1.4.2.2 Acoustoelectronic convolvers

Convolvers are a family of nonlinear acoustoelectronic device which allows for a **fully-analog** computation of the convolution in the time domain between two arbitrary input waves [5], [7], [73]. For SAWs, this is achieved through the **nonlinear interaction** between two slowly propagating waves under a nonlinear medium which, through the **piezoelectric** and **AE** effect, performs a space-averaging of the nonlinear contributes, corresponding to the convolution integral [5], [7]. The nonlinearity used in convolvers is either **mechanical**, introduced by the mechanical discontinuity caused through a metallic film, or **electrical**, through the nonlinear response of semiconductors. The possibility of choosing the two waveforms makes convolvers very flexible, as they can be used as arbitrary filters [5], [103], [104], correlators [7], [73], [105]. For instance, Figure 1.22(a) shows the convolution output, from a degenerate convolver, two square waves and (Figure 1.22(b)) a 13-bit Barker code.

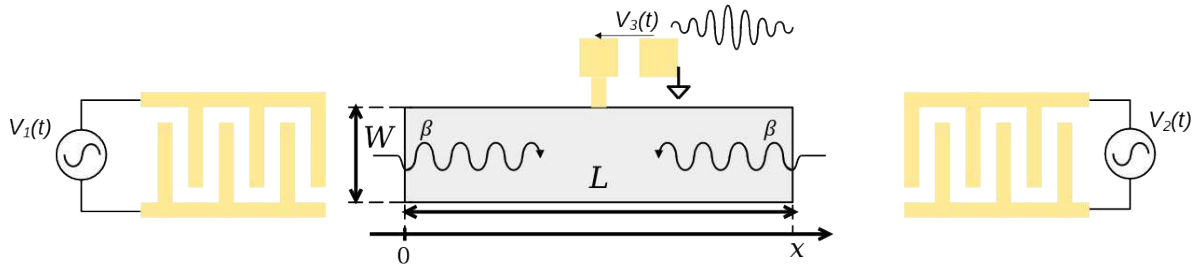


**Figure 1.21: Representation of a degenerate SAW convolver of length  $L$  and width  $W$ .**

In reference to Figure 1.21, a simple demonstration for the response of the convolver can be computed by considering the two input signals at the same frequency:

$$V_1(t) = e^{j(\omega t - \beta x)} \tilde{V}_1(t - x/v_0), \quad (1.34)$$

$$V_2(t) = e^{j(\omega t + \beta x)} \tilde{V}_2(t + x/v_0), \quad (1.35)$$

where  $v_0$  is the speed of the SAW signal,  $\tilde{V}_1(t - x/v_0)$  and  $\tilde{V}_2(t + x/v_0)$  are the shape of the propagating signals from port 1 and port 2. Assuming a pure quadratic response of the convolver, we find:

$$V_3(t) \propto e^{j2\omega t} \int_0^L \tilde{V}_1(t - x/v_0) \cdot \tilde{V}_2(t + x/v_0) dx. \quad (1.36)$$

By applying the change of variable  $\tau = t - x/v_0$ , Equation (1.36) becomes:

$$V_3(t) \propto -e^{j2\omega t} v_0 \int_0^{\tau_0} \tilde{V}_1(\tau) \cdot \tilde{V}_2(2t - \tau) d\tau, \quad (1.37)$$

that corresponds to the time-domain convolution, plus a time contraction. Through the Fourier transform, this is equivalent to the product between the two signals at the sum frequency of the inputs:

$$V_3(2\omega) \propto V_1(\omega) \cdot V_2(\omega), \quad (1.38)$$

As described in Equation (1.38), the total power of the convolution output is bi-linear in terms of the two input ports:

$$P_3(2\omega) = K_{cnv} \cdot P_1(\omega) \cdot P_2(\omega), \quad (1.39)$$

where  $K_{cnv}$  is a bi-linear factor which defines the efficiency of the convolver,  $P_1$  and  $P_2$  are acoustic power generated from port 1 and port 2 respectively at the interface with the convolution plate, and  $P_3$  is the available power from port 3. The convolution efficiency  $\eta_{cnv}$  is usually defined in logarithmic scale:

$$\eta_{cnv} = 10 \cdot \log_{10} \left( \frac{P_3}{P_1 \cdot P_2} \right) = |K_{cnv}|_{dB}. \quad (1.40)$$

The open circuit voltage  $V_{3,oc}$  can be found from Equation (1.39) through the output impedance of the convolver  $Z_{out}$ :

$$V_{3,oc}(2\omega) = 4|Z_{out}| K_{cnv}^{1/2} (P_1(f) P_2(f))^{1/2}, \quad (1.41)$$

Another important characteristic of a convolver is the time bandwidth (TB) product, which is defined by the maximum interaction time of the waves, which derives from the propagation velocity  $v_0$  and the length of the convolver  $L$ , and the bandwidth of the IDTs, which is defined by its geometry:

$$TB = \Delta f \cdot L/v_0. \quad (1.42)$$

#### 1.4.2.2.1 Metallic film convolvers

Metal film SAW convolvers can be divided into three sub-categories:

1. degenerate,
2. nondegenerate,
3. waveguide.

The **degenerate convolver** is the simplest form of convolver, shown in Figure 1.21, it is constituted of a single rectangular metallic film and works best when the input frequency at port 1 and port 2 are the same. It has been demonstrated, under perfect impedance matching, the efficiency is dependent on the geometries of the device and the properties of the substrate as [7], [106]:

$$K_{cnv} \approx \frac{M^2}{W_{eq}^2 \cdot R_{out}}, \quad (1.43)$$

where  $M$  is a constant depending on the substrate,  $R_{out}$  the output resistance of the convolver and  $W_{eq}$  is the minimum between the acoustic beam width and width of the convolver plate. This suggests that in degenerate convolvers, to improve performance, it is convenient to reduce the width  $W$  of the convolver plate and to increase its length  $L$ . In reality, longer devices tend to have higher losses, decreasing the output power as  $e^{-4 \cdot \alpha \cdot L}$ , moreover, decreasing the  $W$  in respect of the acoustic beam's also decreases the overall output power and increases the  $R_{out}$ . In practice, degenerate convolver designs have been shown to possess the lowest values of  $\eta_{cnv}$ , specifically, values up to -95 dBm have been shown to be possible for LiNbO<sub>3</sub> substrates, and -70 dBm for KNbO<sub>3</sub>.

As a way to fix the low efficiency of degenerate convolvers, it is possible to **focus the acoustic beam**, for instance via acoustic couplers, in an acoustic waveguide which is the main principle of the **waveguide convolvers**, shown in Figure 1.23. Indeed, this has enabled a large increase in the efficiency  $\eta_{cnv}$  and the maximum reported value was -71 dBm (Figure 1.24) for a 12  $\mu$ s convolution time on a YZ cut LiNbO<sub>3</sub> substrate [106].

A **nondegenerate convolver**, represented in Figure 1.25, is made from an IDT-like structure with periodicity defined via the **difference between the propagation constants of the two inputs** [7]. Therefore, the two inputs must be at different frequency, which can ease to distinguish the nonlinear propagation of the single inputs from the outputs. Other advantages of this structure are that, due to possessing a lower area and to how they connect, they possess

a lower output capacitance in respect to degenerate convolvers and they are easier to connect for testing because of the differential output. The main drawback of nondegenerate convolver is the necessity to separately design the two input IDTs and that performances are effectively not much higher than degenerate convolvers due to scattering at the multiple metallic interfaces of the convolution plate.

Finally, it must be noted that degenerate convolvers have been demonstrated also for piezo-semiconductors, like GaAs or CdS, their higher nonlinearity factor has enabled a fairly large internal  $\eta_{conv}$  of  $\sim -45$  dBm, however high propagation losses, of 49 dB at 205 MHz, limit sensibly the performance of such technology [73], [107].

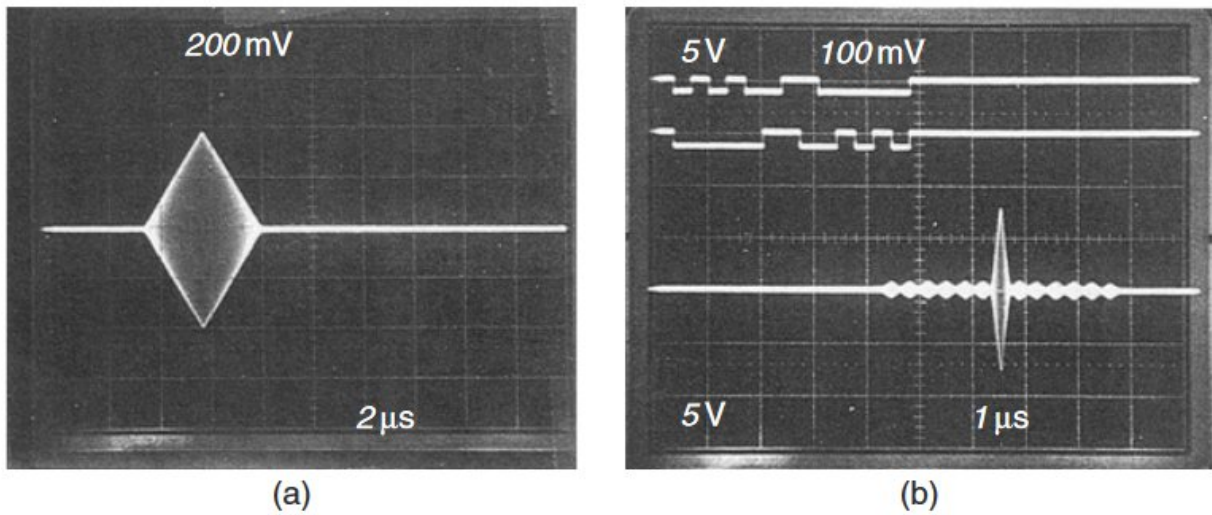


Figure 1.22: Convolution output between (a) two rectangular pulses and (b) a 13-bit Barker code [5].

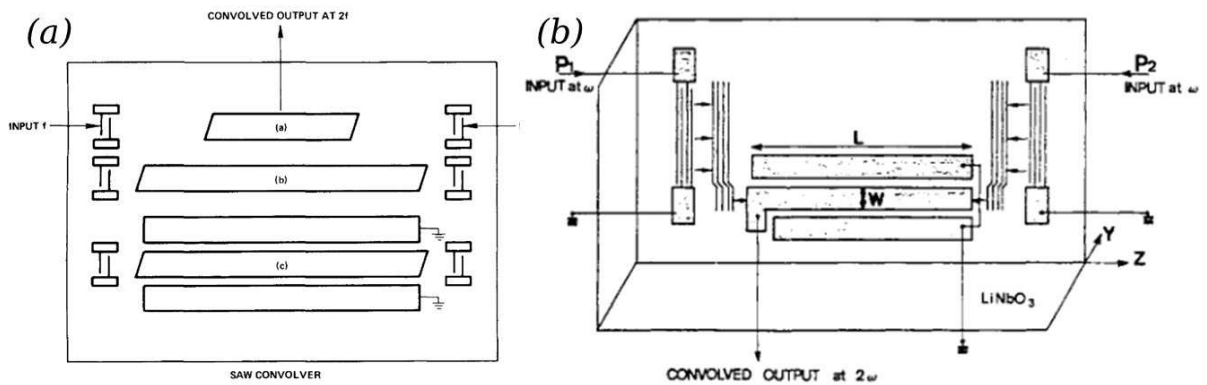


Figure 1.23: (a) The differential waveguide convolver design of Colvin et al. [86] and (b) the optimized waveguide convolver design of Defranould and Maerfeld [106].

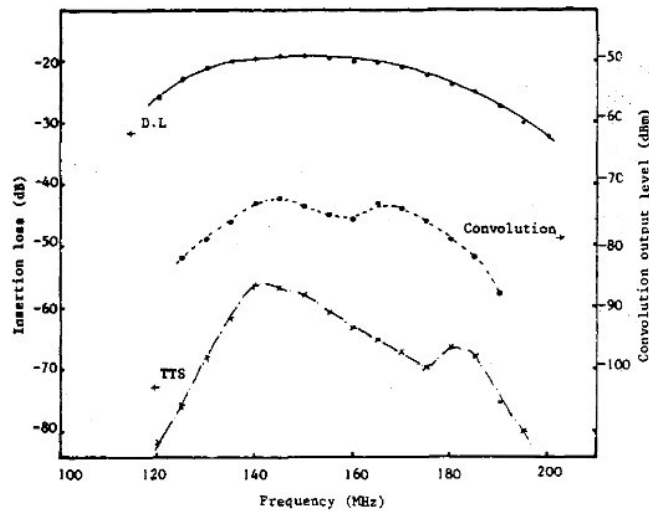


Figure 1.24: Insertion loss and convolution output power in a waveguide convolver for  $P_1 = P_2 = 1 \text{ W}$  [106]

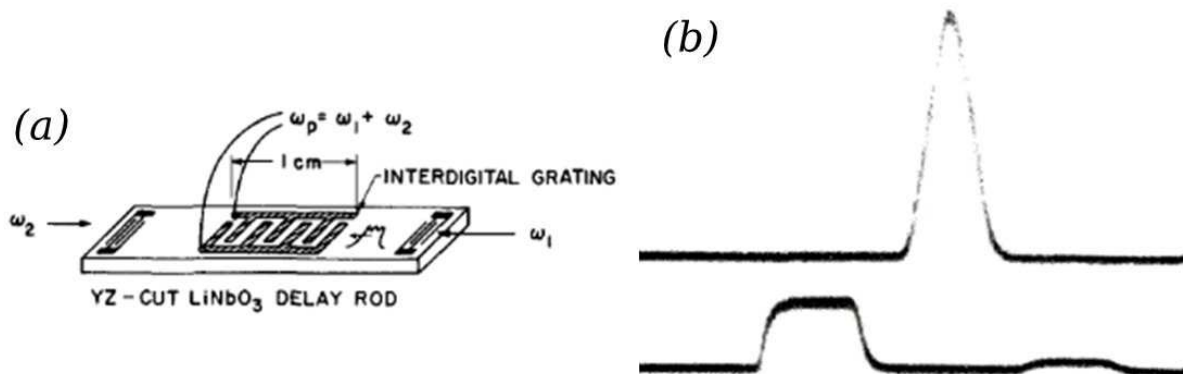


Figure 1.25: (a) Representation of a nondegenerate AE convolver and (b) the envelope of the self-convolution output with two rectangular pulses (top) and of the inputs (bottom) (colors inverted for better visibility) [105].

#### 1.4.2.2.2 Semiconductive film convolvers

Semiconductive-film convolvers use the **nonlinear voltage response of a semiconductor coupled with the electric field** component in the displacement wave of a piezoelectric material, this has enabled a variety of innovative convolver designs [5], [72], [73], [90], [99], [104], [108].

As displayed in Figure 1.26, the electric field in a propagating SAW can be separated into a field component orthogonal to the surface of the piezoelectric  $E_{\perp}$  and one in-plane component  $E_T$ . Therefore, dependently to the field component used by the design, the semiconductive-film convolver architectures can be grouped in **transverse-field** convolvers and **orthogonal-field** convolvers. The orthogonal field convolvers usually use an air-gapped design, and available designs can be subdivided into **degenerate convolvers** and **sampling convolvers**.

Sampling convolvers use an interaction between the waves and an array of Schottky diodes near the surface of the surface of the piezoelectric [73], [87], [109]. Their work principle is explained in Figure 1.27, the application of a voltage pulse on the diode array allows capturing the electric polarization of a traveling SAW, which can thereafter be used in a second moment as a reference for a correlation operation. This has the advantage that the response is programmable and does not require for the two inputs to be synchronized. The drawback of sampling convolvers is in the complexity of the design, which requires a large number of diodes to satisfy Shannon's theorem of sampling, which can be a processing and lithography challenge for high frequencies.

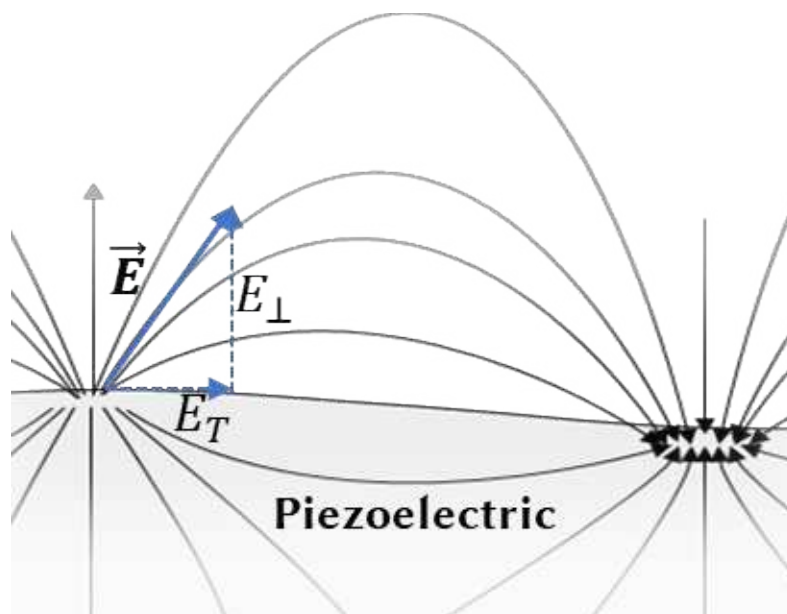


**Figure 1.26: Representation of the electric field in a SAW with a subdivision in an orthogonal component  $E_{\perp}$  and a transverse component  $E_T$ .**

**Degenerate air-gapped semiconductive film (DAGSF)** convolvers use the quadratic voltage response of the voltage output from the electric field stimulus from the piezo-dielectric

[73], [110]. In the model proposed by *Kino et al.* [73], the applied electric field causes the formation of a field-proportional depletion layer of depth  $l_d$ :

$$l_d = \frac{E_{\perp} \cdot \epsilon}{N_D \cdot q}, \quad (1.44)$$

where  $N_D$  is the donor density,  $q$  the electron's charge and  $\epsilon$  the dielectric constant of the semiconductor.

This makes so that the generated voltage is:

$$V_3 = -E_{\perp} \cdot l_d = \frac{E_{\perp}^2 \cdot \epsilon}{N_D \cdot q}, \quad (1.45)$$

which demonstrates the quadratic response. This effect allows for DAGSF devices to have some of the highest values of  $\eta_{conv}$ , as high as **-40 dBm**, however, also requiring for the device to be quite close, which can be challenging to manufacture.

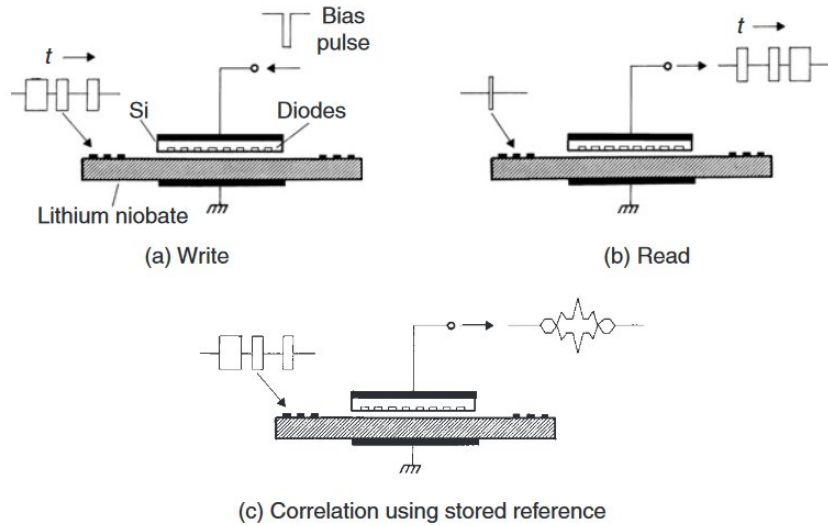


**Figure 1.27** Representation of the operation of a storage convolver [87].

Finally, transverse field convolvers use a similar effect as DAGSF convolvers, with the difference of using the transverse electric field component, for which the semiconductor is placed in direct contact with the piezoelectric substrate. A theory for this kind of device was provided by *Wang and Das* [110]. They demonstrated how, differently than DAGSF devices, the transverse field  $E_T$  is odd in respect to the direction of the SAW, meaning that the amplitude of the transverse-field nonlinear effect is proportional to  $P_1 - P_2$ . However, they also showed that, when a DC current is applied, such symmetry is broken, allowing for the device to be effectively used as a convolver. Thus, *Solie et al.* realized the first transverse field convolver

through a symmetric AE amplifier design via a CdS/LiNbO<sub>3</sub> technology [90], [99]. The applied current caused a double effect of amplification and mixing, which allowed them the highest ever reported **convolution efficiency of -8 dBm** for two input signals of 125 MHz. This is the highest convolution efficiency ever reported. However, the results show that there is still a considerable research work that can be directed in the study of more performant convolvers. Specifically, **air-gapped devices** possess good response due to the lack of mass loading effects. However, they are quite challenging and expensive to produce. Direct-contact devices have shown to possess even better characteristics, but the **mass damping** is a relevant performance-reducing factor.

In conclusion, the best option for high frequency convolvers is to have a massless conductor to piezoelectric substrate. There are currently numerous 2D materials that could be tested but the most mature material on large scale is graphene. **This PhD concentrates on the use of transfer graphene on LiNbO<sub>3</sub> (GoL) for high frequencies acoustoelectronic devices.**

## 1.5 References

- [1] J. Bonet and R. D. Wood, *Nonlinear continuum mechanics for finite element analysis*. Cambridge ; New York, NY, USA: Cambridge University Press, 1997.
- [2] Y. Başar and D. Weichert, *Nonlinear Continuum Mechanics of Solids*. Berlin, Heidelberg: Springer, 2000. doi: 10.1007/978-3-662-04299-1.
- [3] J. T. Oden, ‘NONLINEAR CONTINUUM MECHANICS’, p. 73, 2008.
- [4] Y. Cho and K. Yamanouchi, ‘Nonlinear, elastic, piezoelectric, electrostrictive, and dielectric constants of lithium niobate’, *Journal of Applied Physics*, vol. 61, no. 3, Art. no. 3, Feb. 1987, doi: 10.1063/1.338138.
- [5] D. P. Morgan, *Surface acoustic wave filters: with applications to electronic communications and signal processing*, 2nd ed. Amsterdam ; London: Academic Press, 2007.
- [6] M. Bačić, L. Librić, D. J. Kaćunić, and M. S. Kovačević, ‘The Usefulness of Seismic Surveys for Geotechnical Engineering in Karst: Some Practical Examples’, *Geosciences*, vol. 10, no. 10, Art. no. 10, Oct. 2020, doi: 10.3390/geosciences10100406.
- [7] C. Campbell, *Surface Acoustic Wave Devices and Their Signal Processing Applications*, vol. 89. 1991. Accessed: Aug. 17, 2023. [Online]. Available:

<https://pubs.aip.org/jasa/article/89/3/1479/676393/Surface-Acoustic-Wave-Devices-and-Their-Signal>

- [8] V. V. Lemanov and Yu. V. Ilisavsky, 'Piezoelectricity and acoustoelectronics', *Ferroelectrics*, vol. 42, no. 1, pp. 77–101, May 1982, doi: 10.1080/00150198208008103.
- [9] S. Guerin, S. A. M. Tofail, and D. Thompson, 'Organic piezoelectric materials: milestones and potential', *NPG Asia Mater*, vol. 11, no. 1, Art. no. 1, Mar. 2019, doi: 10.1038/s41427-019-0110-5.
- [10] R. Bechmann, 'Elastic and Piezoelectric Constants of Alpha-Quartz', *Phys. Rev.*, vol. 110, no. 5, pp. 1060–1061, Jun. 1958, doi: 10.1103/PhysRev.110.1060.
- [11] H. Ogi, T. Ohmori, N. Nakamura, and M. Hirao, 'Elastic, anelastic, and piezoelectric coefficients of  $\alpha$ -quartz determined by resonance ultrasound spectroscopy', *Journal of Applied Physics*, vol. 100, no. 5, p. 053511, Sep. 2006, doi: 10.1063/1.2335684.
- [12] R. Tarumi, K. Nakamura, H. Ogi, and M. Hirao, 'Complete set of elastic and piezoelectric coefficients of  $\alpha$ -quartz at low temperatures', *Journal of Applied Physics*, vol. 102, no. 11, p. 113508, Dec. 2007, doi: 10.1063/1.2816252.
- [13] O. Matsuda, T. Tachizaki, T. Fukui, J. J. Baumberg, and O. B. Wright, 'Acoustic phonon generation and detection in GaAs/Al 0.3 Ga 0.7 As quantum wells with picosecond laser pulses', *Phys. Rev. B*, vol. 71, no. 11, Art. no. 11, Mar. 2005, doi: 10.1103/PhysRevB.71.115330.
- [14] J. Soderkvist and K. Hjort, 'The piezoelectric effect of GaAs used for resonators and resonant sensors', *J. Micromech. Microeng.*, vol. 4, no. 1, p. 28, Mar. 1994, doi: 10.1088/0960-1317/4/1/004.
- [15] M. S. Shur, A. D. Bykhovski, and R. Gaska, 'Pyroelectric and Piezoelectric Properties of Gan-Based Materials', *MRS Online Proceedings Library (OPL)*, vol. 537, p. G1.6, Jan. 1998, doi: 10.1557/PROC-537-G1.6.
- [16] G. Weinreich and H. G. White, 'Observation of the Acoustoelectric Effect', *Phys. Rev.*, vol. 106, no. 5, pp. 1104–1106, Jun. 1957, doi: 10.1103/PhysRev.106.1104.
- [17] E. Fukada, 'Bioelectrets and biopiezoelectricity', *IEEE Transactions on Electrical Insulation*, vol. 27, no. 4, pp. 813–819, Aug. 1992, doi: 10.1109/14.155803.
- [18] G. Eberle, H. Schmidt, and W. Eisenmenger, 'Piezoelectric polymer electrets', *IEEE Transactions on Dielectrics and Electrical Insulation*, vol. 3, no. 5, pp. 624–646, Oct. 1996, doi: 10.1109/94.544185.

- [19] V. V. Lemanov, ‘Piezoelectric and pyroelectric properties of protein amino acids as basic materials of Soft State Physics’, *Ferroelectrics*, vol. 238, no. 1, pp. 211–218, Feb. 2000, doi: 10.1080/00150190008008786.
- [20] A. Hernández-Mínguez, Y.-T. Liou, and P. V. Santos, ‘Interaction of surface acoustic waves with electronic excitations in graphene’, *J. Phys. D: Appl. Phys.*, vol. 51, no. 38, Art. no. 38, Sep. 2018, doi: 10.1088/1361-6463/aad593.
- [21] A. R. Hutson and D. L. White, ‘Elastic Wave Propagation in Piezoelectric Semiconductors’, *Journal of Applied Physics*, vol. 33, no. 1, pp. 40–47, Jan. 1962, doi: 10.1063/1.1728525.
- [22] H. Skeie, ‘Electrical and Mechanical Loading of a Piezoelectric Surface Supporting Surface Waves’, *The Journal of the Acoustical Society of America*, vol. 48, no. 5B, pp. 1098–1109, 1970, doi: 10.1121/1.1912249.
- [23] A. Wixforth, J. Scriba, M. Wassermeier, J. P. Kotthaus, Weimann, G, and Schlapp, W, ‘Surface acoustic waves on GaAs/Al<sub>x</sub>Ga<sub>1-x</sub>As heterostructures’, *Physical Review B*, vol. 40, no. 11, p. 7874, Oct. 1989, doi: 10.1103/PhysRevB.40.7874.
- [24] D. F. Nelson, ‘Theory of nonlinear electroacoustics of dielectric, piezoelectric, and pyroelectric crystals’, *J. Acoust. Soc. Am.*, vol. 63, no. 6, p. 11, 1978.
- [25] T. Furukawa, ‘Piezoelectricity and pyroelectricity in polymers’, *IEEE Transactions on Electrical Insulation*, vol. 24, no. 3, pp. 375–394, Jun. 1989, doi: 10.1109/14.30878.
- [26] A. Cuadras, M. Gasulla, and V. Ferrari, ‘Thermal energy harvesting through pyroelectricity’, *Sensors and Actuators A: Physical*, vol. 158, no. 1, pp. 132–139, Mar. 2010, doi: 10.1016/j.sna.2009.12.018.
- [27] A. Savage, ‘Pyroelectricity and Spontaneous Polarization in LiNbO<sub>3</sub>’, *Journal of Applied Physics*, vol. 37, no. 8, pp. 3071–3072, Jun. 2004, doi: 10.1063/1.1703164.
- [28] B. Rosenblum, P. Bräunlich, and J. P. Carrico, ‘Thermally stimulated field emission from pyroelectric LiNbO<sub>3</sub>’, *Applied Physics Letters*, vol. 25, no. 1, pp. 17–19, Oct. 2003, doi: 10.1063/1.1655260.
- [29] V. Miseikis, J. E. Cunningham, K. Saeed, R. O’Rorke, and A. G. Davies, ‘Acoustically induced current flow in graphene’, *Appl. Phys. Lett.*, vol. 100, no. 13, Art. no. 13, Mar. 2012, doi: 10.1063/1.3697403.
- [30] D. S. L. Abergel, V. Apalkov, J. Berashevich, K. Ziegler, and T. Chakraborty, ‘Properties of graphene: a theoretical perspective’, *Advances in Physics*, vol. 59, no. 4, Art. no. 4, Jul. 2010, doi: 10.1080/00018732.2010.487978.

- [31] M. I. Katsnelson, ‘Graphene: carbon in two dimensions’, *Materials Today*, vol. 10, no. 1, pp. 20–27, Jan. 2007, doi: 10.1016/S1369-7021(06)71788-6.
- [32] K. S. Novoselov *et al.*, ‘Electric Field Effect in Atomically Thin Carbon Films’, *Science*, vol. 306, no. 5696, pp. 666–669, Oct. 2004, doi: 10.1126/science.1102896.
- [33] T. Enoki and T. Ando, *Physics and chemistry of graphene: graphene to nanographene*. CRC Press, 2019.
- [34] G. Yang, L. Li, W. B. Lee, and M. C. Ng, ‘Structure of graphene and its disorders: a review’, *Science and Technology of Advanced Materials*, vol. 19, no. 1, pp. 613–648, Dec. 2018, doi: 10.1080/14686996.2018.1494493.
- [35] M. Y. Han, B. Özyilmaz, Y. Zhang, and P. Kim, ‘Energy Band-Gap Engineering of Graphene Nanoribbons’, *Phys. Rev. Lett.*, vol. 98, no. 20, p. 206805, May 2007, doi: 10.1103/PhysRevLett.98.206805.
- [36] K. S. Novoselov *et al.*, ‘Two-dimensional gas of massless Dirac fermions in graphene’, *Nature*, vol. 438, no. 7065, Art. no. 7065, Nov. 2005, doi: 10.1038/nature04233.
- [37] P. Zhao *et al.*, ‘Acoustically Induced Giant Synthetic Hall Voltages in Graphene’, *Phys. Rev. Lett.*, vol. 128, no. 25, p. 256601, Jun. 2022, doi: 10.1103/PhysRevLett.128.256601.
- [38] P. Cea, ‘The quantum hall effect in graphene’, *Mod. Phys. Lett. B*, vol. 26, no. 13, p. 1250084, May 2012, doi: 10.1142/S0217984912500844.
- [39] Y. Cao *et al.*, ‘Unconventional superconductivity in magic-angle graphene superlattices’, *Nature*, vol. 556, no. 7699, Art. no. 7699, Apr. 2018, doi: 10.1038/nature26160.
- [40] M. Yankowitz *et al.*, ‘Tuning superconductivity in twisted bilayer graphene’, *Science*, vol. 363, no. 6431, pp. 1059–1064, Mar. 2019, doi: 10.1126/science.aav1910.
- [41] A. Capasso, A. E. Del Rio Castillo, H. Sun, A. Ansaldo, V. Pellegrini, and F. Bonaccorso, ‘Ink-jet printing of graphene for flexible electronics: An environmentally-friendly approach’, *Solid State Communications*, vol. 224, pp. 53–63, Dec. 2015, doi: 10.1016/j.ssc.2015.08.011.
- [42] E. O. Polat, O. Balci, N. Kakenov, H. B. Uzlu, C. Kocabas, and R. Dahiya, ‘Synthesis of Large Area Graphene for High Performance in Flexible Optoelectronic Devices’, *Sci Rep*, vol. 5, no. 1, p. 16744, Dec. 2015, doi: 10.1038/srep16744.
- [43] G. Vincenzi, ‘Graphene: FET and metal contact modeling’, Université de Toulouse, 2014.
- [44] L. Vicarelli *et al.*, ‘Graphene field effect transistors as room-temperature Terahertz detectors’, *Nature Mater*, vol. 11, no. 10, pp. 865–871, Oct. 2012, doi: 10.1038/nmat3417.

- [45] O. Habibpour, J. Vukusic, and J. Stake, ‘A 30-GHz Integrated Subharmonic Mixer Based on a Multichannel Graphene FET’, *IEEE Transactions on Microwave Theory and Techniques*, vol. 61, no. 2, pp. 841–847, Feb. 2013, doi: 10.1109/TMTT.2012.2236434.
- [46] H. Wang and G. Yu, ‘Direct CVD Graphene Growth on Semiconductors and Dielectrics for Transfer-Free Device Fabrication’, *Adv. Mater.*, vol. 28, no. 25, pp. 4956–4975, Jul. 2016, doi: 10.1002/adma.201505123.
- [47] K. S. Kim *et al.*, ‘Large-scale pattern growth of graphene films for stretchable transparent electrodes’, *Nature*, vol. 457, no. 7230, Art. no. 7230, Feb. 2009, doi: 10.1038/nature07719.
- [48] D. De Fazio *et al.*, ‘High-Mobility, Wet-Transferred Graphene Grown by Chemical Vapor Deposition’, *ACS Nano*, vol. 13, no. 8, pp. 8926–8935, Aug. 2019, doi: 10.1021/acsnano.9b02621.
- [49] F. Bonaccorso, A. Lombardo, T. Hasan, Z. Sun, L. Colombo, and A. C. Ferrari, ‘Production and processing of graphene and 2d crystals’, *Materials Today*, vol. 15, no. 12, pp. 564–589, Dec. 2012, doi: 10.1016/S1369-7021(13)70014-2.
- [50] R. H. Parmenter, ‘The Acousto-Electric Effect’, *Phys. Rev.*, vol. 89, no. 5, Art. no. 5, Mar. 1953, doi: 10.1103/PhysRev.89.990.
- [51] J. M. Shilton *et al.*, ‘Experimental study of the acoustoelectric effects in GaAs-AlGaAs heterostructures’, *J. Phys.: Condens. Matter*, vol. 7, no. 39, pp. 7675–7685, Sep. 1995, doi: 10.1088/0953-8984/7/39/010.
- [52] M. Rotter, A. Wixforth, W. Ruile, D. Bernklau, and H. Riechert, ‘Giant acoustoelectric effect in GaAs/LiNbO<sub>3</sub> hybrids’, *Appl. Phys. Lett.*, vol. 73, no. 15, pp. 2128–2130, Oct. 1998, doi: 10.1063/1.122400.
- [53] R. Adler, ‘Simple theory of acoustic amplification’, *IEEE Transactions on Sonics and Ultrasonics*, vol. 18, no. 3, pp. 115–118, 1971.
- [54] G. S. Kino and T. M. Reeder, ‘A normal mode theory for the Rayleigh wave amplifier’, *IEEE Transactions on Electron Devices*, vol. 18, no. 10, pp. 909–920, 1971.
- [55] C. W. Turner, ‘Recent advances in the amplification of surface elastic waves in layered structures’, *C R C Critical Reviews in Solid State Sciences*, vol. 1, no. 4, Art. no. 4, Nov. 1970, doi: 10.1080/10408437008244240.
- [56] J. H. McFee, ‘Ultrasonic Amplification and Non-Ohmic Behavior in CdS and ZnO’, *Journal of Applied Physics*, vol. 34, no. 5, pp. 1548–1553, 1963, doi: 10.1063/1.1729676.

- [57] E. L. Adler and G. W. Farnell, ‘Effect of Acoustoelectric Interactions on the Electrical Impedance of a CdS Bar’, *The Journal of the Acoustical Society of America*, vol. 39, no. 5A, pp. 960–964, May 1966, doi: 10.1121/1.1909978.
- [58] G. Weinreich, T. M. Sanders, and H. G. White, ‘Acoustoelectric Effect in n-Type Germanium’, *Phys. Rev.*, vol. 114, no. 1, pp. 33–44, Apr. 1959, doi: 10.1103/PhysRev.114.33.
- [59] B. Tell and G. Weinreich, ‘Acoustoelectric Effect and Intervalley Scattering Rates in Antimony-Doped Germanium’, *Phys. Rev.*, vol. 143, no. 2, pp. 584–587, Mar. 1966, doi: 10.1103/PhysRev.143.584.
- [60] K. A. Ingebrigtsen, ‘Linear and Nonlinear Attenuation of Acoustic Surface Waves in a Piezoelectric Coated with a Semiconducting Film’, *Journal of Applied Physics*, vol. 41, no. 2, Art. no. 2, Feb. 1970, doi: 10.1063/1.1658696.
- [61] L. Bandhu, L. M. Lawton, and G. R. Nash, ‘Macroscopic acoustoelectric charge transport in graphene’, *Appl. Phys. Lett.*, p. 5, 2014.
- [62] L. Bandhu and G. R. Nash, ‘Controlling the properties of surface acoustic waves using graphene’, *Nano Research*, vol. 9, pp. 685–691, 2016.
- [63] J. R. Lane, L. Zhang, M. A. Khasawneh, B. N. Zhou, E. A. Henriksen, and J. Pollanen, ‘Flip-chip gate-tunable acoustoelectric effect in graphene’, *Journal of Applied Physics*, vol. 124, no. 19, p. 194302, Nov. 2018, doi: 10.1063/1.5047211.
- [64] D. Roshchupkin, O. Kononenko, R. Fakhrtidinov, E. Emelin, and A. Sergeev, ‘Acoustically Stimulated Charge Transport in Graphene Film’, *Nanomaterials*, vol. 12, no. 24, Art. no. 24, Jan. 2022, doi: 10.3390/nano12244370.
- [65] T. Poole and G. R. Nash, ‘Acoustoelectric Current in Graphene Nanoribbons’, *Sci Rep*, vol. 7, no. 1, p. 1767, Dec. 2017, doi: 10.1038/s41598-017-01979-8.
- [66] S. Okuda *et al.*, ‘Acoustic carrier transportation induced by surface acoustic waves in graphene in solution’, *Appl. Phys. Express*, vol. 9, no. 4, p. 045104, Apr. 2016, doi: 10.7567/APEX.9.045104.
- [67] A. Hernández-Mínguez, A. Tahraoui, J. M. J. Lopes, and P. V. Santos, ‘Acoustoelectric transport at gigahertz frequencies in coated epitaxial graphene’, *Appl. Phys. Lett.*, vol. 108, no. 19, p. 193502, May 2016, doi: 10.1063/1.4949756.
- [68] D. Roshchupkin *et al.*, ‘Surface acoustic wave propagation in graphene film’, *Journal of Applied Physics*, vol. 118, no. 10, Art. no. 10, Sep. 2015, doi: 10.1063/1.4930050.

- [69] L. Bandhu and G. R. Nash, ‘Temperature dependence of the acoustoelectric current in graphene’, *Appl. Phys. Lett.*, vol. 105, no. 26, Art. no. 26, Dec. 2014, doi: 10.1063/1.4905222.
- [70] D. C. Malocha, C. Carmichael, and A. Weeks, ‘Acoustoelectric Amplifier With 1.2-dB Insertion Gain Monolithic Graphene Construction and Continuous Wave Operation’, *IEEE Trans. Ultrason., Ferroelect., Freq. Contr.*, vol. 67, no. 9, Art. no. 9, Sep. 2020, doi: 10.1109/TUFFC.2020.2984176.
- [71] C. Carmichael, D. C. Malocha, and A. Weeks, ‘Asymmetric energy coupling through acoustoelectric effect using graphene on lithium niobite surface acoustic wave delay line in GHz Range’, in *2019 IEEE International Ultrasonics Symposium (IUS)*, Glasgow, United Kingdom: IEEE, Oct. 2019, pp. 702–705. doi: 10.1109/ULTSYM.2019.8925837.
- [72] C. K. Campbell, ‘Applications of surface acoustic and shallow bulk acoustic wave devices’, *Proc. IEEE*, vol. 77, no. 10, pp. 1453–1484, Oct. 1989, doi: 10.1109/5.40664.
- [73] G. S. Kino, S. Ludvik, H. J. Shaw, W. R. Shreve, J. M. White, and D. K. Winslow, ‘Signal Processing by Parametric Interactions in Delay-Line Devices’, *IEEE Transactions on Microwave Theory and Techniques*, vol. 21, no. 4, pp. 244–255, Apr. 1973, doi: 10.1109/TMTT.1973.1127975.
- [74] R. H. Tancrell and M. G. Holland, ‘Acoustic Surface Wave Filters’, *Proceedings of the IEEE*, vol. 59, no. 3, pp. 393–409, Mar. 1971, doi: 10.1109/PROC.1971.8180.
- [75] R. D. Weglein and G. R. Nudd, ‘Space-Harmonic Response of Surface Wave Transducers’, in *1972 Ultrasonics Symposium*, IEEE, 1972, pp. 346–352. doi: 10.1109/ULTSYM.1972.196098.
- [76] C. S. Hartmann, D. T. Bell, and R. C. Rosenfeld, ‘Impulse Model Design of Acoustic Surface-Wave Filters’, *IEEE Transactions on Microwave Theory and Techniques*, vol. 21, no. 4, pp. 162–175, Apr. 1973, doi: 10.1109/TMTT.1973.1127967.
- [77] A. J. Slobodnik, ‘Surface acoustic waves and SAW materials’, *Proceedings of the IEEE*, vol. 64, no. 5, pp. 581–595, May 1976, doi: 10.1109/PROC.1976.10180.
- [78] M. R. T. Tan and C. A. Flory, ‘Minimization of diffraction effects in SAW devices using a wide aperture’, in *IEEE 1986 Ultrasonics Symposium*, Williamsburg, VA, USA: IEEE, 1986, pp. 13–18. doi: 10.1109/ULTSYM.1986.198702.
- [79] W. R. Smith, ‘Key Tradeoffs in SAW Transducer Design and Component Specification’, in *1976 Ultrasonics Symposium*, Sep. 1976, pp. 547–552. doi: 10.1109/ULTSYM.1976.196739.
- [80] W. P. Mason, *Electromechanical transducers and wave filters*. van Nostrand, 1942.

- [81] W. R. Smith, H. M. Gerard, J. H. Collins, T. M. Reeder, and H. J. Shaw, ‘Design of Surface Wave Delay Lines with Interdigital Transducers’, *IEEE Trans. Microwave Theory Techn.*, vol. 17, no. 11, pp. 865–873, Nov. 1969, doi: 10.1109/TMTT.1969.1127076.
- [82] R. M. White and F. W. Voltmer, ‘DIRECT PIEZOELECTRIC COUPLING TO SURFACE ELASTIC WAVES’, *Appl. Phys. Lett.*, vol. 7, no. 12, Art. no. 12, Dec. 1965, doi: 10.1063/1.1754276.
- [83] B. A. Auld and G. S. Kino, ‘Normal mode theory for acoustic waves and its application to the interdigital transducer’, *IEEE Transactions on Electron Devices*, vol. 18, no. 10, pp. 898–908, 1971.
- [84] K. Sugiyama and S. Yoshikawa, ‘Design of Acoustic Surface Wave Filters Using Phase-Coded Transducers’, in *1973 Ultrasonics Symposium*, IEEE, 1973, pp. 445–448. doi: 10.1109/ULTSYM.1973.196238.
- [85] P. V. Wright, ‘Analysis and design of low-loss SAW devices with internal reflections using coupling-of-modes theory’, in *Proceedings., IEEE Ultrasonics Symposium*, Oct. 1989, pp. 141–152 vol.1. doi: 10.1109/ULTSYM.1989.66974.
- [86] R. D. Colvin and P. H. Carr, ‘Surface-acoustic-wave plate convolvers at 1 GHz’, *Appl. Phys. Lett.*, vol. 35, no. 7, pp. 522–523, Oct. 1979, doi: 10.1063/1.91194.
- [87] D. P. Morgan, ‘Surface acoustic wave devices and applications: 5. Signal processing using programmable nonlinear convolvers’, *Ultrasonics*, vol. 12, no. 2, pp. 74–83, 1974.
- [88] J. H. Collins, K. M. Lakin, C. F. Quate, and H. J. Shaw, ‘Amplification of acoustic surface waves with adjacent semiconductor and piezoelectric crystals’, *Appl. Phys. Lett.*, vol. 13, no. 9, pp. 314–316, Nov. 1968, doi: 10.1063/1.1652628.
- [89] L. P. Solie and S. R. Corporation, ‘ACOUSTIC SURFACE WAVE CONVOLVER WITH BIDIRECTIONAL AMPLIFICATION’.
- [90] L. P. Solie, ‘A new mode of operation for the surface-wave convolver’, *Proceedings of the IEEE*, vol. 64, no. 5, pp. 760–763, 1976.
- [91] A. R. Hutson, ‘Acousto-Electric Explanation of Non-Ohmic Behavior in Piezoelectric Semiconductors and Bismuth’, *Phys. Rev. Lett.*, vol. 9, no. 7, pp. 296–298, Oct. 1962, doi: 10.1103/PhysRevLett.9.296.
- [92] A. R. Hutson, J. H. McFee, and D. L. White, ‘Ultrasonic Amplification in CdS’, *Phys. Rev. Lett.*, vol. 7, no. 6, pp. 237–239, Sep. 1961, doi: 10.1103/PhysRevLett.7.237.
- [93] D. L. White, ‘Amplification of Ultrasonic Waves in Piezoelectric Semiconductors’, 1962.
- [94] V. J. Gokhale, Y. Shim, and M. Rais-Zadeh, ‘Observation of the acoustoelectric effect in gallium nitride micromechanical bulk acoustic filters’, in *2010 IEEE International*

- Frequency Control Symposium*, Newport Beach, CA, USA: IEEE, Jun. 2010, pp. 524–529. doi: 10.1109/FREQ.2010.5556273.
- [95] L. Hackett *et al.*, ‘Towards single-chip radiofrequency signal processing via acoustoelectric electron–phonon interactions’, *Nat Commun*, vol. 12, no. 1, Art. no. 1, Dec. 2021, doi: 10.1038/s41467-021-22935-1.
- [96] K. Yoshida and M. Yamanishi, ‘Interaction between Surface Elastic Waves and Drifting Carriers in Layered System’, *Jpn. J. Appl. Phys.*, vol. 7, no. 9, p. 1143, Sep. 1968, doi: 10.1143/JJAP.7.1143.
- [97] M. Yamanishi and K. Yoshida, ‘Possible Application of Surface Acoustoelectronic Interaction to the Investigation of Semiconductor Surface’. 大阪府立大学, Mar. 31, 1969. doi: 10.24729/00008872.
- [98] K. M. Lakin and H. J. Shaw, ‘Surface Wave Delay Line Amplifiers’, *IEEE Transactions on Microwave Theory and Techniques*, vol. 17, no. 11, pp. 912–920, Nov. 1969, doi: 10.1109/TMTT.1969.1127081.
- [99] L. P. Solie, ‘An integrated surface wave convolver/amplifier’, in *1973 Ultrasonics Symposium*, Nov. 1973, pp. 175–177. doi: 10.1109/ULTSYM.1973.196176.
- [100] O. A. C. Nunes, ‘Piezoelectric surface acoustical phonon amplification in graphene on a GaAs substrate’, *Journal of Applied Physics*, vol. 115, no. 23, p. 233715, Jun. 2014, doi: 10.1063/1.4883914.
- [101] Z. Insepov, E. Emelin, O. Kononenko, D. V. Roshchupkin, K. B. Tnyshtykbayev, and K. A. Baigarin, ‘Surface acoustic wave amplification by direct current-voltage supplied to graphene film’, *Appl. Phys. Lett.*, vol. 106, no. 2, Art. no. 2, Jan. 2015, doi: 10.1063/1.4906033.
- [102] Z. Insepov, E. Emelin, O. Kononenko, D. V. Roshchupkin, and K. B. Tnyshtykbayev, ‘Surface Acoustic Wave Amplification by DC-Voltage Supplied to Graphene Film’, *Appl. Phys. Lett.*, vol. 106, no. 023505, p. 9, 2015.
- [103] J. H. Cafarella, ‘Application of SAW Convolver to Spread-Spectrum Communication’, in *IEEE 1984 Ultrasonics Symposium*, IEEE, 1984, pp. 121–126. doi: 10.1109/ULTSYM.1984.198275.
- [104] J. H. Cafarella, W. M. Brown, E. Stern, and J. A. Alusow, ‘Acoustoelectric convolvers for programmable matched filtering in spread-spectrum systems’, *Proc. IEEE*, vol. 64, no. 5, pp. 756–759, 1976, doi: 10.1109/PROC.1976.10206.

- [105] M. Luukkala and G. S. Kino, ‘Convolution and time inversion using parametric interactions of acoustic surface waves’, *Appl. Phys. Lett.*, vol. 18, no. 9, pp. 393–394, May 1971, doi: 10.1063/1.1653713.
- [106] P. Defranould and C. Maerfeld, ‘A SAW planar piezoelectric convolver’, *Proc. IEEE*, vol. 64, no. 5, Art. no. 5, 1976, doi: 10.1109/PROC.1976.10203.
- [107] J. Chambers, I. M. Mason, and C. W. Turner, ‘Acoustic-surface-wave convolution on crystals of CdS, LiNbO<sub>3</sub> and Bi<sub>12</sub>GeO<sub>20</sub>’, *Electron. Lett.*, vol. 8, no. 12, p. 314, 1972, doi: 10.1049/el:19720232.
- [108] G. S. Kino, ‘Acoustoelectric interactions in acoustic-surface-wave devices’, *Proc. IEEE*, vol. 64, no. 5, pp. 724–748, 1976, doi: 10.1109/PROC.1976.10202.
- [109] D. P. Morgan, ‘Signal Processing Using the SAW Diode Convolver’, in *1973 Ultrasonics Symposium*, Nov. 1973, pp. 138–141. doi: 10.1109/ULTSYM.1973.196166.
- [110] W. C. Wang and P. Das, ‘Surface Wave Convolver Via Space Charge Nonlinearity’, in *1972 Ultrasonics Symposium*, IEEE, 1972, pp. 316–322. doi: 10.1109/ULTSYM.1972.196091.



## Contents of the chapter:

|   |    |
|---|----|
| 2 GoL : Graphene on LiNbO <sub>3</sub> .....                | 52 |
| 2.1 Graphene processing.....                                | 52 |
| 2.1.1 Graphene on Si/SiO <sub>2</sub> .....                 | 53 |
| 2.1.2 Challenges for LiNbO <sub>3</sub> .....               | 53 |
| 2.1.3 Metal-graphene contacts.....                          | 54 |
| 2.2 Description of the Process.....                         | 56 |
| 2.2.1 Wafer cutting and substrate cleaning.....             | 57 |
| 2.2.2 Lithographic process.....                             | 59 |
| 2.2.2.1 UV Lithographic process for Liftoff.....            | 60 |
| 2.2.2.2 UV Lithographic process for Patterning.....         | 62 |
| 2.2.2.3 Electron Beam Lithographic process for Liftoff..... | 63 |
| 2.2.3 Metal Deposition and Liftoff.....                     | 65 |
| 2.2.3.1 Liftoff.....  | 65 |
| 2.2.3.2 Backside electrode.....                             | 68 |
| 2.2.4 Graphene Transfer.....                                | 68 |
| 2.2.4.1 Process with the “easy transfer kit”.....           | 69 |
| 2.2.4.2 Process With CVD Graphene on Cu Substrates.....     | 72 |
| 2.2.5 Graphene Annealing.....                               | 76 |
| 2.2.6 Graphene Patterning.....                              | 78 |
| 2.3 Description of Other Methods.....                       | 78 |
| 2.4 Visible-light microscopy.....                           | 81 |
| 2.5 Improvements of the process.....                        | 82 |
| 2.6 References.....   | 83 |

## 2 GoL : Graphene on LiNbO<sub>3</sub>

In this chapter, I review the transfer of graphene as well as the development I made to optimize the transfer, patterning and annealing of graphene on LiNbO<sub>3</sub>.

Indeed, since the discovery of graphene in 2004 [1], achieved through the exfoliation of pyrolytic graphite, several production techniques have been developed to obtain high-quality graphene flakes such as photoexfoliation, ultrasound-aided liquid-phase exfoliation, molecular beam epitaxy [2]. The size of flakes produced through these techniques and electronic properties varies from paper to paper. However, the size of the flakes is not large enough to be used in the development of acoustoelectronic SAW devices such as amplifiers and convolvers, which are in the scale of several mm. **The production of high-quality monocrystalline single and few-layer graphene sheets can be achieved through epitaxy by annealing at high-temperature ( $\approx 1600^\circ\text{C}$ ) monocrystalline SiC wafers [3], [4].** However, as they cannot be grown through standard highly scalable methods, they can only be grown using Chemical Vapor Deposition (CVD), which makes SiC wafers quite expensive.

CVD has proven to be well-scalable technique that has enabled researchers to grow electronic grade graphene on a variety of substrates [5]. For instance, CVD graphene has been grown directly on a variety of substrates like Cu [6], Ni [7], Al<sub>2</sub>O<sub>3</sub> [8]. The drawback is that the produced films are **polycrystalline**. Grain boundaries represent a limitation on the performance, causing a **decrease in mobility**. However, the development of a technique for direct growth of graphene on LiNbO<sub>3</sub> would require significant optimization efforts and was out of the scope of this thesis work.

Finally, in the presented process, **CVD-grown graphene using copper monocrystalline seeds** (that can be found on large scale), and **pre-transferred to a plastic film** was used as they were ready to be transferred.

### 2.1 Graphene processing

The transfer of graphene and its processing can be challenging because of its fragility. Numerous factors affect its properties: graphene is sensible to strain, holes and residual material from the process, which affect the electrical resistivity, the doping, the mobility of charge carriers. Indeed, the sensitivity of graphene to environmental condition has conducted to the development of several kinds of sensors [9] [10]–[13]. The specific shape and the size of the

devices also play a significant role, and it can be chosen to introduce a bandgap in nanoribbons with an “armchair” configuration [14], [15].

The properties of graphene will then depend on several process techniques, as our devices are large enough, the electrical response will be an average of many contributions quote above. The quality of the process will be determined by final device resistivity and compared to manufacturer specifications.

### 2.1.1 Graphene on Si/SiO<sub>2</sub>

Transfer of graphene on Si/SiO<sub>2</sub> is well documented. The temperature stability and the low reactivity with various standard chemical agents make it widely compatible with existing cleanroom processing techniques. Because of this, graphene has been individuated as a possible material for the “post-silicon era”, so that it has been exploited by researchers in the development of high-performance transistors [16], sensors [10], [16], [17], solar cells [17], mixers [18], [19].

A typical process for graphene on Si/SiO<sub>2</sub> substrates involves at least 4 steps:

- the deposition of metal contacts,
- the transfer of graphene,
- the patterning (via Reactive Ion Etching (RIE) using oxygen ions).
- The annealing of graphene.

These steps and the cleaning methods differs between each process. One can note more advanced processing, involving the deposition and patterning of a gate structure, stacking with hexagonal Boron Nitride (hBN) monolayers, etc., which can be found in literature but are out of the scope of this work.

### 2.1.2 Challenges for LiNbO<sub>3</sub>

Although LiNbO<sub>3</sub> is largely compatible with Si processing, its use as a final substrate introduces some processing challenges. The risk factors individuated for the usage of LiNbO<sub>3</sub> were:

1. The strong piezoelectric effect,
2. The pyroelectric effect,
3. The chemical reactions and temperature stability.

The piezoelectric nature of the substrate imposed some restrictions on the mechanical handling of the devices in order to reduce damage due to the formation of strong electric fields during the process. The pyroelectric effect presents similar risks as the latter, but for temperature treatment. In order to alleviate this problem, the main strategy adopted was to use black-type LiNbO<sub>3</sub>, Black LiNbO<sub>3</sub> is achieved via reducing the oxygen content in the crystal by heat treatment in a vacuum, and is ideally non-pyroelectric.

As for the chemical reactions and temperature stability, all clean room processes should be optimized to use low temperatures and low temperature gradients as much as possible, especially because, as discussed in Section 2.2.5, graphene and LiNbO<sub>3</sub> could react chemically, damaging the devices.

### 2.1.3 Metal-graphene contacts

The graphene-metal interfaces can be a considerable portion of the total resistance of the device. The value of contact resistance can be tuned technologically through the choice of the metal, the geometry of the graphene-metal interface, the uniformity of graphene-metal interface. Experimental studies have shown that, as the current flow between the graphene and metal is concentrated on the edges between the two [20]–[22], the value of the contact resistance  $R_C$  is inversely proportional to the width as:

$$R_C = \rho_C / W \quad (2.1)$$

where  $\rho_C$  is the linear contact resistivity expressed in  $\Omega \cdot \mu m$ , and  $W$  is the contact width in  $\mu m$ .

As a consequence, a substantial decrease of contact resistance can be achieved by increasing the effective contact length through patterning [21], [23], for example Smith et al. reported a 32% decrease in Cu-graphene contacts [21]. The introduction of defects in the graphene, located to the contact area, can have a similar effect, and has been demonstrated through UV-ozone treatment [24], or a low-power O<sub>2</sub> plasma etching [25]. Another way to improve the contact is to decrease the distance between the graphene and the metal via the execution of a thermal annealing [21].

The graphene interacts strongly with the contact metal, causing a strong charge doping and a local variation of sheet and contact resistivity, which even extends after contacts [22],

[26]. Depending on the phenomenon of interaction, we distinguish physisorption and chemisorption. **Physisorption** occurs when the variation of the electrical properties of graphene is purely due to the difference in work function between graphene and the metal, which is for instance the case for noble metals like Au [23], [27]–[29], Cu [21], [25], [28], Pt [25], [28], Ag [30], Co [30].

**Chemisorption** instead, describes a scenario where the carbon atoms in graphene and the metal interact chemically, thus changing the electrical configuration, this is the case of Ni [28], [30], [31], Pd [21], [25], [28], [30], [32]–[34], Ti [22], [24], [25], [30], Cr [22], [30]. Of course, the work function difference between a semiconductor and a metal also causes the formation of a rectifying Schottky barrier. However, as represented in Figure 2.1, because of the lack of bandgap, due to its semi-metallic nature, the contact between ideal graphene and a metal remains purely ohmic [22], [35]. Indeed, the process, and effects such as the non-ideality of the source graphene and strain does introduce a small bandgap [14], [15], [36], however, it must be noted that, in the data available in the literature, this effect is usually either very minor, or hidden under the noise level.

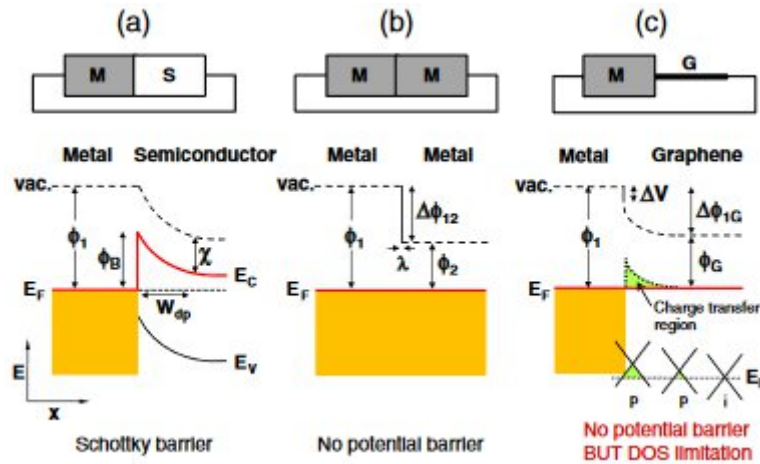


*Figure 2.1 : Energy band diagrams for (a) metal-semiconductor, (b) metal/metal, and (c) metal-graphene contacts.  $E_C$  and  $E_V$  are the energies for the conduction and valence bands, respectively. Image reproduced from [22].*

Interestingly, graphene-semiconductor junctions are well described by a Schottky-Mott model [37], [38], where graphene constitutes the metal contact, and have been used in the development of high-performance diodes and solar cells [17], [37], [39]–[41].

Graphene can be contacted to the metal via bottom contacts, top contacts, sandwich contacts and edge contacts. Top contacts are usually the worst quality due to the resist residue, bottom contacts are less resistive, but also more fragile, as they leave graphene exposed. A sandwich contact combines both and can achieve a decrease in contact resistivity up to 40% compared to top contacts [32], [42].

The results reported in the literature show a significant variance in contact resistivity, not only dependently on the metal, but also within the same metal, this not only highlights the importance of having a clean surface, but also of the quality of the deposited metal. On this subject, *Watanabe et al.* performed a study on graphene contacts using a variety of metal species [30]. Interestingly, they found out a correlation between the contact resistivity and grain sizes of the metal, in particular, contact with smaller grain sizes were the ones with the least contact resistance.

## 2.2 Description of the Process

The process has followed some iterations before being finalized. A base process has been developed starting from an analysis of the current literature for graphene on silicon and was then adapted considering the particularities of  $\text{LiNbO}_3$  substrates, and is displayed in Figure 2.2. The process is divided in several steps, executed in order as described in the list below:

1. Wafer cutting and substrate cleaning;
2. Deposition of a ground back electrode;
3. 1<sup>st</sup> UV lithographic process (liftoff);
4. Bottom metal deposition;
5. 1<sup>st</sup> Lift-off;
6. Graphene transfer;
7. Graphene cleaning;
8. 1<sup>st</sup> annealing;
9. 2<sup>nd</sup> UV lithographic process (patterning);
10. Graphene etching;
11. Graphene cleaning;
12. 3<sup>rd</sup> UV lithographic process (liftoff);
13. Top metal and contact pads deposition;
14. 2<sup>nd</sup> Lift-off;
15. 2<sup>nd</sup> annealing.

In the following sections, every step of the process is discussed with the operational parameters, highlighting eventual differences between different iterations and the reasoning behind each change.

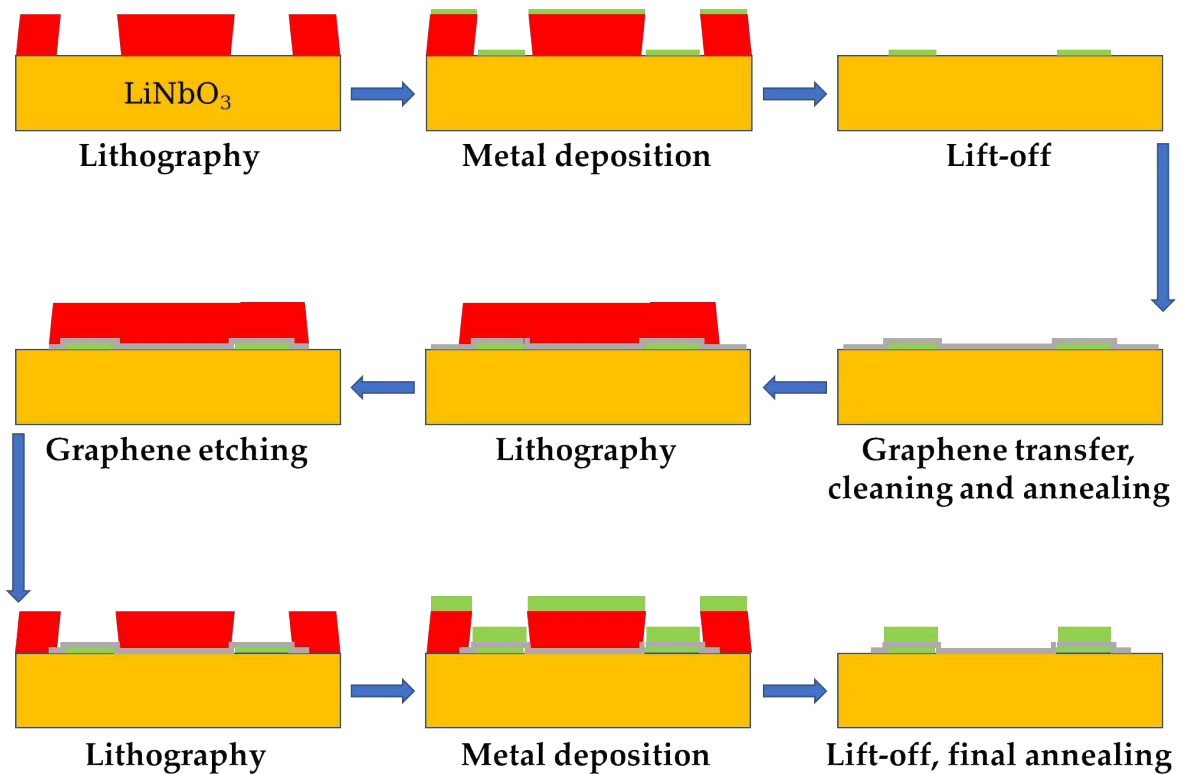


*Figure 2.2: Simplified representation of the process of macro-steps.*

### 2.2.1 Wafer cutting and substrate cleaning

During this step of the process, a 4-inch wafer is diced into smaller samples and cleaned, to be ready for the next steps. Before dicing the wafer, a protective layer of *S1813* photoresist was spin-coated on the wafer, as represented in Figure 2.3. Afterwards, the wafer was placed on a UV-active adhesive in order to keep the pieces in place during the cutting. After the dicing, the strength of the UV adhesive was reduced through UV light, using the *EVG®620* aligner with the recipe “*Flood4inch.rcp*”.

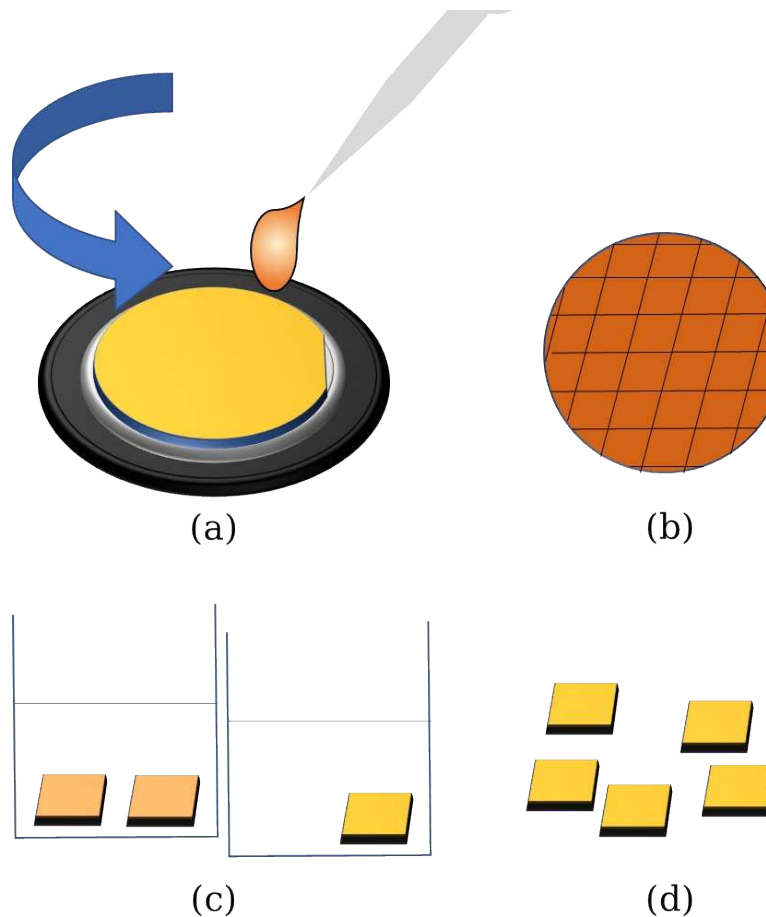


**Figure 2.3: Representation of the dicing process. Spin coating (a), cutting (b), cleaning (c), drying (d).**

The samples were then mechanically separated from the adhesive and the residue was cleaned chemically as described in the following recipe:

1. Wash the sample in acetone for 10 min, to remove the photoresist,
2. Put the samples in Iso-Propyl Alcohol (IPA) for 10 min, this process has to be performed quickly to avoid acetone drying too fast, creating streaks on the sample,
3. Rinse samples in De-Ionized (DI) water for 5 min,
4. Dry the samples with the N<sub>2</sub> gun,
5. Create the piranha solution and let it cool down for 5 min,
6. Put the samples in the piranha solution for 5 min, to remove all remaining organic materials on the substrate,
7. Rinse the samples in DI-water, move gently the beaker to facilitate the dilution of the piranha in water,
8. Exchange DI water and repeat 4 times,

9. Dry the samples with the N<sub>2</sub> gun,
10. Put each sample in a separate box.

The shape and size of the samples had the double functionality of easing the transfer of graphene and help identifying the crystal orientations in the sample in respect to the original wafer. The practical upper limit for the samples was dictated by the sample holder for the UV aligner.

The specific shape of the samples followed some iterations, the first samples were cut as a rectangle (20 mm × 18 mm for z-cut substrates, 20 mm × 22 mm for YX128°) and, in order to help visually identifying the reference axis. To identify the top face, they were marked manually with a diamond tip on a corner. However, the mark was poorly visible and required a microscope to allow for a proper identification of the side it was on. Therefore, it was opted to cut the samples in an **axial-asymmetric shape**, in particular 5°-skewed parallelogram tall 18 mm and wide 20 mm.

## 2.2.2 Lithographic process

A lithographic process has the purpose of creating a photoresist pattern to be used in a later production step, for instance the definition of the metal layers through liftoff or the creation of a etch mask for the patterning of graphene in dry etching.

During each of the lithographic processes, photoresist was deposited uniformly onto the substrate, baked, illuminated, and finally developed. The deposition of the photoresist was done through a spin-coating process, by using the RC-8 spin coater [Karl Suss], depending on the specific process, the baking was performed on a programmable hot plate or in an oven, the impression of the geometries from a mask was achieved through the EVG®620 mask alignment system [EVG Group] or the Electron Beam (EB) lithography machine [Raith Voyager].

As represented in Figure 2.4, the spin-coater is programmed by the user to reach a target angular velocity  $\omega_s$  through a constant angular acceleration  $\dot{\omega}_s$ , and hold motion for a certain spinning time  $\tau_s$ . For each process, the acceleration  $\dot{\omega}_s$  was set to 1500 rpm/s and the target angular velocity was chosen in function of the desired resist thickness. The spin-coater holds the sample on-place through a vacuum contact and before starting the process it is necessary for the sample to be well centered, in order to balance the centrifugal force in the sample. This

results in a uniform distribution of the resist, and in a reduced risk for the sample to be projected away during spinning.

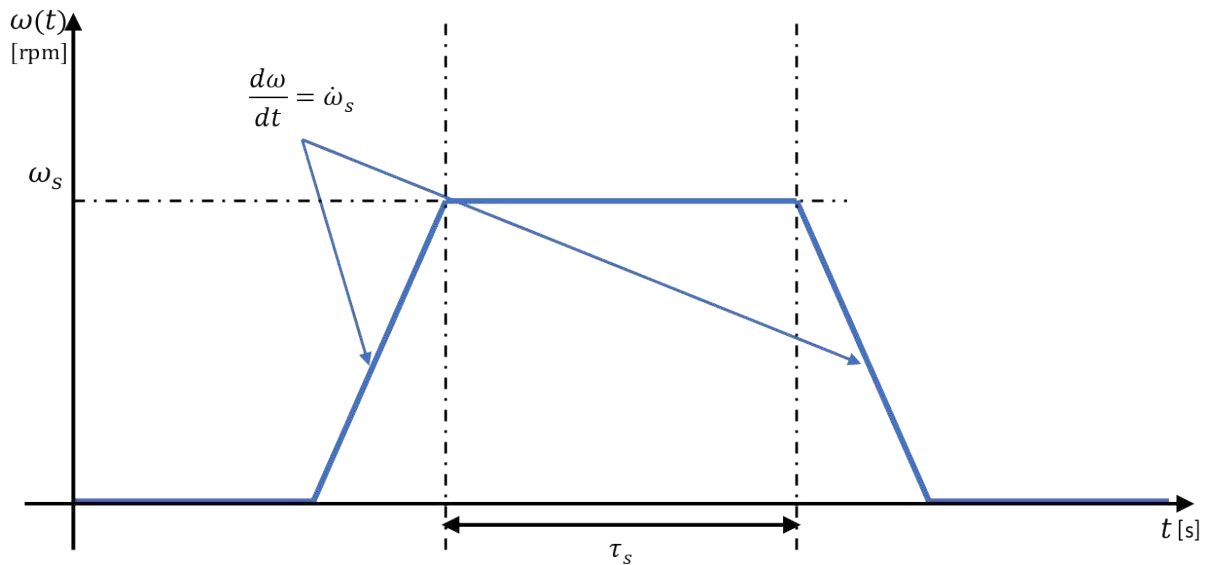


**Figure 2.4:** Typical operation of the spin-coater.

After a baking process, the sample is left to cool down for at least 4 min. The choice of a lithographic machine and the resist is based on the smallest feature size required, in particular the UV setup available allows a minimum resolution  $\sim 1 \mu\text{m}$ , while the EB setup can go down to 10 nm, but is also much slower. After the exposure, the resist was developed with a specific developer solution, washed in DI- $\text{H}_2\text{O}$  to remove any remaining developer and gently dried with the  $\text{N}_2$  gun. Finally, each sample was quickly checked on the microscope to ensure a good quality of the result. The machines used were all placed in the sections with the highest air quality [43] and were illuminated with yellow or red lights to avoid unwanted impressing of the photoresists.

### 2.2.2.1 UV Lithographic process for Liftoff

A liftoff process works best with thick resist layers with undercut walls for the impressed geometries as the negative slope of the walls, as shown in Figure 2.5, favors the deposition of the metal on the top rather than on the walls, simplifying liftoff process. The recipe was derived from a standard liftoff process in MIMENTO, and uses the *AZnLOF2000 0.62* photoresist [44]. The step-by-step process is described as follows:

1. Pre-heat the hot plate to  $110^\circ\text{C}$  20 min before processing;
2. Spin-coat the AZnLOF2000 resist;

3. Bake for 1 min 30 s;
4. Impress the photoresist;
5. Bake for 3 min;
6. Develop the photoresist.

The resist was spin-coated with the following parameters:

- $\omega_s = 3700$  rpm,
- $\dot{\omega}_s = 1500$  rpm/s,
- $\tau_s = 30$  s.

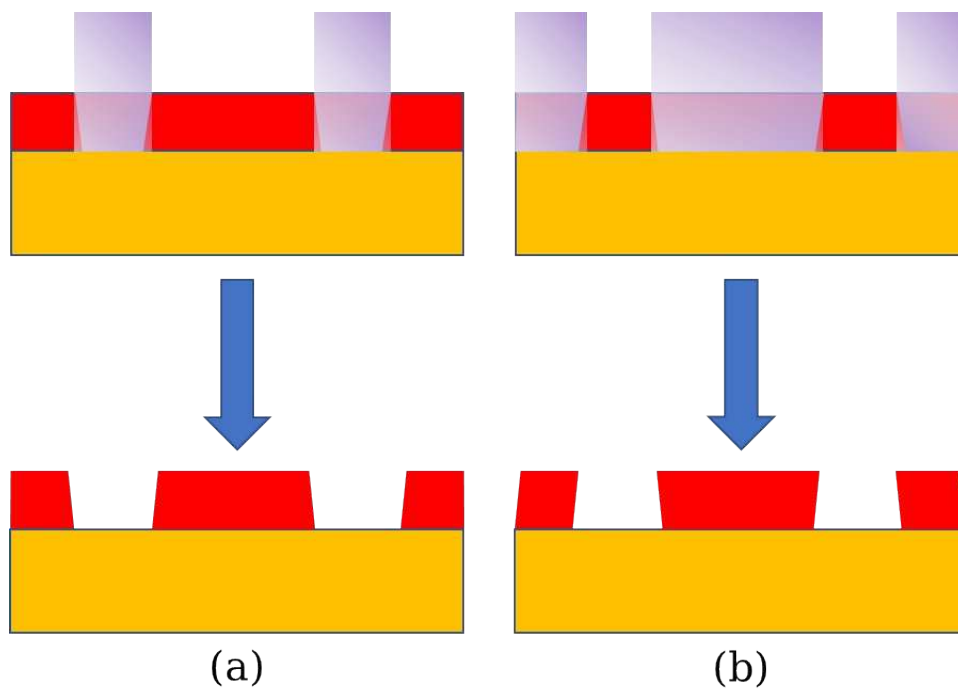


**Figure 2.5:** Representation of section a certain pattern as impressed on a positive (a) or a negative (b) resist.

In order to start the exposure, the aligner machine was set to use the “topside2inchm4.rcp” recipe, with the following parameters:

- Exposure mode = “Constant time”,
- Contact mode = “Vacuum contact”,
- Separation = 200  $\mu\text{m}$ ,
- Stop after contact = “ON”,
- Vacuum contact pressure = 800 mbar.

The dose of UV (ultraviolet) energy density required was **65 mJ/cm<sup>2</sup>** and the exposure time was computed each time from a measure of the output power density of the mercury lamp in mW/cm<sup>2</sup>. After the exposure and the second baking, the samples are finally developed by submersion in the *MF26A* solution for 1 min 30 s, rinsed in DI-H<sub>2</sub>O for 5 min and gently dried with the N<sub>2</sub> gun.

The first batch of samples were made with a slightly different version of the process, which started with the deposition of a layer of the **titanium-based adhesion promotor, Ti Prime** [45], in order to improve stickiness between it and the liftoff photoresist. The deposition of the Ti Prime on the substrate was performed through spin-coating and baking on a hot plate at 110°C for 2 min, the parameters used for the spin-coater were the following:

- $\omega_s = 3000$  rpm,
- $\dot{\omega}_s = 1500$  rpm/s,
- $\tau_s = 20$  s.

However, the usage of this resist was afterward tested to be unnecessary, as following tests with only the AZnLOF resist were just as effective. The usage of Ti Prime was finally dropped starting from the 2<sup>nd</sup> batch of characterization samples, to simplify and speed up the process, and to avoid eventual Ti residue.

### 2.2.2.2 UV Lithographic process for Patterning

The patterning process has been optimized for different resist types. The idea has been to exploit the process itself as a way to optimize the electrical response of the devices. Indeed, researchers have proved that the electrical parameters of processed graphene depend significantly to the doping and scattering caused by photoresist residue [9], [46]. As a consequence, **the possibility of tuning the electrical parameters** of graphene through the resist was explored experimentally as a way to improve AE coupling. The patterning process was made in two variations, by using either the positive *S1813* [47] or the negative *AZnLOF2000* [44] photoresist.

The process for the AZnLOF2000 is functionally identical to what described in Section 2.2.2.1, while the deposition and lithographic process for the S1813 was optimized starting from a standard patterning process. The refined step-by-step process for the S1813 is described as follows:

1. Pre-heat the hot plate to 110°C 20 min before processing;
2. Spin-coat the S1813 resist;
3. Bake for 3 min 30 s;
4. Impress the photoresist;
5. Develop the photoresist.

The parameters used in the spin-coater for a 1.5  $\mu\text{m}$ -thick layer of S1813 were the following:

- $\omega_s = 3500$  rpm,
- $\dot{\omega}_s = 1500$  rpm/s,
- $\tau_s = 30$  s.

For the UV exposure, the recipe “*topside2inchm4.rcp*” was used, with the following parameters:

- Exposure mode = “*Constant time*”,
- Contact mode = “*Vacuum contact*”,
- Separation = 200  $\mu\text{m}$ ,
- Stop after contact = “*ON*”,
- Vacuum contact pressure = 800 mbar.

The exposure time was computed from the defined energy dose of **50 mJ/cm<sup>2</sup>** and the output power density of the mercury lamp in mW/cm<sup>2</sup>. The resist was then developed through submersion in the *NF26A* solution for 1 min 10 s.

The soft-baking temperature and time, and the energy dose during exposition received some iterations to reduce the amount of residue stuck on graphene after processing, which was substantial enough to cause a 3x increase in resistivity. In particular, the first version used a 120°C soft-baking for 2 min, on a hotplate and exposure energy density of **65 mJ/m<sup>2</sup>**.

### 2.2.2.3 Electron Beam Lithographic process for Liftoff

Some of the geometries necessary for the acoustic designs were considerably smaller than what was achievable under UV lithography. Specifically, the 2.5 GHz IDTs required for a resolution of less than 288 nm, which could be achieved only through EB lithography. The EB lithographic process used the resists *CSAR 62 AR-P 62000.09* [48], the *Ti Prime* [45], and

the *Electra 92* [49], the former is an EB-compatible resist capable of resolution  $< 10$  nm, the second is used to improve the adhesion between the substrate and the e-beam resist, the latter allows for the implanted charges to flow away from the substrate, reducing the risk of deformation due to proximity effects from the primary charges stuck on a nonconducting surface. The Ti Prime was needed to guarantee adhesion between CSAR and the substrate. The parameters for the spin-coat deposition of the resists are shown in Table 2-1 and the process steps are described as follows:

1. Heat up the oven at 150°C before processing,
2. Spin-coat the Ti Prime,
3. Spin-coat the CSAR resist,
4. Bake in oven for 30 min,
5. Cool down oven to 85°C,
6. Spin-coat the Electra resist,
7. Bake in oven for 20 min,
8. Impress the resist through EB lithography,
9. Develop the resist.

**Table 2-1: Spin-coating parameters for the resists used in EBL.**

|                          | <i>Resist</i> |                          |            |
|--------------------------|---------------|--------------------------|------------|
|                          | Ti Prime      | CSAR 62 AR-P<br>62000.09 | Electra 92 |
| $\omega_s$ [rpm]         | 4000          | 2000                     | 2000       |
| $\dot{\omega}_s$ [rpm/s] | 2000          | 2000                     | 2000       |
| $\tau_s$ [s]             | 30            | 30                       | 30         |

Before the exposure, the electron gun was set to generate a current in the range of 2.41-2.44 nA with an accelerating potential of 50 kV, and the resist was impressed with a dose of 150  $\mu\text{C}/\text{m}^2$ . For the development, first the Electra layer was dissolved away by bathing the samples 3 times in deionized water for 10-15 s each, afterwards, the impressed CSAR was removed via a 1 min bath in Amyl-Acetate, followed via a 30 s bath in a solution composed of MIBK and IPA with ratio 1:3. The timings in the last step are critical for a good result.

## 2.2.3 Metal Deposition and Liftoff

The production process includes three different steps of metal deposition, one for the bottom graphene contacts, one for the top graphene contacts and one for the back-gate. Both the bottom and top metallic contacts have been deposited via the *MEB600* e-beam evaporation machine (Plassys), while the bottom ground electrode was deposited via the *MP700S* sputtering machine (Plassys).

### 2.2.3.1 Liftoff

In the liftoff process, a metal thin film is deposited on the sample after the creation of the lithographic hard mask through the process defined in Section 2.2.2.1. After the deposition, the mask is removed chemically through a solvent, which mechanically lifts-up the excess metal from the sample. If the metal film is also continuous on the vertical walls, the removal needs to be aided mechanically, generally through the propagation of ultrasounds in the liquid solvent. However, **ultrasounds can also damage the IDTs and the graphene**. Therefore, the strategy used to facilitate the liftoff was to perform the **lithography through negative photoresist** and to deposit the metal through an EB-assisted thermal evaporation. The main advantage of this approach is that **the resulting metal deposition is anisotropic** and favors the direction orthogonal to the face of the sample.

The metal deposition process must be performed right after the lithographic step, in order to keep a good quality of the liftoff resist, the samples were placed on a holder dish and held there by tape. The dishes were placed upside-down on a holder, the vacuum chamber was then closed and the vacuum pump was activated. The recipe is then selected and launched when the vacuum reaches  $10^{-6}$  mbar. When the deposition is complete, the samples are then taken from the holders and placed vertically in beakers with remover solution at 75-80 °C, and left overnight. The **day after**, as the resist is fully dissolved in the solution and the metal is still partially attached to the rest and must be removed through a non-invasive mechanical method. The method used for the first batches of samples is described as follows:

1. Prepare a beaker full of fresh remover solution, one full of IPA, and one full of DI-H<sub>2</sub>O,
2. Grab the sample with a sharp, flat tweezer, holding it vertical,
3. Gently move the sample up and down to ease the separation of the metal,

4. Put it in the second beaker of remover solution, still holding it with the tweezers,
5. Gently move the sample up and down, left and right to remove the remaining metal, maintain the sample vertical,
6. Put it in the IPA-filled beaker, still holding it with the tweezers,
7. Gently move the sample up and down, left and right to remove the remaining metal, still maintain the sample vertical,
8. Leave the sample vertically in IPA for 3 min,
9. Put the sample vertically in the DI-H<sub>2</sub>O beaker, hold it still waiting at least 20 s, for the IPA bubbles to get removed,
10. Place the sample vertically for at least 5 mins,
11. Gently take the sample and put it on a tissue,
12. Gently dry sample with N<sub>2</sub> gun, taking care not to flip it,
13. Refresh the beakers every 3-4 samples.

This method was good in creating clean samples, however, it did not work as well on samples with a high density of devices and took the risk of damages caused by the samples falling from other users bumping on the beakers. Therefore, starting from the production of the acoustic series, the “rocket bubbles” method was used, which had the aim of decreasing the risk of damaging the sample and the amount of solvents necessary. The method is illustrated in Figure 2.6 and explained as follows:

1. Take a pipette, prepare a beaker of remover solution, one of acetone and one of IPA, the liquid should be high about 1 cm,
2. Transfer a sample horizontally on the beaker of remover,
3. Use the pipette to gently blow bubbles on the sample,
4. Transfer the sample in the acetone beaker,
5. Blow bubbles on the sample,
6. Quickly transfer the sample in IPA,
7. Blow bubbles on the sample,
8. Gently dry IPA through the N<sub>2</sub> gun.

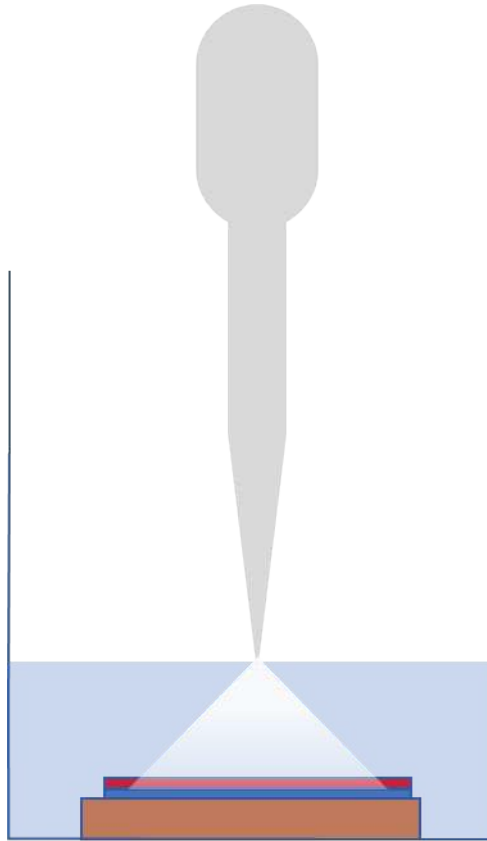


*Figure 2.6: Representation of the rocket bubbles method.*

The recipes used in the characterization samples were slightly different in respect to the acoustic samples. In particular, the characterization samples have been made using an Au/graphene/Au sandwich contact, with the bottom contact composed of a Ti/Au stack to improve adhesion to the substrate and because the top portion needed to be purely of Au, the adhesion, or lack thereof, to the sample depended on the presence of the bottom metal. Since the exposure speed of the EBL is considerably slower, this was not possible without sacrificing the throughput, and therefore number, of the samples. Therefore, for the acoustic samples, it was instead chosen to keep the lithographic areas minimal and to make the top metal of a Cr/Au stack instead.

For both the characterization and acoustic devices, the bottom contacts were composed of a Ti/Au stack of 10 nm/30 nm of Ti, while the top metal was 50 nm in the characterization devices and 150 nm in the acoustic devices.

### 2.2.3.2 Backside electrode

The function of the backside electrode is the creation of an easy-to-access voltage reference, which can also be used as a gate for doping the graphene via the electric field. Since the back electrode does not need particular geometries, the *MP700S* has been chosen because it is faster, and it does not require for the samples to be held upside-down.

Before starting the deposition, a 1.5  $\mu\text{m}$ -thick layer of S1813 photoresist was spin-coated in order to not damage the front face of the sample, and then the samples were put on the shuttle with the protected side down. The shuttle was then put inside the machine, and the chamber was brought to vacuum ( $< 5\text{e-}6$  mbar), in the meantime, the user recipe is selected. The recipe consisted in the following steps:

1. A standard pre-deposition cleaning with  $\text{O}_2$  or Ar ions,
2. The deposition of 10 nm of Cr and 100 nm of Au.

Before each operation, the recipe was checked to be compatible with the current deposition rates and eventually updated to match the current values. In fact, the user sets the deposition time for each material, while the machine operates at given deposition rate which depends on various factors and are provided by the operator. After the deposition, the samples are then taken back from the machine and re-cleaned through the same technique described in the Section 2.2.1.

### 2.2.4 Graphene Transfer

Transfer of CVD-grown graphene from a donor substrate to the final substrate can be achieved through several means [50]. Although direct transfer of graphene to the final substrate can be achieved through direct transfer techniques [51], [52], this cannot be easily achieved on most substrates, therefore, various transfer techniques use an intermediary medium to carry the 2D material from the source to the destination. Most transfer techniques use a **liquid solution**, usually water-based, as an intermediary between the transfer, and employ the deposition of a thin layer of **protective resist** to ensure the mechanical stability of the graphene during the process, this kind of techniques are usually categorized under the name of **wet transfers** and bubble transfer.

On the other end, dry transfer techniques are used to directly transfer graphene between solid substrates to minimize the use of chemical agents. Those kinds of techniques usually

involve the deposition of a mechanically strong, sticky material that sticks to the graphene and can be detached after placing the graphene on the end substrate. Researchers had success in developing techniques using several different materials, for example by using thermal release adhesives [53], water-soluble thin films [54], [55], pressing of various polymer at high temperature [51].

For wet transferring techniques, the graphene is put afloat the liquid surface by means of a total etch of the source substrate in a certain solution, the specifics of the technique depend on the nature of the substrate, for example, etching of Cu and Ni substrates for graphene transfer is usually performed through  $\text{FeCl}_3$  or  $\text{HCl}$  solutions . The main positive aspects of using a wet transfer is the relative **ease of optimization**, with the negative side that residue of the etchant solution can damage the final substrate and cause doping of the graphene, therefore requiring to transfer the graphene/resist stack multiple times in clean water in order to avoid contamination.

During bubble transfer, the graphene layer is detached from a substrate through gas bubbles. The necessary gas can be either generated chemically [50], [56] or through electrochemical decomposition of  $\text{H}_2\text{O}$  [50]. The main advantage of this approach is the ability to **reuse the substrate** to perform other growth of graphene, however, this can require significant optimization work to achieve the best results. Overall, because of the small-scale of production and the relative flexibility, the type of process adopted in the presented work is in the category of wet transfer.

#### 2.2.4.1 Process with the “easy transfer kit”

Most of the samples production was carried out using commercial “easy transfer kit” from Graphenea (Spain) [57]. Each kit is composed of a single packaged  $12\text{ mm} \times 12\text{ mm}$  CVD graphene monolayer that had been grown on copper, been covered with a thin layer of PMMA and then pre-transferred to a holder composed of dust-free paper covered with a water-soluble polymer (PVA). The transfer process was a modified version of the basic process provided by the producer, the changes made were made with the idea of better quality for the devices. The steps for the transfer are represented in Figure 2.7 were:

1. Fill 2 big beakers full of deionized water and cover them,
2. Dissolve the PVA in water,
3. Move the graphene/PMMA in clean water,

4. Cover the bottom surface of a beaker with a clean cellulose towel,
5. transfer on the final substrate,
6. dry sample,
7. remove protective resist.

Before operating the transfer, a transfer-aiding substrate of Si/SiO<sub>2</sub> was cleaned, on the SiO<sub>2</sub> side, with O<sub>2</sub> plasma through the RIE machine (recipe “*residue\_removal*”). This had the added benefit of improving the adhesion of water, which created a water pillow between the graphene/PMMA foil and the substrate, reducing the risk of damage between the multiple transfers.

While removing the PVA, the detachment of graphene from the holder was aided mechanically by tilting slightly the holder with an angle of ~45°. Afterwards, the beaker was covered and the graphene was left to rest for 10 min to let PVA residue dissolve completely in the water. The foil was then grabbed through the transfer substrate, transferred to the second water beaker, and left for another 10 min. Finally, the graphene was carefully taken with the final substrate and then left to dry overnight in a vertical position inside the beaker with the towel. The vertical position favors the water to flow naturally downwards so that it can get absorbed in the towel, which also makes easier for the samples to remain vertical more easily due to the added drag.

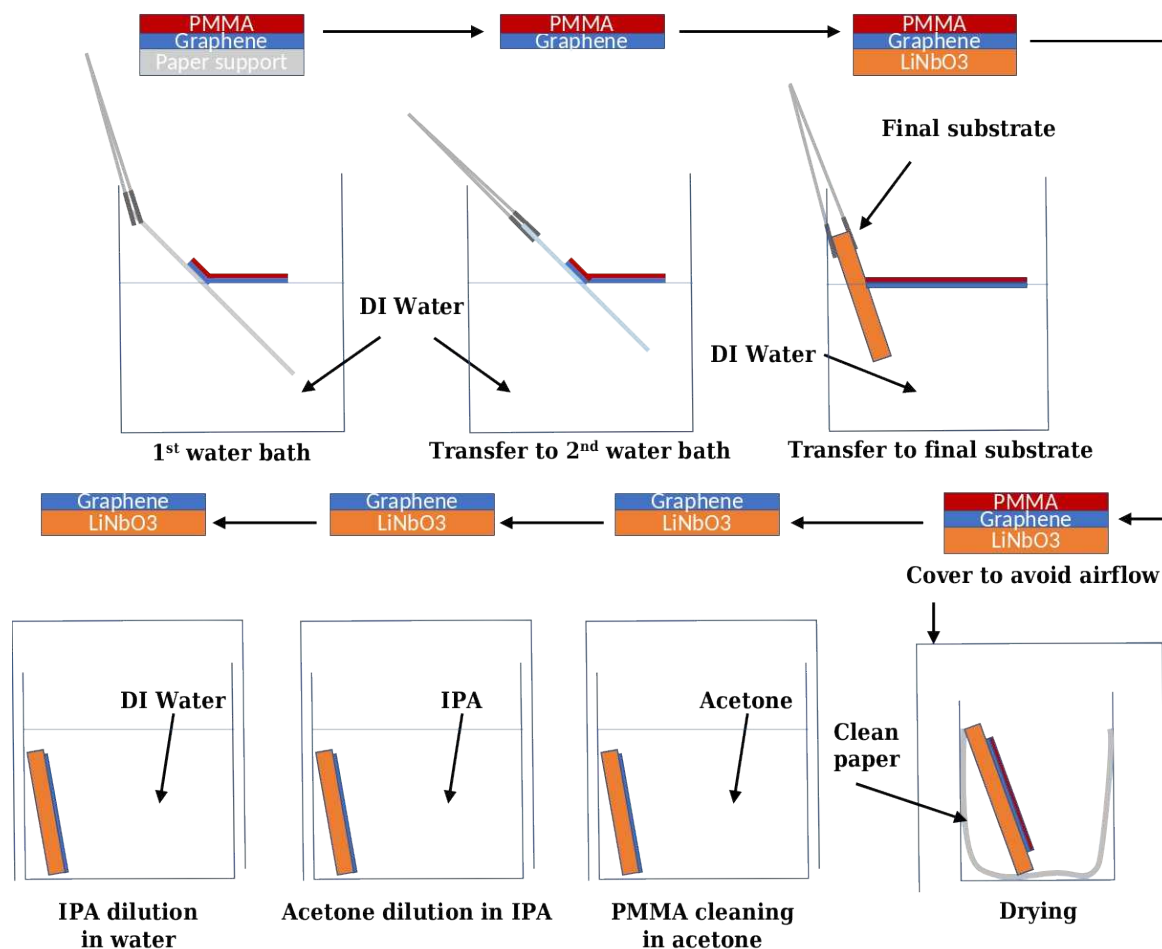


**Figure 2.7: Representation of the traphene transfer and cleaning process.**

After the samples were dry, a beaker of acetone with a depth slightly higher than that of the samples (of ~5 mm), and the PMMA is cleaned off by submerging the samples vertically in acetone, and leaving them vertically, using the edge of the beaker as support, for 4h. The acetone cannot be removed immediately, as the fast evaporation can damage both the graphene and the substrate, therefore needs to be first dissolved in IPA, and then in clean water. For this, a beaker is filled with IPA with roughly the same depth as the acetone and, after letting the beaker rest covered to dissipate the waves, the sample is grabbed from the acetone beaker and, while keeping it vertical, is quickly placed in the IPA beaker, and left to rest for 20 min. Finally, a beaker filled with deionized water is prepared, and the sample, while still being held vertically, is taken from the IPA beaker and placed in the water beaker. Differently from the last step, before leaving the sample in position, it is held still with the tweezers for ~1 min, while underwater, until the bubbles of IPA stop surfacing. After 20 min in water, the sample is taken from the water beaker, placed on a clean cellulose tissue and then gently dried with the N<sub>2</sub> gun.

### 2.2.4.2 Process With CVD Graphene on Cu Substrates

A process for wet transfer of graphene has been studied starting from the available literature. The CVD graphene has been grown on single-crystal Cu substrate and was provided in foils of various sizes. During the CVD process, graphene was deposited on both sides, however, due to several factors, the quality of the two sides were different, in particular, the graphene on a specific face was less homogeneous. Therefore, for the best quality of the transferred graphene, the process requires to take good care not to damage the good side, and to remove the graphene on the other side before carrying out the transfer. The process is composed of the following steps:

1. Deposit the protective resist for the transfer,
2. Clean the backside,
3. Etch the Cu,
4. Clean the etch residues,
5. Transfer the graphene on the substrate,
6. Dry sample,
7. Remove the protective resist.

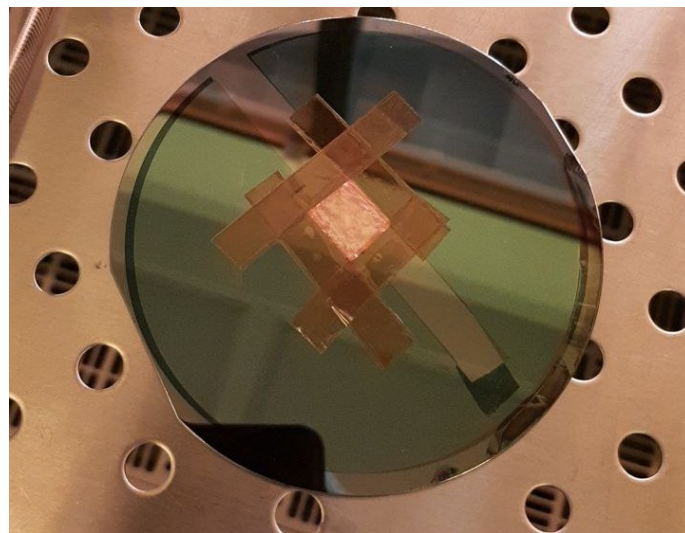


**Figure 2.8 :** *A piece of graphene/Cu with the protective resist (Az10xt) deposited.*

The deposition of the protective resist was performed through a spin-coating process. With this purpose, the graphene/Cu foils were cut in smaller pieces (~15 mm × 15 mm) that were big enough to be processed with the destination substrate. The cut foil piece was then placed at the center of a 4'' SiO<sub>2</sub>/Si wafer, and fixed through Kapton tape, as shown in Figure 2.8. The wafer

was then placed on the spin-coater, some drops of resist were put on the foil and spun at a certain velocity in order to achieve a certain thickness. Two different resist types were tested for the transfer of graphene because of their good availability, the *AZ10xt-1000cP* [58] and *PMMA-A4* [59], each required different process parameters. The thickness vs. spin-speed curves of the resists is shown in Figure 2.9; in particular, Figure 2.9 (a) shows the curves for AZ10xt-1000cP, and Figure 2.9 (b) shows the curves for PMMA. In both cases, the resist was spun at the speed of 2000 rpm, with acceleration 3000 rpm/s, achieving a thickness of  $\sim 5 \mu\text{m}$  for the AZ10xt-1000cP and  $\sim 4 \mu\text{m}$  for the PMMA-A4. The thickness of the resist layer was chosen as a way to decrease the risk of damage to the graphene during the rest of the process and as a way to improve visibility during the transfer.

After the deposition was complete, the samples were covered to avoid dust and were left to dry overnight at room temperature, this was done as a way to reduce as much as possible the residue of resist on the graphene's surface through reduction of the stickiness between them.

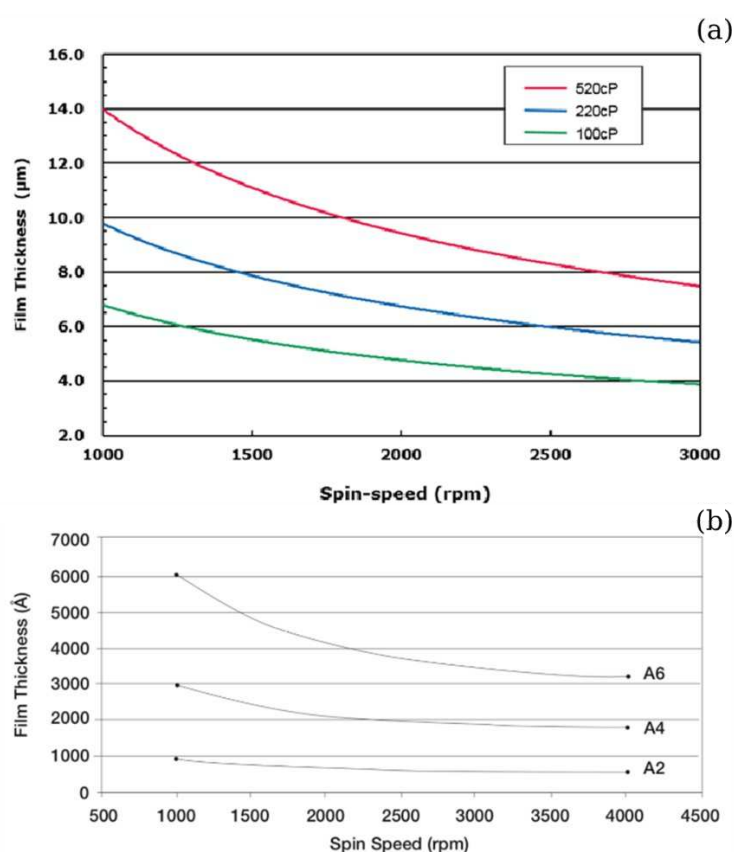


**Figure 2.9: Film thickness vs. spin speed for the resists AZ10xt (a) and PMMA (b).**

Afterward, the samples were flipped, assured on a  $\text{SiO}_2$  wafer through Kapton tape and then placed in the RIE machine to completely remove the graphene on the backside through

exposure in O<sub>2</sub> plasma at 75W for 60s. After being removed from the RIE machine, the edges of the foil that were left uncovered by the protective resist, have been cut away from the rest, so that the samples were finally ready for the transfer.

For the presented process, it was chosen to use FeCl<sub>3</sub> as etchant and for optimizing the concentrations used, several tests were performed by etching the Cu of several 13 mm × 13 mm foils in beakers with different concentrations of FeCl<sub>3</sub>. The solutions have been prepared by diluting a saturated solution of etchant with pure H<sub>2</sub>O, the solutions were prepared in ratios 1:0, 1:20, 1:5 and the quantity of liquid in the beaker was kept above 3 cm to ease the manual scooping the monolayer with a small substrate.

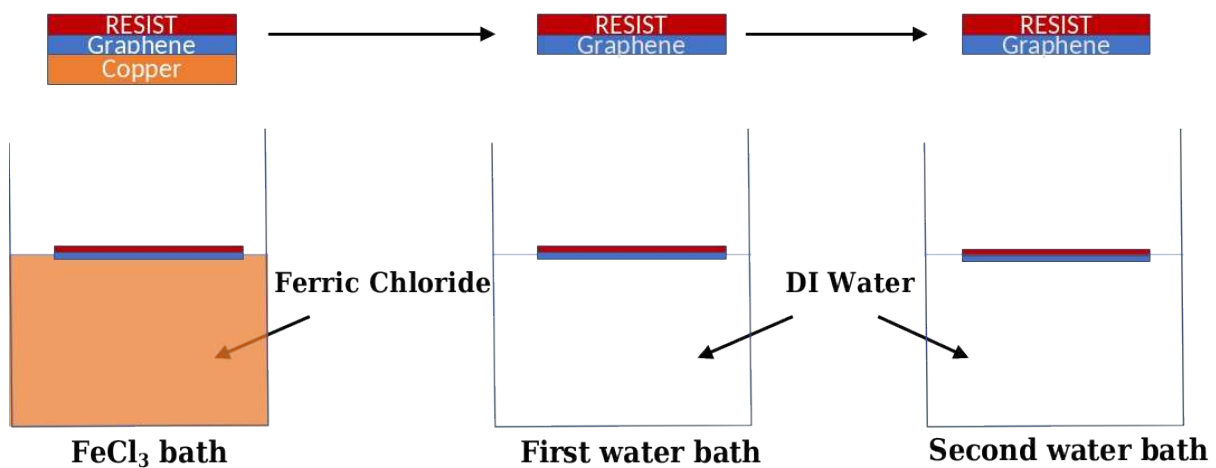
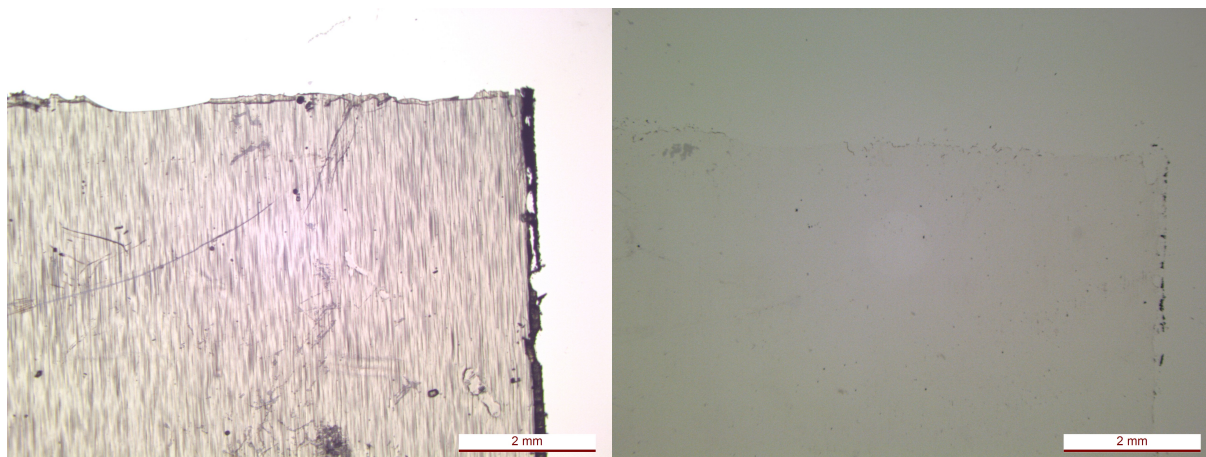


**Figure 2.10: Representation of the etching process of the Cu.**

The etching process is represented in Figure 2.10, the foil was placed floating on the surface of the solution with the resist up, and the samples were left at room temperature and periodically checked every 10 min until the Cu was completely removed, which was indicated by the color of the sample. Afterwards, the residue etchant on graphene/resist was diluted away by transferring it in a beaker full of pure H<sub>2</sub>O and then left for 10 min, this operation was performed 2 times. In the first etching trial, the Cu was etched away very quickly, in less than 5 min, it was considered that this could damage the graphene, the final optimization step, the etching time was of ~20 min for a ratio of 1:5. After the second water bath, the substrate/graphene/resist, was left to dry overnight, and then cleaned from the residual resist via the same technique as described in Section 2.2.4.1.

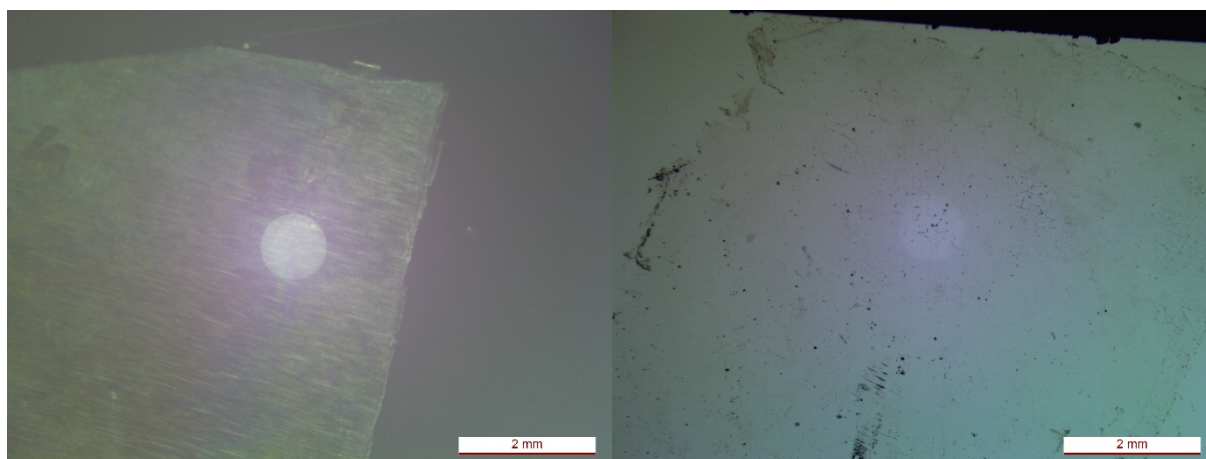


(a)

(b)

**Figure 2.11:** Microscope image of the edge of a small (~13 mm × 13 mm) graphene transferred from a Cu substrate onto a white LiNbO<sub>3</sub> substrate. (a) includes the protective AZ10xt, in (b) the resist was cleaned off.

Figure 2.11(a) and Figure 2.12(a) show the graphene with the protective resist (respectively AZ10xt and PMMA-A4) transferred to a white LiNbO<sub>3</sub> substrate, while Figure 2.11(b) and Figure 2.12(b) show the same sample after cleaning, the damage was mostly due to mechanical handling during the transfer, and the thicker AZ10xt is visibly less damaged due to the higher mechanical strength from the thicker resist.



(a)

(b)

**Figure 2.12:** Microscope image of the edge of a small (~13 mm × 13 mm) graphene transferred from a Cu substrate onto a white LiNbO<sub>3</sub> substrate. (a) includes the protective PMMA-A4, in (b) the resist was cleaned off.

Finally, this technique was tested for foils of bigger dimensions (~25 mm × 20 mm), however, the bigger size of the sheet and the thick resist used were the cause of some problems.

Specifically, the resist could crack, and some bubbles could be formed during the transfer process. Those bubbles can be formed either while moving the sheet between each bath, or during the final transfer to the destination substrate. Once they were made, it was impossible to remove the bubbles without creating cracks. The protective resist prevented the bubbles from popping off during transfer Figure 2.13(a), however, once cleaned off, they exploded, tearing locally the graphene's surface Figure 2.13(b).

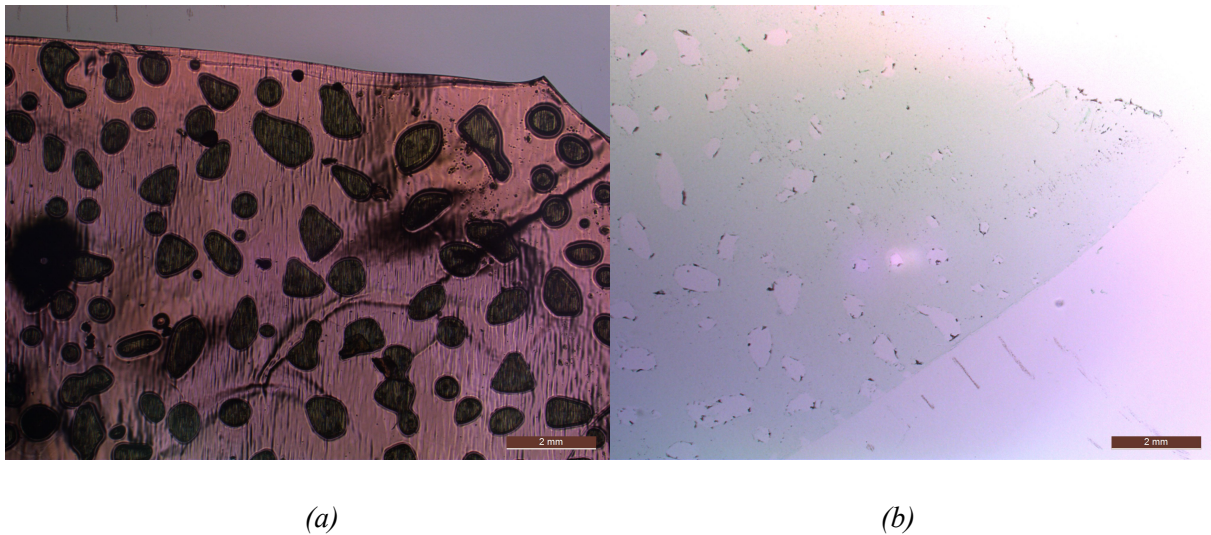


*Figure 2.13: Microscope image of the edge of a big ( $\sim 25 \text{ mm} \times 20 \text{ mm}$ ) graphene transferred from a Cu substrate onto a  $\text{SiO}_2$  substrate. (a) includes the protective AZ10xt coating layer and highlights the air bubbles, in (b) the resist was cleaned off, creating holes in the graphene layer.*

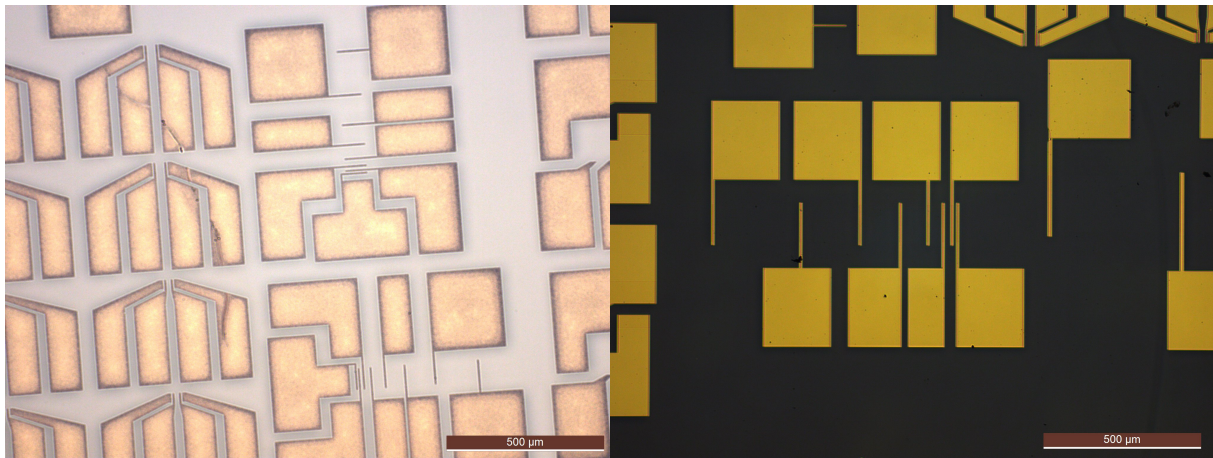
## 2.2.5 Graphene Annealing

In the production of graphene-based devices, the **annealing** process has the role of strengthening the **adhesion between it and the substrate**, improving the quality of the metal-graphene contacts, decomposition of photoresist residue [9]. Standard graphene annealing procedures are performed at a temperature range either under vacuum, or in an inert atmosphere, like nitrogen, or argon.

In this case, the annealing was performed through a controlled-atmosphere furnace machine capable of executing the annealing in a specific atmosphere. The annealing process was performed and was executed as follows:

1. The samples were placed on a holder (a Si wafer),
2. The holder, with the samples on, was put inside the machine,
3. The process recipe was selected and executed.

The recipe was composed in the replacement of the atmosphere, a slow rise time to the target annealing temperature, which is held for a defined amount of time, after which the oven is let to cool down at ambient temperature.



(a)

(b)

**Figure 2.14: Picture of a z-cut Black  $\text{LiNbO}_3$ /graphene sample after annealing at 450 °C for 1 h (a) and another after annealing at 120 °C for 2 h.**

The process was tested with both  $\text{N}_2$  and Ar atmospheres with similar results. The recipe was optimized in terms of the annealing temperature and annealing time. In particular, the final recipe is composed of an annealing temperature **120 °C for 2 h under Ar atmosphere**.

It must be noted that first version of the recipe has been performed considering temperature **450 °C** and annealing time 1 h, to also help in the removal of the resist residue. Interestingly, as displayed in Figure 2.14, this caused significant damage to the sample, as the black, z-cut,  $\text{LiNbO}_3$  substrate changed color to white, and the graphene effectively disappeared. Afterward, trials at 250 °C (1 h) and 150 °C (2 h) were also performed, however, the first one still returned with damaged graphene and the substrate still changed color, which also happened in the latter.

The change in color in the crystal could have been caused by a segregation of the Li ions in the crystal, diffusion of  $\text{O}_2$  molecules adsorbed on the crystal, or diffusion of Ti residue because of the usage of Ti prime. Regarding the removal of graphene, not much has been reported for reactivity specifically between graphene and lithium niobate. However, *Konar et al.* reported the **formation of  $\text{Li}_2\text{C}_2$**  from the reaction between LiH and graphite in the temperature range between 400°C and 800°C [60] while exploring ion intercalation of Li between the graphene planes. Indeed, even a very small reaction speed between the Li in

LiNbO<sub>3</sub> and graphene would at least significantly damage the monolayer over the annealing time.

## 2.2.6 Graphene Patterning

Because of their thickness, etching of graphene monolayers is relatively easy to perform through the RIE method. This is usually done by using O<sub>2</sub> plasma and has been reported via different RF power, gas pressures, and process time, for instance *Hsu et al.* used an etching time of 30 s, but did not report other process parameters [61], *Watanabe et al.* performed etching over 15 s under 100 W of RF power and pressure 10 Pa [30]. Of course, the parameters of the process change from machine to machine and require a specific optimization. Furthermore, as black LiNbO<sub>3</sub> substrates were chosen as the main substrates, the process must be tuned to minimize the doping of the substrate through oxygen implantation.

*Table 2-2: Process parameters for graphene etching.*

|                    |                  |
|--------------------|------------------|
| <b>Temperature</b> | <i>20 °C</i>     |
| <b>RF power</b>    | <i>80 W</i>      |
| <b>Pressure</b>    | <i>100 mTorr</i> |
| <b>Time</b>        | <i>27 s</i>      |

The etching process was optimized to use the **Corial 200R** [62], the RIE was performed with oxygen plasma and the optimized parameters are reported in Table 2-2. The dose of implanted oxygen did not alter the properties of the substrate significantly.

## 2.3 Description of Other Methods

A modified version of the GoL process was developed for studying the effect of a periodically poled LiNbO<sub>3</sub> (PPLN) substrate. The poled structures were impressed on a white Z+ cut LiNbO<sub>3</sub> substrate by applying a strong electric field locally, capable of inverting the crystal domains.

In order to invert the domains, a coercive electric field of ~21 kV/mm [63] was applied to the setup in Figure 2.15 in a patterned area of a thick S1828 photoresist layer. The poling setup used was composed of Trek 20/20C [64] High-Voltage Amplifier (HVA), capable of providing a DC voltage of up to 20 kV with currents of ±20 mA, a R&S®HMF2525 [65]

function generator to generate the voltage stimulus necessary to drive the amplifier, and a R&S®RTB2002 oscilloscope [66] to visualize the voltage provided to the HVA and its output current during the poling process through its auxiliary outputs. All was controlled by the user via a computer provided with a specific LabVIEW program.

In order to assure the best compatibility with the LiNbO<sub>3</sub> substrate and assure the best uniformity of the electric field inside the crystal, the end electrodes to the substrate were made of a conductive aqueous solution of a Li salt (LiCl) dissolved in H<sub>2</sub>O and non-poled regions were achieved through a thick patterned photoresist layer.

The recipe for the deposition and patterning of the S1828 used was the following:

1. Spin-coat the Ti-Prime adhesion promoter ( $\omega_s = 4000$  rpm;  $\dot{\omega}_s = 1000$  rpm/s,  $\tau_s = 30$  s),
2. Spin-coat the S1828 ( $\omega_s = 4000$  rpm;  $\dot{\omega}_s = 1000$  rpm/s,  $\tau_s = 30$  s),
3. bake in oven at 90° C for 30 min,
4. Expose resist with dose 90 mJ/cm<sup>2</sup> (use hard-contact between mask and sample).

After processing the sample was placed in the enclosure as represented in Figure 2.16 so that the poling could be performed. After the poling, a graphene monolayer was then transferred and cleaned on the PPLN using the same techniques as previously described in Section 2.2.4. The final sample is shown in Figure 2.17.

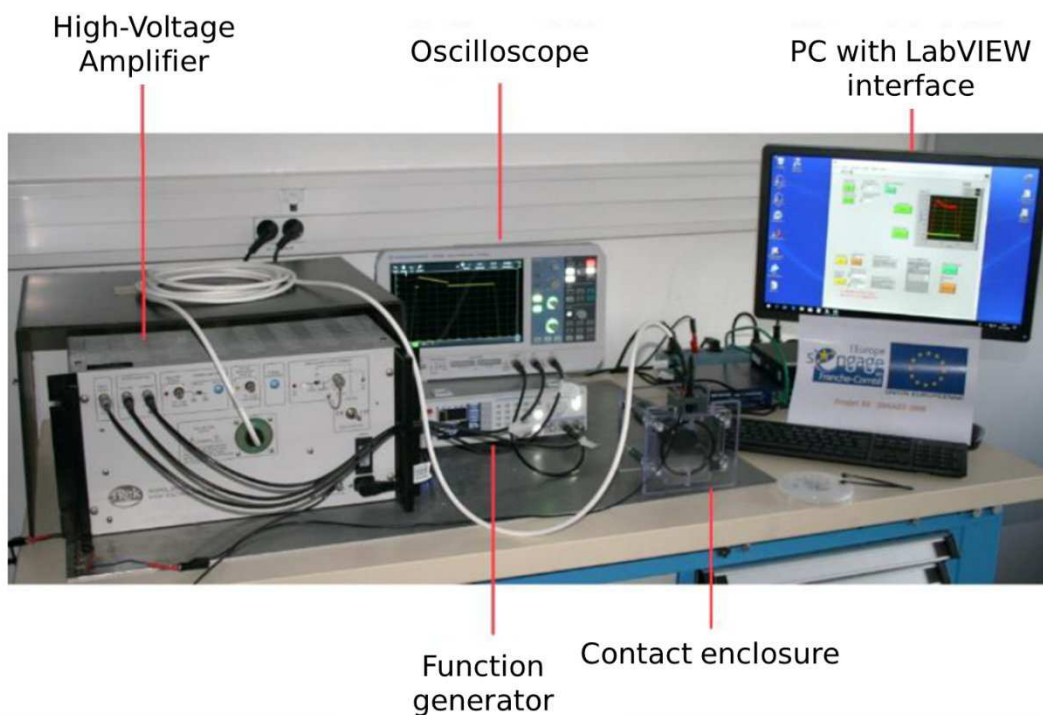


*Figure 2.15: Photo of the setup used in the poling process [63].*

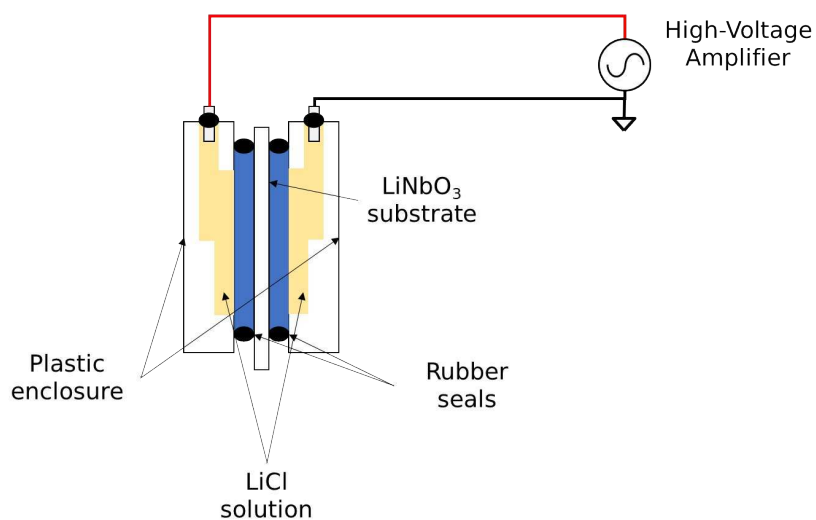
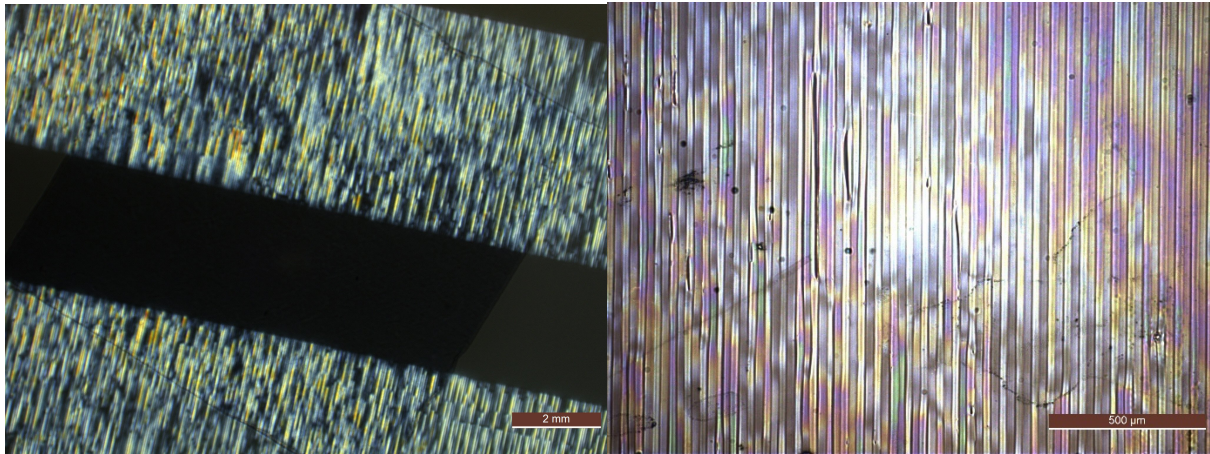


*Figure 2.16: Schematic of the contact enclosure used for poling.*



(a)

(b)

**Figure 2.17:** *Picture of the transferred graphene film, (a) with (b) and without protective resist, on a  $z^+$  white PPLN sample.*

## 2.4 Visible-light microscopy

The transferred and processed graphene was characterized using visible-light optical microscopy, with a Leica DM8000 [67], to check for the uniformity of graphene samples by visually checking for the presence of holes or folds of the graphene surface. This is done by checking the contrast between the color of the graphene area and the substrate. This is especially useful for graphene transferred to  $\text{SiO}_2$  thin films, as the difference in refractive index between the two causes a high contrast change which greatly enhances the visibility of graphene mono and multi-layers [68], [69]. The experiments of transfer on  $\text{SiO}_2$  (Figure 2.13) agree with this principle and defects in the uniformity of the layers were easily visible. While visibility on white  $\text{LiNbO}_3$  is lower than the former, graphene is still relatively well visible if the optics are well focused, as shown in Figure 2.11 and Figure 2.12. Black  $\text{LiNbO}_3$  samples are considerably worse in this sense, and also required for optimization of the image capture parameters, specifically of the light intensity, the aperture of the diaphragm, the incidence angle of the microscope light, the exposure time, the numerical saturation and color gamma. Table 2-3 describes the specific settings used for imaging using a 20x objective; it must be noted that the values used could vary due to the specific objective used, the microscope, and the sample.

*Table 2-3: Typical image acquisition settings for a GoL device with a black-type substrate, using the Leica DM8000 microscope.*

|                           |                     |
|---------------------------|---------------------|
| <b>Acquisition type</b>   | <i>Bright Field</i> |
| <b>Exposure time</b>      | <i>~30 ms</i>       |
| <b>Light intensity</b>    | <i>~6000</i>        |
| <b>Diaphragm aperture</b> | <i>14 (MAX)</i>     |
| <b>Gamma</b>              | <i>6-7</i>          |
| <b>Saturation</b>         | <i>0.95</i>         |
| <b>Numerical Gain</b>     | <i>1</i>            |

Finally, Figure 2.18 shows a graphene device on a black substrate (YX-128° cut), with different image capture settings, both images were taken using a 20x objective and diaphragm aperture set to the maximum. The unoptimized photo, displayed in Figure 2.18(a), shows a slightly lighter color tone where the graphene is present, which is highlighted in Figure 2.18(b), with the optimized settings applied.

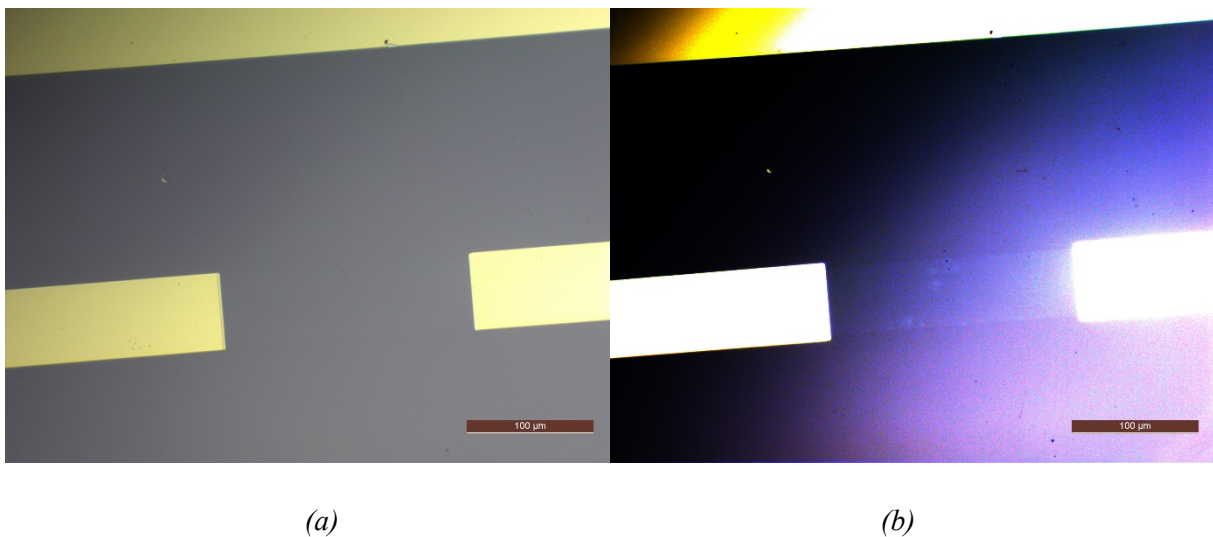


*Figure 2.18: Microscope images of the same graphene device without optimization (a) and with optimized image capture settings (b).*

## 2.5 Improvements of the process

While good results were overall achieved for the produced devices, in line with the current state of the art for CVD graphene on other substrates, there is some margin for improvement. Some techniques can be used to further improve the quality of the process and will be explored in future works. In particular, the following points are presented:

- Graphene transfer,
- Graphene patterning.

The transfer of graphene onto LiNbO<sub>3</sub> substrates was part of the process most prone to error. As previously discussed, this was because multiple long cleaning steps were needed to ensure a good quality necessary for the following steps of process. In order to alleviate this problem, a dry transfer process could be developed [53], [70], [71], or graphene monolayers could be grown directly on LiNbO<sub>3</sub> substrates through deposition. Direct CVD growth of graphene on LiNbO<sub>3</sub> would be favorable for achieving the best yields and performance. However, some research efforts are also being directed in developing novel growth techniques, in particular, *Xu et al.* [72] recently demonstrated growth of multi-layer graphene through annealing of carbon ions implanted in Cu thin-films on LiNbO<sub>3</sub> and they claim that monolayer growth is achievable through this method.

The patterning process of graphene could also be improved by reducing the quantity of photoresist residue on it. This can be done by limiting contact between graphene and photoresists through a prior deposition of a sacrificial layer. For this purpose, researchers have demonstrated the usage of thin films of aluminum [61] and nickel [73], yielding a higher quality of devices in respect to standard processes. This was partially explored also in this work, with partially good results, however, this process still needs further optimization as the etch rate of Al was too aggressive, which lead to the detachment of graphene from the substrate.

## 2.6 References

- [1] K. S. Novoselov *et al.*, ‘Electric Field Effect in Atomically Thin Carbon Films’, *Science*, vol. 306, no. 5696, pp. 666–669, Oct. 2004, doi: 10.1126/science.1102896.
- [2] F. Bonaccorso, A. Lombardo, T. Hasan, Z. Sun, L. Colombo, and A. C. Ferrari, ‘Production and processing of graphene and 2d crystals’, *Materials Today*, vol. 15, no. 12, pp. 564–589, Dec. 2012, doi: 10.1016/S1369-7021(13)70014-2.
- [3] K. Yu *et al.*, ‘In situ atomic-scale observation of monolayer graphene growth from SiC’, *Nano Res.*, vol. 11, no. 5, pp. 2809–2820, May 2018, doi: 10.1007/s12274-017-1911-x.
- [4] S.-H. Bae *et al.*, ‘Unveiling the carrier transport mechanism in epitaxial graphene for forming wafer-scale, single-domain graphene’, *Proc Natl Acad Sci USA*, vol. 114, no. 16, Art. no. 16, Apr. 2017, doi: 10.1073/pnas.1620176114.

- [5] H. Wang and G. Yu, 'Direct CVD Graphene Growth on Semiconductors and Dielectrics for Transfer-Free Device Fabrication', *Adv. Mater.*, vol. 28, no. 25, pp. 4956–4975, Jul. 2016, doi: 10.1002/adma.201505123.
- [6] X. Li *et al.*, 'Large-Area Synthesis of High-Quality and Uniform Graphene Films on Copper Foils', *Science*, vol. 324, no. 5932, pp. 1312–1314, Jun. 2009, doi: 10.1126/science.1171245.
- [7] A. Reina *et al.*, 'Large Area, Few-Layer Graphene Films on Arbitrary Substrates by Chemical Vapor Deposition', *Nano Lett.*, vol. 9, no. 1, pp. 30–35, Jan. 2009, doi: 10.1021/nl801827v.
- [8] Z. Chen *et al.*, 'Direct growth of wafer-scale highly oriented graphene on sapphire', *Science Advances*, vol. 7, no. 47, p. eabk0115, Nov. 2021, doi: 10.1126/sciadv.abk0115.
- [9] J. W. Suk *et al.*, 'Enhancement of the Electrical Properties of Graphene Grown by Chemical Vapor Deposition via Controlling the Effects of Polymer Residue', *Nano Lett.*, vol. 13, no. 4, pp. 1462–1467, Apr. 2013, doi: 10.1021/nl304420b.
- [10] Y. Liu, X. Dong, and P. Chen, 'Biological and chemical sensors based on graphene materials', *Chem. Soc. Rev.*, vol. 41, no. 6, pp. 2283–2307, 2012, doi: 10.1039/C1CS15270J.
- [11] E. W. Hill, A. Vijayaraghavan, and K. Novoselov, 'Graphene Sensors', *IEEE Sensors J.*, vol. 11, no. 12, pp. 3161–3170, Dec. 2011, doi: 10.1109/JSEN.2011.2167608.
- [12] F. Yavari and N. Koratkar, 'Graphene-Based Chemical Sensors', *J. Phys. Chem. Lett.*, vol. 3, no. 13, pp. 1746–1753, Jul. 2012, doi: 10.1021/jz300358t.
- [13] S. Okuda *et al.*, 'Graphene Surface Acoustic Wave Sensor for Simultaneous Detection of Charge and Mass', *ACS Sens.*, vol. 3, no. 1, pp. 200–204, Jan. 2018, doi: 10.1021/acssensors.7b00851.
- [14] L. Liu and Z. Shen, 'Bandgap engineering of graphene: A density functional theory study', *Applied Physics Letters*, vol. 95, no. 25, p. 252104, Dec. 2009, doi: 10.1063/1.3276068.
- [15] M. Y. Han, B. Özyilmaz, Y. Zhang, and P. Kim, 'Energy Band-Gap Engineering of Graphene Nanoribbons', *Phys. Rev. Lett.*, vol. 98, no. 20, p. 206805, May 2007, doi: 10.1103/PhysRevLett.98.206805.
- [16] L. Vicarelli *et al.*, 'Graphene field effect transistors as room-temperature Terahertz detectors', *Nature Mater.*, vol. 11, no. 10, pp. 865–871, Oct. 2012, doi: 10.1038/nmat3417.
- [17] A. Khan, R. R. Kumar, J. Cong, M. Imran, D. Yang, and X. Yu, 'CVD Graphene on Textured Silicon: An Emerging Technologically Versatile Heterostructure for Energy and

- Detection Applications’, *Advanced Materials Interfaces*, vol. 9, no. 1, p. 2100977, 2022, doi: 10.1002/admi.202100977.
- [18] O. Habibpour, J. Vukusic, and J. Stake, ‘A 30-GHz Integrated Subharmonic Mixer Based on a Multichannel Graphene FET’, *IEEE Transactions on Microwave Theory and Techniques*, vol. 61, no. 2, pp. 841–847, Feb. 2013, doi: 10.1109/TMTT.2012.2236434.
- [19] B. Sensale-Rodriguez *et al.*, ‘Broadband graphene terahertz modulators enabled by intraband transitions’, *Nat Commun*, vol. 3, no. 1, p. 780, Apr. 2012, doi: 10.1038/ncomms1787.
- [20] H. Murrmann and D. Widmann, ‘Current crowding on metal contacts to planar devices’, *IEEE Transactions on Electron Devices*, vol. 16, no. 12, pp. 1022–1024, Dec. 1969, doi: 10.1109/T-ED.1969.16904.
- [21] J. T. Smith, A. D. Franklin, D. B. Farmer, and C. D. Dimitrakopoulos, ‘Reducing Contact Resistance in Graphene Devices through Contact Area Patterning’, *ACS Nano*, vol. 7, no. 4, pp. 3661–3667, Apr. 2013, doi: 10.1021/nn400671z.
- [22] K. Nagashio and A. Toriumi, ‘Density-of-States Limited Contact Resistance in Graphene Field-Effect Transistors’, *Jpn. J. Appl. Phys.*, vol. 50, no. 7R, p. 070108, Jul. 2011, doi: 10.1143/JJAP.50.070108.
- [23] S. Min Song, T. Yong Kim, O. Jae Sul, W. Cheol Shin, and B. Jin Cho, ‘Improvement of graphene–metal contact resistance by introducing edge contacts at graphene under metal’, *Applied Physics Letters*, vol. 104, no. 18, p. 183506, May 2014, doi: 10.1063/1.4875709.
- [24] W. Li *et al.*, ‘Ultraviolet/ozone treatment to reduce metal-graphene contact resistance’, *Appl. Phys. Lett.*, vol. 102, no. 18, Art. no. 18, May 2013, doi: 10.1063/1.4804643.
- [25] J. A. Robinson *et al.*, ‘Contacting graphene’, *Applied Physics Letters*, vol. 98, no. 5, p. 053103, Feb. 2011, doi: 10.1063/1.3549183.
- [26] G. Giovannetti, P. A. Khomyakov, G. Brocks, V. M. Karpan, J. van den Brink, and P. J. Kelly, ‘Doping Graphene with Metal Contacts’, *Phys. Rev. Lett.*, vol. 101, no. 2, p. 026803, Jul. 2008, doi: 10.1103/PhysRevLett.101.026803.
- [27] R. S. Sundaram *et al.*, ‘The Graphene–Gold Interface and Its Implications for Nanoelectronics’, *Nano Lett.*, vol. 11, no. 9, Art. no. 9, Sep. 2011, doi: 10.1021/nl201907u.
- [28] T. Cusati *et al.*, ‘Electrical properties of graphene-metal contacts’, *Sci Rep*, vol. 7, no. 1, Art. no. 1, Dec. 2017, doi: 10.1038/s41598-017-05069-7.

- [29] S. Venica, F. Driussi, A. Gahoi, P. Palestri, Lemme, Max C, and L. Selmi, ‘On the Adequacy of the Transmission Line Model to Describe the Graphene–Metal Contact Resistance’, *IEEE Transactions on Electron Devices*, vol. 65, no. 4, pp. 1589–1596, 2018.
- [30] E. Watanabe, A. Conwill, D. Tsuya, and Y. Koide, ‘Low contact resistance metals for graphene based devices’, *Diamond and Related Materials*, vol. 24, pp. 171–174, Apr. 2012, doi: 10.1016/j.diamond.2012.01.019.
- [31] A. Venugopal, L. Colombo, and E. M. Vogel, ‘Contact resistance in few and multilayer graphene devices’, *Applied Physics Letters*, vol. 96, no. 1, p. 013512, Jan. 2010, doi: 10.1063/1.3290248.
- [32] A. D. Franklin, S.-J. Han, A. A. Bol, and V. Perebeinos, ‘Double Contacts for Improved Performance of Graphene Transistors’, *IEEE Electron Device Letters*, vol. 33, no. 1, pp. 17–19, Jan. 2012, doi: 10.1109/LED.2011.2173154.
- [33] F. Xia, V. Perebeinos, Y. Lin, Y. Wu, and P. Avouris, ‘The origins and limits of metal–graphene junction resistance’, *Nature Nanotech*, vol. 6, no. 3, Art. no. 3, Mar. 2011, doi: 10.1038/nnano.2011.6.
- [34] H. Zhong *et al.*, ‘Realization of low contact resistance close to theoretical limit in graphene transistors’, *Nano Res.*, vol. 8, no. 5, Art. no. 5, May 2015, doi: 10.1007/s12274-014-0656-z.
- [35] F. Giubileo and A. Di Bartolomeo, ‘The role of contact resistance in graphene field-effect devices’, *Progress in Surface Science*, vol. 92, no. 3, pp. 143–175, Aug. 2017, doi: 10.1016/j.progsurf.2017.05.002.
- [36] M. Topsakal, S. Cahangirov, and S. Ciraci, ‘The response of mechanical and electronic properties of graphene to the elastic strain’, *Applied Physics Letters*, vol. 96, no. 9, p. 091912, Mar. 2010, doi: 10.1063/1.3353968.
- [37] S. Tongay, M. Lemaitre, X. Miao, B. Gila, B. R. Appleton, and A. F. Hebard, ‘Rectification at Graphene-Semiconductor Interfaces: Zero-Gap Semiconductor-Based Diodes’, *Phys. Rev. X*, vol. 2, no. 1, p. 011002, Jan. 2012, doi: 10.1103/PhysRevX.2.011002.
- [38] S.-J. Liang, W. Hu, A. Di Bartolomeo, S. Adam, and L. K. Ang, ‘A modified Schottky model for graphene-semiconductor (3D/2D) contact: A combined theoretical and experimental study’, in *2016 IEEE International Electron Devices Meeting (IEDM)*, San Francisco, CA, USA: IEEE, Dec. 2016, p. 14.4.1-14.4.4. doi: 10.1109/IEDM.2016.7838416.

- [39] A. Di Bartolomeo, ‘Graphene Schottky diodes: An experimental review of the rectifying graphene/semiconductor heterojunction’, *Physics Reports*, vol. 606, pp. 1–58, Jan. 2016, doi: 10.1016/j.physrep.2015.10.003.
- [40] C.-C. Chen, M. Aykol, C.-C. Chang, A. F. J. Levi, and S. B. Cronin, ‘Graphene-Silicon Schottky Diodes’, *Nano Lett.*, vol. 11, no. 5, pp. 1863–1867, May 2011, doi: 10.1021/nl104364c.
- [41] S. Tongay *et al.*, ‘Graphene/GaN Schottky diodes: Stability at elevated temperatures’, *Applied Physics Letters*, vol. 99, no. 10, p. 102102, Sep. 2011, doi: 10.1063/1.3628315.
- [42] C. Gong *et al.*, ‘Metal–Graphene–Metal Sandwich Contacts for Enhanced Interface Bonding and Work Function Control’, *ACS Nano*, vol. 6, no. 6, pp. 5381–5387, Jun. 2012, doi: 10.1021/nn301241p.
- [43] ‘ISO 14644-1:2015(en), Cleanrooms and associated controlled environments — Part 1: Classification of air cleanliness by particle concentration’. Accessed: Jul. 09, 2023. [Online]. Available: <https://www.iso.org/obp/ui/en/#iso:std:iso:14644:-1:ed-2:v1:en>
- [44] Merck KGaA, ‘AZ@nLOF™ 2000 Series’. [Online]. Available: [https://www.microchemicals.com/micro/tds\\_az\\_nlof2000\\_series.pdf](https://www.microchemicals.com/micro/tds_az_nlof2000_series.pdf)
- [45] MicroChemicals GmbH, ‘TI PRIME adhesion promoter’. Aug. 2002. Accessed: Jul. 09, 2023. [Online]. Available: [https://microchemicals.com/micro/tds\\_ti\\_prime.pdf](https://microchemicals.com/micro/tds_ti_prime.pdf)
- [46] C. Gong *et al.*, ‘Rapid Selective Etching of PMMA Residues from Transferred Graphene by Carbon Dioxide’, *J. Phys. Chem. C*, vol. 117, no. 44, pp. 23000–23008, Nov. 2013, doi: 10.1021/jp408429v.
- [47] The Dow Chemical Company, ‘MICROPOSIT™ S1800™ G2 SERIES PHOTORESISTS’. The Dow Chemical Company, Mar. 2014. Accessed: Jul. 09, 2023. [Online]. Available: <https://kayakuam.com/wp-content/uploads/2019/09/S1800-G2.pdf>
- [48] ‘Positive E-Beam Resists AR-P 6200 (CSAR 62)’. Accessed: Jul. 07, 2023. [Online]. Available: [https://www.allresist.com/wp-content/uploads/sites/2/2020/03/AR-P6200\\_CSAR62english\\_Allresist\\_product-information.pdf](https://www.allresist.com/wp-content/uploads/sites/2/2020/03/AR-P6200_CSAR62english_Allresist_product-information.pdf)
- [49] Allresist GmbH, ‘Protective Coating PMMA Electra 92 (AR-PC 5090)’. Accessed: Jul. 09, 2023. [Online]. Available: [https://www.allresist.com/wp-content/uploads/sites/2/2022/05/Allresist\\_Product-information-Protective-Coating-AR-PC-5090\\_5091-English-web.pdf](https://www.allresist.com/wp-content/uploads/sites/2/2022/05/Allresist_Product-information-Protective-Coating-AR-PC-5090_5091-English-web.pdf)
- [50] S. Ullah *et al.*, ‘Graphene transfer methods: A review’, *Nano Res.*, vol. 14, no. 11, pp. 3756–3772, Nov. 2021, doi: 10.1007/s12274-021-3345-8.

- [51] G. J. M. Fechine *et al.*, ‘Direct dry transfer of chemical vapor deposition graphene to polymeric substrates’, *Carbon*, vol. 83, pp. 224–231, Mar. 2015, doi: 10.1016/j.carbon.2014.11.038.
- [52] A. Shivayogimath *et al.*, ‘Do-It-Yourself Transfer of Large-Area Graphene Using an Office Laminator and Water’, *Chem. Mater.*, vol. 31, no. 7, Art. no. 7, Apr. 2019, doi: 10.1021/acs.chemmater.8b04196.
- [53] J. D. Caldwell *et al.*, ‘Technique for the Dry Transfer of Epitaxial Graphene onto Arbitrary Substrates’, *ACS Nano*, vol. 4, no. 2, Art. no. 2, Feb. 2010, doi: 10.1021/nn901585p.
- [54] H. Van Ngoc, Y. Qian, S. K. Han, and D. J. Kang, ‘PMMA-Etching-Free Transfer of Wafer-scale Chemical Vapor Deposition Two-dimensional Atomic Crystal by a Water Soluble Polyvinyl Alcohol Polymer Method’, *Sci Rep*, vol. 6, no. 1, Art. no. 1, Dec. 2016, doi: 10.1038/srep33096.
- [55] S. Y. Yang *et al.*, ‘Metal-Etching-Free Direct Delamination and Transfer of Single-Layer Graphene with a High Degree of Freedom’, *Small*, vol. 11, no. 2, pp. 175–181, Jan. 2015, doi: 10.1002/sml.201401196.
- [56] R. Abdalrheem *et al.*, ‘Comparative Studies on The Transfer of Chemical Vapor Deposition Grown Graphene Using Either Electrochemical Delamination or Chemical Etching Method’, *J. Phys.: Conf. Ser.*, vol. 1083, no. 1, p. 012038, Aug. 2018, doi: 10.1088/1742-6596/1083/1/012038.
- [57] Graphenea, Inc., ‘Graphenea Monolayer Graphene on Polymer Film Datasheet’. Accessed: Oct. 10, 2022. [Online]. Available: [https://cdn.shopify.com/s/files/1/0191/2296/files/Graphenea\\_Monolayer\\_Graphene\\_on\\_Polymer\\_Film\\_Datasheet\\_02-16-2022.pdf?v=1645025331](https://cdn.shopify.com/s/files/1/0191/2296/files/Graphenea_Monolayer_Graphene_on_Polymer_Film_Datasheet_02-16-2022.pdf?v=1645025331)
- [58] Merck KGaA, ‘AZ®10XT Series’. Mar. 2021. Accessed: Jul. 01, 2023. [Online]. Available: [https://www.microchemicals.com/micro/tds\\_az\\_10xt\\_photoresist.pdf](https://www.microchemicals.com/micro/tds_az_10xt_photoresist.pdf)
- [59] Kayaku Advanced Materials, ‘NANO™ PMMA and Copolymer’. Apr. 2021. [Online]. Available: <https://kayakuam.com/wp-content/uploads/2020/07/KAM-PMMA-Datasheet-7.1.pdf>
- [60] S. Konar, U. Häusserman, and G. Svensson, ‘Intercalation Compounds from LiH and Graphite: Relative Stability of Metastable Stages and Thermodynamic Stability of Dilute Stage Id’, *Chem. Mater.*, vol. 27, no. 7, pp. 2566–2575, Apr. 2015, doi: 10.1021/acs.chemmater.5b00235.

- [61] A. Hsu, H. Wang, K. K. Kim, J. Kong, and T. Palacios, ‘Impact of Graphene Interface Quality on Contact Resistance and RF Device Performance’, *IEEE Electron Device Lett.*, vol. 32, no. 8, Art. no. 8, Aug. 2011, doi: 10.1109/LED.2011.2155024.
- [62] ‘Corial 200R RIE etch system | Corial’. Accessed: Jul. 15, 2023. [Online]. Available: <https://corial.plasmatherm.com/en/products/corial-200r-rie-etch-tool>
- [63] A. Matic, ‘Résonateurs à domaines ferroélectriques périodiques sur coupes obliques de niobate de lithium pour les applications de filtrage radiofréquences’, phdthesis, Université Bourgogne Franche-Comté, 2020. Accessed: Sep. 19, 2023. [Online]. Available: <https://theses.hal.science/tel-03141526>
- [64] Advanced Energy, Inc., ‘TREK 20/20C Datasheet’. Accessed: Sep. 19, 2023. [Online]. Available: <https://www.advancedenergy.com/getmedia/c041b7d0-3a9a-48cd-ac83-96418180276d/en-hv-amplifier-trek-20-20c-data-sheet.pdf>
- [65] Rohde & Schwarz GmbH & Co KG, ‘© Rohde & Schwarz; R&S® HMF2525 Arbitrary Function Generator’.
- [66] Rohde & Schwarz GmbH & Co KG, ‘© Rohde & Schwarz; R&S®RTB2000 Oscilloscope’. 2023. Accessed: Sep. 19, 2023. [Online]. Available: [https://scdn.rohde-schwarz.com/ur/pws/dl\\_downloads/pdm/cl\\_brochures\\_and\\_datasheets/specifications/3607\\_4270\\_22/RTB2000\\_dat-sw\\_en\\_3607-4270-22\\_v1700.pdf](https://scdn.rohde-schwarz.com/ur/pws/dl_downloads/pdm/cl_brochures_and_datasheets/specifications/3607_4270_22/RTB2000_dat-sw_en_3607-4270-22_v1700.pdf)
- [67] ‘Leica DM8000 M High Throughput Inspection Review System Leica DM8000 M’. Accessed: Aug. 02, 2023. [Online]. Available: <https://www.leica-microsystems.com/products/light-microscopes/p/leica-dm8000-m/>
- [68] P. Blake *et al.*, ‘Making graphene visible’, *Applied Physics Letters*, vol. 91, no. 6, p. 063124, Aug. 2007, doi: 10.1063/1.2768624.
- [69] S. Roddaro, P. Pingue, V. Piazza, V. Pellegrini, and F. Beltram, ‘The Optical Visibility of Graphene: Interference Colors of Ultrathin Graphite on SiO<sub>2</sub>’, *Nano Lett.*, vol. 7, no. 9, pp. 2707–2710, Sep. 2007, doi: 10.1021/nl071158l.
- [70] J. W. Suk *et al.*, ‘Transfer of CVD-grown monolayer graphene onto arbitrary substrates’, *ACS Nano*, vol. 5, no. 9, pp. 6916–6924, Sep. 2011, doi: 10.1021/nn201207c.
- [71] L. Banszerus *et al.*, ‘Ultrahigh-mobility graphene devices from chemical vapor deposition on reusable copper’, *Science Advances*, vol. 1, no. 6, p. e1500222, Jul. 2015, doi: 10.1126/sciadv.1500222.
- [72] Y. Xu, F. Lu, Y. Liu, and C. Ma, ‘Direct graphene synthesis on LiNbO<sub>3</sub> substrate by C implantation on Cu covering layer’, *Mater. Res. Express*, vol. 9, no. 11, p. 115602, Nov. 2022, doi: 10.1088/2053-1591/ac9f03.

[73] S. Kumar, N. Peltekis, K. Lee, H.-Y. Kim, and G. S. Duesberg, 'Reliable processing of graphene using metal etchmasks', *Nanoscale Res Lett*, vol. 6, no. 1, Art. no. 1, Dec. 2011, doi: 10.1186/1556-276X-6-390.

## Contents of the chapter:

|   |     |
|---|-----|
| 3 Raman spectroscopy of GoL.....                              | 92  |
| 3.1 Elements of Theory.....                                   | 92  |
| 3.2 Graphene.....   | 93  |
| 3.2.1 Estimation of layer number and defects.....             | 95  |
| 3.3 Description of the Experiments.....                       | 99  |
| 3.3.1 Analysis of the uniformity of the Hall bar devices..... | 108 |
| 3.3.2 Results for graphene on PPLN.....                       | 110 |
| 3.4 References.....   | 116 |

### 3 Raman spectroscopy of GoL

As previously discussed, microscope images of graphene samples are a fast and powerful tool for checking the presence of damages in the devices, however, as visibility is usually quite low, **Raman spectroscopy** is a much more effective tool for checking the quality of the graphene. Moreover, due to resonance effect, it is possible to detect a **single layer or multilayers** very quickly. Researchers have studied the Raman peaks of graphene and their ratios in function of the number of layers [1]–[3], doping [4], [5], strain [4], [6] and defects in the crystal, such as dislocation, vacancies and edges. In this chapter, I will characterize the films that will be used in the next section.

#### 3.1 Elements of Theory

Raman spectroscopy is a powerful analytical technique which enables to collect information on material through the light scattered from the material, using a monochromatic source, typically a laser focused on the sample. This process is, for the most part, linear (Rayleigh scattering), however, some photons are inelastically scattered and their energy changes due to an electron-phonon process. The energy of the scattered photon shifts due to the emission of a phonon, in a Stokes Raman scattering, or the absorption of a phonon, in an anti-Stokes Raman scattering. The Raman scattering process, represented in Figure 3.1, results in a frequency dispersion of the reflected light that is collected in several peaks, each corresponding to a unique phonon, which is a unique signature of the interatomic and intermolecular bonds of the material.

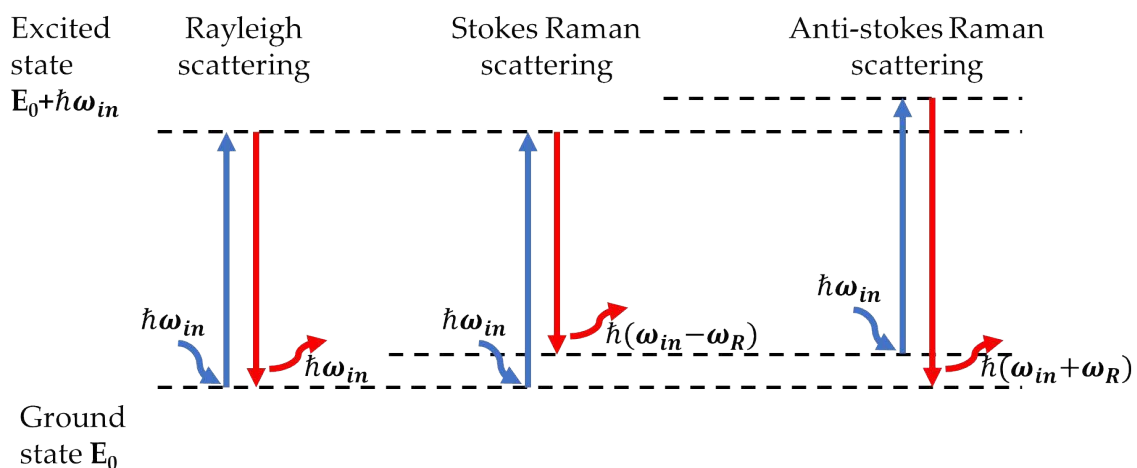


*Figure 3.1: Representation of Rayleigh and Raman scattering process.*

## 3.2 Graphene

The Raman peaks in graphene that are used the most for the characterization of the samples are the **G**, the **D** and the **2D**. Although, it must be noted that the naming and the physical origin of some of the peaks that are discussed in the following have changed over the years, which may be the cause of confusion. Therefore, all of the named peaks are accompanied by their frequency so that the reader may use that as a reference when referring to other works.

In order to understand the information that is carried in the graphene peaks, a brief explanation of the origin of the discussed peaks is hereby provided. Researchers have computed the normal modes for the graphene's crystal structure [7]–[9], which allows for **3 acoustic** and **3 optical** normal modes:

$$\Gamma_{vib} = A_{2u} \oplus B_{2g} \oplus E_{1u} \oplus E_{2g}. \quad (3.1)$$

As described in Figure 3.2, the modes are subdivided in **two doubly degenerate** modes [7],  **$B_{2g}$  and  $E_{2g}$** , and two nondegenerate modes,  **$A_{2u}$  and  $E_{1u}$**  [8]:

- **$B_{2g}$**  is Raman-active, it is represented by an **out-of-plane** optical wave,
- **$E_{2g}$**  is Raman-active, it is represented by an **in-plane** optical wave,
- **$A_{2u}$**  is infrared-active, it is represented by an acoustic **out-of-plane** wave,
- **$E_{1u}$**  is infrared-active, it is represented by an in-plane acoustic **in-plane** wave.

The phonon scattering processes are represented in Figure 3.3, and the corresponding Raman peaks for graphene on Si/SiO<sub>2</sub> are represented in Figure 3.4.

The **G-band** corresponds to a single-phonon scattering process of  $E_{2g}$  and lies at Raman shift  $\omega(G) \sim 1581 \text{ cm}^{-1}$ . The G-band is a resonant mode and therefore its measured characteristics do not change much with the incidence angle of the laser [1].

The **D-band** lies at  $\omega(D) \sim 1340 \text{ cm}^{-1}$ , it corresponds to the breathing mode of a 6-atoms ring, as displayed in Figure 3.3(e), for symmetry reasons, it cannot be excited on monocrystalline graphene single layers, the only possibility for this mode to appear in the Raman plot is in the presence of defects [1]. In the Raman process of the D peak, displayed in Figure 3.3(c), the charge is bounced between the edges of the  $K$  and  $K'$  zones.

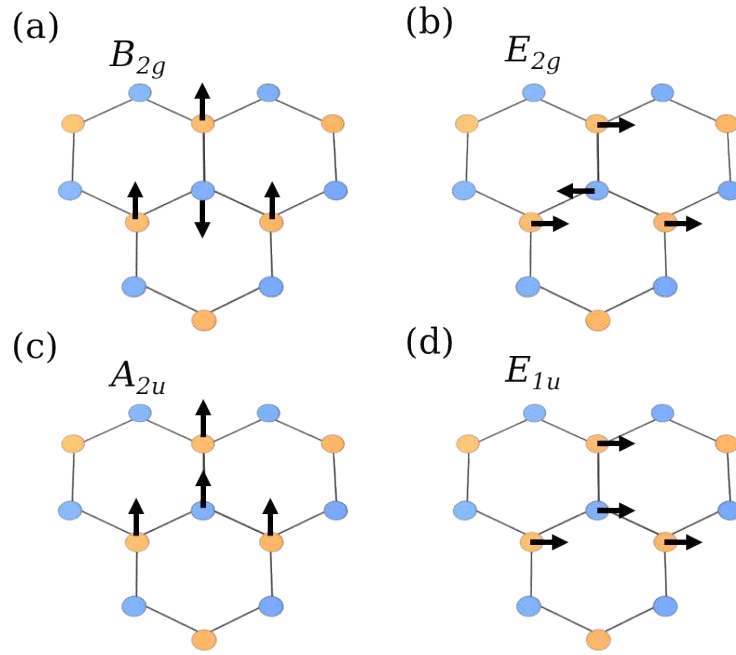


**Figure 3.2:** Visualization of the normal phonon modes in graphene (a)  $B_{2g}$ , (b)  $E_{2g}$ , (c)  $A_{2u}$  and (d)  $E_{1u}$ .

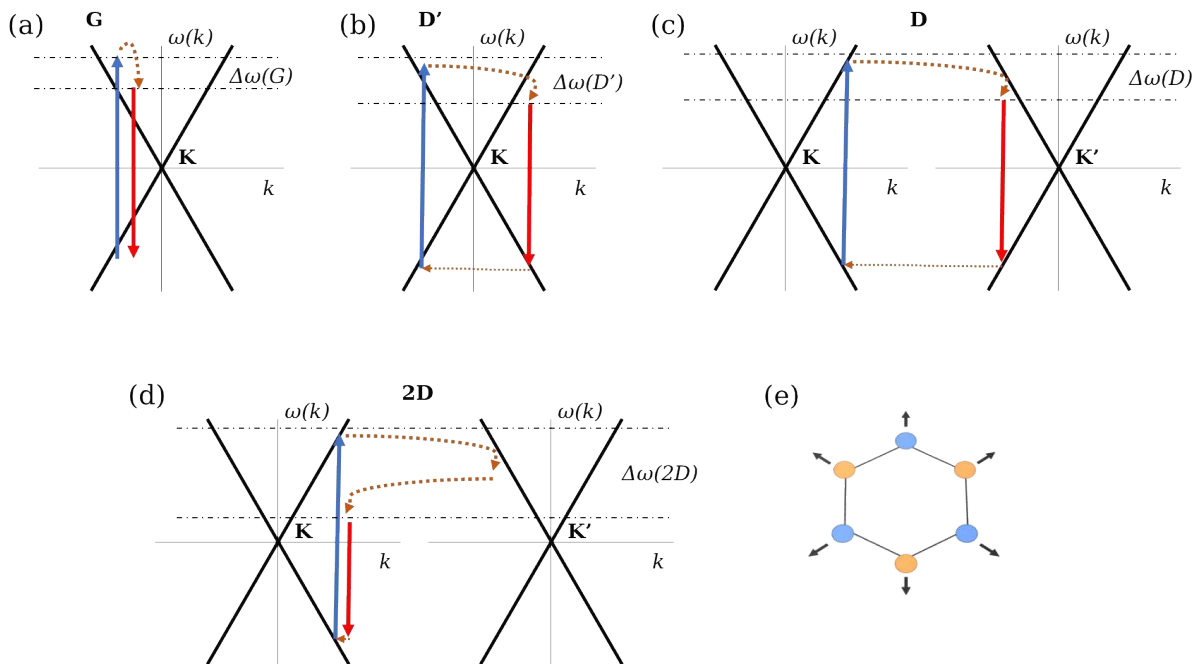


**Figure 3.3:** Visualization of the energy transitions in a Raman process describing the (a) G band, (b) the  $D'$  band, (c) the D band and the 2D band. (e) represents the “breathing” phonon of the D band.

We must note that, in GoL, the D peak was on the same region of a considerably bigger LiNbO<sub>3</sub> peak in z-cut substrates (Figure 3.5(a)) and in YX-128° substrates (Figure 3.5(a)). Of course, the latter may be extracted as background before interpolating the peaks, however, given the low intensity of the D peak and the noise level it was considered that the estimation error could become too big. Instead, we chose to use the D'' peak, as it follows similar rules as the D.

The **2D-band** is the overtone of the D band and it lies at  $\omega(2D) \sim 2695 \text{ cm}^{-1}$  and its process is represented in Figure 3.3(d), differently from the D peak, it is always present [1].

The **D'-band** lies at  $\omega(D') \sim 1620 \text{ cm}^{-1}$ , it is similar to the D band, but its process happens within the same K zone, as in Figure 3.3(b).

The **D''-band** lies at  $\omega(D'') \sim 2450 \text{ cm}^{-1}$ , it is formed by the combination of a D phonon and a longitudinal acoustic phonon.

### 3.2.1 Estimation of layer number and defects

Researchers have demonstrated that 2D, D and G peaks can be used as an indicator for **estimating the number of layers** [1], [3], [4], [10], [11]. The effects of the increase in the layer count are explained in Figure 3.4. The data clearly shows that for mono to few-layer graphene systems, the amplitude of the **G peak**  $I(G)$  increases sharply, up to ~20 layers [12], [13].

Another interesting effect is on the **2D band**, where its amplitude  $I(2D)$  decreases with the number of layers, and its shape changes completely, as it divides into a number of sub-peaks coinciding with the total of graphene layers. Finally, the intensity of the D'' and the D peaks ( $I(D'')$  and  $I(D)$ ), remain relatively stable with the layer number, as shown in Figure 3.4(d) and (d) respectively, however, their Full-Width Half-Maximum (FWHM) widens considerably.

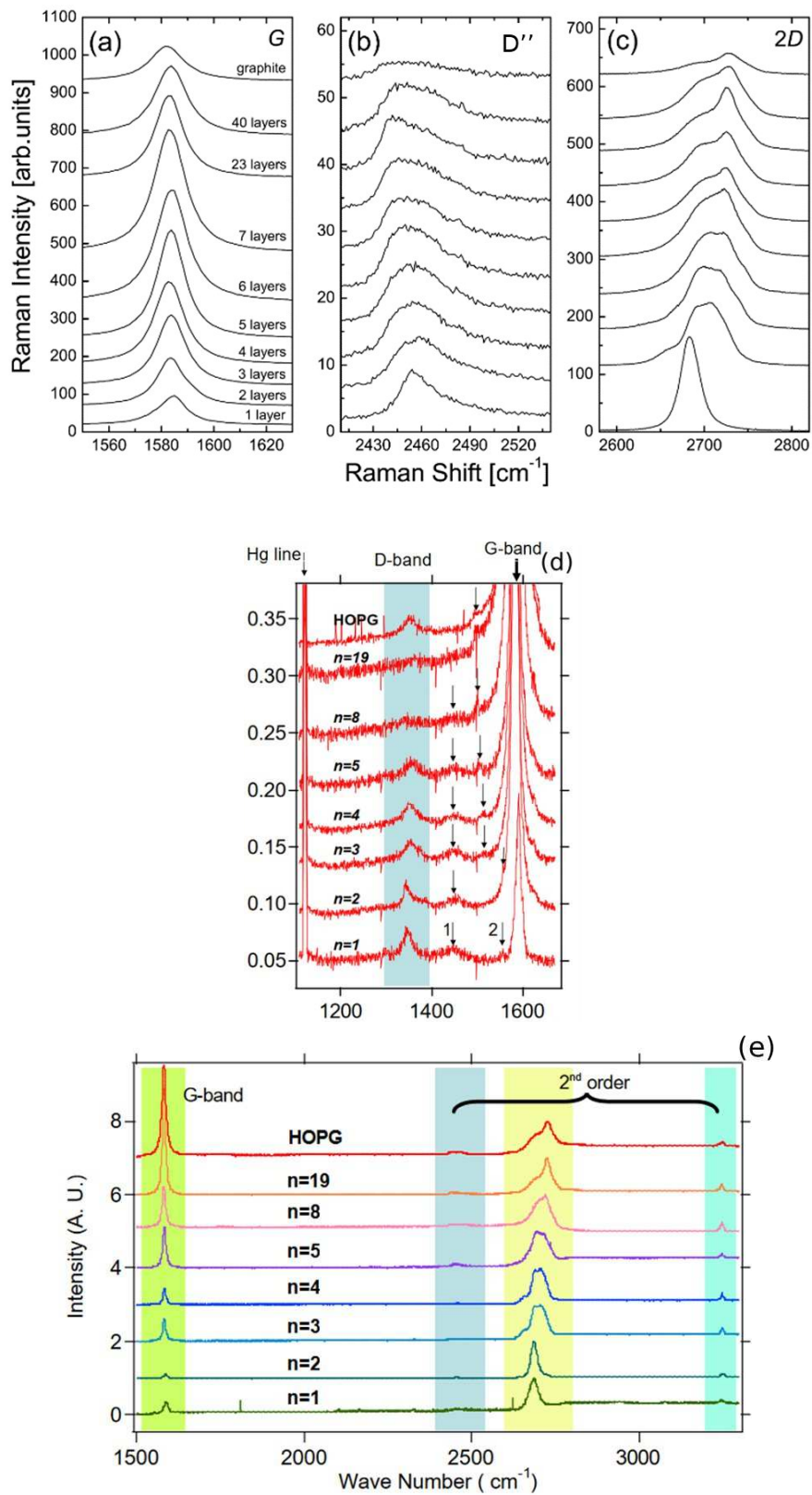


**Figure 3.4:** Raman peaks for samples from single-layer graphene to graphite (graphene on  $\text{SiO}_2/\text{Si}$ ). The data in (a), (b) and (c) are from [11] and the data in (d) and (e) are from [12].

All of this suggests to use the  $I(D)/I(G)$ ,  $I(D'')/I(G)$ , or the  $I(2D)/I(G)$  ratio to estimate the number of layers, in particular current literature usually uses the latter, as  $I(D) \sim 0$  in ideal graphene, and it suggests that graphene samples with  $I(2D)/I(G) > \sim 1.8$  are monolayers and samples with  $I(2D)/I(G) > \sim 1$  are bilayers. However, the bands and their peak values change significantly also due to factors such as doping, strain and edge defects in smaller devices [4], [5] and therefore, for values of  $I(2D)/I(G) \sim 1.8$ , other factors should be used as reference, such as the FWHM of the peaks and the number of sub-peaks in the 2D region.

**Doping and strain** can be monitored through the value of  $\omega(G)$ ,  $FWHM(G)$  and  $\omega(2D)$  [4]–[6], [13], [14]. In particular, *Das et al.* [5] demonstrated experimentally that the shift in  $\omega(G)$  is always positive in respect to both positive and negative charge doping, while the opposite is true for  $\omega(2D)$ . On the other end, they also demonstrated a sharp decline in  $FWHM(G)$  from  $\sim 20$  in pristine conditions and saturates at  $\sim 8$  for doping  $n \approx \pm 10^{13} \text{ cm}^{-2}$ .

Strain causes similar effects, but the different sensitivities of the G and 2D bands allow to distinguish the two effects. This is usually expressed through the ratio  $\Delta\omega(2D)/\Delta\omega(G)$ , which has been reported to be much greater when applying tensile strain ( $(\Delta\omega(2D)/\Delta\omega(G))|_{\epsilon^{uniaxial}} = 2.2 \pm 0.2$ ), than for doping ( $(\Delta\omega(2D)/\Delta\omega(G))|_{n^{hole}} = 0.7 \pm 0.05$ ).

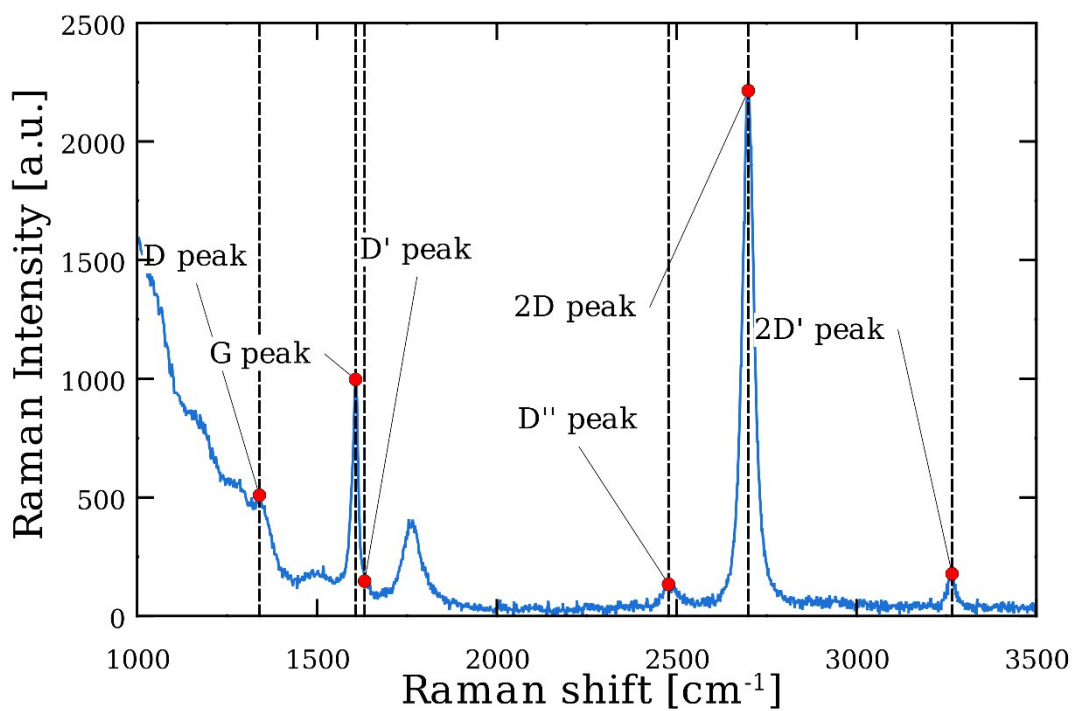
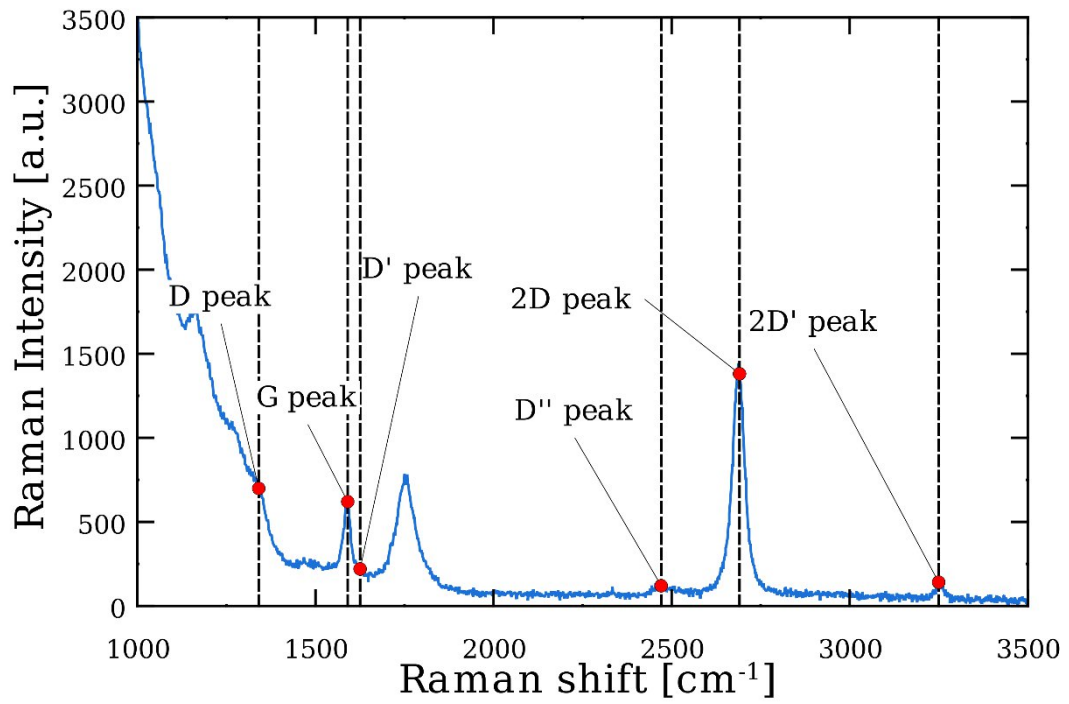


*Figure 3.5: Typical Raman plots of a GoL sample using a Z-cut substrate (a) and a YX-128° substrate (b).*

### 3.3 Description of the Experiments

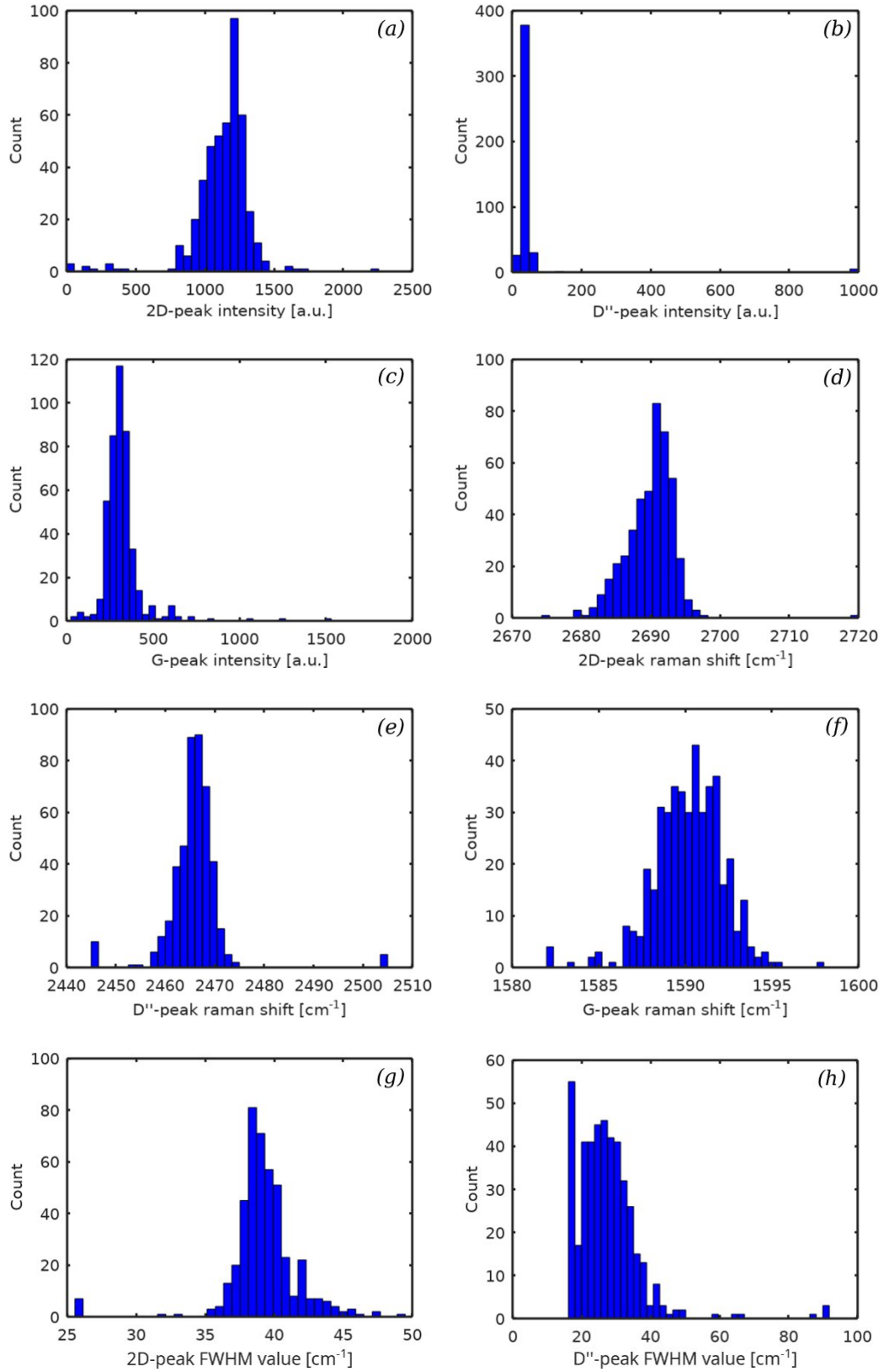
The unpolarized Raman spectra and a mapping of graphene on LiNbO<sub>3</sub> have been done in backscattering geometry using **532 nm** excitation (Monovista, S&I). The acquisition time for the spectrum was 20 s, using a laser power of 10 mW and an objective with a magnification of 100X. For acquiring the Raman map, some zones with graphene were identified beforehand as described in Section 2.4, and the presence of graphene was confirmed manually by acquiring the Raman spectrum at the corners of the defined map, and by taking some sample points in the middle. After the acquisition, the background was extracted and the peaks have been interpolated using pseudo-Voigt profiles (1/2 Gaussian and 1/2 Lorentzian) and the processed values for the G, 2D and D'' peaks were saved and analyzed.

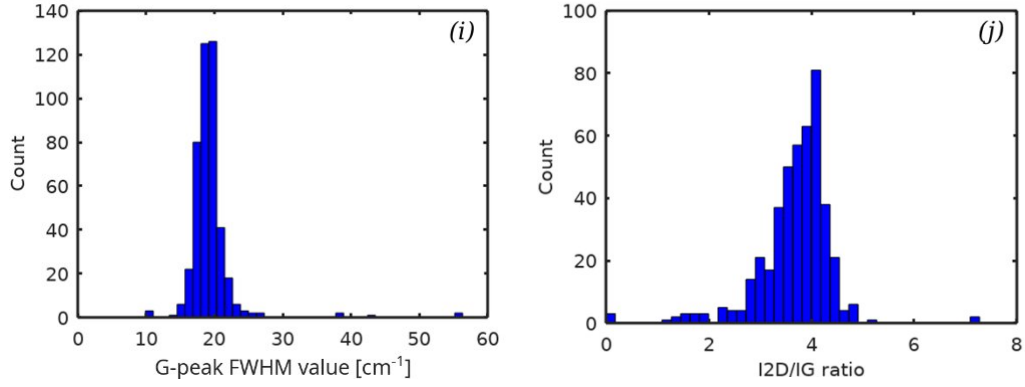
The uniformity of the samples was visualized through a statistical analysis of the extracted values, and the presence of holes or folds was visualized through a 3D plotting of the values. For each Raman point, qualitative analysis of doping and residual strain was performed through  $FWHM(G)$  and the  $\Delta\omega(2D)/\Delta\omega(G)$  ratio considering the thresholds defined in Section 3.2.1:

$$\frac{\Delta\omega(2D)}{\Delta\omega(G)} = \frac{\omega(2D) - \omega(2D)_0}{\omega(G) - \omega(G)_0}, \quad (3.2)$$

where  $\omega(2D)_0$  and  $\omega(G)_0$  are the value of respectively  $\omega(2D)$  and  $\omega(G)$  at  $n = 0$ , and the values used for the calculations were the ones found in the literature from pristine graphene.

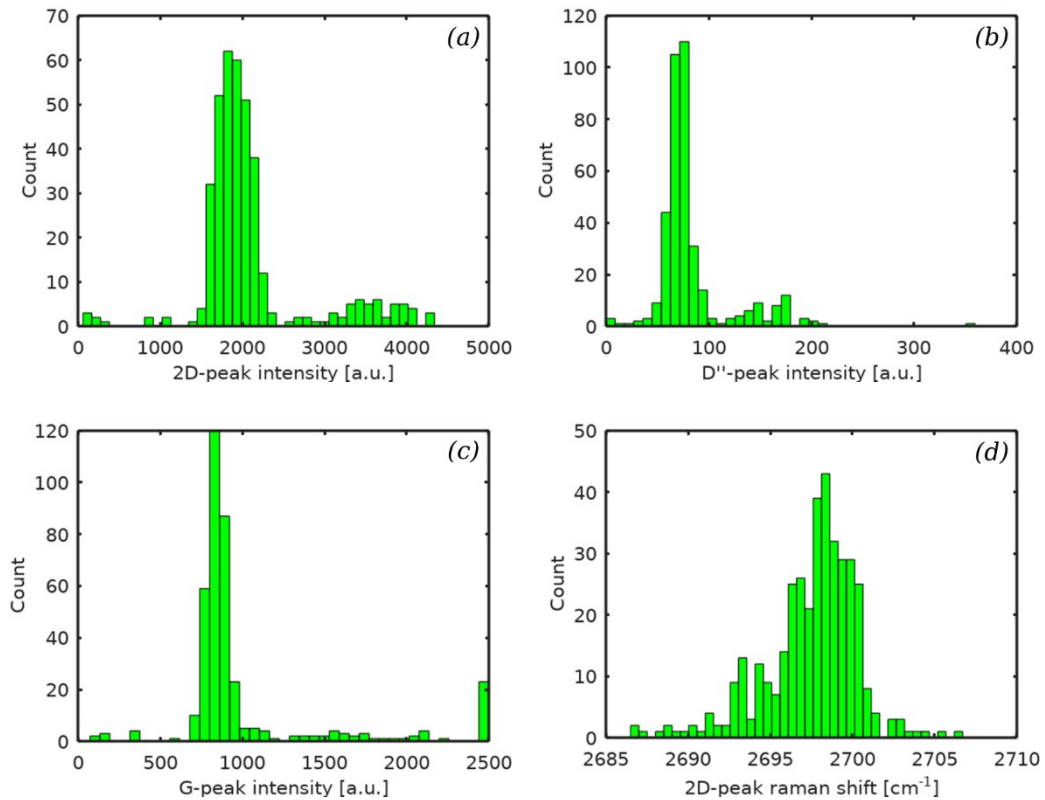
The characterization has been performed for each sample type (transfer tests, low frequency, RF, AE characterization series, and AE convolvers) and the results have been confronted with the state of the art and the other samples that were already produced and characterized. Figure 3.5 displays a typical Raman plot after the complete production cycle. The set of results of the Raman maps for a GoL device processed using the AZnLOF and the S1813 photoresist during patterning are shown respectively in Figure 3.6 and Figure 3.7.

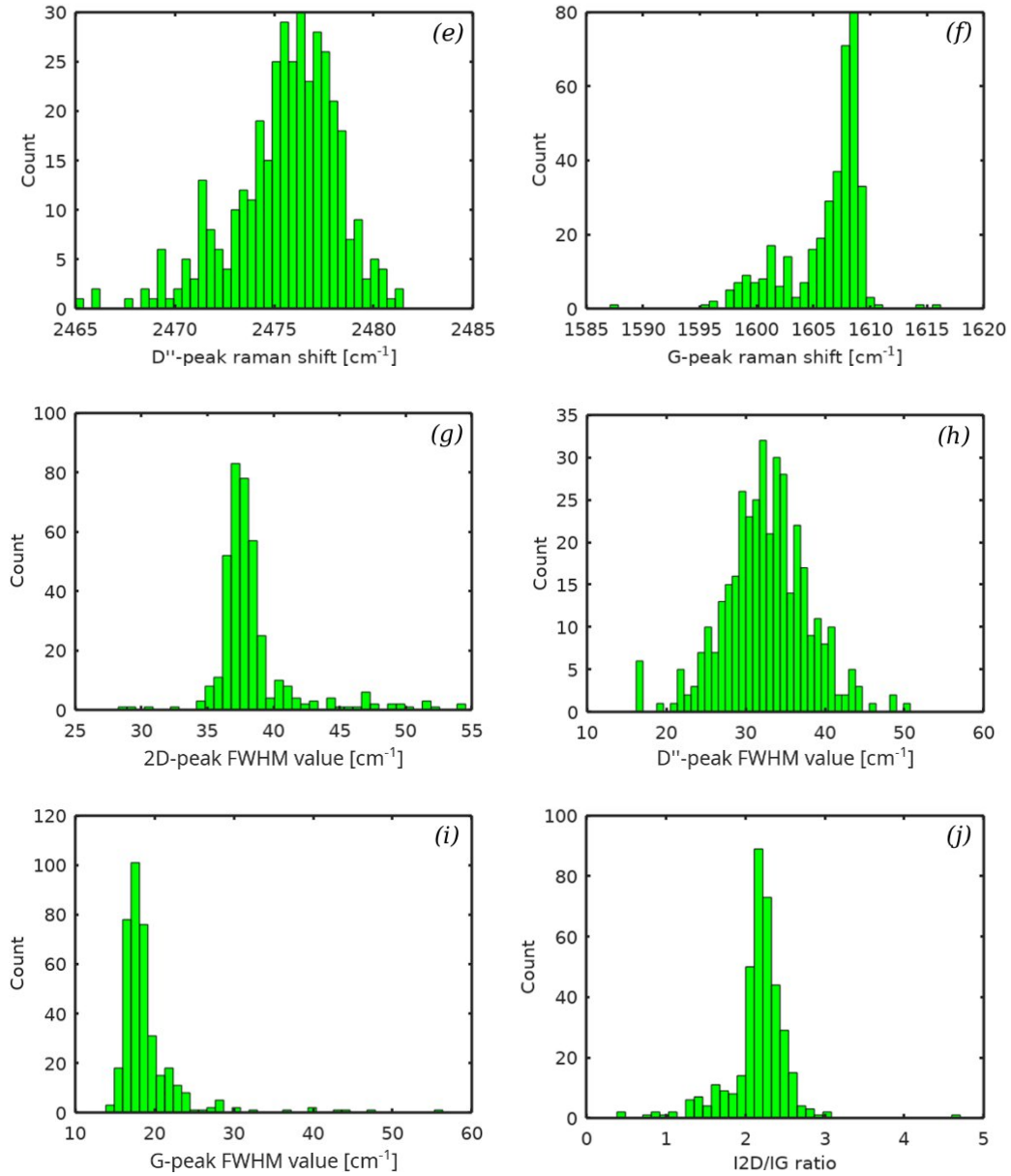




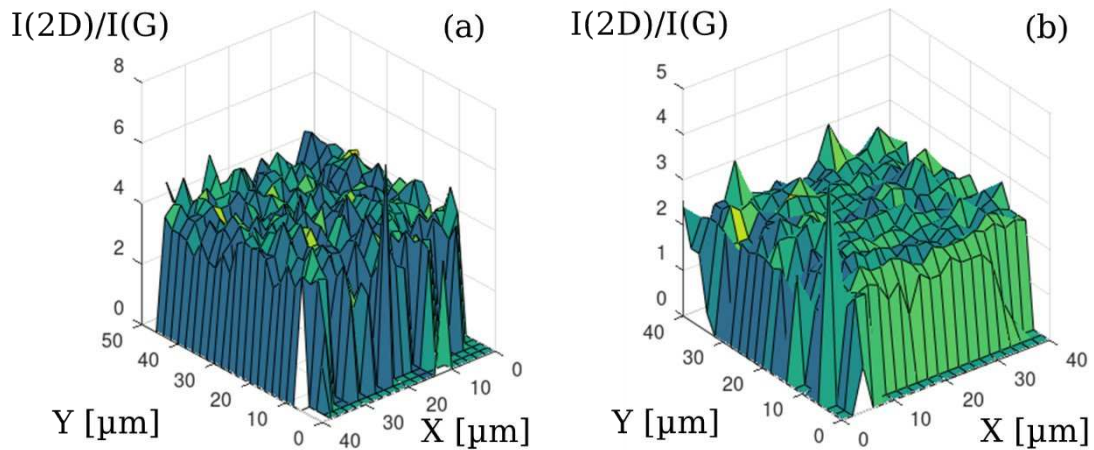
**Figure 3.6:** Histograms of the interpolated values of the (a) (b) (c) intensities, (d) (e) (f) shifts and (g) (h) (i) FWHM of the graphene peaks. (j) is the histogram of the  $I(2D)/I(G)$  ratio. The data was taken from a sample with graphene patterned using the AZnLOF as hard mask.

As shown in Figure 3.6(j) and Figure 3.7(j), the graphene resulted in both process variations is of good quality and the  $I(2D)/I(G)$  ratio stays mostly above the defined threshold of  $\sim 1.8$  for undoped monolayers ( $\sim 4.4$  for AZnLOF and  $\sim 2.1$  for S1813). As demonstrated by the 3D plot of the Raman maps, in Figure 3.8, the value of  $I(2D)/I(G)$  remains fairly constant within the surface of the sample and drops out at the edges.



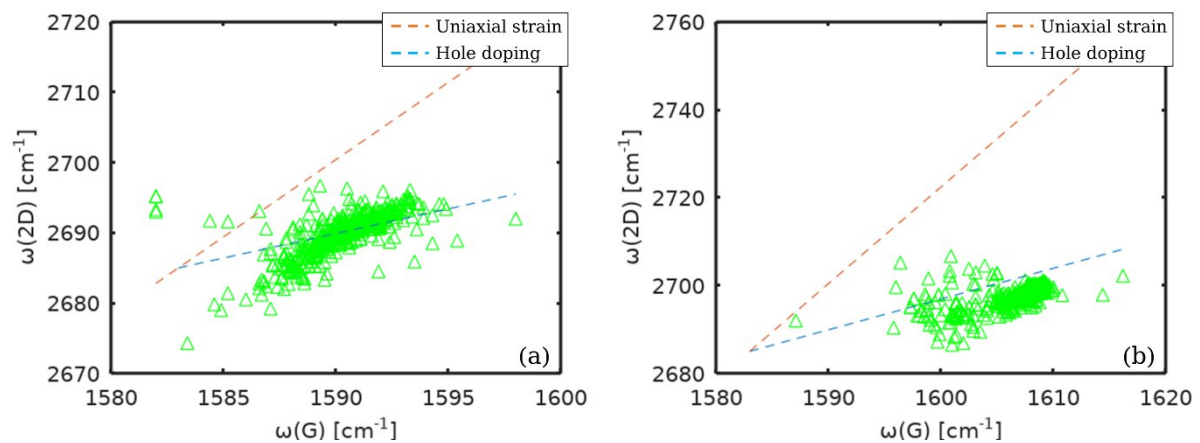


**Figure 3.7:** Histograms of the interpolated values of the (a) (b) (c) intensities, (d) (e) (f) shifts and (g) (h) (i) FWHM of the graphene peaks. (j) is the histogram of the  $I(2D)/I(G)$  ratio. The data was taken from a sample with graphene patterned using the S1813 as hard mask.



**Figure 3.8:** 3D plot of the  $I(2D)/I(G)$  ratio vs. position for (a) an AZnLOF and (b) an S1813 patterning-type sample.

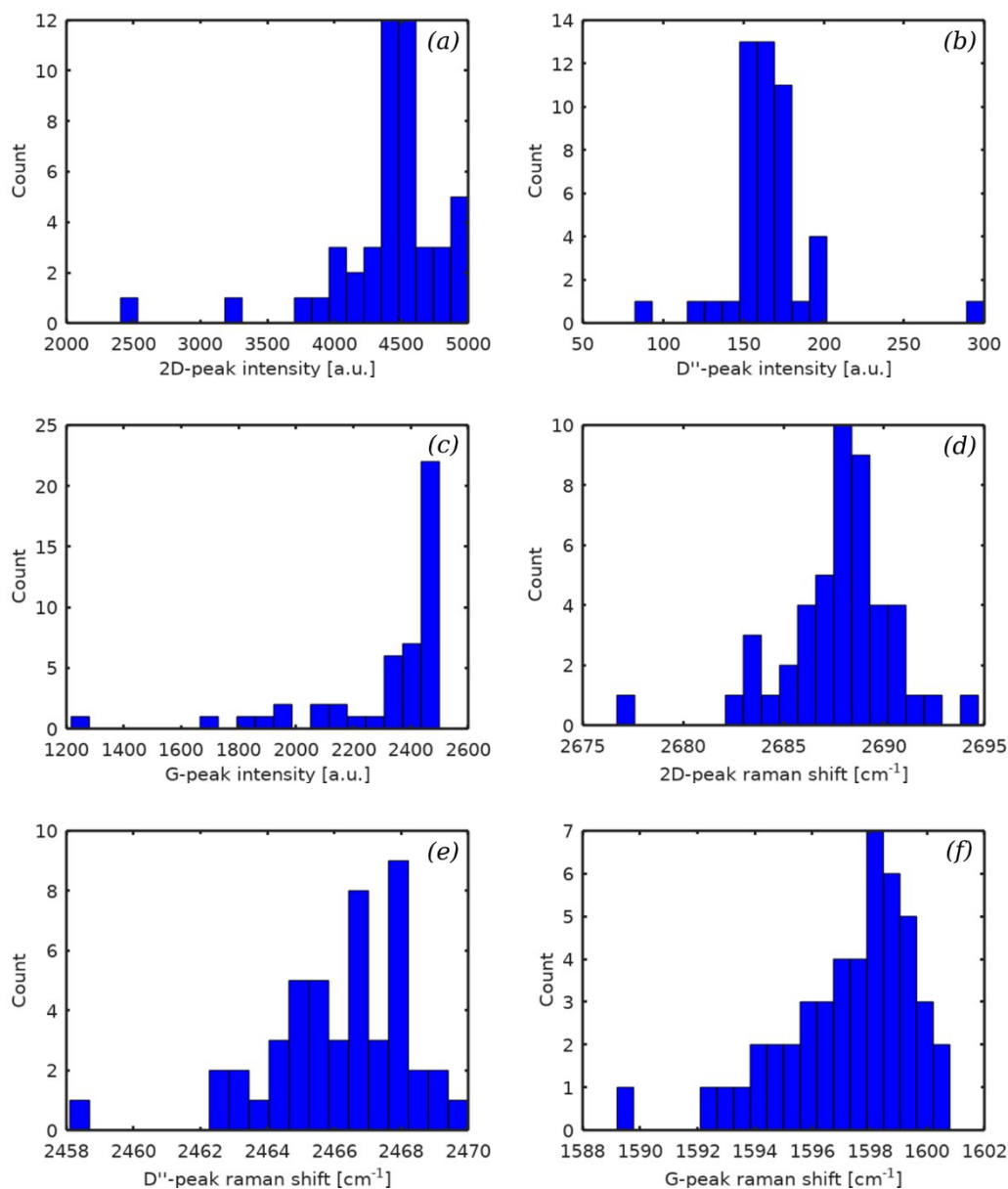
The differences between the two processes can be attributed to variation within the graphene sheets used and the doping caused by the photoresist residue and the local atmosphere. This hypothesis was first confirmed through the  $\text{FWHM}(G) < 20$  in Figure 3.6(i) and Figure 3.7(i), and then through the plot of  $\omega(G)$  vs  $\omega(2D)$  in Figure 3.9, which shows the points to align with the **hole doping line**  $\Delta\omega(2D)/\Delta\omega(G) = 0.7$ . Interestingly, the points in the S1813 plot, Figure 3.9(b), are slightly displaced from the curve, indicating a slight tensile strain [15]. This was possibly due to higher resist residue or an higher amount of dust on the substrate.

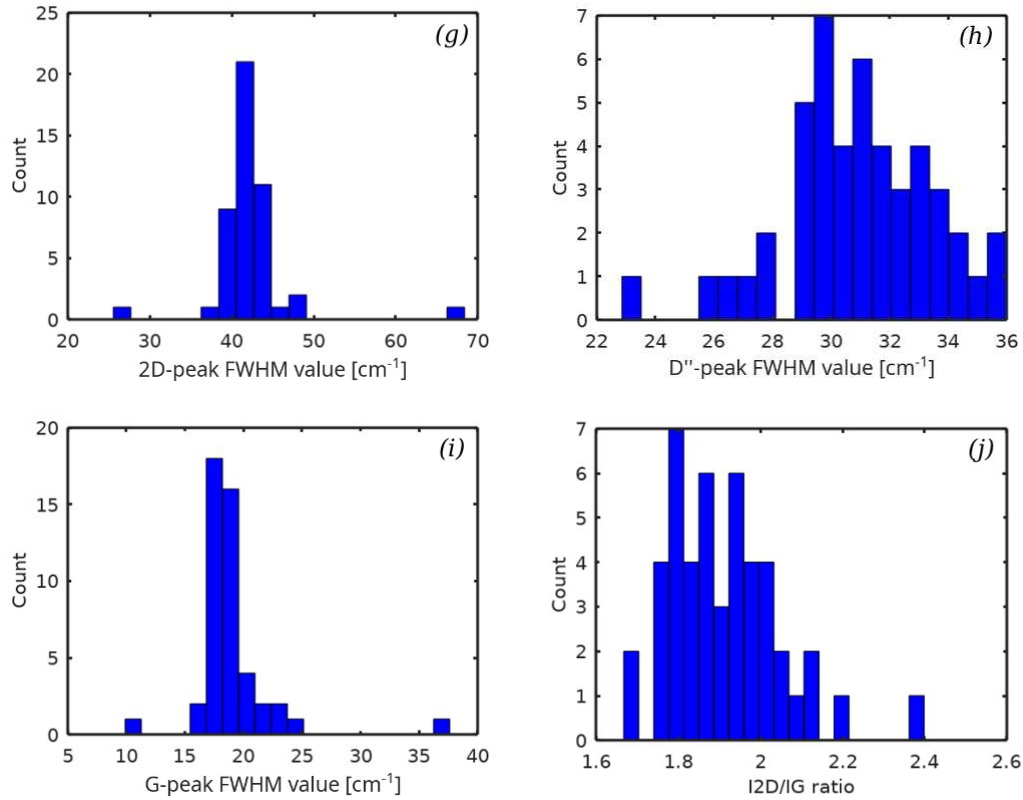


**Figure 3.9:** Plot of  $\omega(G)$  vs  $\omega(2D)$  for (a) an AZnLOF and (b) a S1813 patterning-type sample.

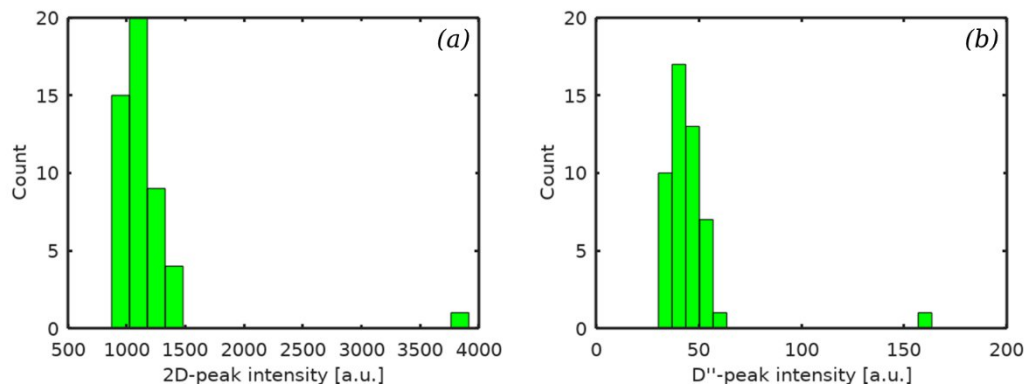
The set of results of the Raman maps for the graphene transfer tests using PMMA and Az10xt, described in Section 2.2.4.2, are shown respectively in Figure 3.10 and Figure 3.11. As shown in Figure 3.10(j) and Figure 3.11 (j), the graphene used is a uniform monolayer and

the  $I(2D)/I(G)$  ratio is  $\sim 2$  for both samples. Although, the **sample transferred using Az10xt** seems the most uniform between the two. This could have been due to the specific zone analyzed, the mechanical handling of both samples, or the resist used. As demonstrated by the 3D plot of the Raman maps, in Figure 3.12, the value of  $I(2D)/I(G)$  remain fairly constant within the sample's surface and drop out at the edges.





**Figure 3.10: Histograms of the interpolated values of the (a) (b) (c) intensities, (d) (e) (f) shifts and (g) (h) (i) FWHM of the graphene peaks. (j) is the histogram of the  $I(2D)/I(G)$  ratio. The data was taken from a graphene sheet transferred from Cu using PMMA.**



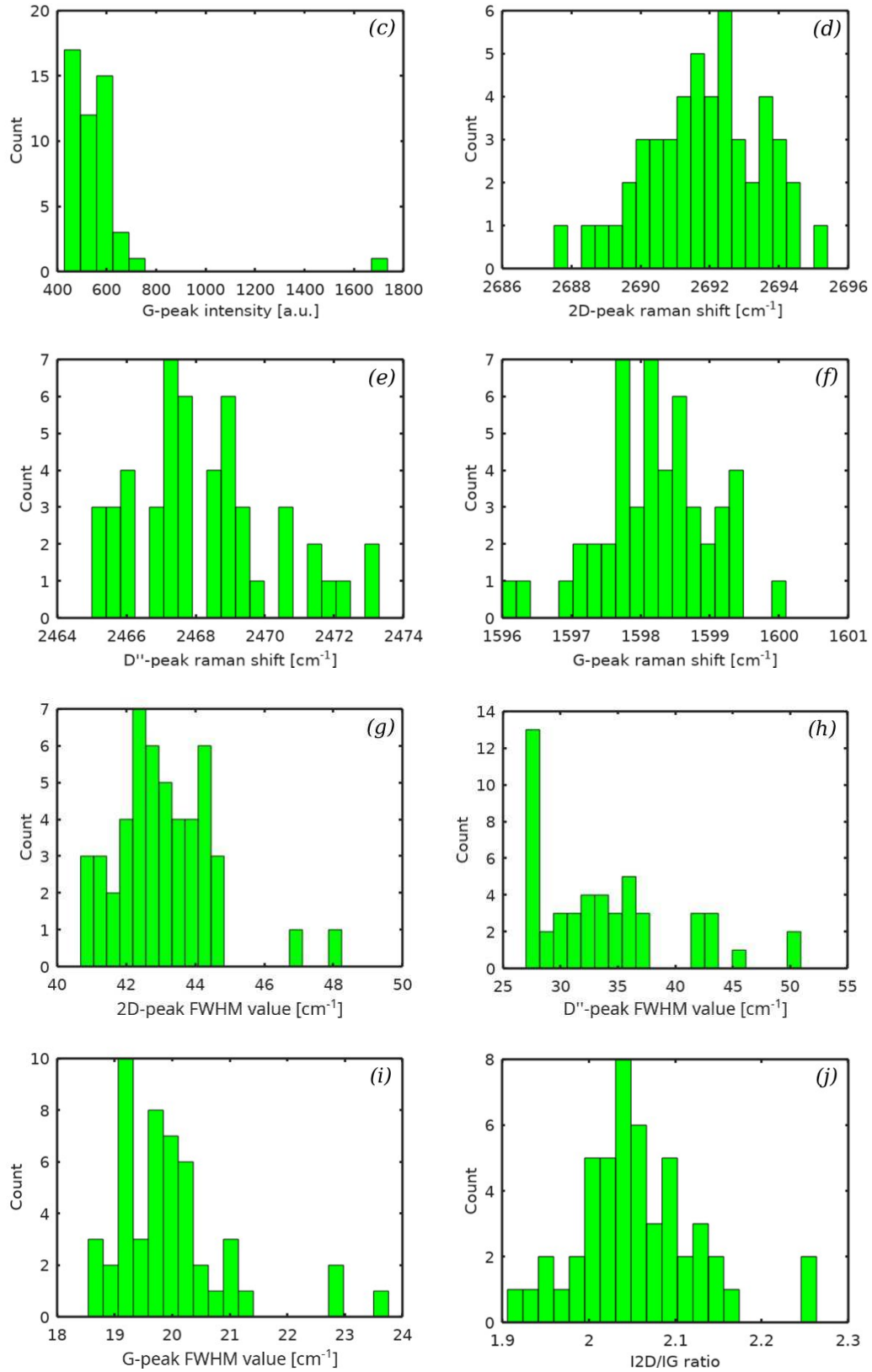


**Figure 3.11:** Histograms of the interpolated values of the (a) (b) (c) intensities, (d) (e) (f) shifts and (g) (h) (i) FWHM of the graphene peaks. (j) is the histogram of the  $I(2D)/I(G)$  ratio. The data was taken from a graphene sheet transferred from Cu using Az10xt.

Finally, the  $\text{FWHM}(G) < 20$  for both samples (Figure 3.10(i) and Figure 3.11(i)) indicate the presence of doping. The plot of  $\omega(G)$  vs  $\omega(2D)$  in Figure 3.13, seems to confirm a slight **p-doping** of the graphene, alongside to a **significant tensile strain**, as the points mostly follow the direction described by the line  $\Delta\omega(2D)/\Delta\omega(G) = 2.2$ . This is likely due to the lack of annealing before the measure.

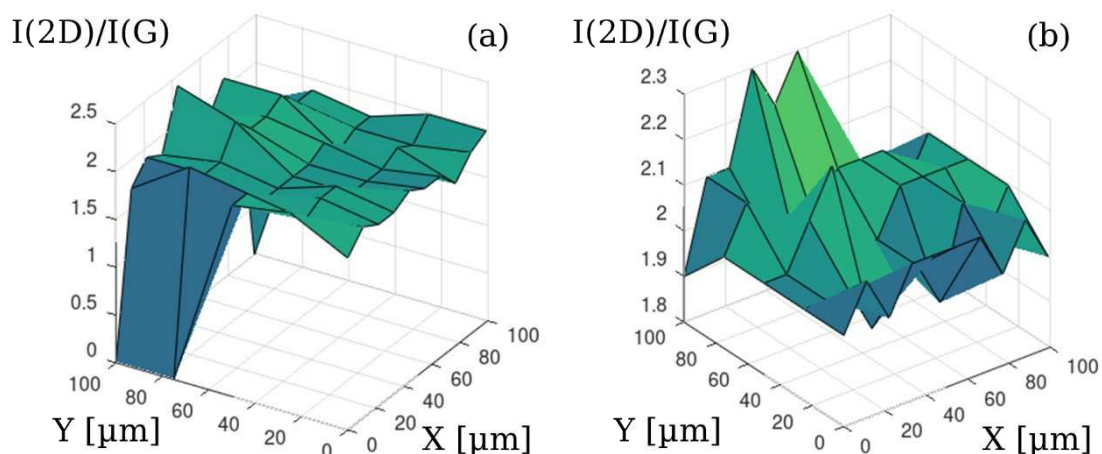


*Figure 3.12: 3D plot of the  $I(2D)/I(G)$  ratio vs. position for graphene transferred using (a) PMMA and (b) AZ10xt.*

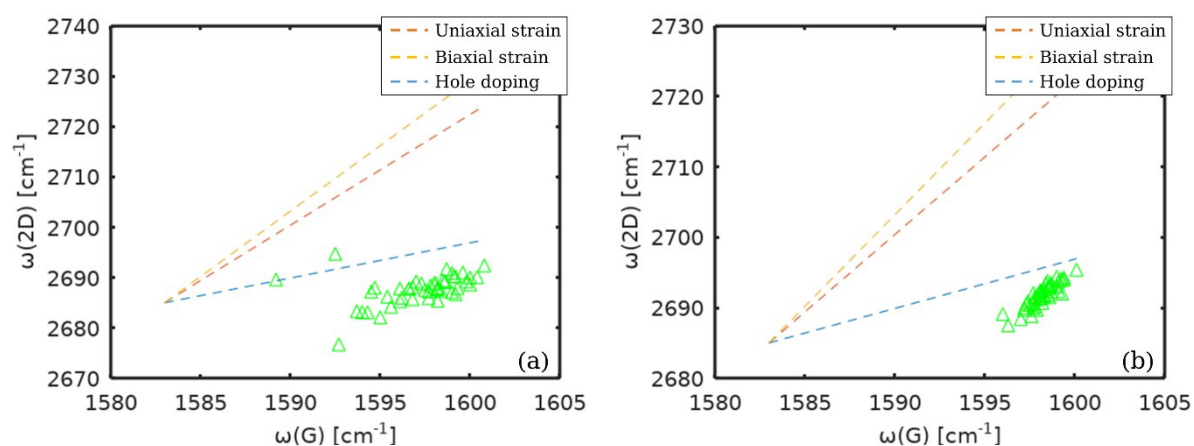
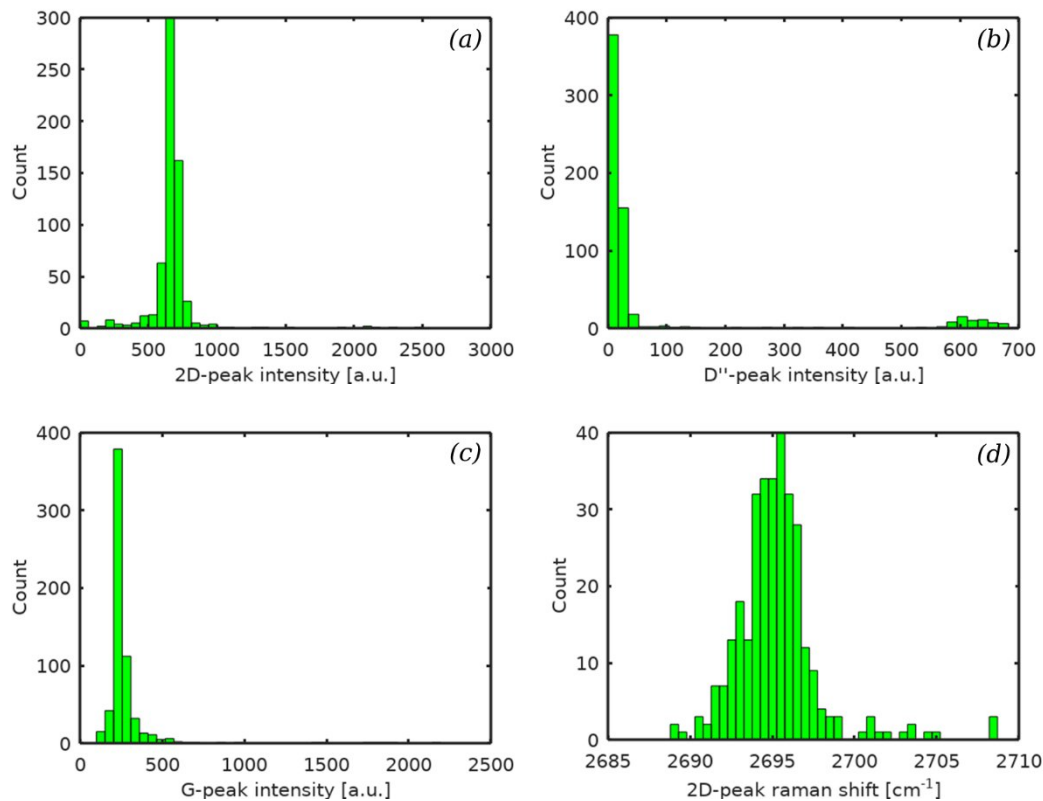


*Figure 3.13: Plot of  $\omega(G)$  vs  $\omega(2D)$  for transferred graphene using (a) PMMA and (b) AZ10xt as a protective layer.*

### 3.3.1 Analysis of the uniformity of the Hall bar devices

The uniformity of the device was analyzed via a large Raman map of the whole device after the Hall effect characterization discussed in Chapter 4.2. The interpolated results from the Raman map, shown in Figure 3.14, are in line with the other samples processed with the S1813 resist in the patterning step (see Section 2.2.6). The values of  $\text{FWHM}(G)$ , in Figure 3.14(i), and the distribution of  $\omega(2D)$  vs  $\omega(G)$ , in Figure 3.15(a), indicates that the sample is hole-doped.

It must be noted that the **doping was probably mostly due to the local atmosphere** in the Raman setup, however, as the points match quite well with the pure-doping line, this indicates the samples are not much strained, which closely matches the other S1813-processed devices. The plot of the ratio  $I(2D)/I(G)$  in Figure 3.14(j) show that the ratios are closely packed around 3, however, the peak is somewhat less sharp than other S1813-processed, indicating a higher defect rate. This is visually confirmed via the color map in Figure 3.15(b), which shows the presence of some defects near ports 6 and 11 which likely acted as scattering centers during the Hall effect characterization.



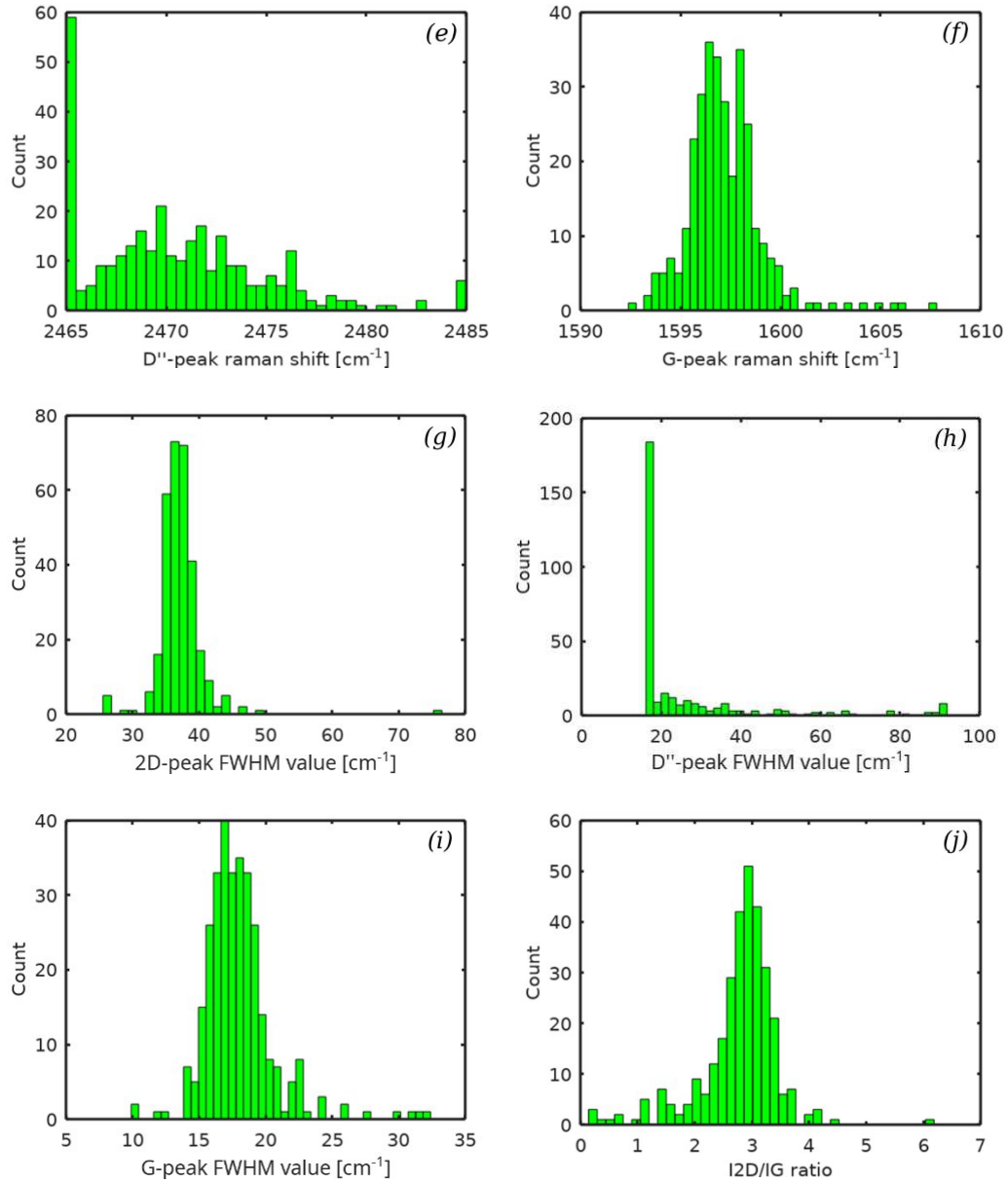


**Figure 3.14:** Histograms of the interpolated values of the (a) (b) (c) intensities, (d) (e) (f) shifts and (g) (h) (i) FWHM of the graphene peaks. (j) is the histogram of the  $I(2D)/I(G)$  ratio. The data was taken from the Hall bar after Hall effect measurements.

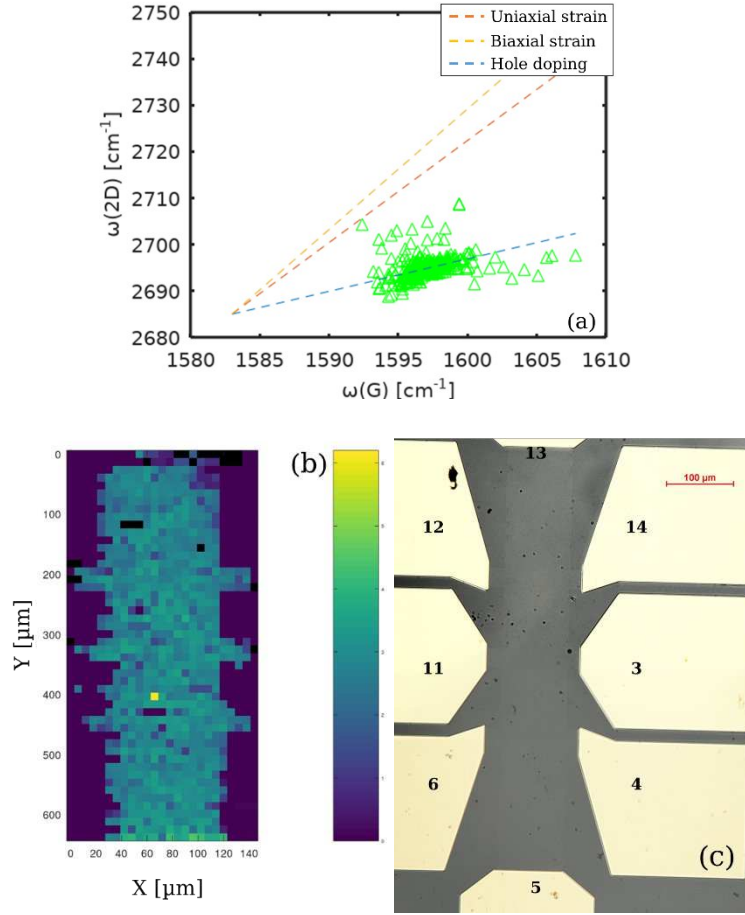


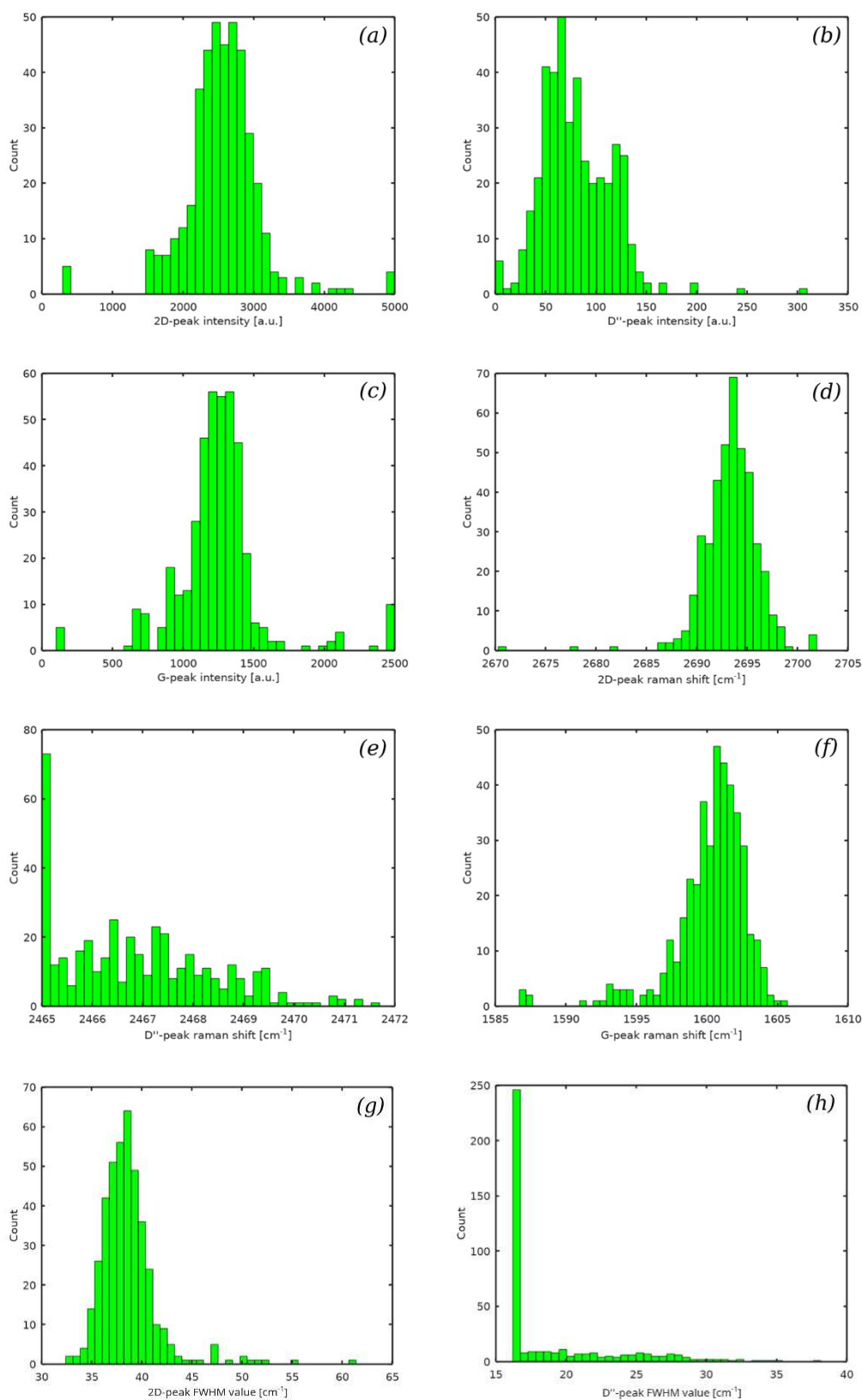
**Figure 3.15:** Plot of (a)  $\omega(G)$  vs  $\omega(2D)$  as an indicator of doping, (b) 2D distribution of  $I(2D)/I(G)$  over the Hall bar and (c) picture of the Hall bar before the Hall Effect measurements, with the same orientation as (b) and the reference port number for each pad.

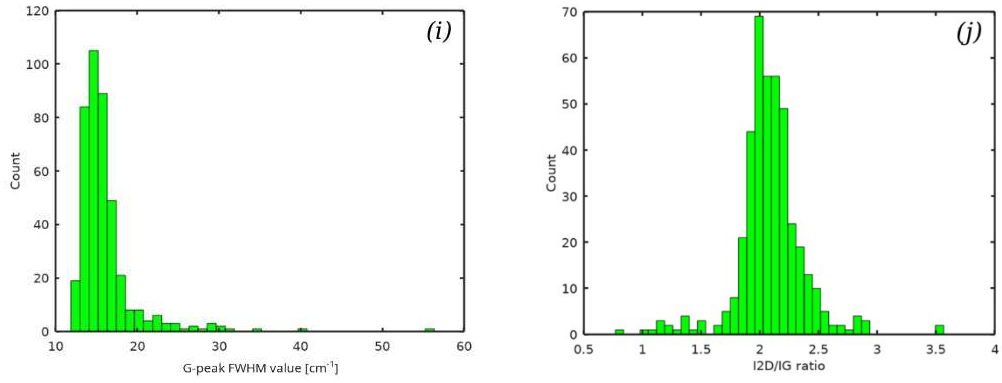
### 3.3.2 Results for graphene on PPLN

The technique described has been used to characterize the graphene transferred to a Periodically-Poled Lithium Niobate (PPLN) structure. The objective of this experiment was to find out the influence of the crystal cut on the properties of graphene. With this objective, a PPLN sample has been produced with the technique described in Chapter 2.3.

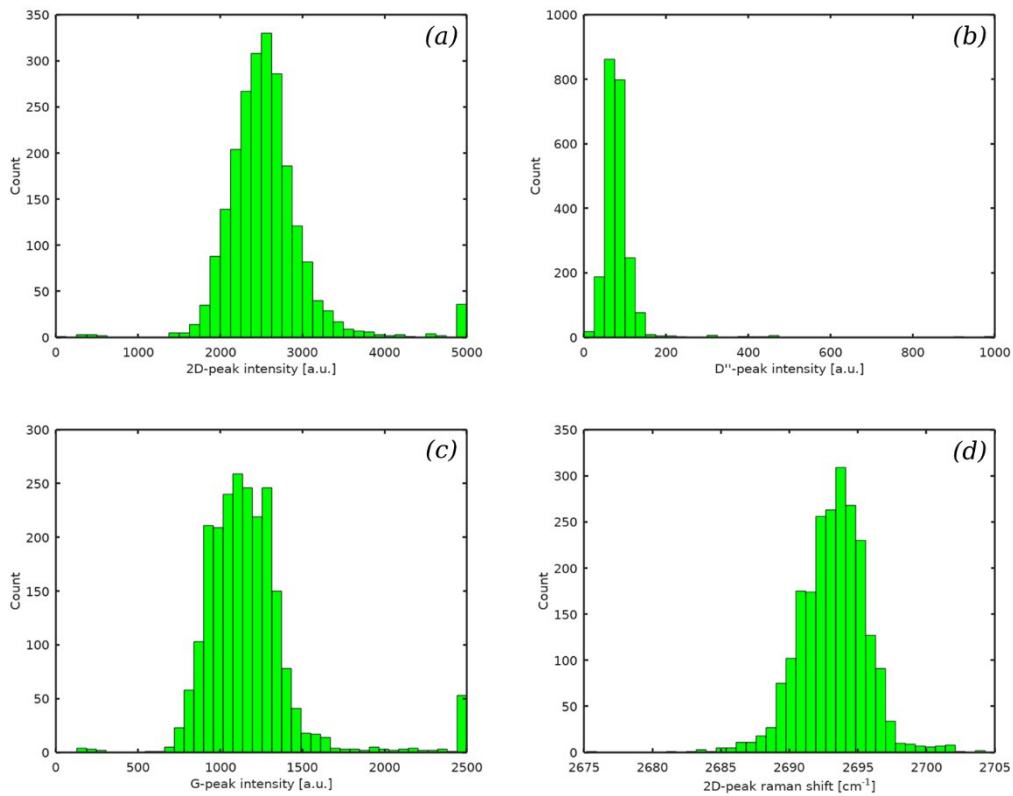
The graphene-on-PPLN sample was characterized through a linear Raman map via the previously described technique as described in order to visualize the effects of the periodic structure on the graphene monolayer. The analysis was divided in two linear mappings performed over a length of 5 mm on the graphene-covered area. The distribution of the interpolated peaks computed from the first Raman map, in Figure 3.16, and from the second one, in Figure 3.17, are compatible. The values of FWHM(G) collected indicate the presence

of doping and the  $\omega(2D)$  vs  $\omega(G)$  plots from Figure 3.18 also indicate the presence of some residual strain.





**Figure 3.16:** Histograms of the interpolated values of the (a) (b) (c) intensities, (d) (e) (f) shifts and (g) (h) (i) FWHM of the graphene peaks. (j) is the histogram of the  $I(2D)/I(G)$  ratio. The data was taken from the first mapping of graphene transferred to z-cut white PPLN.



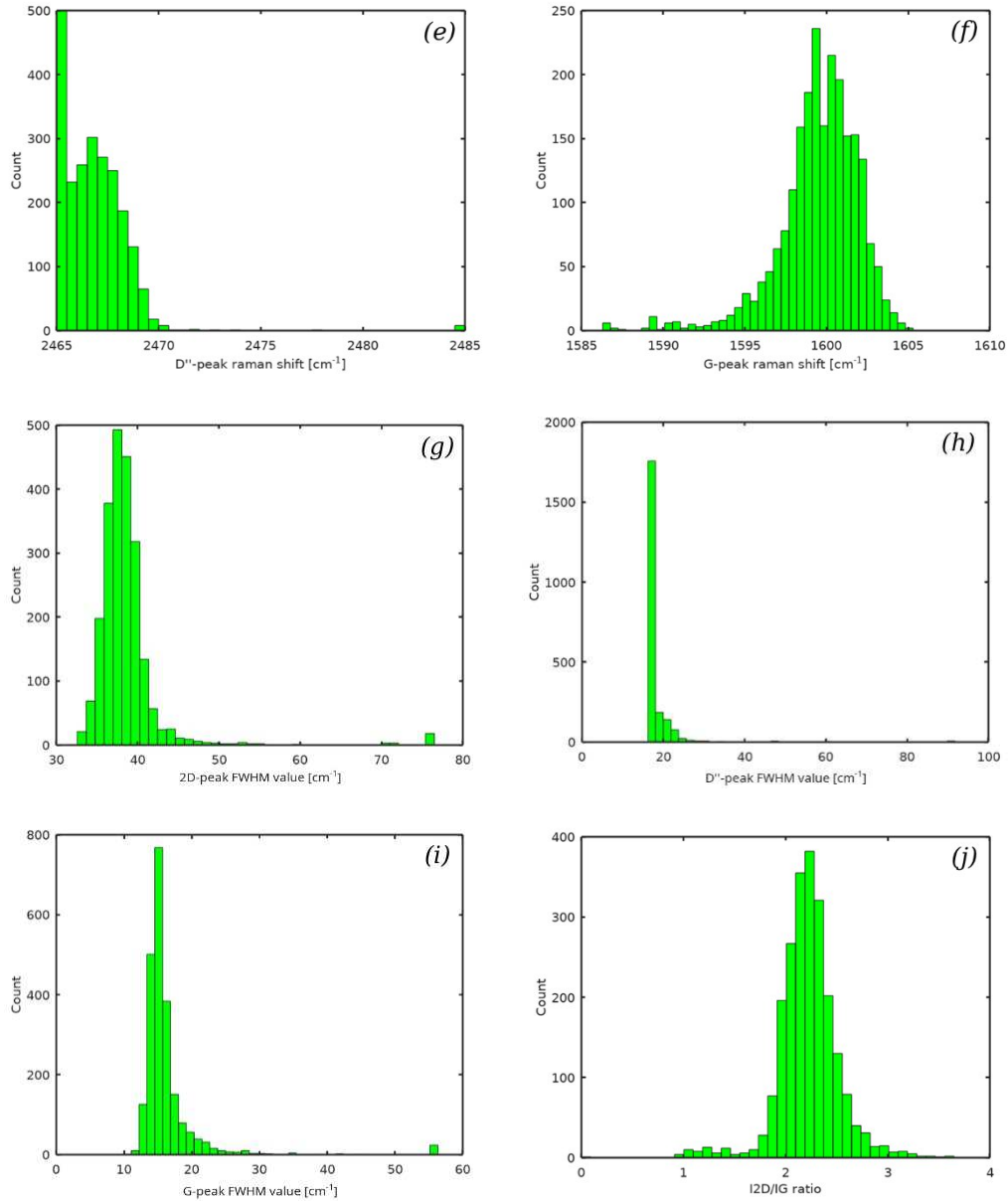


**Figure 3.17:** Histograms of the interpolated values of the (a) (b) (c) intensities, (d) (e) (f) shifts and (g) (h) (i) FWHM of the graphene peaks. (j) is the histogram of the  $I(2D)/I(G)$  ratio. The data was taken from the second mapping of graphene transferred to z-cut white PPLN.

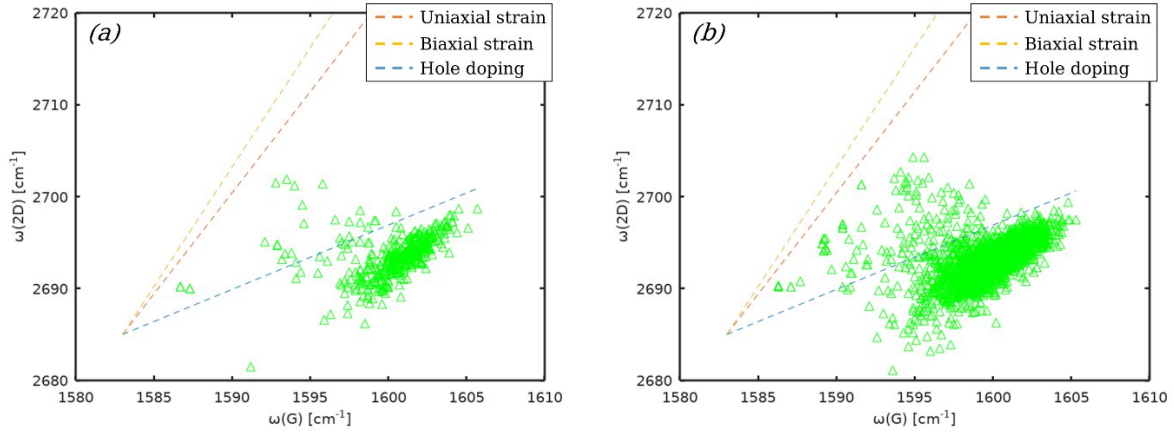


**Figure 3.18: Plot of  $\omega(G)$  vs  $\omega(2D)$  for the same graphene on PPLN device (a) first mapping and (b) second mapping.**

The variation of the Raman shift, the Raman intensity, the FWHM of the peaks, and the ratios are represented in Figure 3.19 and Figure 3.20, this shows a certain periodicity in  $I(G)$ ,  $I(2D)$  the ratio  $I(2D)/I(G)$  and  $\Delta\omega(2D)/\Delta\omega(G)$ . The periodic pattern in the  $I(G)$ ,  $I(2D)$ , and  $I(2D)/I(G)$  can be explained by a different sensitivity of the two peaks with respect to the incident angle of the laser and the  $\Delta\omega(2D)/\Delta\omega(G)$  variations, albeit small, indicate a variation in the strain due to the structure. No considerable difference due to the difference in the crystal face could be found.

In conclusion, I investigated all the GoL samples produced as described in Chapter 2. The main results are all the samples are single layer of graphene and p-doped. The study of PPLN demonstrates that the spontaneous polarization of  $\text{LiNbO}_3$  does not induce a significant change of carrier or properties of graphene. There is, however, some slight stress observed close to the electric contact of devices or PPLN domains but that may be attributed to the physical step of the contact.

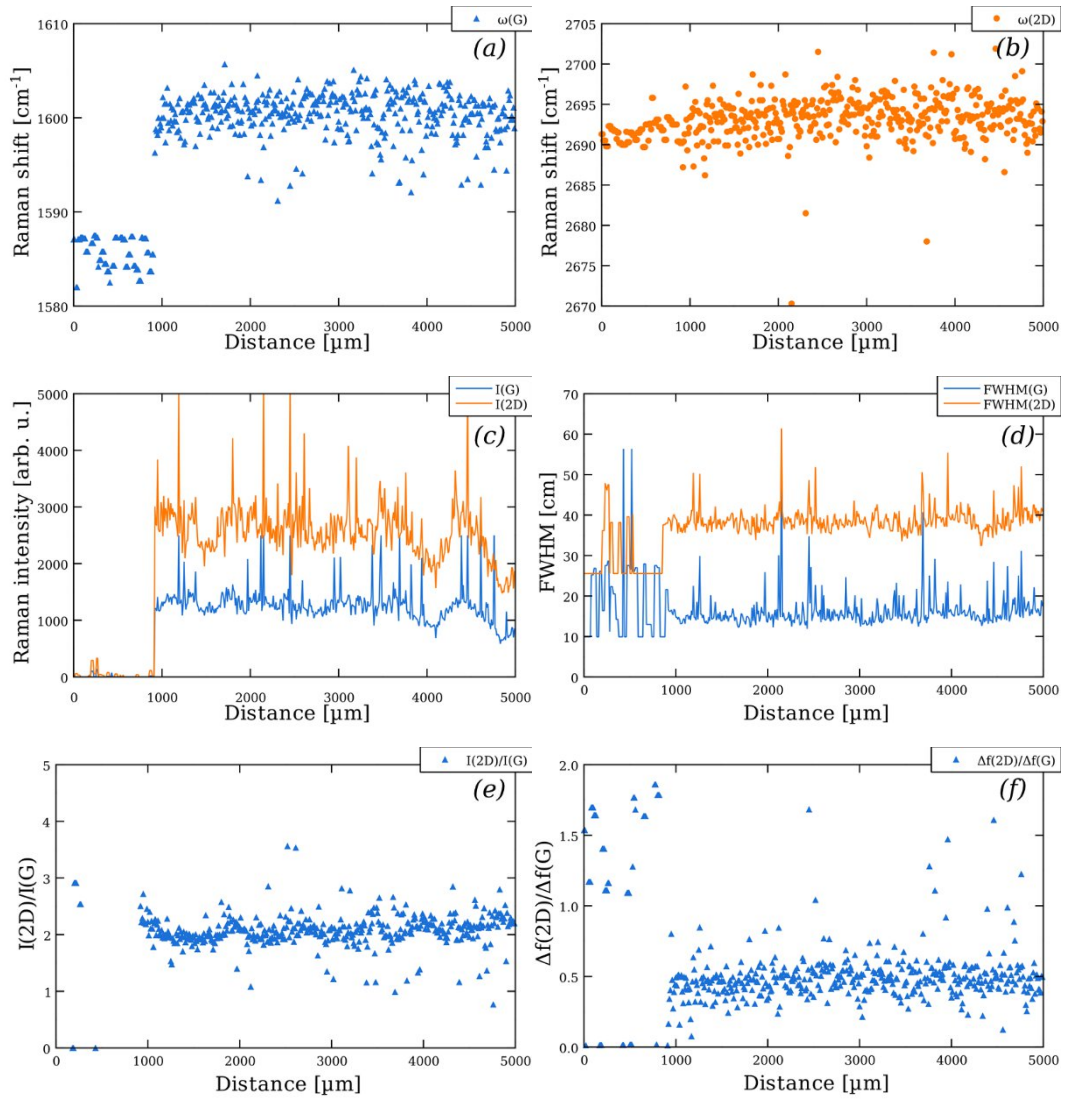


**Figure 3.19: Study of the 2D and G peak vs. laser position of (a) (b) the Raman shift (c) (d) intensity, (e) the ratio  $I(2\text{D})/I(\text{G})$  and (f) relative shift  $\Delta\omega(2\text{D})/\Delta\omega(\text{G})$ . The data was taken from the first mapping of graphene transferred to z-cut white PPLN.**

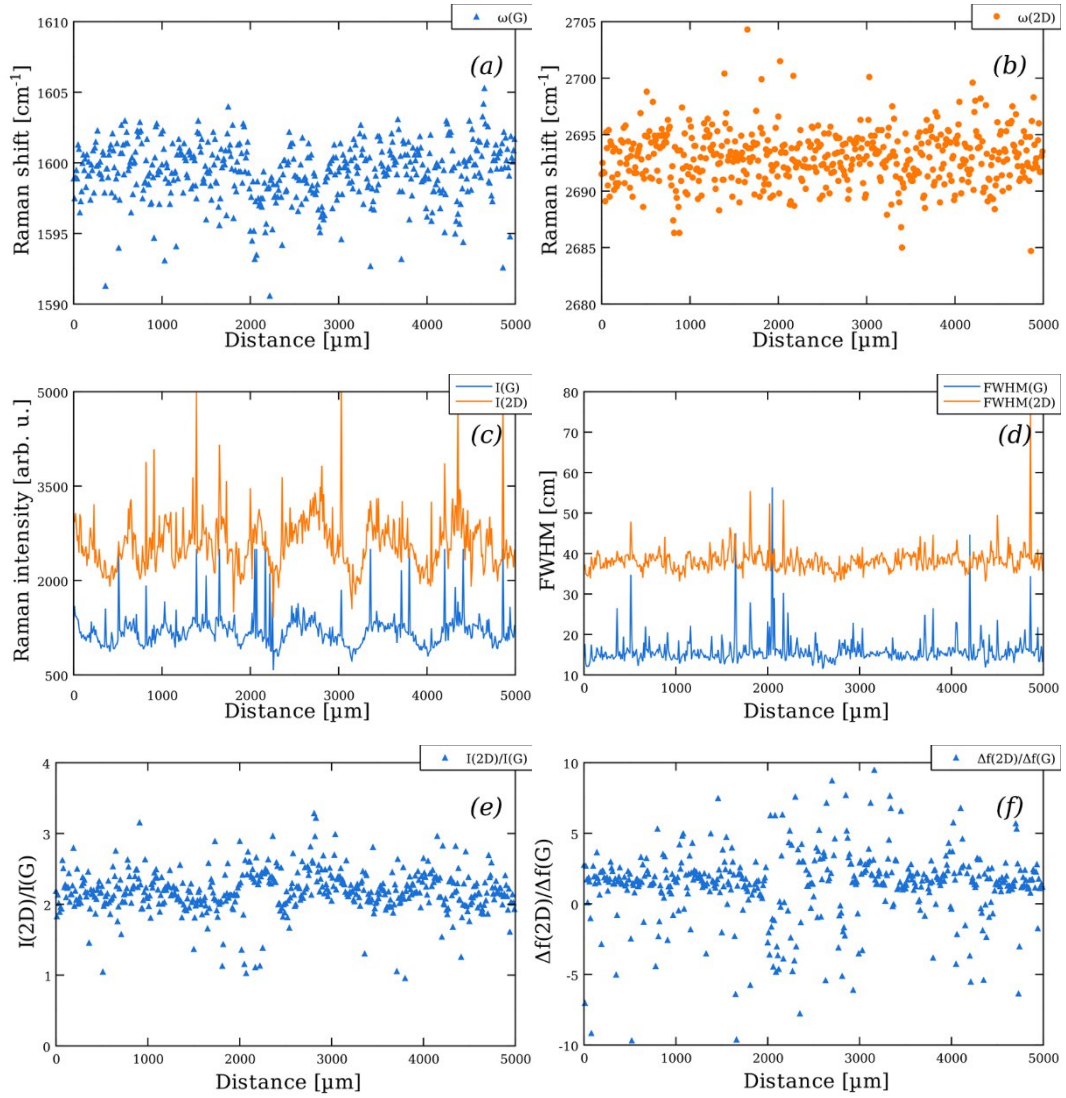


**Figure 3.20: Study of the 2D and G peak vs. laser position of (a) (b) the Raman shift (c) (d) intensity, (e) the ratio  $I(2D)/I(G)$  and (f) relative shift  $\Delta\omega(2D)/\Delta\omega(G)$ . The data was taken from the second mapping of graphene transferred to z-cut white PPLN.**

### 3.4 References

- [1] A. C. Ferrari *et al.*, ‘Raman Spectrum of Graphene and Graphene Layers’, *Phys. Rev. Lett.*, vol. 97, no. 18, p. 187401, Oct. 2006, doi: 10.1103/PhysRevLett.97.187401.
- [2] V. Kumar, A. Kumar, D.-J. Lee, and S.-S. Park, ‘Estimation of Number of Graphene Layers Using Different Methods: A Focused Review’, *Materials*, vol. 14, no. 16, p. 4590, Aug. 2021, doi: 10.3390/ma14164590.

- [3] I. Calizo, I. Bejenari, M. Rahman, G. Liu, and A. A. Balandin, ‘Ultraviolet Raman microscopy of single and multilayer graphene’, *Journal of Applied Physics*, vol. 106, no. 4, p. 043509, Aug. 2009, doi: 10.1063/1.3197065.
- [4] A. C. Ferrari and D. M. Basko, ‘Raman spectroscopy as a versatile tool for studying the properties of graphene’, *Nature Nanotech*, vol. 8, no. 4, pp. 235–246, Apr. 2013, doi: 10.1038/nnano.2013.46.
- [5] A. Das *et al.*, ‘Monitoring dopants by Raman scattering in an electrochemically top-gated graphene transistor’, *Nature Nanotech*, vol. 3, no. 4, Art. no. 4, Apr. 2008, doi: 10.1038/nnano.2008.67.
- [6] N. Papasimakis *et al.*, ‘Strain engineering in graphene by laser irradiation’, *Appl. Phys. Lett.*, vol. 106, no. 6, Art. no. 6, Feb. 2015, doi: 10.1063/1.4907776.
- [7] S. Reich and C. Thomsen, ‘Raman spectroscopy of graphite’, *Philosophical Transactions of the Royal Society of London. Series A: Mathematical, Physical and Engineering Sciences*, vol. 362, no. 1824, pp. 2271–2288, Nov. 2004, doi: 10.1098/rsta.2004.1454.
- [8] R. J. Nemanich, G. Lucovsky, and S. A. Solin, ‘Infrared active optical vibrations of graphite’, *Solid State Communications*, vol. 23, no. 2, pp. 117–120, Jul. 1977, doi: 10.1016/0038-1098(77)90663-9.
- [9] F. Tuinstra and J. L. Koenig, ‘Raman Spectrum of Graphite’, *The Journal of Chemical Physics*, vol. 53, no. 3, pp. 1126–1130, Sep. 2003, doi: 10.1063/1.1674108.
- [10] A. Das, B. Chakraborty, and A. K. Sood, ‘Raman spectroscopy of graphene on different substrates and influence of defects’, *Bull Mater Sci*, vol. 31, no. 3, pp. 579–584, Jun. 2008, doi: 10.1007/s12034-008-0090-5.
- [11] D. Yoon, H. Moon, H. Cheong, J. Choi, J. Choi, and B. Park, ‘Variations in the Raman Spectrum as a Function of the Number of Graphene Layers’, *J. Korean Phy. Soc.*, vol. 55, no. 3(2), pp. 1299–1303, Sep. 2009, doi: 10.3938/jkps.55.1299.
- [12] A. Gupta, G. Chen, P. Joshi, S. Tadigadapa, and Eklund, ‘Raman Scattering from High-Frequency Phonons in Supported n-Graphene Layer Films’, *Nano Lett.*, vol. 6, no. 12, pp. 2667–2673, Dec. 2006, doi: 10.1021/nl061420a.
- [13] A. C. Ferrari, ‘Raman spectroscopy of graphene and graphite: Disorder, electron–phonon coupling, doping and nonadiabatic effects’, *Solid State Communications*, vol. 143, no. 1, pp. 47–57, Jul. 2007, doi: 10.1016/j.ssc.2007.03.052.
- [14] J. E. Lee, G. Ahn, J. Shim, Y. S. Lee, and S. Ryu, ‘Optical separation of mechanical strain from charge doping in graphene’, *Nat Commun*, vol. 3, no. 1, Art. no. 1, Aug. 2012, doi: 10.1038/ncomms2022.

- [15] M. A. Bissett, M. Tsuji, and H. Ago, ‘Strain engineering the properties of graphene and other two-dimensional crystals’, *Phys. Chem. Chem. Phys.*, vol. 16, no. 23, pp. 11124–11138, 2014, doi: 10.1039/C3CP55443K.

## Contents of the chapter:

|   |     |
|---|-----|
| 4 DC electrical analysis.....                     | 120 |
| 4.1 DC Resistivity of Graphene and Contacts.....  | 120 |
| 4.1.1 Theory.....                                 | 120 |
| 4.1.2 State-of-the-art graphene.....              | 123 |
| 4.1.3 Design of the characterization devices..... | 123 |
| 4.1.4 Description of the experiments.....         | 124 |
| 4.2 Hall effect.....                              | 129 |
| 4.2.1 Hall effect Theory.....                     | 130 |
| 4.2.1.1 Classical Hall effect.....                | 130 |
| 4.2.1.2 Quantum Hall effect.....                  | 132 |
| 4.2.1.3 Quantum Hall effect in graphene.....      | 134 |
| 4.2.2 Description of the experiment.....          | 135 |
| 4.3 Discussion of the results.....                | 148 |
| 4.4 References.....                               | 149 |

## 4 DC electrical analysis

In this chapter, I conducted a low-frequency and DC analysis of the graphene films. The analysis is divided in two parts. In the first part, I will describe the resistive measurements of the film performed before Radio Frequency (RF) and Acousto-Electric (AE) measurements. In the second part, I will present the Hall effect measurements conducted to investigate the type carriers as compared to the Raman analysis. Hall measurements were conducted in the laboratory GEMaC (Groupe d'Étude de la Matière Condensée) of the Université de Versailles Saint-Quentin-en-Yvelines thank to Professors Yves Dumont and Joseph Scola.

### 4.1 DC Resistivity of Graphene and Contacts

The resistivity of graphene and of the metal contacts can be a very important factor in the overall performance of the device's performances, in fact, as discussed in Section 2.1.3, the graphene-metal contacts may be a significant contribute to the total resistivity. For the devices produced, and especially for the acoustoelectronic devices, the precise knowledge of the electrical properties of the processed devices is quite important. Because of this, the sheet resistivity and the contact resistivity of processed devices have been characterized separately through the Transmission Line Method (TLM).

#### 4.1.1 Theory

The TLM method, ideated by *W. Shockley* [1], is a standard analysis technique used for estimating the resistivity of a conductive material probed at different distances with some electric contacts, as shown in Figure 4.1 (a). The idea of the model stems from the fact that the charge transfer between the tested material and the metal happens continuously on the contact overlap, which causes a current gradient at the “internal” interface, as represented in Figure 4.1(b). Therefore, the contact interface is described by a transmission line-like model, via a per-unit-of-length contact inductance  $L$ , capacitance  $C$ , conductance  $G$ , and resistance  $R$ :

- the inductance  $L$ , expressed in H/m, and the capacitance  $C$ , expressed in F/m, depend on the materials used and the production process;
- the resistance  $R$ , expressed in  $\Omega/\text{m}$ , depends on the sheet resistivity of the probed material  $\rho_{\square}$ , in  $\Omega/\square$ , and the contact width  $W$ , in m, as described in Equation (4.1);

$$R = \frac{\rho_{\square}}{W}, \quad (4.1)$$

- the conductance  $G$ , expressed in S/m, depends on the contact area resistivity  $\Lambda_C$  between the metal and the probed material, in  $\Omega \cdot \text{m}^2$ , and the contact width  $W$ , in m, as expressed in Equation (4.2).

$$G = \frac{W}{\Lambda_C}, \quad (4.2)$$

The field distribution is found through the telegrapher's equations considering the steady state of the DC limit ( $\partial/\partial t \rightarrow 0$ ,  $\omega \rightarrow 0$ ) for a linear propagation ( $\partial/\partial y = 0$ ,  $\partial/\partial z = 0$ ):

$$\nabla^2 V - LC \frac{\partial^2 V}{\partial t^2} = (RC + GL) \cdot \frac{\partial V}{\partial t} + GR \cdot V \Rightarrow \frac{\partial^2 V}{\partial x^2} = GR \cdot V = \frac{\rho_{\square}}{\Lambda_C} \cdot V, \quad (4.3)$$

$$\nabla^2 I - LC \frac{\partial^2 I}{\partial t^2} = (RC + GL) \cdot \frac{\partial I}{\partial t} + GR \cdot I \Rightarrow \frac{\partial^2 I}{\partial x^2} = GR \cdot I = \frac{\rho_{\square}}{\Lambda_C} \cdot I, \quad (4.4)$$

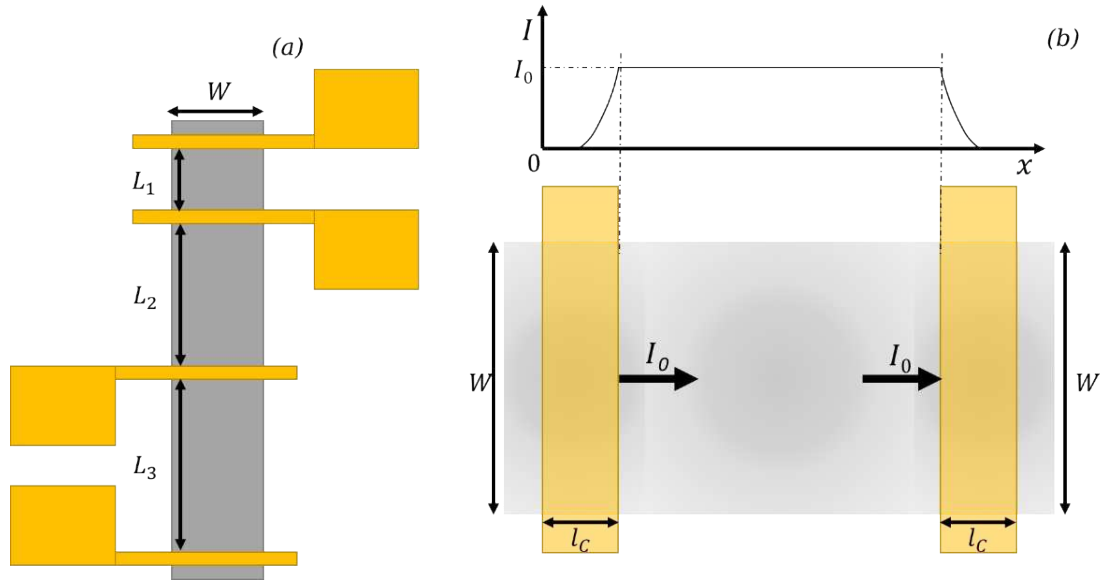


**Figure 4.1:** (a) Representation of a TLM characterization device, (b) visual representation of the distributed current transfer.

The solutions of Equation (4.1) and Equation (4.2) are in the form  $C_0 \cdot e^{\gamma x} + C_1 \cdot e^{-\gamma x}$ , where  $\gamma = \sqrt{G \cdot R} = \sqrt{\rho_{\square} / \Lambda_C}$ , more specifically, from the consideration that away from the contacted area the current flowing is null, the voltage drop along the at the whole contact is:

$$V_0 = \frac{I_0}{W} \sqrt{\rho_{\square} \cdot \Lambda_C} \cdot \coth(\gamma \cdot l_c), \quad (4.5)$$

where  $I_0$  is the current and  $l_c$  the contact length. This lets us define the contact resistance  $R_C$  as:

$$R_C = \frac{V_0}{I_0} = \frac{\sqrt{\rho_{\square} \cdot \Lambda_C}}{W} \cdot \coth(\gamma \cdot l_c). \quad (4.6)$$

For increasing values of  $\gamma$  and  $l_c$ ,  $\coth(\gamma \cdot l_c)$  tends exponentially towards 1 and  $R_C$  becomes invariant to the contact length  $\frac{\sqrt{\rho_{\square} \cdot \Lambda_C}}{W}$  the charge transfer is essentially restricted at the edge between the two materials over an effective channel length  $L_{eCH} \approx \gamma^{-1}$ . In this scenario, instead of estimating  $\Lambda_C$  and  $\rho_{\square}$  separately, it can be more convenient to instead introduce a linear contact resistivity  $\rho_C$ :

$$\rho_C = R_C \cdot W \cong \sqrt{\rho_{\square} \cdot \Lambda_C} \quad (4.7)$$

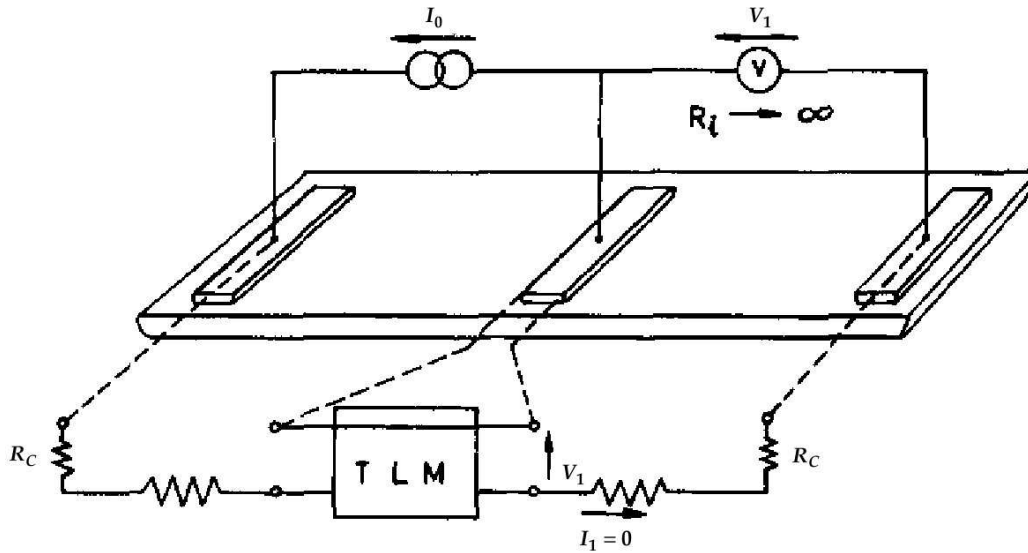


**Figure 4.2: Measurement setup for the contact-end resistance [2].**

The value of  $\gamma$  can be estimated through the measurement of the contact end resistance  $R_e$  [2], which can be measured as shown in Figure 4.2. The value of  $R_e$  is described as a function of  $\gamma$ ,  $\rho_{\square}$ ,  $\Lambda_C$ ,  $W$  and  $l_c$ :

$$R_e = \frac{V_1}{I_0} = \frac{\sqrt{\rho_{\square} \cdot \Lambda_C}}{W \cdot \sinh(\gamma \cdot l_c)} \quad (4.8)$$

Therefore, the value of  $\gamma$  can be computed from the ratio  $R_C/R_e$  as:

$$\frac{R_C}{R_e} = \cosh(\gamma \cdot l_c) \Rightarrow \gamma = \frac{1}{l_c} \cdot \operatorname{acosh}\left(\frac{R_C}{R_e}\right). \quad (4.9)$$

### 4.1.2 State-of-the-art graphene

Current literature treats graphene-metal contacts as following the “current-crowding” case described in Equation (4.5). Researchers have performed experimental analysis of the  $\gamma$  factor [3]–[5] for CVD graphene, and found estimated value of  $\sim 714 \text{ mm}^{-1}$  for Au, stable with electric field doping, and of  $\sim 434 \text{ mm}^{-1}$  for Ni/Au contacts. The actual graphene resistivity  $\rho_{\square}$  and contact resistivity  $\rho_C$  depends mainly on the processing and material chosen.

### 4.1.3 Design of the characterization devices

The TLM characterization devices have been designed to be compliant with the resolution of the lithographic process and to guarantee a contact size greater than the effective channel length of Au-graphene contacts of  $\sim 2.8 \mu\text{m}$  [3], [4]. Figure 4.3 shows the TLM design for a  $180 \mu\text{m}$ -wide graphene bar and the dimensions are defined through a scaling factor  $L_0$  as defined in Table 4-1. The first TLM design consisted of a  $120 \mu\text{m}$ -wide graphene bar probed with 8 differently spaced Au contacts and the others are replicated from the first one with a scaling factor of 2 and 0.5 respectively. This was done to evaluate size-related effects on devices, like dust, or holes, and the contact types manufactured and tested have been in either a bottom metal or “sandwich” configuration.

*Table 4-1: Dimensions of the TLM devices.*

| $W/L_0$ | $L_C/L_0$ | $L_S/L_0$ | $L_1/L_0$ | $L_2/L_0$ | $L_3/L_0$ | $L_4/L_0$ | $L_5/L_0$ | $L_6/L_0$ | $L_7/L_0$ |
|---------|-----------|-----------|-----------|-----------|-----------|-----------|-----------|-----------|-----------|
| 12      | 0.8       | 21        | 1         | 2         | 4         | 8         | 12        | 18        | 24        |

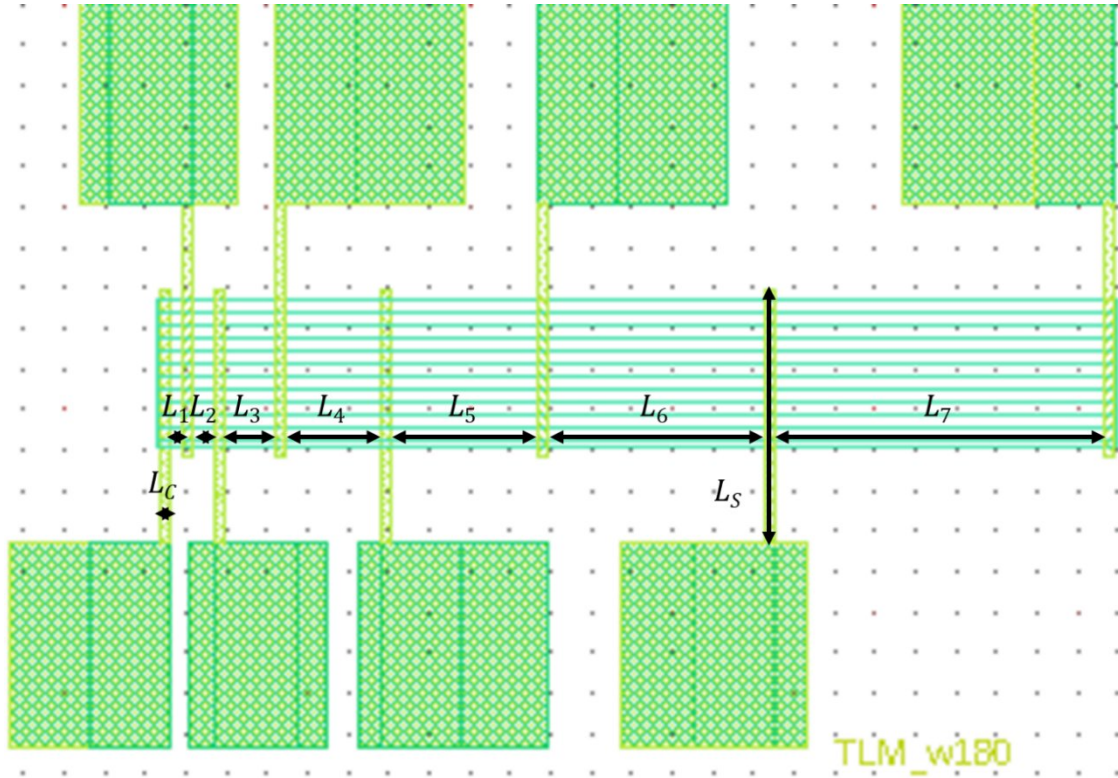


*Figure 4.3: Layout of 180  $\mu\text{m}$ -wide TLM device. The graphene zone is textured in teal stripes and the green zone is textured in green.*

#### 4.1.4 Description of the experiments

The resistive measurements have been performed in the controlled environment of the clean room and the resistance have been measured with the 4-points method using the Keithley 6221 [6] and Keithley 2182A [7] combo. The separated current source and voltage measurement enables for higher flexibility in the measurements, allowing extracting both  $R_c$  and  $R_e$ . Both instruments have been controlled via a specifically-made LabVIEW program, whose interface, represented in Figure 4.4, allowed to easy setup a measurement through a continuous mode and a pulsed mode. With reference to Figure 4.5, each measurement was composed of:

- a defined number of steps to be averaged  $N$ ,
- the time interval between pulses  $PI$ , defined as multiples of the power line cycles (PLC),
- the current pulse width  $T_{CP}$ ,
- the source delay  $T_{SD}$ ,
- the number of low-current measurements (NLCM),

- the low-current  $I_{low}$ , defining the current while not measuring,
- the high-current  $I_{high}$ , defining the current during the measure.

The value of  $I_{high}$  could be set either as constant, or defined through a ramp. The source delay time  $T_{SD}$  sets when the voltage measurement is performed after the current is switched to  $I_{high}$ . If  $NLCM > 0$  the system voltage measurement before switching the current from  $I_{low}$  to  $I_{high}$  ( $NLCM = 1$ ), or both before and after ( $NLCM = 2$ ). Before actually performing the measurements and saving the data, a current sweep was performed on a test resistance to check for the presence of a Schottky-type voltage barrier which was either completely absent from the devices, or under the noise level of the setup.

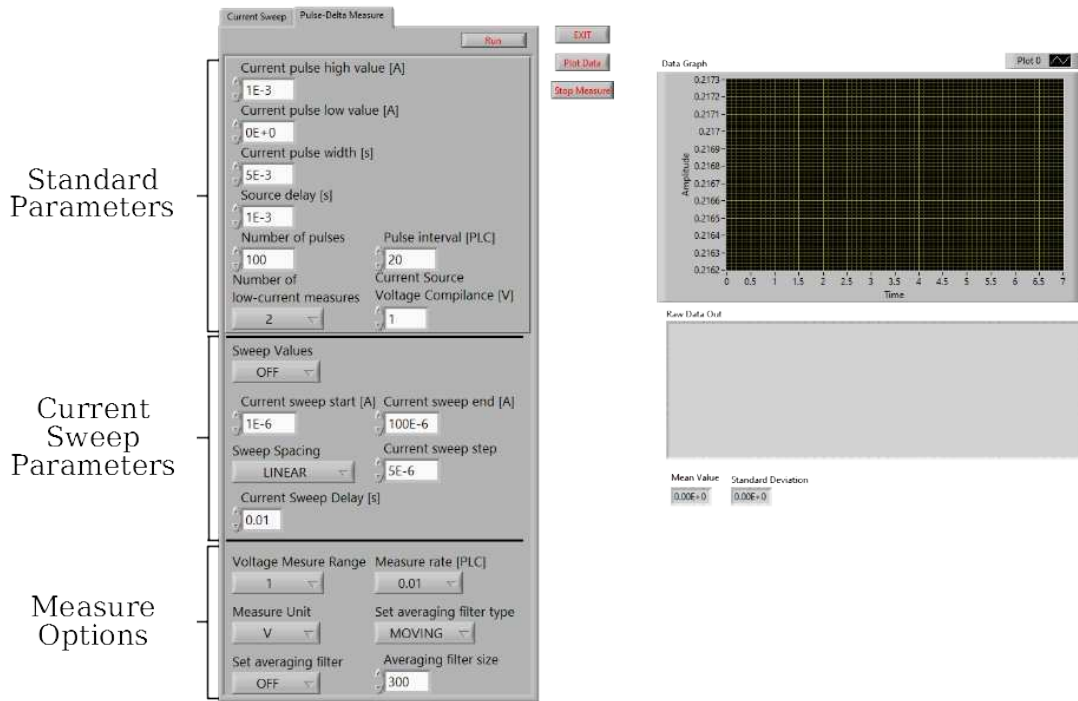


**Figure 4.4:** The LabVIEW measurement interface.

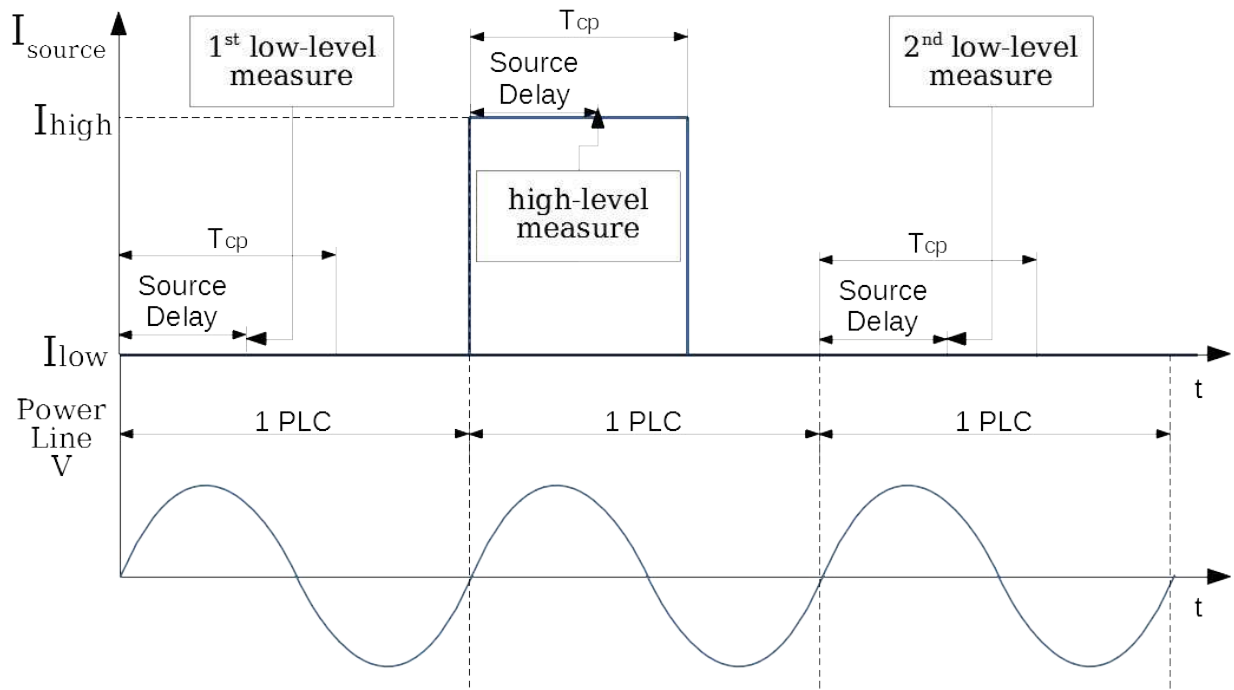


**Figure 4.5: Representation of a pulse-type measurement.**

Before each measurement session, the samples were left to rest for 1-2 weeks inside the sample boxes at 20 °C in a dark environment after the production was complete. This was done in order to let transitory effects dissipate, like accumulated pyroelectric charges and various gases adsorbed on the graphene during the productions.

In order to let the heat dissipate in between the measurement, each point was stimulated with a current amplitude of 100 nA, which was in pulsed with pulse width  $T_{CP} = 500 \mu s$  and total delay between each pulse 400 ms. The results were averaged over  $N=100$  measurements, and the uncertainty for each averaged point was in the range few percent points.

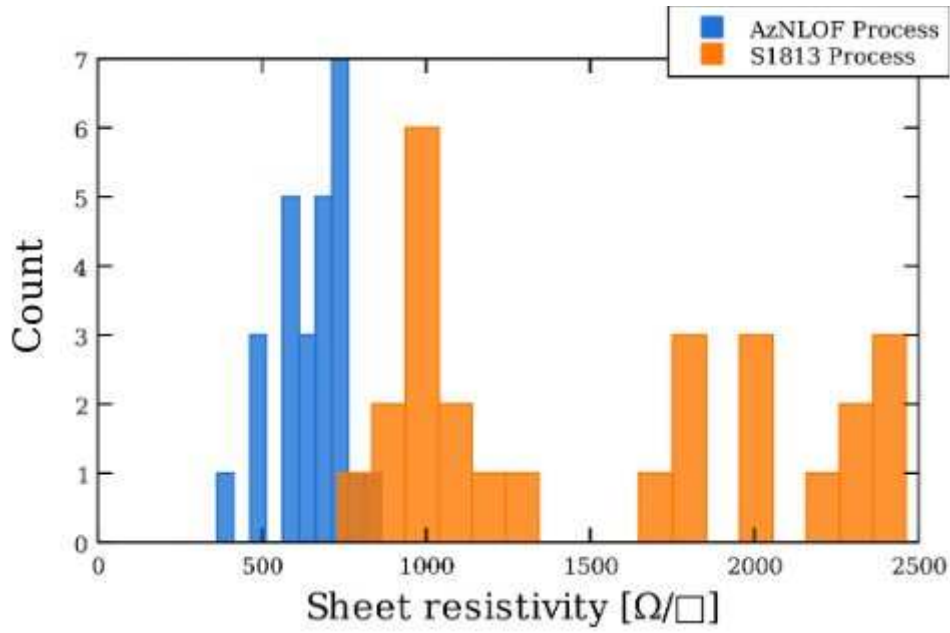


*Figure 4.6: Distribution of the processed graphene's sheet resistivity between the AZnLOF process variation (in blue) and the S1813 process variation (in orange).*

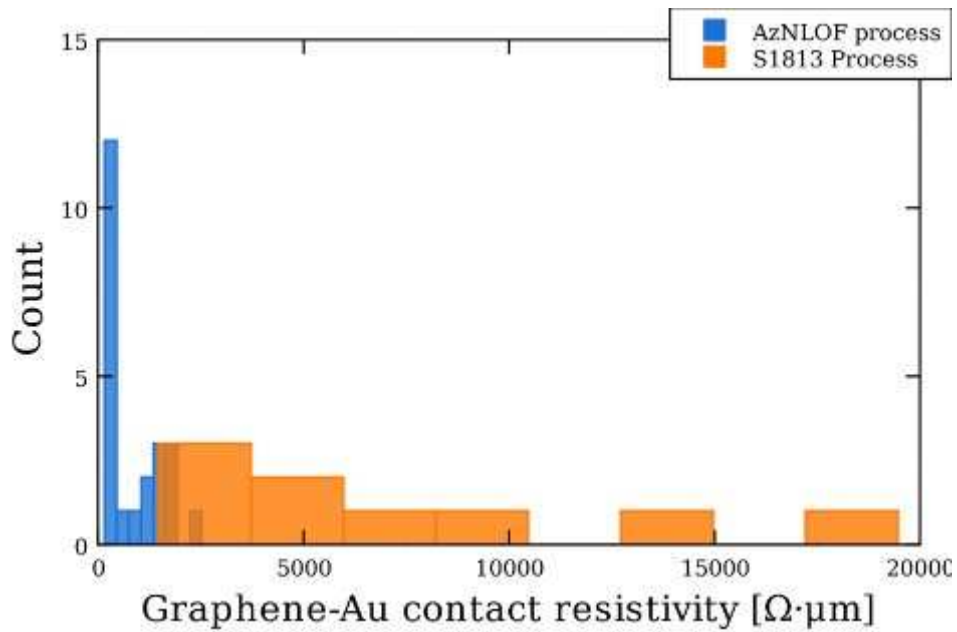


*Figure 4.7: Distribution of contact resistivity between graphene and Au for devices made with the AZnLOF process variation (in blue) and the S1813 process variation (in orange).*

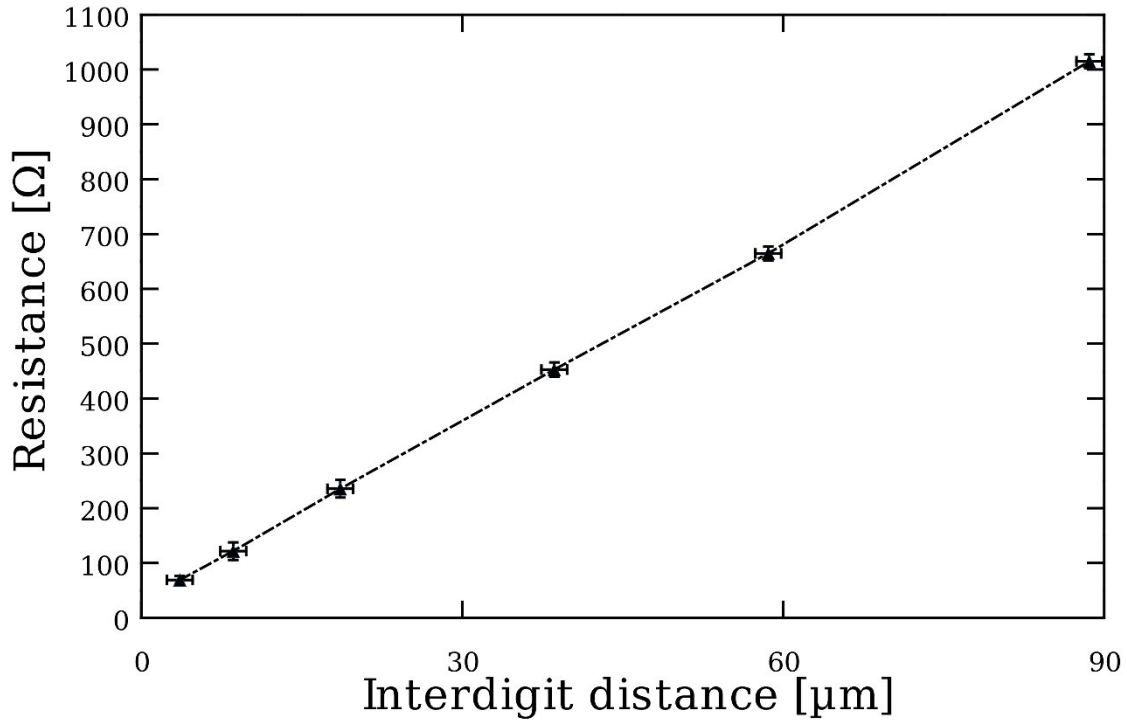


*Figure 4.8: A typical TLM plot from a sandwich-type Au-contacted device made with the AZnLOF process variation. The sheet resistivity  $\rho_{\square}$  is  $664 \Omega/\square$  and the contact resistivity  $\rho_c$  is  $413 \Omega \cdot \mu\text{m}$ .*

Figure 4.6 and Figure 4.7 show respectively the distribution of the sheet resistivity and contact resistivity for both AZnLOF-process (in blue) and the S1813 (in orange), while Figure 4.8 shows a complete TLM measure plot. The data show how the graphene resistivity most close to the range of values declared by the manufacturer for clean graphene on Si/SiO<sub>2</sub> [8] were the ones corresponding to the **AZnLOF process variation**, which is also in agreement with the Raman measurements in Section 3.3. The **S1813** allows for a resistivity increase up to **~4 times** in respect to the AZnLOF process, at the price of a higher contact resistivity and more variability in the results. It must be pointed out, however, that other factors could have contributed to the higher resistance, for example, aging of the graphene monolayers, of the chemicals used during the process, or the mechanical handling of the devices.

As reported in Table 4-2, the estimation of the **effective channel length** of the processed devices was found to be in the range **[2.7, 23] μm** and the large uncertainty in the results is largely uncorrelated to both  $\rho_c$ ,  $\rho_{\square}$ , and the dimensions of the devices, but instead is to be attributed to misalignment between the lithographic processes for the top and bottom contacts

in the range of 1  $\mu\text{m}$  [1]. The reported values for  $L_{eCH}$  suggest that the length of the contact resistance can be an important factor in determining the overall resistivity of the devices.

Still, the reported values are in the same order of magnitude as other estimated values for Au-graphene contacts via the photocurrent method of 1.6  $\mu\text{m}$  for top-contacted graphene [3].

*Table 4-2: The estimated values of  $\gamma$  and of channel length  $L_{eCH}$ .*

| Sheet resistivity<br>[ $\Omega/\square$ ] | Contact resistivity<br>[ $\Omega \mu\text{m}$ ] | $\gamma$ [ $\text{mm}^{-1}$ ] | $L_{eCH}$<br>[ $\mu\text{m}$ ] | Device width<br>[ $\mu\text{m}$ ] |
|---|---|-------------------------------|--------------------------------|-----------------------------------|
| 664.3                                     | 413.1   | 375.5                         | 2.7                            | 60                                |
| 717.0                                     | 383.8   | 280.5                         | 3.6                            | 60                                |
| 506.0                                     | 1300  | 42.8                          | 23.4                           | 180                               |
| 592.1                                     | 4605  | 147.2                         | 6.8                            | 180                               |
| 490.3                                     | 1190  | 70.0                          | 14.3                           | 120                               |
| 592.1                                     | 4605  | 147.2                         | 6.8                            | 180                               |
| 652.8                                     | 1922  | 62.0                          | 16.1                           | 180                               |

## 4.2 Hall effect

The Hall effect is a physical phenomenon of moving charges inside a conductive material immersed in a magnetic field. It was first discovered by Edwin Hall in 1879 by applying magnetic fields on a thin Au leaf and it finds use as a powerful characterization technique, enabling to evaluate both the number of charge carriers, their sign (electrons or holes) and their mobility [9].

For 2D systems, Hall effect is a quantum effect [9]–[14] that finds practical applications for both the fields of metrology [10], [12] and material characterization, to extract the effective mass of moving charges [15].

## 4.2.1 Hall effect Theory

### 4.2.1.1 Classical Hall effect

The classical Hall effect (CHE) phenomenon is visualized in Figure 4.9, where a certain current  $I_x$  flows in a simple rectangular (Hall bar) structure. In the case of no magnetic field, the charges move straight between the top and bottom electrodes, causing a voltage drop  $V_x$ , as shown in Figure 4.9(a). However, in the presence of an orthogonal magnetic field  $B_z$ , the cyclotron momentum causes the charges to accumulate on a side rather than another, causing in term a certain voltage differential  $V_y$  which can be directly measured via a standard voltage probe.

In systems where the charge propagation is purely of one type, holes or electrons, the voltage, the voltage  $V_y$  in equilibrium condition can be computed via Faraday's law:

$$F_y = 0 = q \cdot (E_y + v_x B_z) \Rightarrow V_y = - q v_x B_z w, \quad (4.10)$$

where  $w$  is the width of the Hall bar and  $v_x$  is the propagation velocity of the charges along the x-axis. The voltage values are linearly dependent on the applied current, therefore, it is more useful to instead consider the resistances  $R_{xx} = V_x/I_x$  and  $R_{xy} = V_y/I_x$ . The value of  $R_{xx}$  is defined via the **sheet resistivity**  $\rho_{xx}$ , the device's length  $l$  and its width  $w$  as in Equation (4.11).

Finally, by applying the definition of  $I_x$  in terms of charge propagation velocity  $v_x$ , **surface charge density**  $n_s$  and the electron charge  $q$  in Equation (4.12), and of  $v_x$  in terms of the **charge mobility**  $\mu_x$  and electric field component  $E_x$  Equation (4.13), the  $R_{xy}$  is defined as in Equation (4.14).

$$R_{xx} = V_x/I_x = \rho_{xx} \cdot l/w \quad (4.11)$$

$$I_x = n_s \cdot q \cdot v_x \cdot w \quad (4.12)$$

$$v_x = \mu_x \cdot E_x \quad (4.13)$$

$$R_{xy} = \frac{V_y}{I_x} = \frac{-B_z}{n_s \cdot q} \quad (4.14)$$

Finally, the resistivity  $\rho_{xx}$  is found from  $R_{xx}$  when  $B_z \simeq 0$  as:

$$\rho_{xx} = R_{xx} \cdot \frac{w}{l} = \frac{1}{q \cdot \mu_x \cdot n_s} \quad (4.15)$$

This allows estimating  $n_s$  and  $\mu_x$  respectively as:

$$n_s = \frac{B_z}{R_{xy} \cdot q} \quad (4.16)$$

$$\mu_x = \frac{B_z}{\rho_{xx} \cdot q} \quad (4.17)$$

It must be noted that experimentally, as the injected charges propagate in a shorter effective width due to the applied  $B_z$ , the value of  $R_{xx}$  rises for increasing values of  $B_z$ . In particular, in the case of a perfectly uniform sample,  $R_{xx}(-B_z) = R_{xx}(+B_z)$ , however, the position of the  $V_y$  probes and scattering introduced by the non-uniformities in the samples cause  $R_{xy}$  to pour into  $R_{xx}$ , and the measured resistance is:

$$R'_{xx} = R_{xx} + \alpha \cdot R_{xy} \quad (4.18)$$

where  $R'_{xx}$  is the **uncorrected resistance** and  $\alpha$  is a **constant** whose value can be found through numerical optimization.

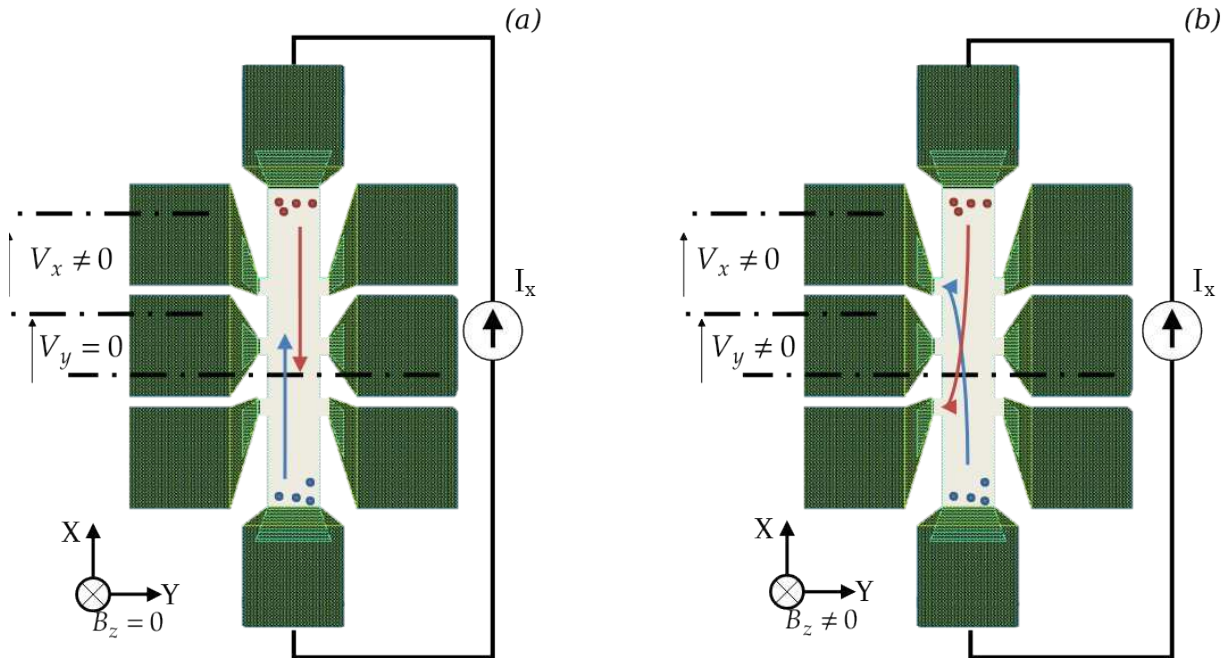


**Figure 4.9: Representation of the charge motions in a semiconductive Hall bar without (a) and with (b) the application of a magnetic field.**

### 4.2.1.2 Quantum Hall effect

Differently from the classical effect, the quantum Hall effect (QHE) is limited to 2D or quasi-2D electron gases at low temperature. The result is the quantization of the Hall resistance in plateaus, as described in Figure 4.10:

$$R_{xy} = \frac{h}{\nu \cdot q^2}, \quad (4.19)$$

where  $\nu$  is the filling factor of the electron energy levels. Depending on the value of  $\nu$ , we distinguish an integer QHE, when  $\nu$  is an integer, and a fractional QHE, where  $\nu$  has a fractional value. The integer QHE was first discovered by *Von Klitzing* in 1980 [12], the physical explanation of this phenomenon is to be found in the modification of the electron energy states caused by the quantization of the cyclotron frequency at strong magnetic fields, called Landau quantization, as displayed in Figure 4.11:

$$\omega_c = \frac{q \cdot B_z}{m^*}. \quad (4.20)$$

This restricts the electron states in bands around the energy levels:

$$E_L(j) \approx E_0 + (j + 1/2) \cdot \hbar \omega_c, \quad (4.21)$$

where  $j$  is an integer value. For integer QHE, the filling factor is therefore defined as the number of Landau bands  $J$  with energy  $E_L(J)$  less than the Fermi energy  $E_F$ , multiplied by a factor  $g_s$  that takes into account the degeneracy, for standard semiconductors like Si,  $g_s = 2$  due to  $\pm 1/2$  spin electrons:

$$\nu = g_s \cdot j. \quad (4.22)$$

At the absolute temperature of 0 K the peaks are delta functions, in reality the width of each of the generated bands depends on the average scattering-free time  $\tau_i$  as  $\Gamma_i = \hbar/\tau_i$ . As  $\tau_i$  depends on both the uniformity of the samples and the temperature, QHE is effectively restricted to uniform samples and at low temperatures.

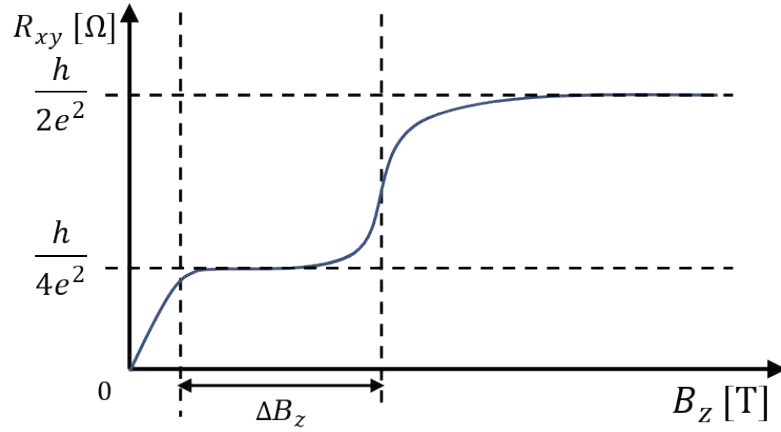


Figure 4.10: Representation of  $R_{xy}$  in an integer QHE with  $\nu = 2$  and  $\nu = 4$ .

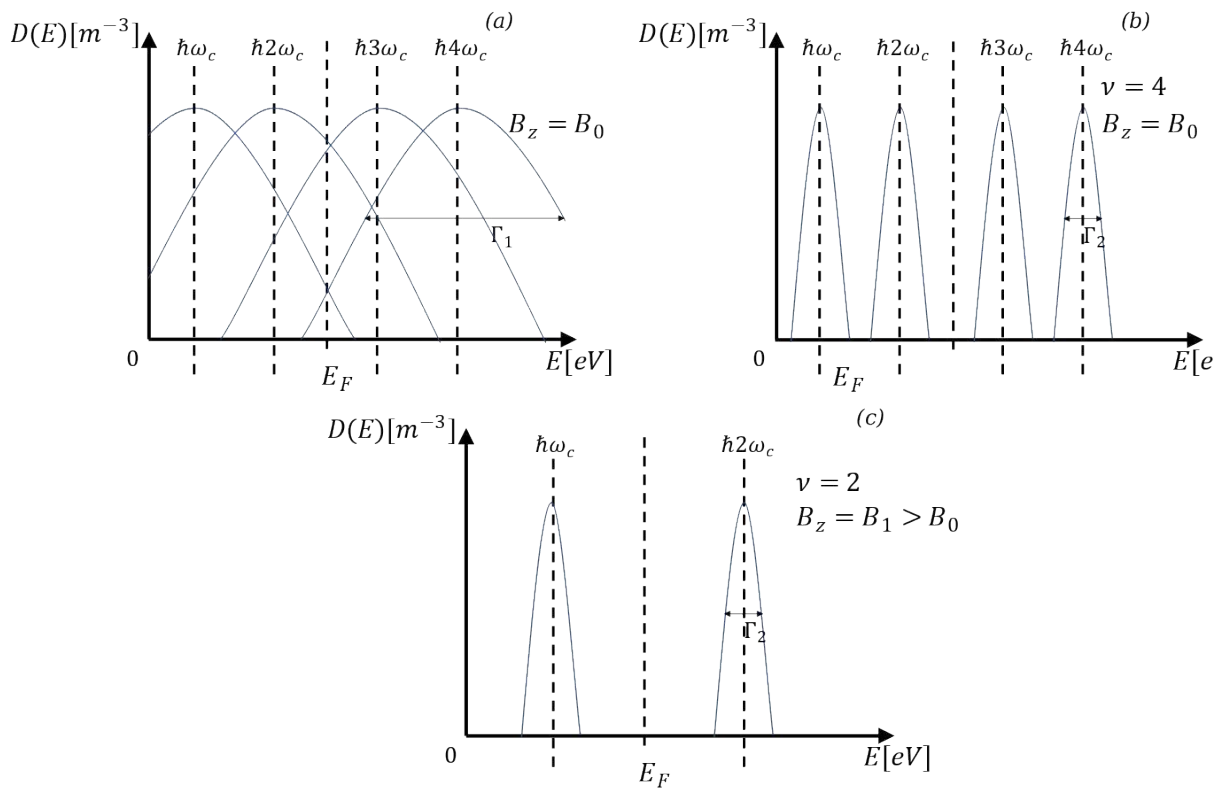


Figure 4.11: Representation of the density of electron energy states (a) for Landau splitting and high temperature, causing no visible plateau in  $R_{xy}$ , (b) Landau splitting at low temperature, causing a resistance plateau at  $R_{xy} = h/4 \cdot q^2$ , (c) Landau splitting at low temperature and a higher incidence field, causing a plateau at  $R_{xy} = h/2 \cdot q^2$ .

### 4.2.1.3 Quantum Hall effect in graphene

Due to the particular band structure of massless Dirac charges in graphene, the resulting Landau levels are not equidistant and are described by [15]–[17], as represented in Figure 4.12:

$$E_L(n) = v_f \cdot \sqrt{2jq\hbar B_z}, \quad (4.23)$$

where  $v_f=10^6$  m/s is the Fermi velocity. The formula for the Hall resistance follows a similar schema as (4.19), however, because of the particular band structure, one must take into account also for the valley degeneracy ( $g_s = 4$ ) and the Landau level  $E_L(0) = 0$ , therefore:

$$\nu = g_s \cdot \left(j + \frac{1}{2}\right). \quad (4.24)$$

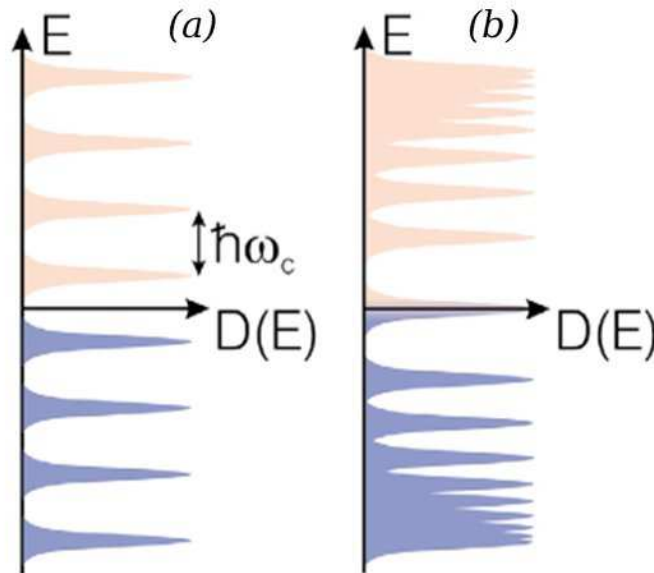


**Figure 4.12: Representation of Landau levels for (a) a standard material and (b) a Dirac massless electron material.**

Researchers have demonstrated both classical Hall and effects on graphene monocrystalline flakes [10], [15], [17], [18] and in CVD-grown graphene [19], [20]. Exfoliated monocrystalline graphene devices exhibit the best results, for example, *Novoselov et al.* demonstrated a room temperature QHE plateau at  $\nu = 2$  after applying a sufficient electric field doping [17]. CVD-grown graphene instead has usually worse performances due to grain-boundary scattering, a quantized value is usually detectable for fields in the range of 10-20 T for undoped graphene in temperature  $< 2$  K, however, more values can be visible when a strong electric-field doping is applied [19], [20].

## 4.2.2 Description of the experiment

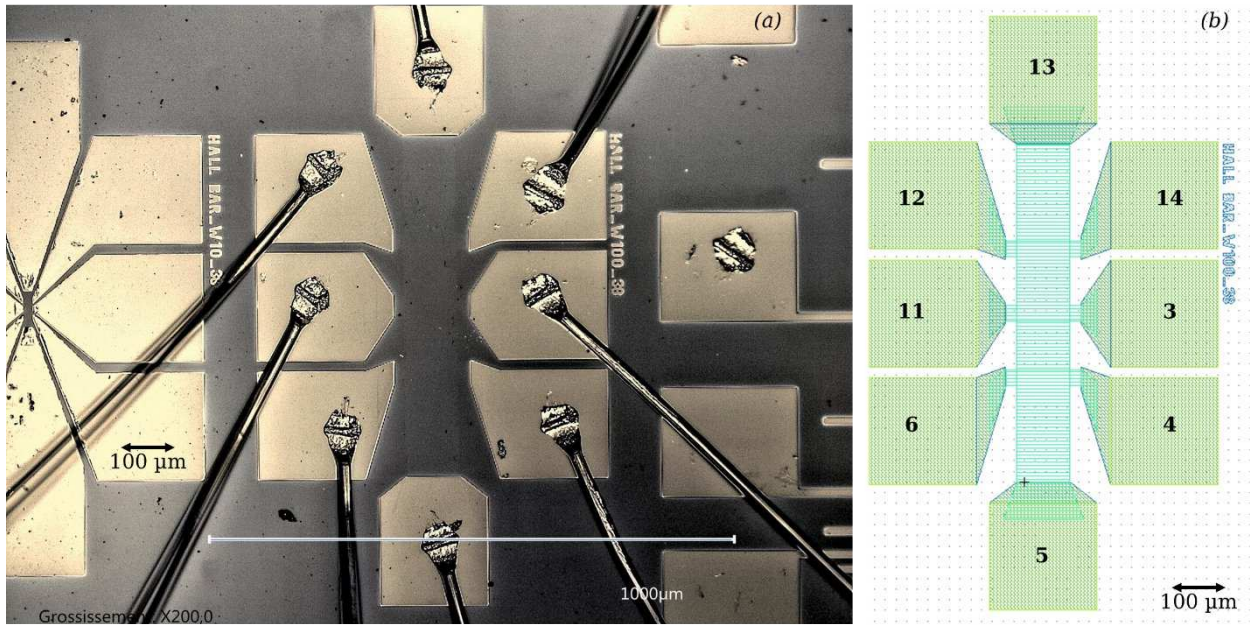


**Figure 4.13:** The  $100\ \mu\text{m} \times 630\ \mu\text{m}$  Hall bar used for characterization (a) microscope image and (b) layout.

The measurements were carried out through a Physical Property Measurement System by Quantum Design PPMS® [21] which was able to stimulate the sample with magnetic fields in the range of  $[-9, 9]$  T and cool down the sample down to the **temperature of 2 K**. The system was furnished with 3 IV bridges of which:

- bridge 1 was connected to an internal thermistor,
- bridge 2 was connected to provide  $I_x$  and measure  $V_y$ ,
- bridge 3 was connected to measure  $V_x$ .

The sample used was a  $100\ \mu\text{m} \times 630\ \mu\text{m}$  Hall bar, represented in Figure 4.13. It must be noted that, as a consequence of the pyroelectric nature of the substrate and the wide temperature range the device had to sustain, a significant electric field can arise which could damage the devices. Therefore, in order to reduce this risk as much as possible, the strategy adopted was to cool down the sample as slowly as possible, with a cooling rate of 0.01 K/min.

After the production, the sample had to be diced in pieces large around  $1\ \text{cm} \times 1\ \text{cm}$ , in order to fit on the sample holder without covering the pads. Before the measurement, a specific Hall bar was chosen with the aid of a microscope and resistive measurement, considering the devices not damaged during the cut, then the sample was placed on the sample holder and kept in place with the aid of a thermal grease, as represented in Figure 4.14(a), after that, the

corresponding contacts have been wired bonded to the holder (Figure 4.14(b)). The characterization was performed via the following steps:

1. Insert the sample in the machine;
2. Activate vacuum;
3. Connect the bridges to the device (Figure 4.14(c));
4. Measure and save the resistance of the Hall bar;
5. Select the optimal excitation ports for  $I_x$  and measure ports for  $V_x$  and  $V_y$ ;
6. Stabilize temperature to 295 K;
7. Sweep  $B_z$ , start Hall measures, save response, to calibrate the factor  $\alpha$  (4.18);
8. Cool down to 273 K;
9. Test the linearity of the contacts;
10. Sweep  $B_z$ , start Hall measures, save response, counter check  $\alpha$ ;
11. Cool down to 100 K, measure and save variations on  $R_{xx}$  and  $R_{xy}$  at  $B_z = 0$ ;
12. Sweep  $B_z$ , start Hall measures, save response;
13. Cool down to 10 K;
14. Sweep  $B_z$ , start Hall measures, save response;
15. Cool down to 5 K;
16. Sweep  $B_z$ , start Hall measures, save response;
17. Cool down to 2 K;
18. Sweep  $B_z$ , start Hall measures, save response.

**Table 4-3: Room-temperature DC resistance of the measured device (applied current 5  $\mu\text{A}$ ).**

| <b>I+</b> | <b>I-</b> |           |           | <b>V+</b>     |               |               |               |
|-----------|-----------|-----------|-----------|---------------|---------------|---------------|---------------|
| <b>13</b> | <b>5</b>  | /         |           | <b>3</b>      | <b>6</b>      | <b>12</b>     | <b>14</b>     |
| //        | //        | <b>V-</b> | <b>3</b>  | -             | 21 $\Omega$   | 1589 $\Omega$ | 1600 $\Omega$ |
| //        | //        |           | <b>4</b>  | 20.4 $\Omega$ | 0.02 $\Omega$ | -             | 1591 $\Omega$ |
| //        | //        |           | <b>6</b>  | -             | -             | 1613 $\Omega$ | -             |
| //        | //        |           | <b>14</b> | -             | -             | 30.6 $\Omega$ | -             |

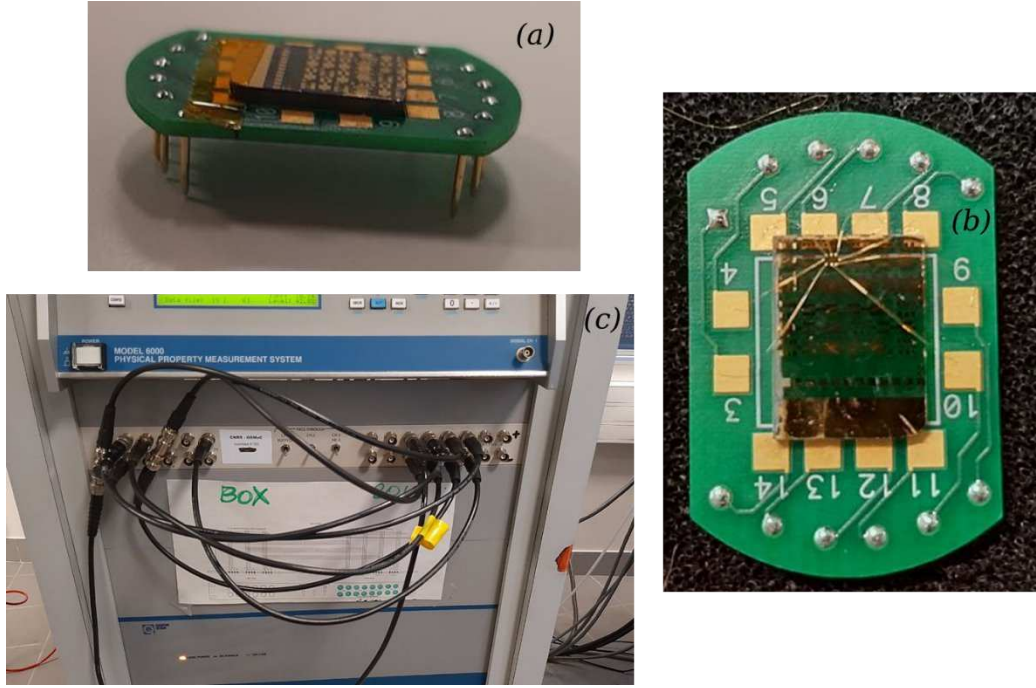


*Figure 4.14: Image of the sample transferred on the sample holder (a) before (b) and after wire-bonding. Figure (c) shows the connection setup to the bridges.*

*Table 4-4: Connections for the measurement setup, N.A. stays for Not Available.*

| Bridge 2 |    |    |    | Bridge 3 |      |    |    |
|----------|----|----|----|----------|------|----|----|
| I+       | I- | V+ | V- | I+       | I-   | V+ | V- |
| 13       | 5  | 12 | 14 | N.A.     | N.A. | 3  | 14 |

In reference to Figure 4.13(b), the measured resistance are the ones shown in Table 4-3 and the final connections to bridge 2 and bridge 3 are described in Table 4-4. The polarity of the voltmeter in Bridge 2 and Bridge 3 and of the current source in Bridge 2 were chosen so that hole doping would result in  $R_{xy} > 0$  for  $B_z > 0$  and viceversa for  $B_z < 0$ .

Afterward, the vacuum was activated and a certain amount of time was waited until it stabilized to the target value. The presence of a diode barrier was checked at the temperature of 273 K by exciting the sample via a current of  $\pm 5 \mu\text{A}$ , as shown in Figure 4.15(c), and the results for  $R_{xy}$  and  $R'_{xx}$  are shown in Figure 4.15(a) and Figure 4.15(b) respectively. The results show a small resistance variation for both  $R_{xy}$  and  $R'_{xx}$ , however, as the increasing trend is common

to both the  $+5 \mu\text{A}$  and  $-5 \mu\text{A}$  branches and is quite continuous in between, this is rather an indication of dopant gases still desorbing from the sample.

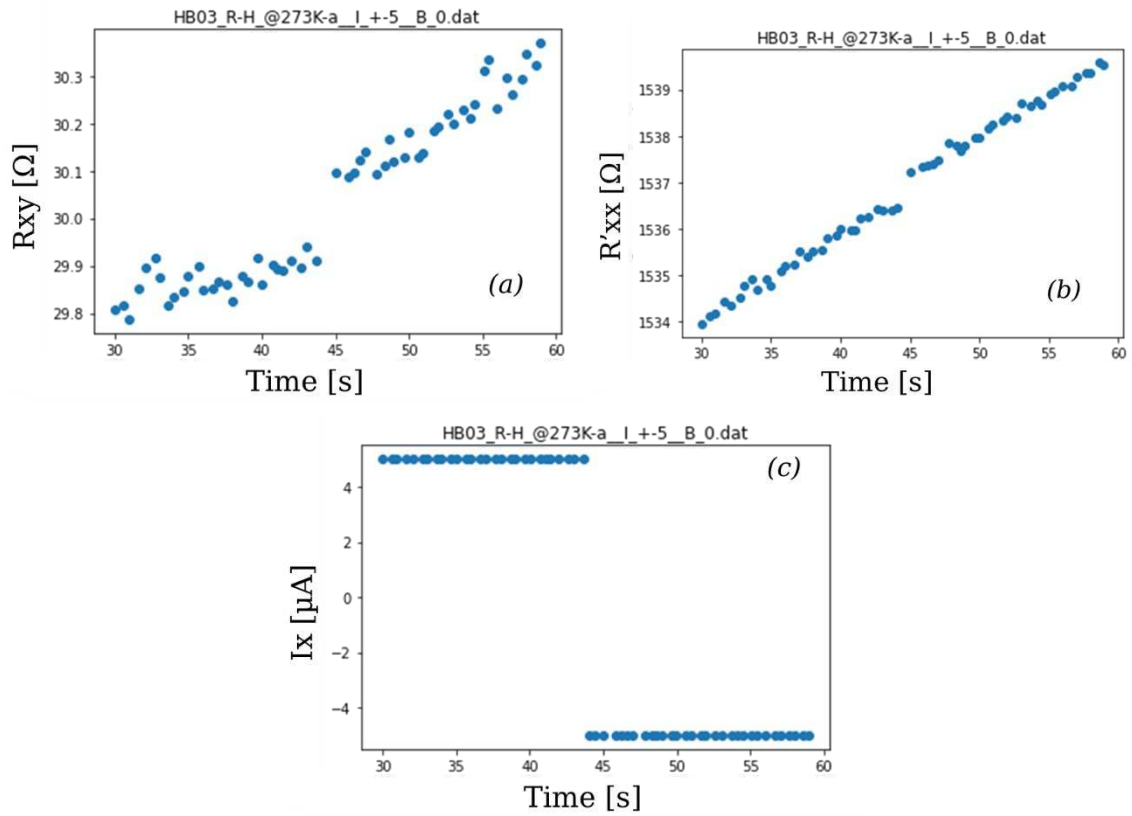


*Figure 4.15: Measurement of (a)  $R_{xy}$  and (b)  $R'_{xx}$  under  $B_z = 0$  and (c) current stimulus  $I_x = \pm 5 \mu\text{A}$ .*

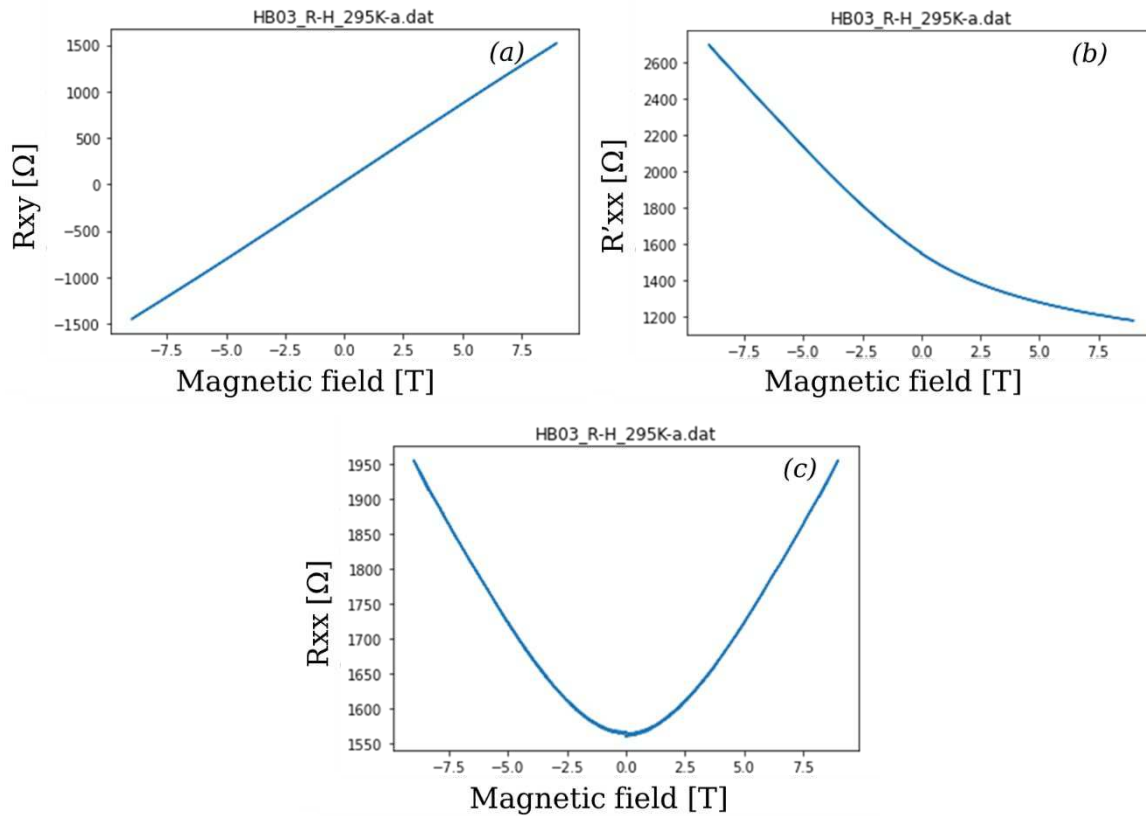


**Figure 4.16:** Measurement at the temperature of 295 K of (a) the Hall resistance  $R_{xy}$ , (b) the uncorrected resistance  $R'_{xx}$  and (c) the corrected  $R_{xx}$ . The excitation current was 5  $\mu$ A and the correction factor used was  $\alpha = 0.5103$ .

The **room-temperature** characterization is shown in Figure 4.16, through that, it could be found  $\alpha = -0.5103$ , the 0-field resistivity  $\rho_{xx} = 1044 \text{ } \Omega/\square$ , carrier density  $n_s = 3.75 \cdot 10^{12} \text{ cm}^{-2}$  and carrier mobility  $\mu_x = 1594 \text{ cm}^2/\text{Vs}$ . The relatively big value of  $\alpha$  was probably caused by a difference in the resistivity of the device between the left and the right side in between contacts. This was possibly confirmed via a Raman mapping performed after the Hall effect measurements, shown in Section 3.1.4, which revealed some scattering centers on the left side of the device.

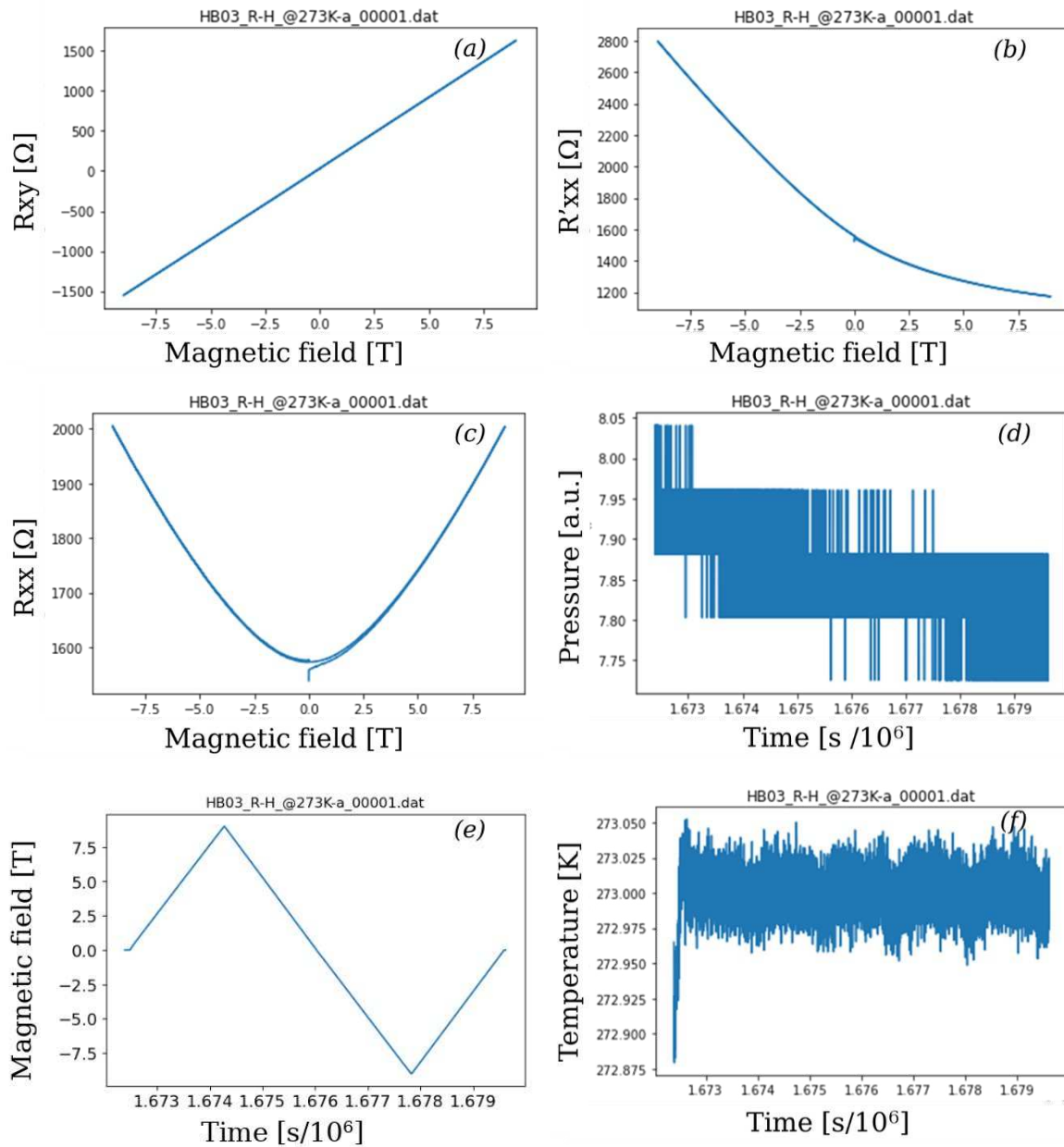


**Figure 4.17:** Measurement at the temperature of 273 K of (a) the Hall resistance  $R_{xy}$ , (b) the uncorrected resistance  $R'_{xx}$  and (c) the corrected  $R_{xx}$ , (d) the local pressure vs. time, (e) the applied magnetic field  $B_z$  vs. time and (f) current temperature vs. time. The excitation current was 5  $\mu$ A and the correction factor used was  $\alpha = 0.5103$ .

The characterization at the temperature 273 K is shown in Figure 4.17 and through that it was found in a 0-field resistivity  $\rho_{xx} = 1051 \Omega/\square$ , carrier density  $n_s = 3.5 \cdot 10^{12} \text{ cm}^{-2}$  and carrier mobility  $\mu_x = 1696 \text{ cm}^2/\text{Vs}$ . Interestingly, the resistance in Figure 4.17(c) experiences a transitory effect, increasing slightly even during while  $B_z = 0$ . However, this effect quickly

dissipated, and the cause was probably a temperature difference between the thermistor and the actual sample or electric-field doping caused by the pyroelectric effect of the substrate.

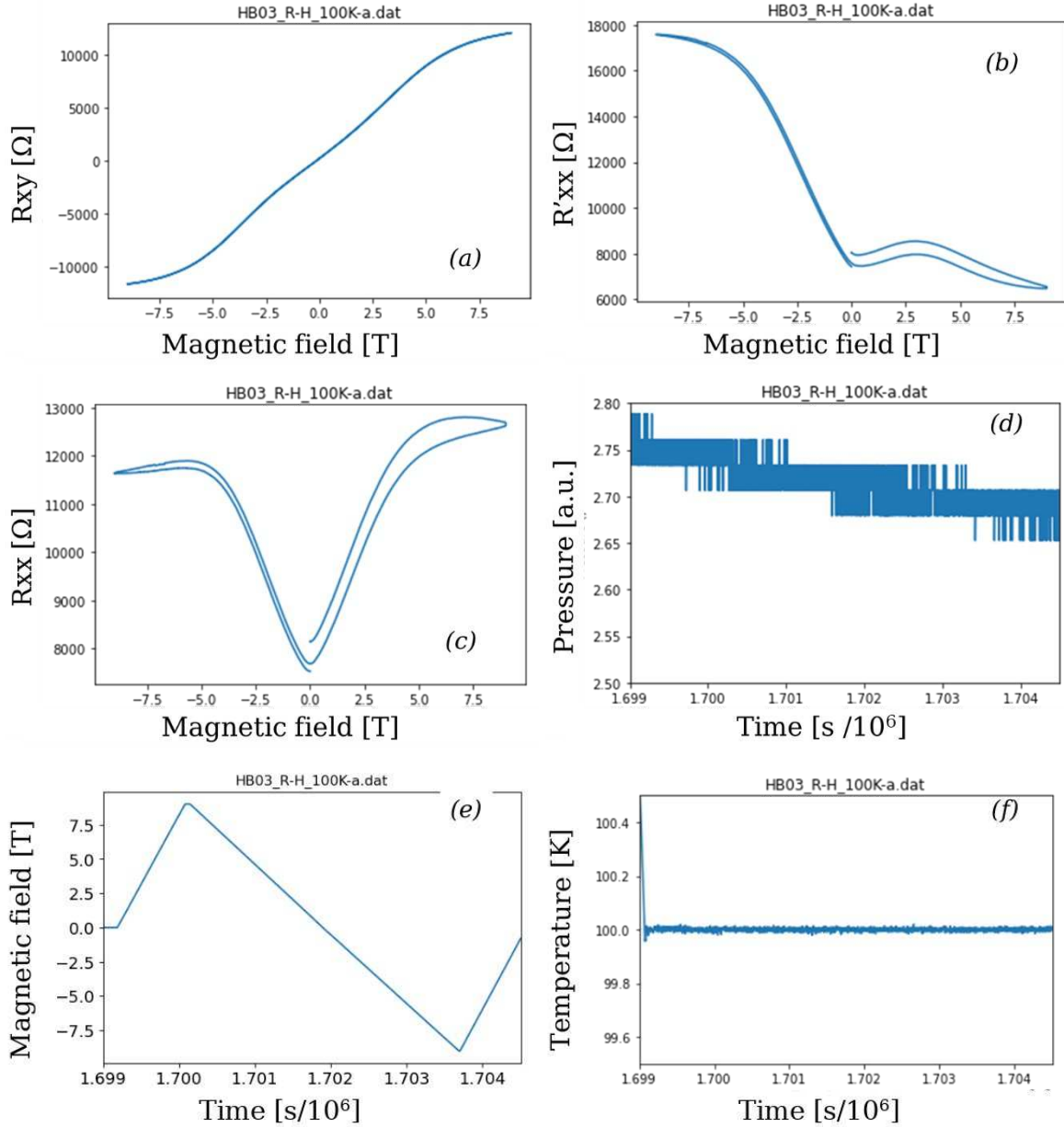


**Figure 4.18:** Measurement at the temperature of 100 K of (a) the Hall resistance  $R_{xy}$ , (b) the uncorrected resistance  $R'_{xx}$  and (c) the corrected  $R_{xx}$ , (d) the local pressure vs. time, (e) the applied magnetic field  $B_z$  vs. time and (f) current temperature vs. time. The excitation current was 5  $\mu$ A and the correction factor used was  $\alpha = 0.5103$ .

The characterization at the temperature **100 K** is shown in Figure 4.18, through it was found a 0-field resistivity  $\rho_{xx} = 5027 \Omega/\square$ , the carrier density and mobility were found by considering the range of  $B_z = [-0.3, 0.3]$  T, distant from quantum effects, returning respectively  $n_s = 4.08 \cdot 10^{11} \text{ cm}^{-2}$  and  $\mu_x = 3049 \text{ cm}^2/\text{Vs}$ .

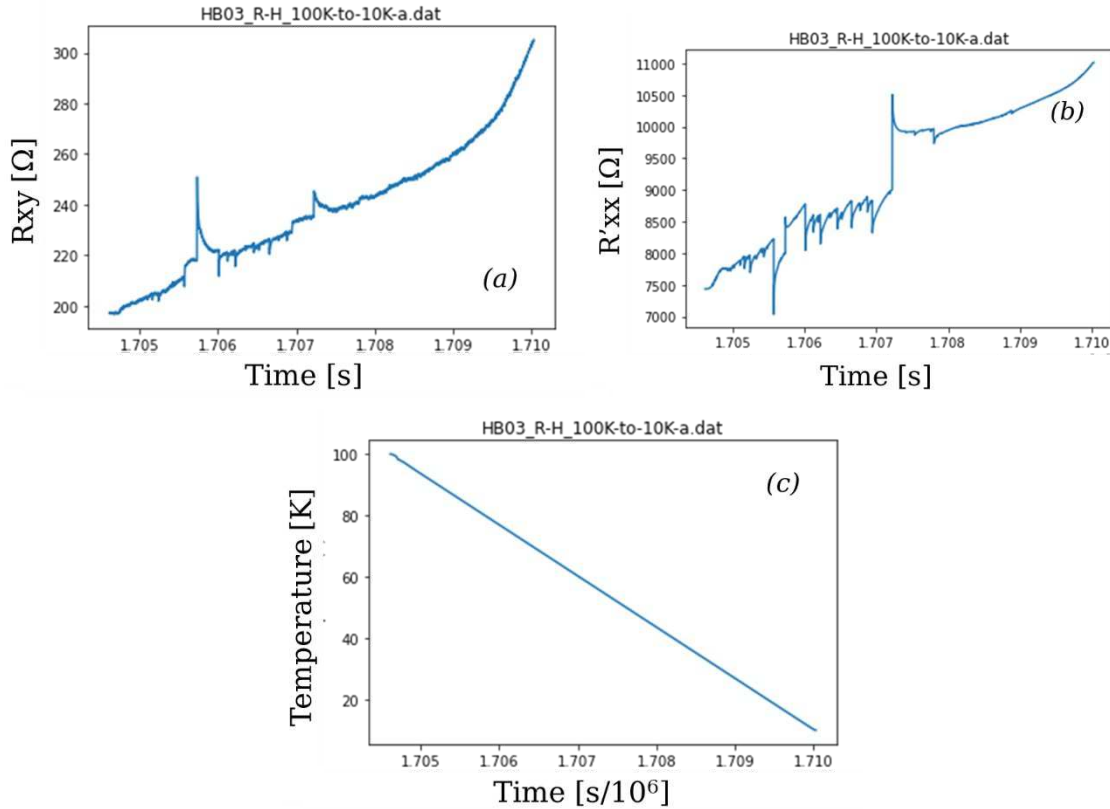


**Figure 4.19: Measurement of (a)  $R_{xy}$  and (b)  $R'_{xx}$  under  $B_z = 0$  and  $I_x = \pm 5 \mu\text{A}$  (c) during the cooling from 100 K to 10 K.**

In the data, a significant hysteresis effect is visible, especially in the portion corresponding to  $B_z > 0$ . This could be due to several factors, for example, some residual doping from the big temperature difference and the pyroelectric could not have been completely dissipated. In order to confirm this fact, the resistance was measured while cooling down the temperature from 100 K to 10 K (Figure 4.19(c)), at  $B_z = 0$ , Figure 4.19(a) and Figure 4.19(b) show the captured data, which display **several sharp peaks due to the accumulation of charges and sudden discharges**. The sharp discharges suggest that, even considering all of the precautions taken, the pyroelectrically generated fields during cooling were strong enough to overcome either the vacuum or the dielectric substrate. An additional reason might be found

from the variation in local pressure during the measurement Figure 4.18(d), in particular, the pressure variation is somewhat consistent with the variation in resistance between  $B_z > 0$  and  $B_z < 0$ .

Either way, the amplitude of the hysteresis was decreasing over time, accordingly with the hypothesis presented, and the effects were expected to decrease in the experiments to follow, which was then confirmed in the measurement of 5 K and 2 K.

The characterization at the temperature **10 K** is shown in Figure 4.20, through it was found a 0-field resistivity  $\rho_{xx} = 7087 \Omega/\square$ , the carrier density and mobility were found through the range of  $B_z = [-0.3, 0.3]$  T, distant from quantum effects, returning respectively  $n_s = 3.73 \cdot 10^{11} \text{ cm}^{-2}$  and  $\mu_x = 2364 \text{ cm}^2/\text{Vs}$ . Interestingly, Figure 4.20(c) still shows a considerable hysteresis which is compatible with what discussed above for the 100 K measures.

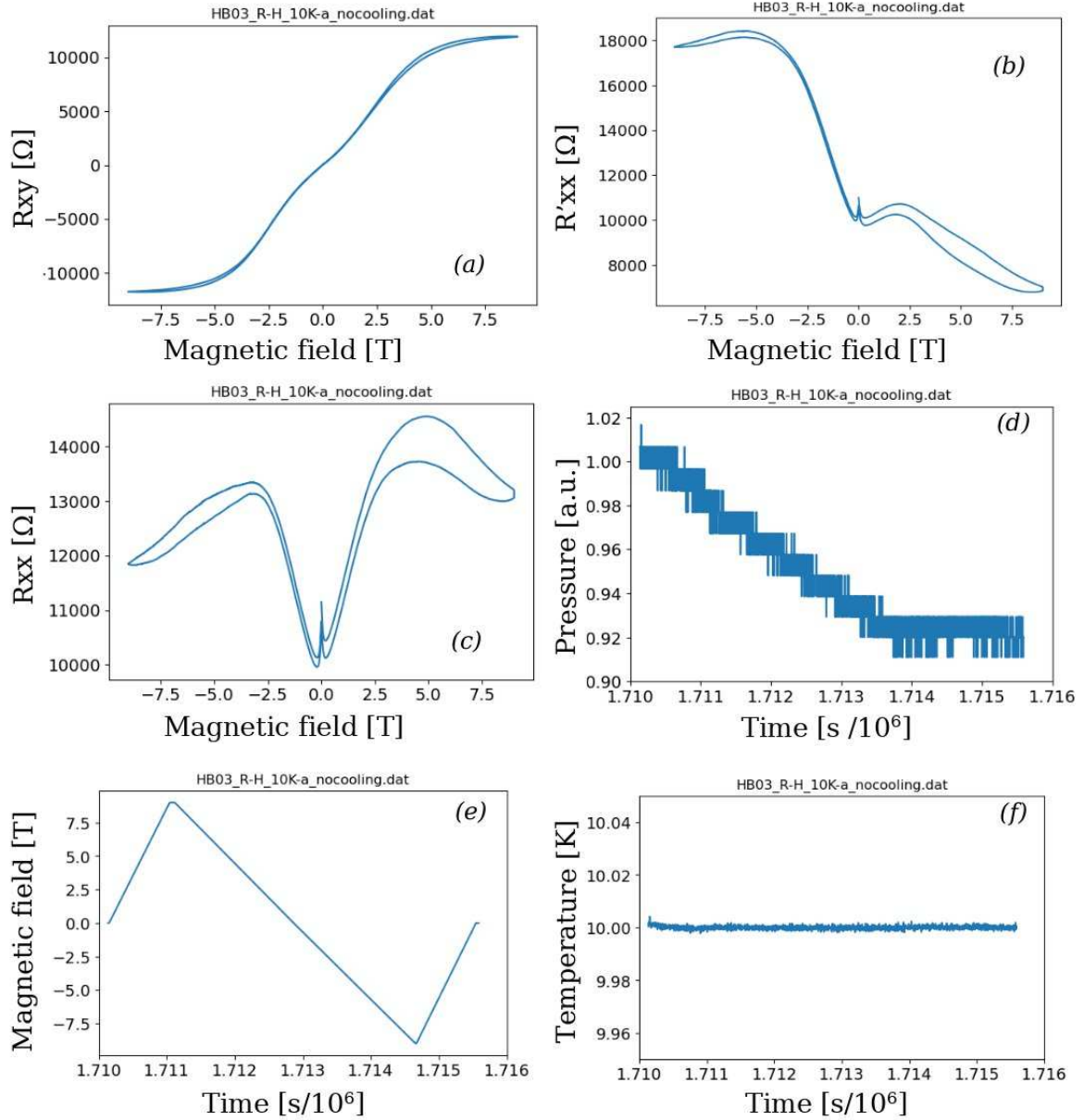


**Figure 4.20:** Measurement at the temperature of 10 K of (a) the Hall resistance  $R_{xy}$ , (b) the uncorrected resistance  $R'_{xx}$  and (c) the corrected  $R_{xx}$ , (d) the local pressure vs. time, (e) the applied magnetic field  $B_z$  vs. time and (f) current temperature vs. time. The excitation current was 5  $\mu$ A and the correction factor used was  $\alpha = 0.5103$ .

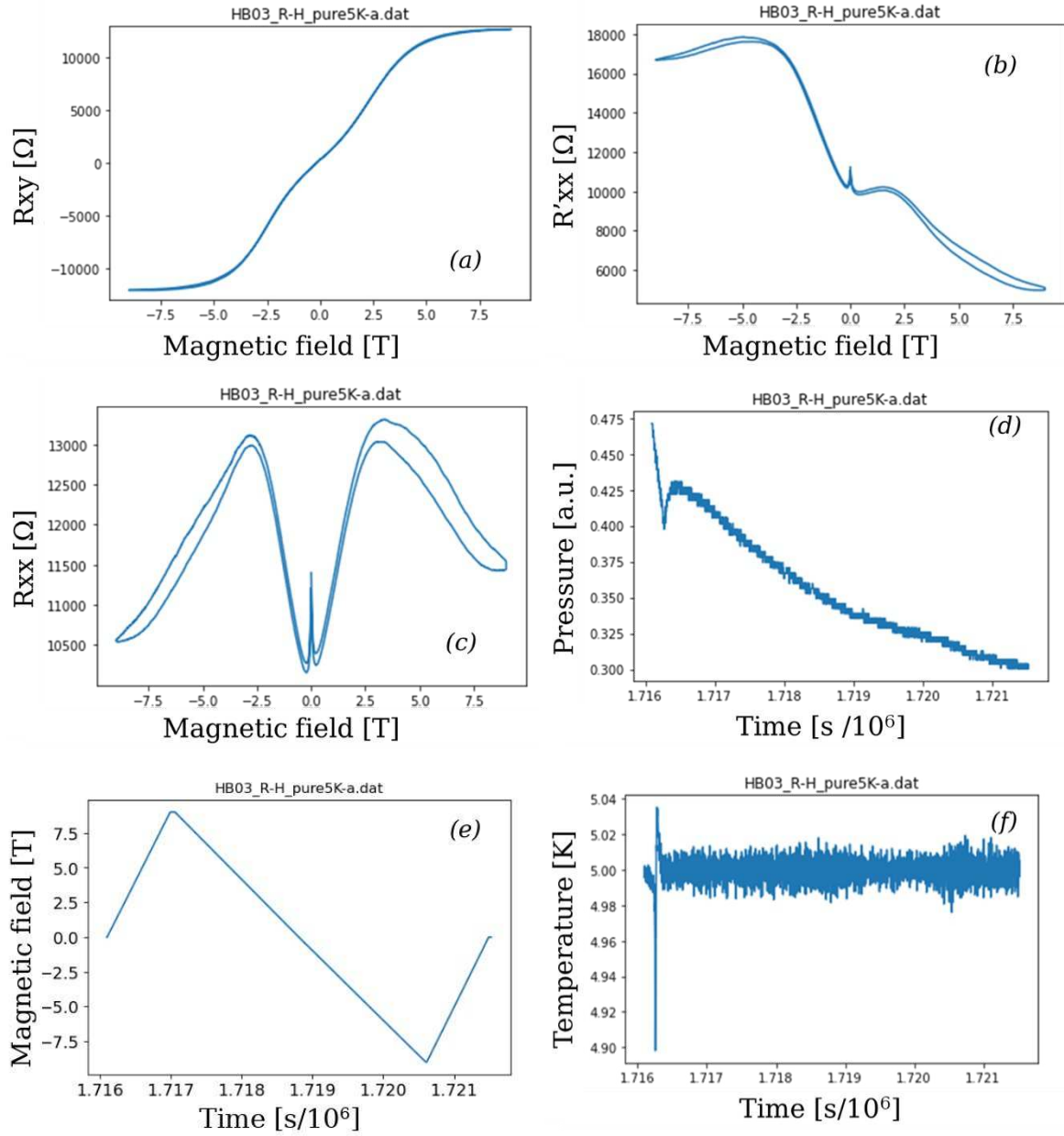


**Figure 4.21: Measurement at the temperature of 5 K of (a) the Hall resistance  $R_{xy}$ , (b) the uncorrected resistance  $R'_{xx}$  and (c) the corrected  $R_{xx}$ , (d) the local pressure vs. time, (e) the applied magnetic field  $B_z$  vs. time and (f) current temperature vs. time. The excitation current was 5  $\mu$ A and the correction factor used was  $\alpha = 0.5103$ .**

The characterization at the temperature **5 K** is shown in Figure 4.21, it was found a 0-field resistivity  $\rho_{xx} = 7488 \Omega/\square$ , the carrier density and mobility were found through the range of  $B_z = [-0.3, 0.3]$  T, distant from quantum effects, returning  $n_s = 3.55 \cdot 10^{11} \text{ cm}^{-2}$  and  $\mu_x = 2352 \text{ cm}^2/\text{Vs}$ .

The sharp rise in  $R_{xx}$  shown in Figure 4.20(c) is from the measurements during the cool-down from 100 K. Interestingly, Figure 4.20(c) still shows a considerable hysteresis which is compatible with what discussed above for the 100 K measures.

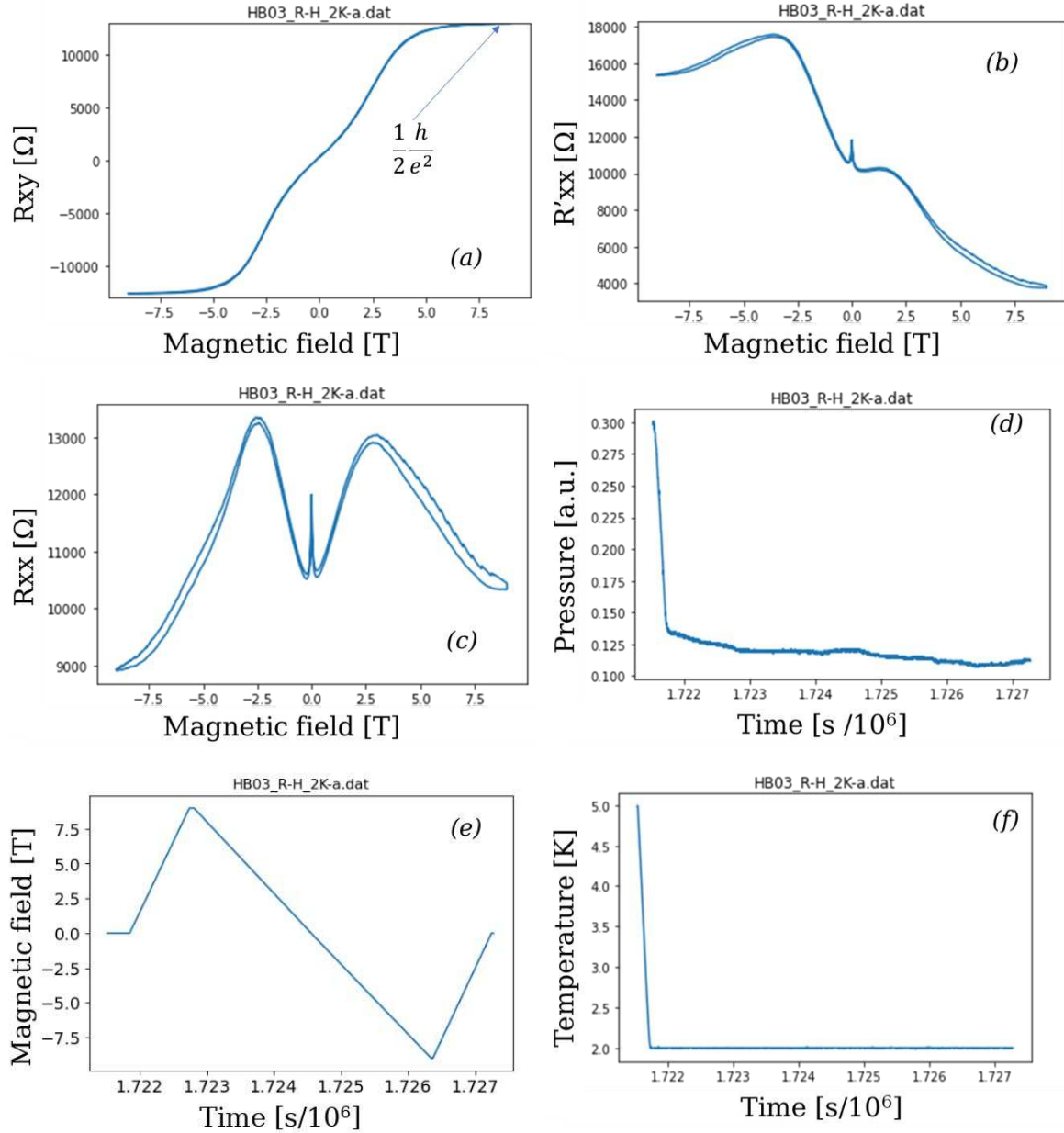


**Figure 4.22:** 1<sup>st</sup> measurement at the temperature of 2 K of (a) the Hall resistance  $R_{xy}$ , (b) the uncorrected resistance  $R'_{xx}$  and (c) the corrected  $R_{xx}$ , (d) the local pressure vs. time, (e) the applied magnetic field  $B_z$  vs. time and (f) current temperature vs. time. The excitation current was 5 μA and the correction factor used was  $\alpha = 0.5103$ .

The **1<sup>st</sup> characterization at the temperature 2 K** is shown in Figure 4.22, it was found a 0-field resistivity  $\rho_{xx} = 7733 \Omega/\square$ , the carrier density and mobility were found through the range of  $B_z = [-0.3, 0.3]$  T, distant from quantum effects, returning respectively  $n_s = 3.48 \cdot 10^{11} \text{ cm}^{-2}$  and  $\mu_x = 2395 \text{ cm}^2/\text{Vs}$ . The QHE plateau of  $\nu = 2$  was found at  $B_z = 9$  T, while the Hall resistance value at  $B_z = -9$  T is within 3%.

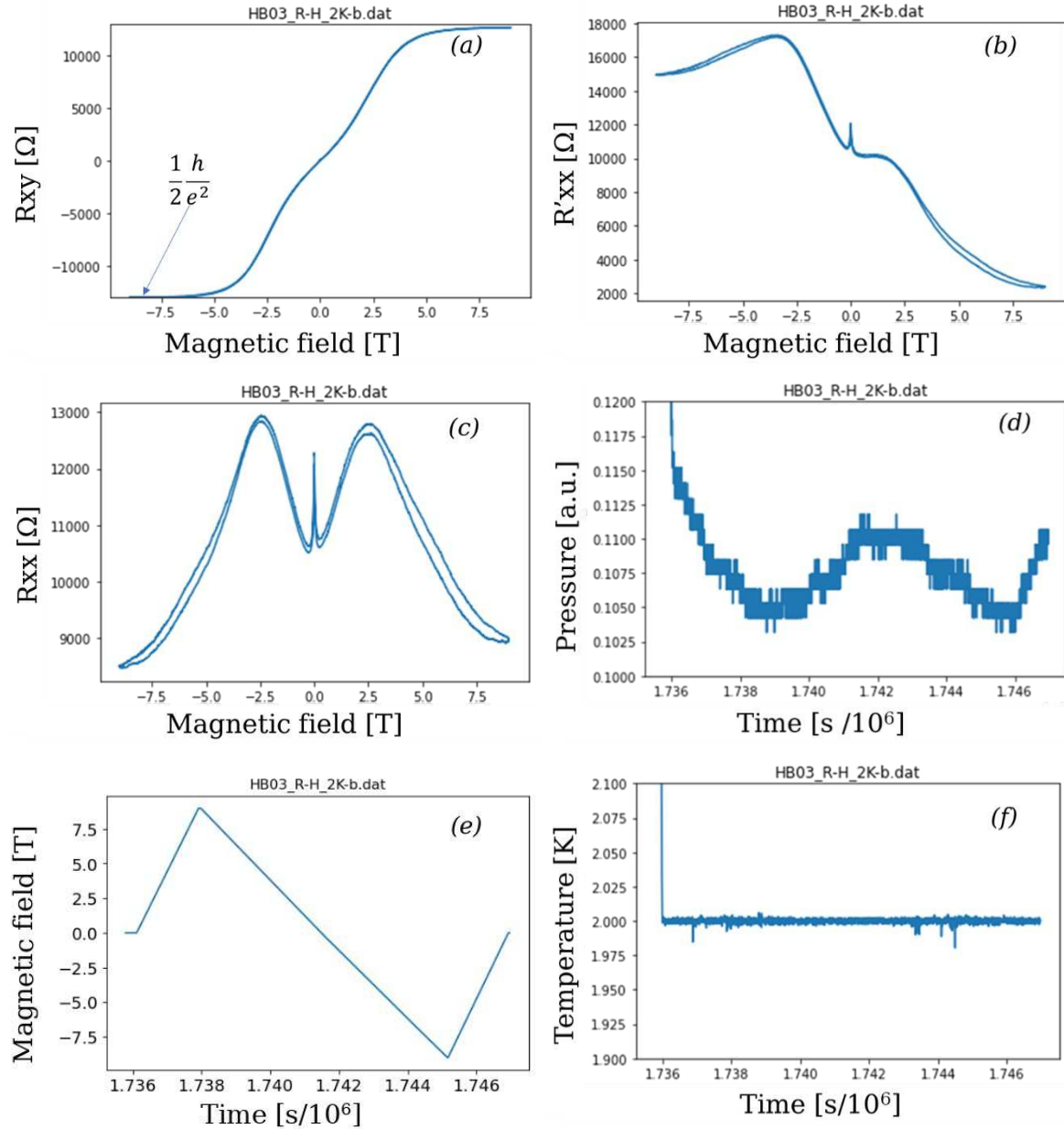


**Figure 4.23:** 2<sup>nd</sup> measurement at the temperature of 2 K of (a) the Hall resistance  $R_{xy}$ , (b) the uncorrected resistance  $R'_{xx}$  and (c) the corrected  $R_{xx}$  (d) the local pressure vs. time, (e) the applied magnetic field  $B_z$  vs. time and (f) current temperature vs. time. The excitation current was 5  $\mu\text{A}$  and the correction factor used was  $\alpha = 0.5103$ .

The 2<sup>nd</sup> characterization at the temperature 2 K is shown in Figure 4.23, it was found a 0-field resistivity  $\rho_{xx} = 8047 \Omega/\square$ , the carrier density and mobility were found through the range of  $B_z = [-0.3, 0.3]$  T, distant from, quantum effects, returning respectively  $n_s = 3.24 \cdot 10^{11} \text{ cm}^{-2}$  and  $\mu_x = 2395 \text{ cm}^2/\text{Vs}$ . The QHE plateau of  $\nu = 2$  was found at  $B_z = -9$  T, while the Hall resistance value at  $B_z = 9$  T is within 3%.

This time the hysteresis effect is considerably reduced, compatibly to previously discussed. Interestingly, it should also be noted that its maximum corresponds with the valleys in pressure Figure 4.23(d).

### 4.3 Discussion of the results

The characterization of the resistivity through TLM demonstrates the possibility of tuning the resistivity of graphene through processing, by choosing opportunely the process photoresists it was possible to **tune the resistivity of the graphene from  $\sim 600\text{-}700 \Omega/\square$  using the negative AZnLOF photoresist to  $1400\text{-}2000 \Omega/\square$  using the positive S1813 photoresist, closer to the optimal value for AE coupling with YX-128° LiNbO<sub>3</sub> of  $800 \text{ k}\Omega/\square$ .**

The reported values of the effective channel lengths  $L_{eCH}$  and contact resistivity  $\rho_c$  are in good agreement with the current state of the art, indicating a good quality of the process and suggesting that, when necessary to reduce the overall contact resistance  $R_c$ , the designs of the layouts should maximize both the overlap between the graphene and the metal contacts and the contact length.

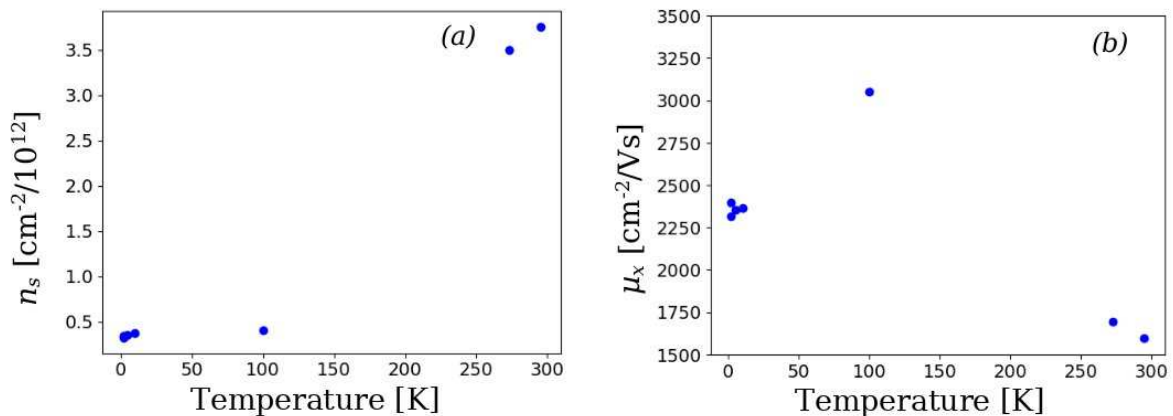


**Figure 4.24: Extracted values of (a) the density of charge carriers and (b) their mobility vs. temperature.**

The results from CHE characterization are summarized in Figure 4.24(a) and Figure 4.24(b). The data highlights a **charge mobility higher than the value of 1500 cm<sup>2</sup>/Vs** reported for graphene on Si/SiO<sub>2</sub> substrates from the same manufacturer [8]. The sign of the Hall voltage  $V_{xy}$  reveals that the device is **p-doped with a carrier density > 3.2 · 10<sup>11</sup> cm<sup>-2</sup>**.

A Raman characterization of the Hall bar device performed (see Section 3.1.4) shows the presence of some defects near on the left side of the Hall bar (with reference of Figure 4.13), which explains the relatively large value of  $\alpha = 0.501$ .

The QHE measurements revealed the presence of a  $\frac{1}{2} \cdot \frac{h}{q^2}$  **valley for  $B_z \sim 9$  T** at the temperature of **2 K**, in good agreement with other experiments of undoped CVD graphene. However, the data showed a **significant hysteresis effect** after cooling down the samples, this effect dissipated partially over time and was likely because of the pyroelectric and ferroelectric nature of the substrate.

## 4.4 References

- [1] A. Goetzberger and R. M. Scarlett, ‘RESEARCH AND INVESTIGATION OF INVERSE EPITAXIAL UHF POWER TRANSISTORS’, Air Force Atomic Laboratory, Wright-Patterson Air Force Base, Ohio, A1-TOR-64–207, Sep. 1964. Accessed: Sep. 16, 2023. [Online]. Available: <https://apps.dtic.mil/sti/citations/AD0605376>
- [2] H. H. Berger, ‘Models for contacts to planar devices’, *Solid-State Electronics*, vol. 15, no. 2, pp. 145–158, Feb. 1972, doi: 10.1016/0038-1101(72)90048-2.
- [3] R. S. Sundaram *et al.*, ‘The Graphene–Gold Interface and Its Implications for Nanoelectronics’, *Nano Lett.*, vol. 11, no. 9, Art. no. 9, Sep. 2011, doi: 10.1021/nl201907u.
- [4] S. Venica, F. Driussi, A. Gahoi, P. Palestri, Lemme, Max C, and L. Selmi, ‘On the Adequacy of the Transmission Line Model to Describe the Graphene–Metal Contact Resistance’, *IEEE Transactions on Electron Devices*, vol. 65, no. 4, pp. 1589–1596, 2018.
- [5] W. S. Leong, H. Gong, and J. T. L. Thong, ‘Low-Contact-Resistance Graphene Devices with Nickel-Etched-Graphene Contacts’, *ACS Nano*, vol. 8, no. 1, pp. 994–1001, Jan. 2014, doi: 10.1021/nn405834b.

- [6] Keithley Instruments, ‘Model 6220 DC Current Source Model 6221 AC and DC Current Source Users Manual’. Oct. 2008. [Online]. Available: [https://download.tek.com/manual/622x-900-01%20\(C%20-%20Oct%202008\)\(User\).pdf](https://download.tek.com/manual/622x-900-01%20(C%20-%20Oct%202008)(User).pdf)
- [7] Keithley Instruments, ‘Model 2182A Nanovoltmeter User’s Manual’. Jul. 2022. [Online]. Available: [https://download.tek.com/manual/2182A-900-01C\\_July\\_2022\\_User.pdf](https://download.tek.com/manual/2182A-900-01C_July_2022_User.pdf)
- [8] Graphenea, Inc., ‘Graphenea Monolayer Graphene on Polymer Film Datasheet’. Accessed: Oct. 10, 2022. [Online]. Available: [https://cdn.shopify.com/s/files/1/0191/2296/files/Graphenea\\_Monolayer\\_Graphene\\_on\\_Polymer\\_Film\\_Datasheet\\_02-16-2022.pdf?v=1645025331](https://cdn.shopify.com/s/files/1/0191/2296/files/Graphenea_Monolayer_Graphene_on_Polymer_Film_Datasheet_02-16-2022.pdf?v=1645025331)
- [9] H. L. Stormer, ‘Nobel Lecture: The fractional quantum Hall effect’, *Rev. Mod. Phys.*, vol. 71, no. 4, pp. 875–889, Jul. 1999, doi: 10.1103/RevModPhys.71.875.
- [10] R. Ribeiro-Palau *et al.*, ‘Quantum Hall resistance standard in graphene devices under relaxed experimental conditions’, *Nature Nanotech*, vol. 10, no. 11, Art. no. 11, Nov. 2015, doi: 10.1038/nnano.2015.192.
- [11] B. Huckestein, ‘Scaling theory of the integer quantum Hall effect’, *Rev. Mod. Phys.*, vol. 67, no. 2, pp. 357–396, Apr. 1995, doi: 10.1103/RevModPhys.67.357.
- [12] K. von Klitzing, ‘The quantized Hall effect’, *Rev. Mod. Phys.*, vol. 58, no. 3, pp. 519–531, Jul. 1986, doi: 10.1103/RevModPhys.58.519.
- [13] H. L. Stormer, D. C. Tsui, and A. C. Gossard, ‘The fractional quantum Hall effect’, *Rev. Mod. Phys.*, vol. 71, no. 2, pp. S298–S305, Mar. 1999, doi: 10.1103/RevModPhys.71.S298.
- [14] H. L. Störmer, R. Dingle, A. C. Gossard, W. Wiegmann, and M. D. Sturge, ‘Two-dimensional electron gas at a semiconductor-semiconductor interface’, *Solid State Communications*, vol. 29, no. 10, pp. 705–709, Mar. 1979, doi: 10.1016/0038-1098(79)91010-X.
- [15] Y. Zhang, Y.-W. Tan, H. L. Stormer, and P. Kim, ‘Experimental observation of the quantum Hall effect and Berry’s phase in graphene’, *Nature*, vol. 438, no. 7065, Art. no. 7065, Nov. 2005, doi: 10.1038/nature04235.
- [16] P. Cea, ‘The quantum hall effect in graphene’, *Mod. Phys. Lett. B*, vol. 26, no. 13, p. 1250084, May 2012, doi: 10.1142/S0217984912500844.
- [17] K. S. Novoselov *et al.*, ‘Room-Temperature Quantum Hall Effect in Graphene’, *Science*, vol. 315, no. 5817, pp. 1379–1379, Mar. 2007, doi: 10.1126/science.1137201.
- [18] B. T. Schaefer *et al.*, ‘Magnetic field detection limits for ultraclean graphene Hall sensors’, *Nat Commun*, vol. 11, no. 1, Art. no. 1, Aug. 2020, doi: 10.1038/s41467-020-18007-5.

- [19] H. Cao *et al.*, ‘Electronic transport in chemical vapor deposited graphene synthesized on Cu: Quantum Hall effect and weak localization’, *Applied Physics Letters*, vol. 96, no. 12, p. 122106, Mar. 2010, doi: 10.1063/1.3371684.
- [20] T. K. Chau, D. Suh, and H. Kang, ‘Quantum Hall Effect across Graphene Grain Boundary’, *Materials*, vol. 15, no. 1, Art. no. 1, Jan. 2022, doi: 10.3390/ma15010008.
- [21] The Quantum Design PPMS, ‘PPMS® Physical Measurement Property System’. Accessed: Sep. 16, 2023. [Online]. Available: <https://www.qdusa.com/products/ppms.html>



## Contents of the chapter:

|   |     |
|---|-----|
| 5 Acousto-Electric current measurements.....  | 154 |
| 5.1 Introduction.....   | 154 |
| 5.2 Paper : Acousto-electric measurements at 2.5 GHz on graphene transferred onto YX128°-LiNbO <sub>3</sub> ..... | 154 |
| 5.2.1 Abstract.....   | 154 |
| 5.2.2 Introduction.....   | 155 |
| 5.2.3 Microfabrication .....  | 156 |
| 5.2.4 Results.....  | 159 |
| 5.2.5 Discussion and concluding remarks.....  | 163 |
| 5.3 Follow-up on AE Characterization.....   | 167 |
| 5.3.1 Characterization at 2.0 GHz and 3 GHz.....  | 168 |
| 5.3.2 Saturation power and breakdown of the IDTs.....   | 172 |
| 5.3.3 Automation of the setup.....  | 175 |
| 5.4 Conclusion.....   | 177 |
| 5.5 References.....   | 177 |

## 5 Acousto-Electric current measurements

### 5.1 Introduction

This chapter presents the experiments I performed for the characterization of the acousto-electronic coupling of graphene on LiNbO<sub>3</sub>. The made with surface acoustic waves (SAW) delay-line at 2.5 GHz measured with graphene on LiNbO<sub>3</sub>. These results are the object of a paper that I reproduce and where you can find all the details and bibliographic references. This work as compared to literature present several breakthroughs:

- Method of production,
- Experimental set-up
- Operation frequency higher than any other previously reported work thanks to graphene.

Finally, Section 5.3 presents the other measurements performed in the range 1.0 GHz – 3.5 GHz and a stress analysis of the transducers.

This work paves the way for the acoustic convolver presented in Chapter 6.

### 5.2 Paper : Acousto-electric measurements at 2.5 GHz on graphene transferred onto YX128°-LiNbO<sub>3</sub>

#### 5.2.1 Abstract

Surface acoustic wave delay lines with an operational frequency of 2.5 GHz have been designed to measure the acoustoelectronic transport of carriers in graphene transferred onto YX128°-LiNbO<sub>3</sub> piezoelectric substrate. The monolayer of graphene on LiNbO<sub>3</sub> presented sheet resistance in the range of **733 to 1230 Ω/□** and ohmic contact resistivity **with gold of 1880 to 5200 Ωμm**. The measurements with different interaction lengths on graphene bars have allowed the extraction of carrier absorption and mobility parameters from the acousto-electric current. Graphene presented higher acousto-electronic interaction in the GHz range than previously reported values in the range of 100s MHz with carrier absorption losses of 109 m<sup>-1</sup> and mobility for acoustically generated charges of 101 cm<sup>2</sup>/Vs.

## 5.2.2 Introduction

The development of micro-acoustic technologies have allowed major breakthroughs in both the miniaturization and performances of analog filters operating in the radiofrequency and microwave regimes [1], [2]. Passive linear micro-acoustic filters are at the heart of high-end communication technologies, however, in order to enable more complex and performant architectures, considerable attempts have been dedicated to the development of nonreciprocal and nonlinear micro-acoustic devices.

The Acousto-Electric (AE) effect is the generation of a DC electric current from the propagation of an acoustic wave. This phenomenon is present in piezoelectric semiconductors like CdS [3]–[5], ZnO [5], GaN [6], or in heterostructures like GaAs/AlGaAs [7], [8] or GaAs/LiNbO<sub>3</sub> [9]. On the other end, the indirect AE effect is at the base of AE amplifiers, which are nonreciprocal devices able to perform both amplification or attenuation of acoustic waves by applying a DC bias on a piezoelectric semiconductor or a semiconductor, in semiconductors/piezoelectric heterostructures [10]. The gain applied to the acoustic field depends on the majority charge carriers and the direction of the current with respect to the acoustic field.

**Acoustoelectronic convolvers** can achieve analog signal convolution through nonlinear interaction between two contra-propagating waves under a conductive medium [1], [11], which can be a metallic film [12], or a semiconductive film [13]. However, the performance of such devices is restricted by phenomena of mass loading, and, in particular, the frequency of convolver devices is so far limited to 100s of MHz [1], [11]. To improve the performance of such devices, it is necessary to use materials that would enable higher AE coupling and lower power losses, while also providing high charge mobility. Since the discovery of graphene, some research efforts have been devoted to the measurements of the AE effect in graphene-based structures up to 1 GHz [14]–[23]. As graphene is not piezoelectric. Different heterostructures have been developed: direct excitation on graphitized SiC [18], graphene transferred onto LiNbO<sub>3</sub> [15], [16], [19], [21], or integrated graphene/SiO<sub>2</sub>/Si with LiNbO<sub>3</sub> by means of a flip-chip technique [22]. Indeed, graphene is an appealing material for AE coupling and the manipulation of electric charges by acoustic waves. Because of its low mass density, graphene disturbs only slightly through mass loading the micro-acoustic waves propagating in piezoelectric substrates [23]. Moreover, graphene possesses a **high charge carrier mobility which allows high-frequency operations**. Even if the control of the electrical properties of 2D materials, along with the electrical contacts, remains challenging [24], its resistivity can be

tuned either electrically or through processing in order to optimize the AE coupling. For instance, *Malocha et al.* have recently demonstrated that graphene is a good candidate for AE energy coupling devices and AE SAW amplifier architectures based on  $\text{LiNbO}_3$  with operational frequencies of 145 and 933 MHz [25], [26]. Moreover, they succeeded in tuning the resistivity from 975 to  $1500 \Omega/\square$  through a gate/oxide structure on a piezoelectric substrate. Nevertheless, the potential interest of graphene for AE relies on its potential for ultra-high working frequency. A real breakthrough would be if analog convolver performances would exceed greatly the one achieved by digital processing. This work focuses on the micro-fabrication process of SAW delay lines with an operational frequency of 2.5 GHz and integrated with a graphene monolayer. Measures of AE current and SAW propagation losses were done, and compared to the literature.

### 5.2.3 Microfabrication

The schematic representation of the studied AE device, consisting of a SAW delay line and a graphene zone, is given in Figure 5.1. The SAW delay line consists of two interdigital transducers (IDTs), each consisting of 14 electrode pairs with an aperture of  $80 \mu\text{m}$  and a **periodicity of  $1.35 \mu\text{m}$** , each digit having a width of  $288 \text{ nm}$ .

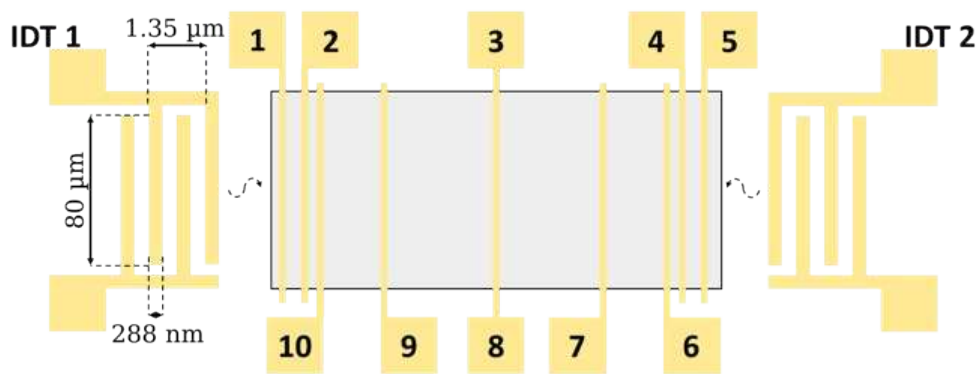


**Figure 5.1:** Schematic representation of AE device based on a SAW delay line and graphene layer (gray zone). Numbered zones indicate the measurement pads.

The distance between IDT 1 and IDT 2 is **2 mm**. Black  $\text{YX-128}^\circ$   $\text{LiNbO}_3$  substrates (rotation of the Y axis by  $128^\circ$  around X, and wave propagation along X) were diced into chips with the size of  $20 \text{ mm} \times 22 \text{ mm}$  and cleaned in acetone, sulfochromic acid, and de-ionized (DI) water. Figure 5.2 gives the flowchart for the microfabrication of the SAW delay lines and its integration with graphene. The samples, between each fabrication step, were cleaned by using

acetone, Iso-Propyl Alcohol (IPA), and de-ionized (DI) water. The IDTs were patterned by means of electron-beam lithography. The first step consisted in the microfabrication of the IDTs and charge-collecting electrodes for graphene. A positive resist (ARP 6200.09), coated by a conductive resist (Electra 92), was used for this purpose. After e-beam writing, the Electra resist was dissolved in DI-water and the ARP 6200.09 resist was developed by submerging the sample first in Amyl-acetate for 1 min and then in MIBK:IPA (with a ratio 1:3) for 30 s. The surface was pretreated in O<sub>2</sub> plasma for 5 s and **Ti (10 nm)/Au (30 nm)** layers were deposited by means of e-beam evaporation. The remover 1165 solution was used for the liftoff process. In the second step, the transfer of graphene was carried out by using a transfer kit of a 10 mm × 10 mm graphene sheet on a water-soluble polymer from Graphenea Foundry (Spain) [27]. To pattern the transferred graphene, a protecting positive S1813 photoresist was spun and structured by means of ultraviolet (UV) lithography (EVG 680 aligner). The unprotected graphene was etched by oxygen plasma for 30 s. The protective resist coating was dissolved in remover solution 1165. The contact pads were fabricated by UV lithography using the photoresist AZNLOF 2000 and a liftoff process of sputtered Ti (10 nm)/Au (200 nm). Finally, annealing was done in argon atmosphere at 120°C for 90 minutes to improve the conductivity of the graphene, the adhesion between the graphene and the substrate, and the graphene-metal electrical contacts. It is to note that the graphene disappeared on LiNbO<sub>3</sub> at temperatures greater than 150°C, which is lower than annealing temperatures used for graphene on silicon wafers. Unpolarized Raman spectra and a mapping of graphene on LiNbO<sub>3</sub> have been done in backscattering geometry using 532 nm excitation (Monovista, S&I). The acquisition time of a spectrum was 20 s using a laser power of 10 mW and an objective with a magnification of 100X.

Electrical characterization of ohmic contact and sheet resistance have been measured by applying Transmission Line Model (TLM) method [28]. The resistive measurements were performed using the 4-point probe method, through a Keithley 6221 current source and a Keithley 6182 nano-voltmeter. In order to limit temperature changes due to power dissipation, the current source was set to generate short pulses at ±50 nA, and the voltage measurements were taken after the transient effects. Finally, Figure 5.3 shows the setup for the AE measurements. It was composed of a high-power signal generator operating in the frequency range from 100 kHz to 6 GHz (Keysight N5181B), connected through port 1 to the IDT 1, and the AE current was measured through a Source Measurement Unit (Keithly 2636B), isolated from the High-Frequency component of a 6 GHz bias-tee (ZFBT-6G+) connected to port 2, which is then connected to pads 1-10. For the measurements of the scattering parameters, a

Vector Network Analyzer (VNA Keysight P5004) was used, connecting port 1 to IDT 1 and port 2 to IDT 2.

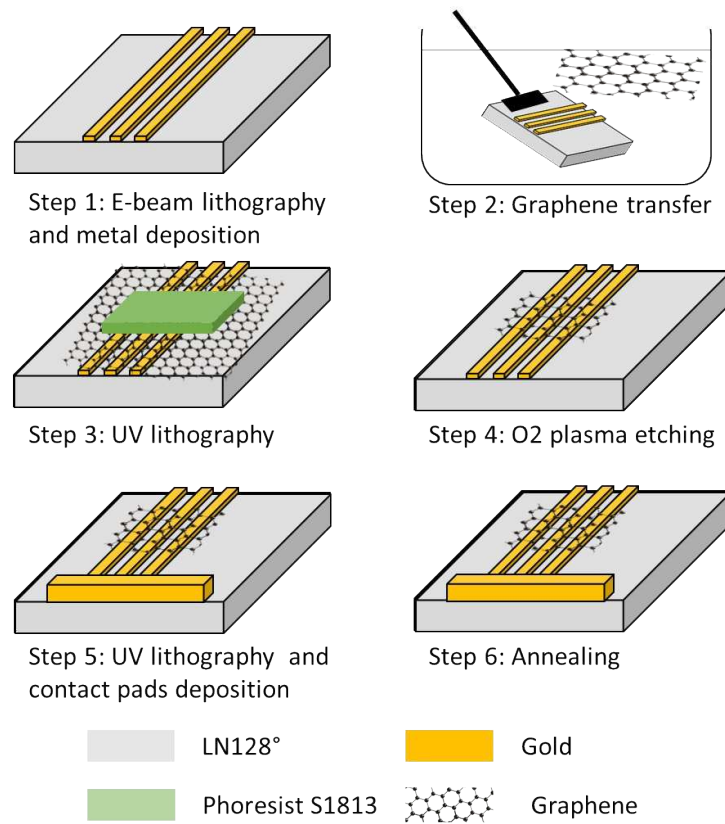


*Figure 5.2: Flowchart of microfabrication of SAW delay line with integrated graphene monolayer.*

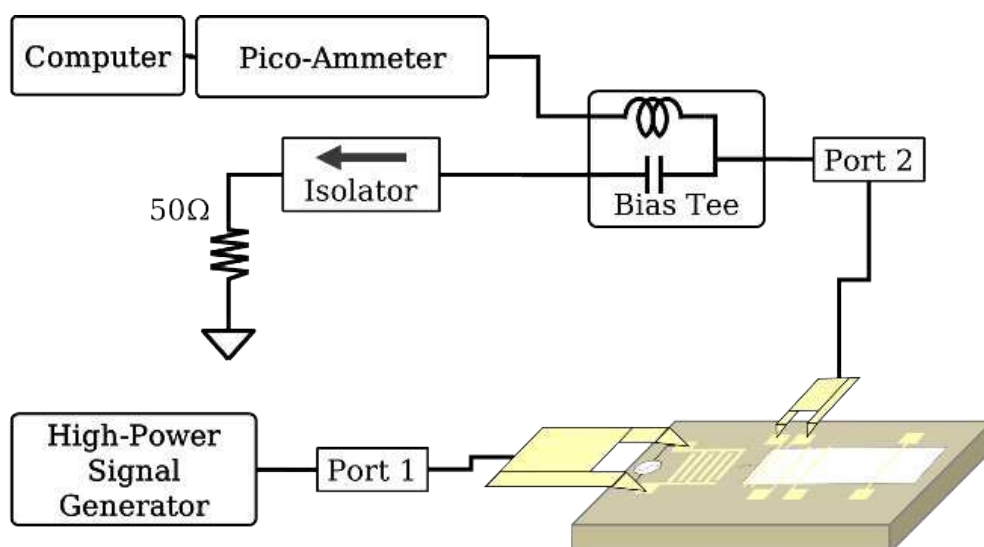


*Figure 5.3: Representation of the setup used for the AE current measurements.*

## 5.2.4 Results

The first analysis of the homogeneity of the processed devices has been performed by means of an optical microscope. As the visibility of graphene on  $\text{LiNbO}_3$  is quite limited (few percent of contrast), more precise measures have been carried out by using Raman spectroscopy [29]–[31]. The Raman spectra have been fitted using pseudo-Voigt profiles and the 2D and G intensities and their ratio were mapped to check the homogeneity of the layer (Figure 5.4). Figure 5.4(a) represents a typical Raman spectrum of graphene on  $\text{LiNbO}_3$  after processing. The 2D/G ratio stays firmly above  $\sim 3.3$  across all the transferred graphene zone and steeply decreases where the graphene had been etched away (Figure 5.4(b)). This confirms that the transferred graphene is monolayer [29], and uniform on all our devices. No imperfections such as holes or folds along the graphene sheet have been observed.

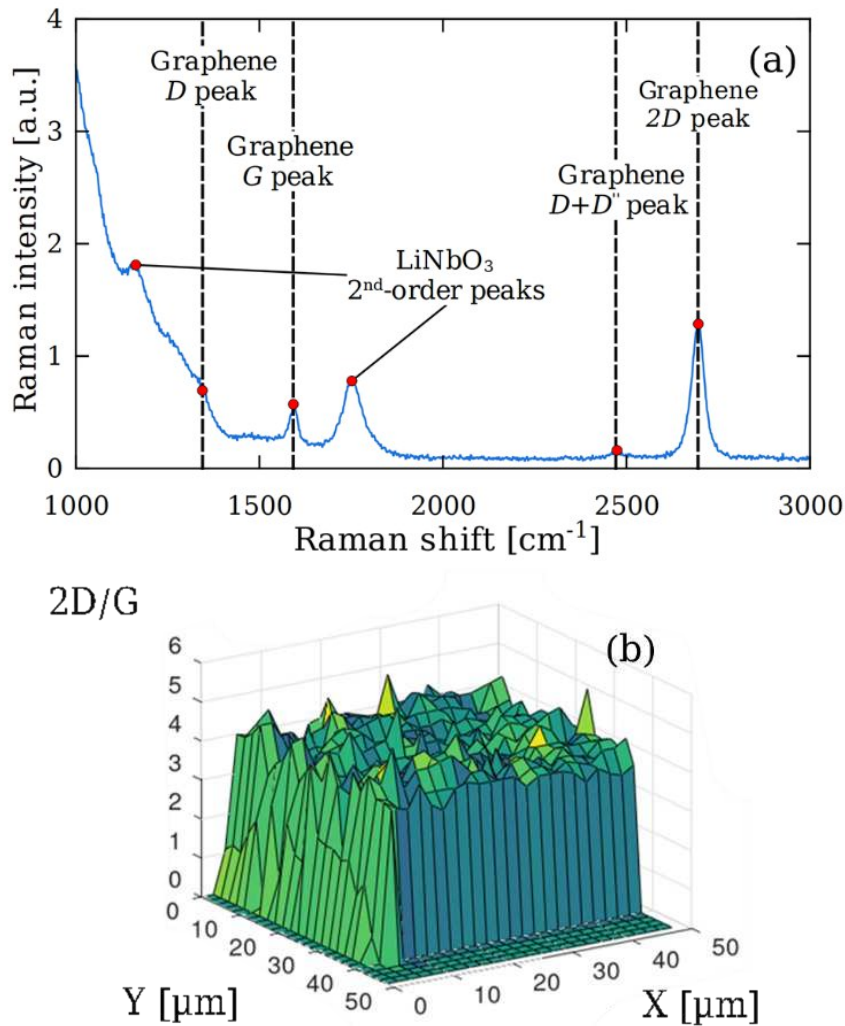


**Figure 5.4:** Typical Raman spectra of graphene transferred onto  $\text{LiNbO}_3$  (a) and mapping of 2D/G ratio on a  $50 \mu\text{m} \times 50 \mu\text{m}$  area made by collecting  $25 \times 25$  points (b).

In order to further confirm the high quality of graphene, the DC resistivity values have been analyzed by applying the TLM method in which a sheet of graphene is contacted in multiple differently spaced points. The resistance as a function of the distance between the contacts (in the range from 10  $\mu\text{m}$  to 135  $\mu\text{m}$ ) was recorded from a TLM device with a width of 80  $\mu\text{m}$  at ambient conditions (in air at 25°C). The resistivity of graphene and the contact resistance were extracted from the fitting procedure, described elsewhere [28], [32]–[34]. The measured resistance (that of graphene and contacts) was plotted as a function of pin-pin distance (Figure 5.5). The intercept on the resistance axis represents the total contact resistance, which is equal to:

$$R_{tot} = 2 \cdot (R_m + R_i), \quad (5.1)$$

Where the factor 2 originates from the two contact points,  $R_m$  is the resistance of the gold contact/layer, and  $R_i$  is the resistance of the graphene-metal interface. Therefore, the value of the contact resistivity has been estimated by multiplying the interface resistance by the length of the gold/graphene contact. The resistivity of the graphene has been found by multiplying the slope of the curve, which is the line resistivity in  $\Omega/\mu\text{m}$ , by the width of the TLM device. The resistivity of the graphene was 733.4  $\Omega/\square$  and the resistance of the gold contacts of  $\sim 21 \Omega$ . The contact resistivity between the graphene and gold was 1880  $\Omega\mu\text{m}$ . Further measurements on other TLM devices revealed that the resistivity values can vary considerably on the same sample, and the graphene sheets resistivity and contact resistivity have been found to be in the range of 733-1230  $\Omega/\square$  and 1880-5200  $\Omega\mu\text{m}$ , respectively.

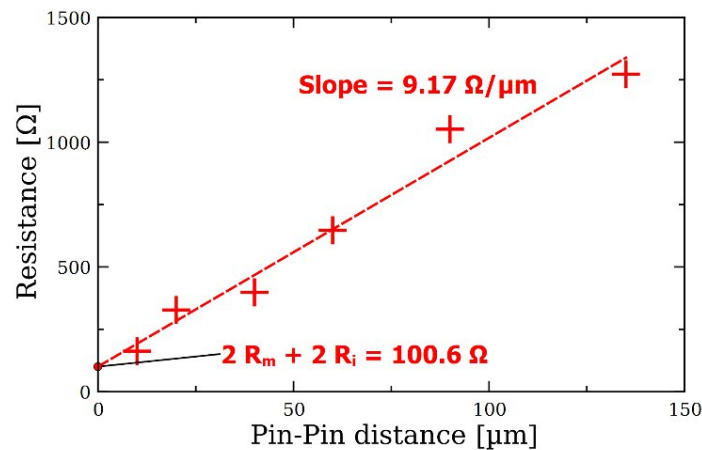


**Figure 5.5:** TLM plot for a 80  $\mu\text{m}$ -wide graphene device with electrical gold contacts.

The measurements of the scattering parameters of a SAW delay line with graphene have been taken in the frequency range between **1 GHz and 4 GHz** (Figure 5.6 (a) and (b)) by using a VNA and GS probes on IDT 1 and 2 with a wave impedance of  $50 \Omega$  (Figure 5.3). The scattering parameters of the SAW delay line confirmed a first-order resonance around 2.5 GHz with an insertion loss of value 30 dB. The secondary peaks visible in Figure 5.6 (b) are due to bulk-guided modes and secondary SAW modes of the transducers. The high insertion losses could be due to impedance mismatch and propagation losses. The total lost power, with respect to the IDT1 input, has been computed from the scattering parameters as:

$$\frac{P_{lost}}{P_{in,1}} = \frac{|a_1|^2 - |b_1|^2 - |b_2|^2}{|a_1|^2} = 1 - |S_{11}|^2 - |S_{21}|^2, \quad (5.2)$$

where  $a_1$ ,  $b_1$  and  $b_2$  are the Kurokawa wave parameters for the input electromagnetic wave at port 1 and output electromagnetic wave at ports 1 and 2, respectively [35], and considering the contact pads on each IDT as reference planes. The resulting lost power was plotted in Figure 5.6(c) and showed that **a considerable portion of the acoustic power was lost during transmission**. This could be due to the long delay line (2 mm) and high-frequency losses of the acoustic wave. Further characterization of other delay line devices operating in the 2.2 GHz - 2.7 GHz range yielded similar results, both in devices with or without graphene.

The acoustic current has been generated through a high-power signal generator connected directly to IDT and the AE current has been measured by means of an ammeter, connected to a probe placed on adjacent pads.

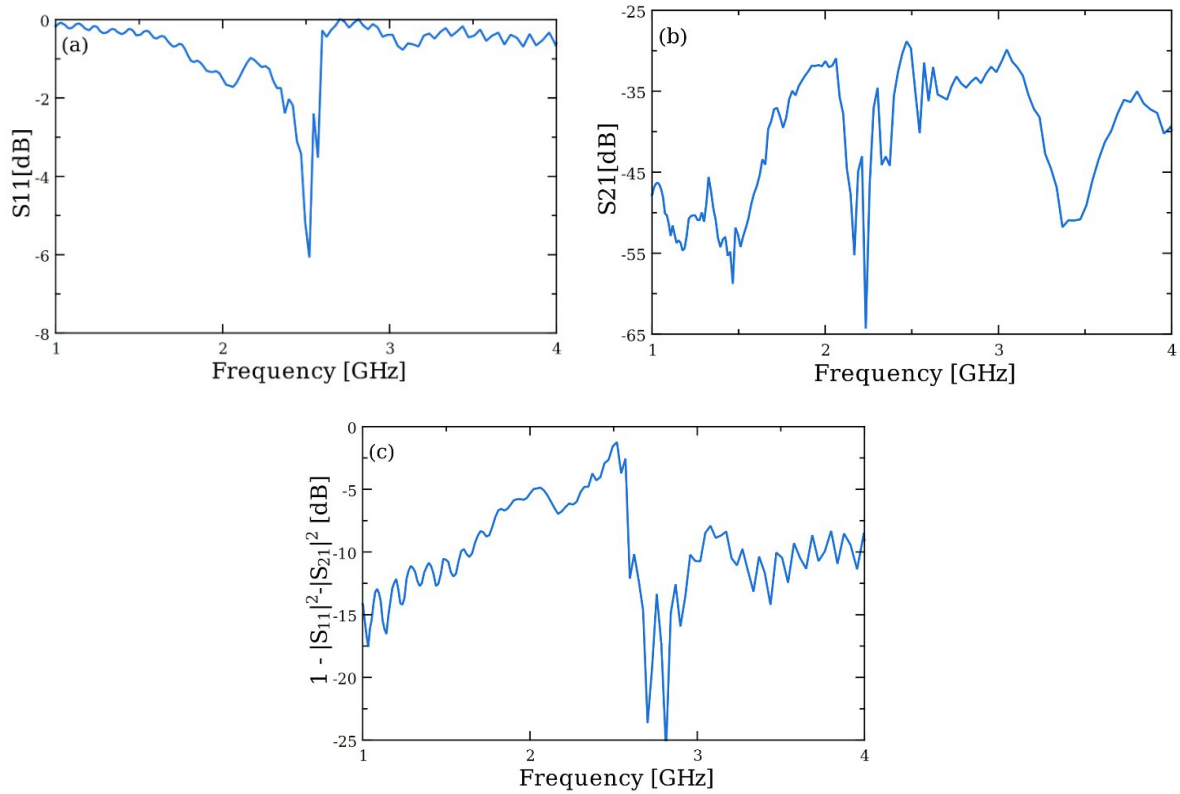


**Figure 5.6:**  $S_{11}$  (a),  $S_{21}$  (b) and dissipated power (c) vs. input frequency of a SAW IDT line based on  $128^\circ\text{YX LiNbO}_3$  with graphene, measured between IDT 1 and IDT 2.

In order to shield the instrumentation from the microwave electromagnetic field component, both for protection of the instrumentation and for better accuracy, the probe was first connected by a bias-tee whose RF branch was connected to an isolator and a load of  $50\ \Omega$ , while the DC branch was connected to the ammeter (Figure 5.3), the AE current collected have been therefore logged. The AE currents of graphene as a function of input power (acquired with different pins) are presented in Figure 5.7.

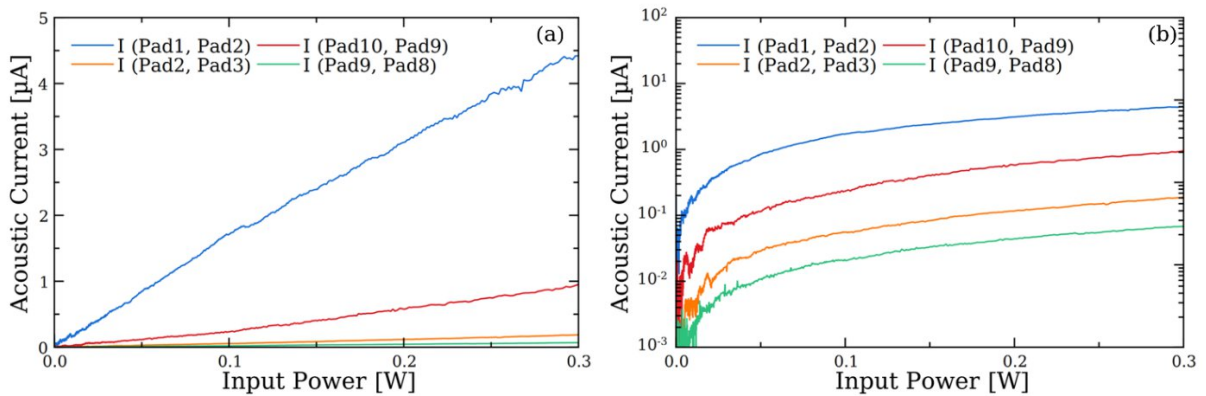


**Figure 5.7:** AE current in linear scale (a) and in logarithmic scale (b) as a function of input power.

During each measurement for the AE current generator has first been set up to generate a signal at 2.5 GHz with low amplitude (0 dBm), the frequency has then been slowly tuned manually while the AE current was monitored. The frequency that maximizes the current value was found to be at 2.507 GHz, which was in line to the resonant frequency of the IDTs (Figure 5.6 (a) and (b)). Once the central frequency was found, the power has been gradually increased up to 0.3 W. Afterwards the same power sweep has been also repeated for the other data points. The central frequency did not show a significant shift with excitation power and we can neglect dissipation and temperature effects.

### 5.2.5 Discussion and concluding remarks

In the absence of an external magnetic field, the current of a hybrid piezoelectric-2D electron system for a short-circuited AE current loop [7]–[9] is described by the following equation:

$$I_{AE} = \mu_{AE} \cdot P \cdot \alpha_{AE} / v_0, \quad (5.3)$$

where  $\mu_{AE}$  is the mobility of AE-coupled charge carriers,  $P$  - the acoustic power,  $\alpha_{AE}$  - the attenuation coefficient for the acoustic field due to the interaction with the charge carriers, and  $v_0$  - the speed of the surface wave. For the 2D electron system on piezoelectric, assuming a simple relaxation model for the SAW-charge carriers interactions, the value of  $\alpha_{AE}$  can be found as [7]:

$$\alpha_{AE} = \beta_0 \cdot \frac{K_{eff}^2}{2} \cdot \frac{\rho_M / \rho_\square}{1 + (\rho_M / \rho_\square)^2}, \quad (5.4)$$

where  $\beta_0$  is the SAW wavenumber,  $K_{eff}^2$  - the effective piezoelectric coupling factor (equal to 0.056 for YX128° LiNbO<sub>3</sub>),  $\rho_\square$  - the surface resistivity, and  $\rho_M$  - a constant, equal to approximately 800 k $\Omega$  for YX128° LiNbO<sub>3</sub> (Chapter 1.3).

In order to correctly evaluate the power (Equation (5.3)), it is necessary to estimate the different contributions to the decrease in the amplitude of the acoustic field from the IDTs to the graphene. The power at the graphene interface can be calculated as:

$$P_i(\Delta x) = \eta_{IDT,i} \cdot \eta_{P,i} \cdot P_{in} \cdot e^{-2\alpha \cdot \Delta x}, \quad (5.5)$$

where  $i$  identifies either port 1 or port 2,  $P_{in}$  is the input electrical power,  $\eta_{IDT,i}$  - the conversion efficiency between the electrical signal at the IDT and acoustic power in the delay line, the

efficiency  $\eta_{P,i}$  - a factor representing the power loss due to the cables, probes and various connectors between the input port on the VNA and the corresponding contact pads on the sample,  $\Delta x$  - the distance between the IDT and the first pad on the graphene, and  $\alpha$  represents the losses of the acoustic field due to damping. If assuming that the ohmic losses are negligible, all of the input electric power is either reflected back or converted to SAW:

$$\eta_{P,i} \cdot P_{in} = |a_i|^2 = |b_i|^2 + 2 \cdot P_A, \quad (5.6)$$

where  $P_A$  is the acoustic power generated at one side of the IDT and the factor 2 derives from the a-directionality of our IDT design, meaning that the electrical power is split equally between both the left and right sides. From Equation (5.6), the value of the  $\eta_{IDT,i}$  can be found from the related scattering parameter  $S_{ii}$  as:

$$\eta_{IDT,i} = \frac{P_A}{|a_i|^2} = \frac{1 - |S_{ii}|^2}{2}. \quad (5.7)$$

At resonance,  $|S_{11}| = -6$  dB for port 1, which implies  $\eta_{IDT,1} = \mathbf{0.37}$ , while  $|S_{22}| = -5.9$  dB for port 2, which leads to  $\eta_{IDT,2} = \mathbf{0.37}$ . The values of  $\eta_{P,1}$  and  $\eta_{P,2}$  were measured experimentally and their values were  $\sim 0.83$ . The  $\alpha$  can be found from  $S_{11}$  and  $S_{21}$  by rewriting Equation (5.6) in terms of the electric wave in port 2 instead of the acoustic power at port 1:

$$\eta_{P,1} \cdot |a_1|^2 = |b_1|^2 + 2 \cdot e^{2\alpha \cdot L} \cdot \frac{|b_2|^2}{\eta_{IDT,2} \eta_{P,2}}, \quad (5.8)$$

where  $L$  is the length of the delay line and  $|b_2|^2 / \eta_{IDT,2} \eta_{P,2}$  is the acoustic wave's power on IDT 2. Finally, (5.8) can be manipulated in order to find:

$$\alpha = \frac{1}{2 \cdot L} \cdot \log \left( |S_{21}|^{-2} \cdot \eta_{IDT,2} \cdot \eta_{IDT,1} \cdot \eta_{P,2} \cdot \eta_{P,1} \right). \quad (5.9)$$

By performing a characterization of a delay line without graphene, it was found  $\alpha = \mathbf{1550 \text{ m}^{-1}}$ , which means that the acoustic wave, when it reaches the graphene is reduced by a factor of  $\sim 0.053$ . Different sets of AE current measurements have been performed, the acoustic current was recorded by using the ammeter between the pads 1-2, 2-3, 10-9, and 9-8. The distances between the different couples of pads were  $14.5 \text{ }\mu\text{m}$ ,  $414 \text{ }\mu\text{m}$ ,  $40.5 \text{ }\mu\text{m}$ , and  $344.3 \text{ }\mu\text{m}$ , respectively. The data collected are represented in Figure 5.8. The AE current was always oriented in the same direction as the propagation direction of the acoustic field. This indicates that **the major charge carriers are holes, due to the p-doping of the graphene** caused by the adsorption of  $\text{O}_2$  and  $\text{H}_2\text{O}$  [31]. AE current varies linearly with the input power according to

the Equation (5.3) (Figure 5.7(a)), and the maximum reached values for different distances between the pads were 4.5  $\mu\text{A}$ , 188 nA, 950 nA and 68 nA, respectively (Figure 5.7(b)). The current values changed significantly with the increase of the measurement distance: the maximum current measured from pads 1-2 is  $\sim 4.7$  times higher than what was measured on pads 10-9, and  $\sim 66.2$  times higher than for pads 9-8. This effect could be due to the previously discussed power losses on the delay line itself. To check this hypothesis, the AE current amplitude at 0.3 W of input power, has been plotted with respect to the average distance to the first contact pad (Figure 5.8), showing an exponential decrease with the distance.

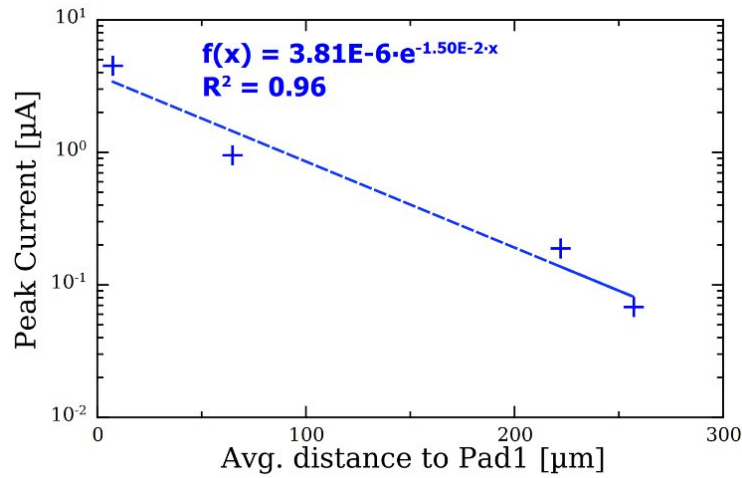


**Figure 5.8: Acoustic current at 0.3 W, 2.507 GHz vs. average distance from Pad 1.**

By using (5.3) and (5.4), it is possible to find the values of the loss factor  $\alpha_{AE}$  and charge mobility from the data acquired.  $\alpha_{AE} = 109 \text{ m}^{-1}$  and  $\mu_{AE} = 101 \text{ cm}^2/\text{Vs}$  were estimated for a measured graphene resistivity of  $\sim 800 \Omega/\square$  for the studied AE device. Table 5-1 reports a comparison of AE parameters of graphene transferred to  $\text{LiNbO}_3$  in the range of 11 MHz to 2.5 GHz. The graphene DC resistivity varies from  $0.8 \text{ k}\Omega/\square$  (this work) in air to  $154 \text{ k}\Omega/\square$  in vacuum [17]. Considering only values in air, the resistivity varies from 0.8 to  $4.8 \text{ k}\Omega/\square$  in good agreement with properties of CVD graphene transferred onto  $\text{Si}/\text{SiO}_2$  [36]. The DC mobility  $\mu$  of our graphene is expected to be of the order of  $1500 \text{ cm}^2/\text{Vs}$  as compared to one in the graphene/ $\text{Si}/\text{SiO}_2$ , as well [16], [25], [27]. Meanwhile, the acousto-electronic mobility, given in Table 5-1, differs significantly from DC mobility. Mobilities between 68 and  $109 \text{ cm}^2/\text{Vs}$  for low-resistivity graphene and from 5 to  $15 \text{ cm}^2/\text{Vs}$  as measured through AE effect (Table 5-1). This shows that the mobility (5.3) and (5.4) is not the DC mobility. Four possible reasons were identified for the discrepancies between the theoretical values and the results:

- One of the main reasons is that the mobility in AE is due to the inhomogeneous electric field (over the acoustic wavelength in the range of microns) and transverse electric field accompanying the acoustic wave. As for DC mobility, it is measured with an electric field longitudinal to the plane of graphene.
- The amplitude of the electric field in the graphene may differ from the one within the piezoelectric dielectric material. Indeed, a dead layer forms on the ferroelectric surface of LiNbO<sub>3</sub> which may attenuate the amplitude of the electric field at the interface with the graphene [37].

**Table 5-1: Comparison of values of  $\alpha_{AE}$  and  $\mu_{AE}$  measured on graphene/YX128°-LiNbO<sub>3</sub> at room temperature with the literature data. The frequency and the typical feature size of the devices are indicated, as well.**

| Ref.       | $\rho$ [k $\Omega$ / $\square$ ] | $\alpha_{AE}$ [m <sup>-1</sup> ] | $\mu_{AE}$ [cm <sup>2</sup> /Vs] | $FoM_{AE} = \alpha_{AE} \cdot \mu_{AE}$ [cm <sup>2</sup> /Vsm] | Size [ $\mu$ m] | Freq. [MHz]       |
|------------|----------------------------------|----------------------------------|----------------------------------|--|-----------------|-------------------|
| [14]       | 4.8                              | 29*                              | 68*                              | 2001*  | 30              | 110               |
| [17]       | 154 (vac.)                       | 2910*                            | 8                                | 23280  | 200, 300, 500   | 11,32, 97,18, 356 |
| [16]       | 77* (vac.)                       | 1100                             | 15                               | 16500  | 300             | 11,32, 269        |
| [15]       | -                                | 150                              | 5                                | 750  | 29              | 332               |
| [25], [26] | 0.9-1.5 (gate)                   | -                                | -                                | -  | 127             | 331               |
| This work  | 0.8                              | 109                              | 101                              | 12000  | 14, 40, 344     | 2500              |

\* are values computed from data

- is for data not available

- The difference in the mobility (109 cm<sup>2</sup>/Vs) measured at 2.5 GHz with the one (68 cm<sup>2</sup>/Vs) extracted from the data by *Miseikis et al.* at 110 MHz [14]. As both papers consider CVD graphene transferred onto LiNbO<sub>3</sub> [38], one can consider dependence on the wavelength of the acoustic field, which was 1.6  $\mu$ m and 30  $\mu$ m, respectively. However,

this interpretation doesn't follow *Venugopal et al.* [39] predictions. Indeed, they reported a significant decrease in mobility for transport distances less than  $\sim 5 \mu\text{m}$  due to a switch in the prevalent charge transport mechanism from quasi-ballistic to diffusive one. In our case, the highest mobility was found with a wavelength of  $1.6 \mu\text{m}$  which is much smaller than the reported critical distance of  $5 \mu\text{m}$  *Venugopal et al.* [39]. The higher resistance due to defects and scattering of carriers may explain the lower mobility observed by *Miseikis et al.*

- Finally, a fourth hypothesis is that we have separated the acoustic losses in the  $\text{LiNbO}_3$  substrate from the losses in graphene (Equations 5.5 – 5.9). Consequently, we have estimated a lower loss factor,  $\alpha_{AE}$ , of graphene and increased mobility with respect to the literature data measured at similar power but including acoustic losses. Unfortunately, very limited information is available on this topic in the literature (Table 5-1).

Surface Acoustic wave delay lines operating at 2.5 GHz have been designed in order to measure the AE transport of graphene. Even if the insertion loss of our device remained quite high due to the unoptimized impedance matching at  $50 \Omega$  and wave damping in  $\text{LiNbO}_3$ , the results showed that graphene presents a very strong AE interaction in the GHz range. In the previous discussion, a high uncertainty still exists in the definition of the AE mobility from the DC mobility. The extracted AE mobility shows values much higher than the reported ones, indicating a better AE coupling in the GHz frequency range. In the literature, the generic (5.3) and (5.4) have been verified for classical semiconductors and piezoelectric structures but little attention has been paid to the reliability of estimated values in the case of 2D materials. This indicates that there is still experimental and theoretical work to be done in this direction.

### 5.3 Follow-up on AE Characterization

This section exposes further results of AE characterization performed for different frequencies of the excited SAW signal and stress-testing of the IDTs to find their maximum operable power range. The studies were first performed manually, as described in Section 5.2.4, and then via the automated bench described in Section 5.3.3.

### 5.3.1 Characterization at 2.0 GHz and 3 GHz

As visible in the response of the IDTs shown in Figure 5.6, two smaller side lobes around 2.0 GHz and 3.0 GHz could be present in some delay lines due to fabrication defects, which have allowed to perform an AE characterization at said frequencies.

Because of the unreliability of the aforementioned peaks, the value of  $\alpha$  computed from the scattering parameters was unreliable due to a likely contribution of bulk waves to  $S_{21}$ . Therefore, when processing the data, the value of  $\alpha$  used when applying (5.5) was the lowest value measured in between all delay lines possessing a **propagating peak** at said frequency. It must be noted that, because of this, the computed values for the mobility  $\mu_{AE}$  and of the defined coupling figure of merit  $FoM_{AE} = \alpha_{AE} \cdot \mu_{AE}$  are underestimated.

For the test frequencies of 2.0 GHz,  $\alpha$  was found to be in the  $[1300, 4000]$   $\text{m}^{-1}$  range and for 3.0 GHz therefore the value used when computing was  $[1200, 1800]$   $\text{m}^{-1}$ , therefore, the values of  $\alpha$  used at  $\sim 2.0$  GHz was  $1300 \text{ m}^{-1}$  and at 3.0 GHz  $1200 \text{ m}^{-1}$ .

Figure 5.9 shows the scattering parameters of the device 'R4\_C8' used in the 2.0 GHz AE characterization shown in Figure 5.10 (a), using an input SAW at frequency of 2.017 GHz. The data in Figure 5.9 (c) were computed via Equation (5.2). The data shows saturation around  $P_{in} = 0.5 \text{ W}$ , which is preceded by an "overshoot". This effect could be reproduced on many of the samples and is further discussed in Section 5.3.2. and  $\eta_{IDT,1}$  was  $\sim 0.46$ . Figure 5.10 (b) tests the generated  $I_{AE}$  with the superposition of a DC current  $I_{DC}$  of  $-1.13 \mu\text{A}$  for a resistance of  $250 \Omega$  and a sheet resistance of  $\sim 2000 \Omega/\square$ , which was chosen to cancel the current at  $P_{in} = +20 \text{ dBm}$  and shows that, especially for higher values of  $P_{in}$ , the difference in current increases. From a quick test of the device performed afterwards, its response for  $I_{DC} = 0 \mu\text{A}$  did not change, which probably indicated attenuation on the SAW of the contra-propagating DC current. Because of how the setup was made at the time of measurement, it was not possible to measure directly the output power at IDT 2, for which this effect was further explored in a second moment, as described in Section 6.3.

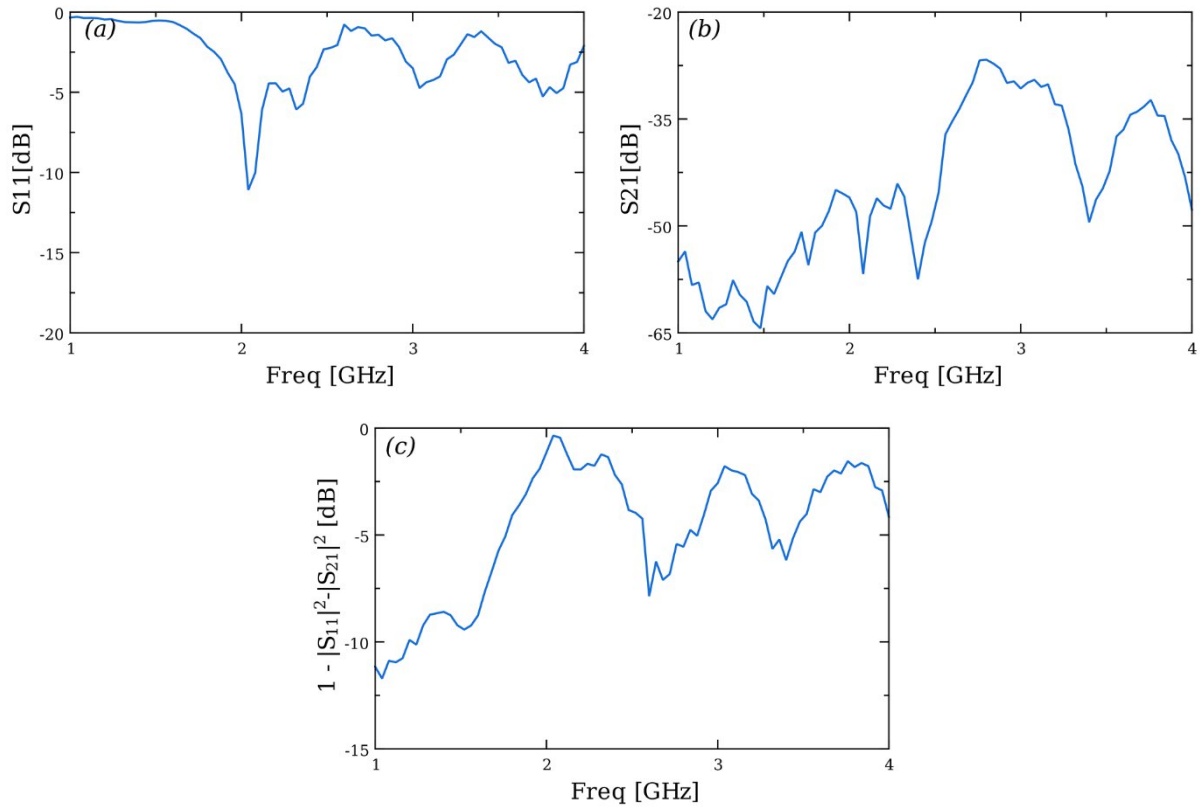


**Figure 5.9:**  $S_{11}$  (a),  $S_{21}$  (b) and relative dissipated power (c) vs. input frequency of the device 'R4\_C8'.

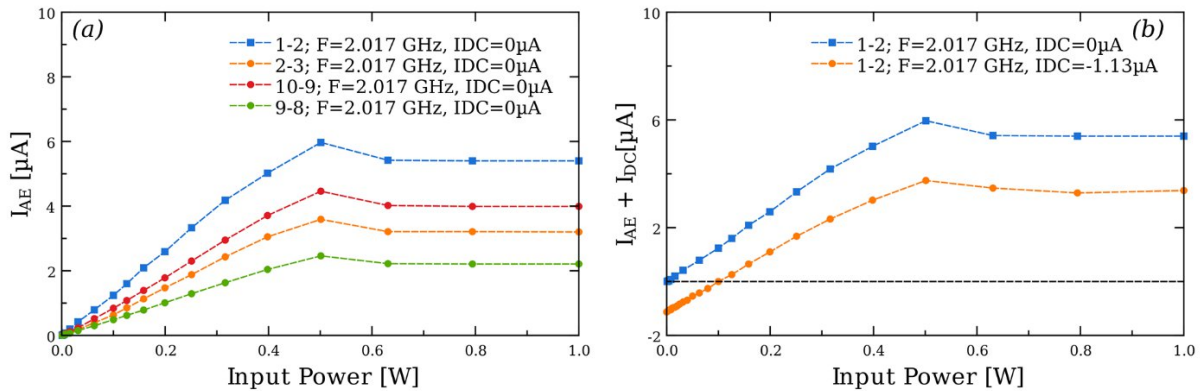


**Figure 5.10:** (a) Measurements of  $I_{AE}$  vs. SAW input power at 2.017 GHz for the device 'R4\_C8', showing the saturation effect for all probed distances. (b) shows the AE response when applying a contra-propagating DC current of  $1.13 \mu\text{A}$  (the black dotted line represents  $I_{AE} + I_{DC} = 0 \mu\text{A}$ ).

Figure 5.11 shows the scattering parameters of the device 'R4\_C7' used for both a 2.0 GHz and a 3.0 GHz AE characterization, shown in Figure 5.12(a) and (b). The data confirms the presence of a saturation effect around 300-400 mW. The values found for  $\eta_{IDT,1}$  were 0.27 and 0.45 for 3.0 GHz and 2.0 GHz respectively.

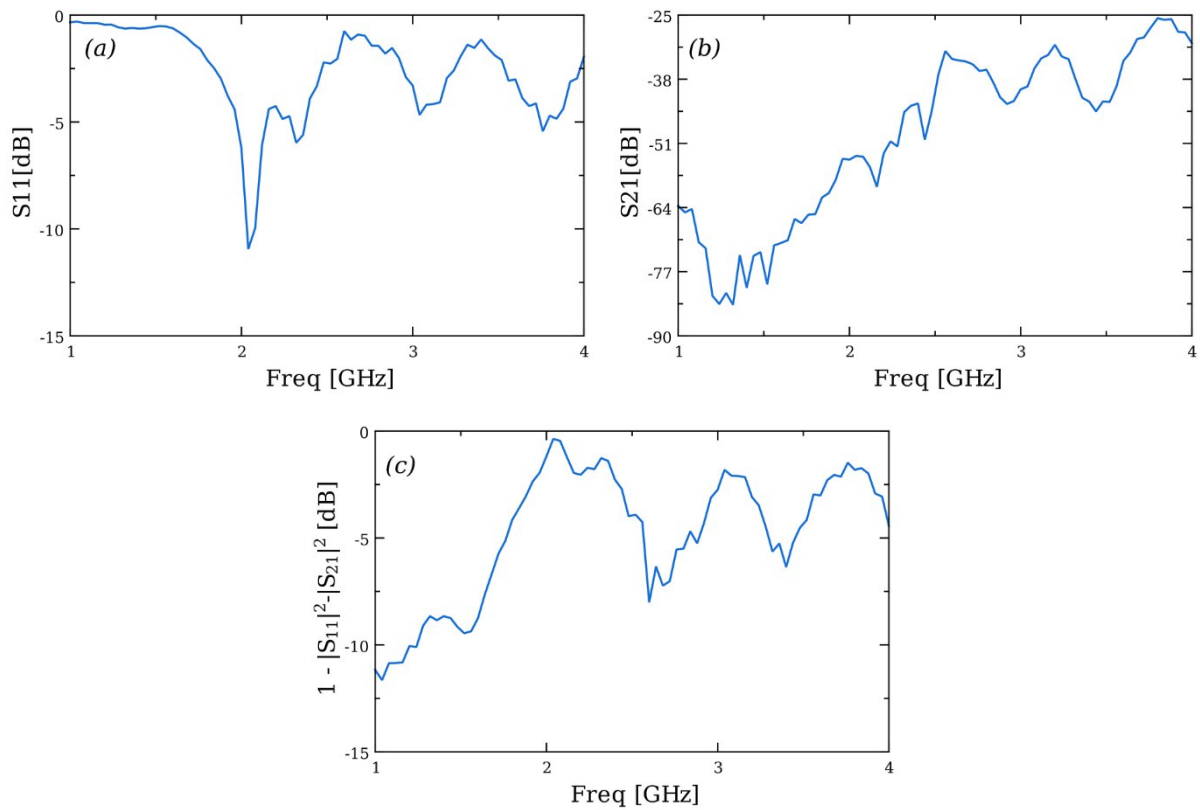


**Figure 5.11:**  $S_{11}$  (a),  $S_{21}$  (b) and relative dissipated power (c) vs. input frequency of the device 'R4\_C7'.

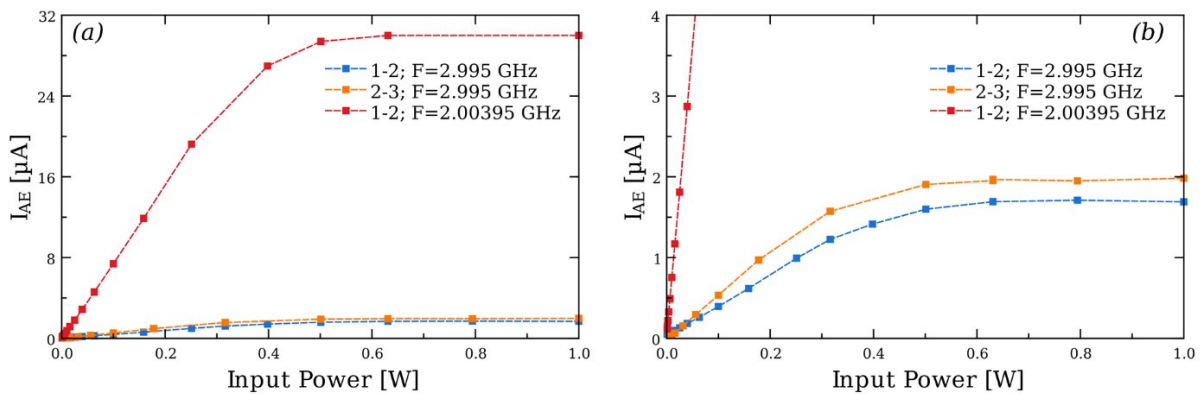


**Figure 5.12:** (a), (b) Measurements of  $I_{AE}$  vs. SAW input power at ~2.004 GHz and 2.995 GHz for the device 'R4\_C7'.

Finally, Figure 5.13 shows the scattering parameters of the device 'R2\_C8' used for the AE characterization at 2.994 GHz and 2.976 GHz, shown in Figure 5.14. The data confirms the presence of a saturation effect around 300-400 mW, like other samples. The value of  $\eta_{IDT,1}$  found at 3.0 GHz was 0.31.

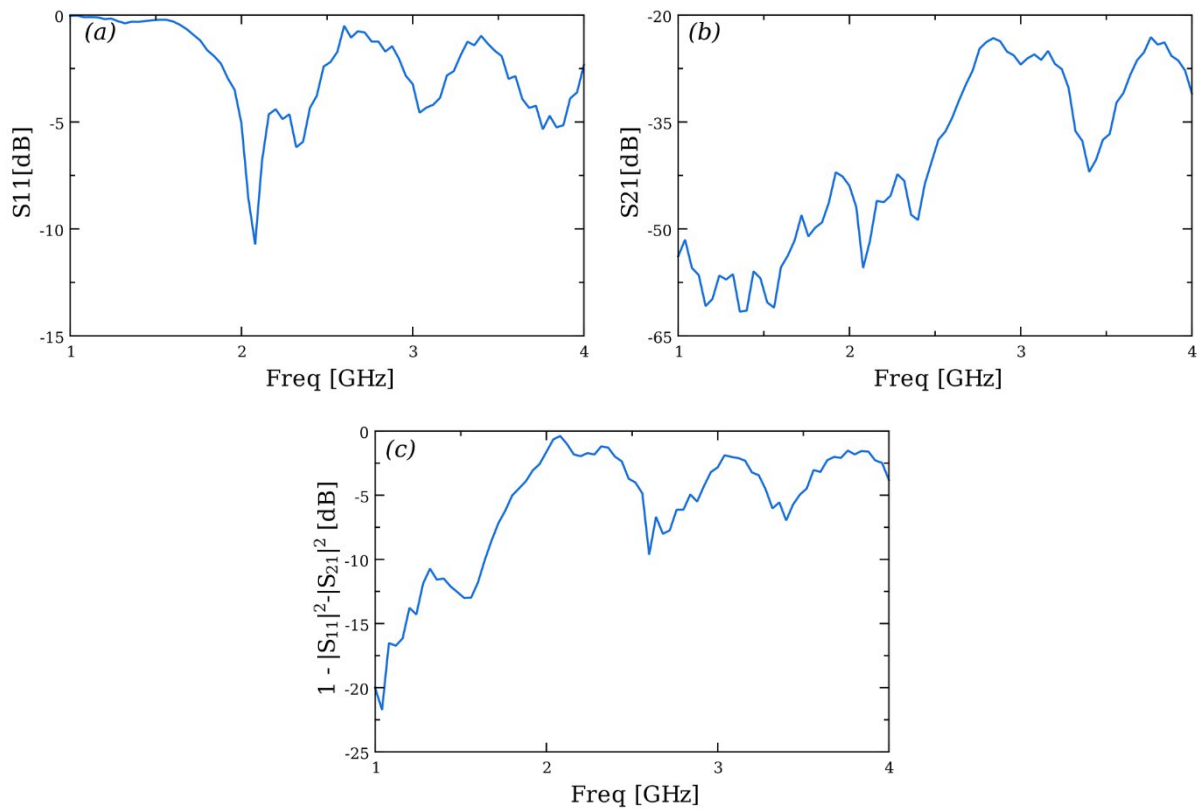


**Figure 5.13:**  $S_{11}$  (a),  $S_{21}$  (b) and relative dissipated power (c) vs. input frequency of the device 'R2\_C8'.

The results for AE coupling at different input frequencies are summed up in Table 5-2. Overall, the data demonstrates the best reported AE coupling for GoL at the input frequency of 2.976 GHz and suggest an optimal input power range of 0 W – 0.3 W.

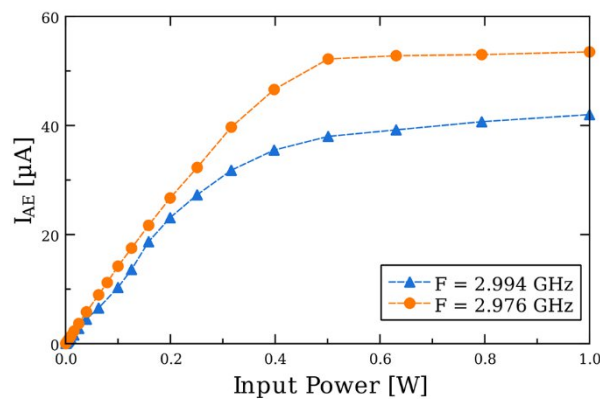


**Figure 5.14:** Measurements of  $I_{AE}$  vs. SAW input power at  $\sim$ 2.994 GHz and 2.976 GHz for the device 'R2\_C8'.

*Table 5-2: Results for AE coupling of the devices tested.*

| Ref            | Device | $\rho_{\square}$<br>[k $\Omega$ / $\square$ ] | $\alpha$ [m <sup>-1</sup> ] | $\mu_{AE}$<br>[cm <sup>2</sup> /Vs] | $FoM_{AE} = \alpha_{AE} \cdot \mu_{AE}$<br>[cm <sup>2</sup> /Vsm] | Freq.<br>[GHz] |
|----------------|--------|---|-----------------------------|-------------------------------------|---|----------------|
| Figure 5.10    | R4_C8  | 2.0   | 220                         | 24.7                                | 5440  | 2.017          |
| Figure 5.12(b) | R4_C7  | 0.9   | 159                         | 23.4                                | 3740  | 2.995          |
| Figure 5.12(a) | R4_C7  | 0.9   | 106                         | 277.7                               | 29570   | 2.004          |
| Figure 5.14    | R2_C8  | 0.8   | 132                         | 509                                 | 67090   | 2.994          |
| Figure 5.14    | R2_C8  | 0.8   | 131                         | 592                                 | 77550   | 2.976          |

### 5.3.2 Saturation power and breakdown of the IDTs

The data captured showed a certain nonlinear coupling for high levels of power. As previously discussed for the results shown in Figure 5.10, Figure 5.12 and Figure 5.14, a significant saturation effect starts to be visible for  $P_{in} \sim 0.3-0.4$  W. More interestingly, some experiments, as visible in Figure 5.10, show a pronounced decrease in coupling after 0.5 W, while some devices experienced a failure for a high enough power at the right SAW frequency. Specifically, most failures were observed at the main peak of the IDTs, rather than the side lobes. For instance, Figure 5.15 shows the measurement at 2.57 GHz performed for the device ‘R3\_C7’, showing a critical failure at 0.25 W, after which there was still signal, but much weaker.

The first hypothesis was that the IDT broke due to the strong input signal, to counter check this argument the  $S_{11}$  of the IDT was remeasured after the AE characterization (Figure 5.16), demonstrating that the peak was considerably wider and shifted, confirming the damaging of the transducers. This seems to indicate the **stress of the IDTs as a major contributing factor of the saturation effect**, but it doesn’t confirm the exact cause. Various possible causes have been individuated to explain the saturation and the breakdown:

- The samples could have been heated up locally due to mechanical or electrical dissipation, shifting the resonant frequency to lower values and eventually breaking the IDTs due to thermally generated strain between bulk LiNbO<sub>3</sub>, polycrystalline Au, and Ti;

- The metal could have detached from the substrate due to a combination of a high displacement amplitude and frequency;
- The displacement could have been large for each digit of the IDTs to start touching each other, eventually breaking;
- Scattering events from small dust particles in the air and on the substrate could have attenuated the signal during propagation;
- The effect could be caused by other secondary effects (i.e., nonlinearity piezoelectricity, nonlinear stiffness, electrostriction, flexoelectricity).

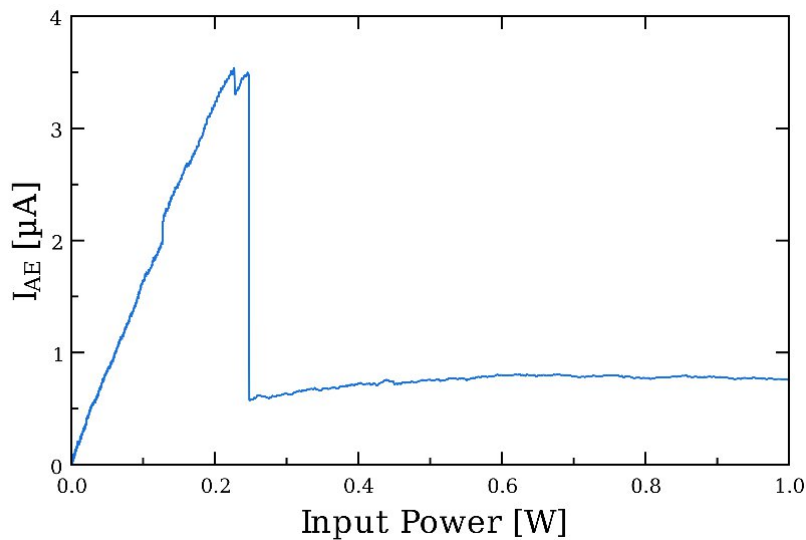


*Figure 5.15: Measurements of  $I_{AE}$  performed on the device ‘R3\_C7’ for a SAW frequency of 2.5725 GHz, showing a failure at  $P_{in} = 0.25$  W.*

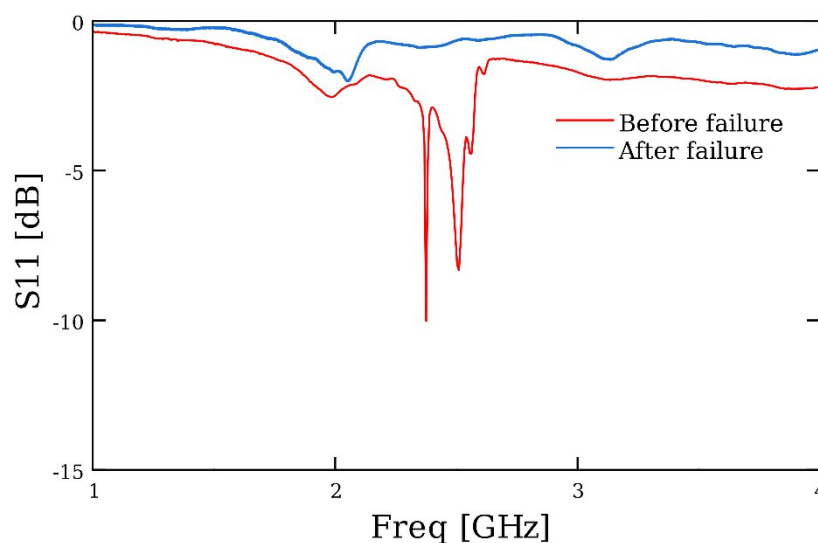


*Figure 5.16:  $S_{11}$  for the device ‘R3\_C7’ before and after the breakdown.*

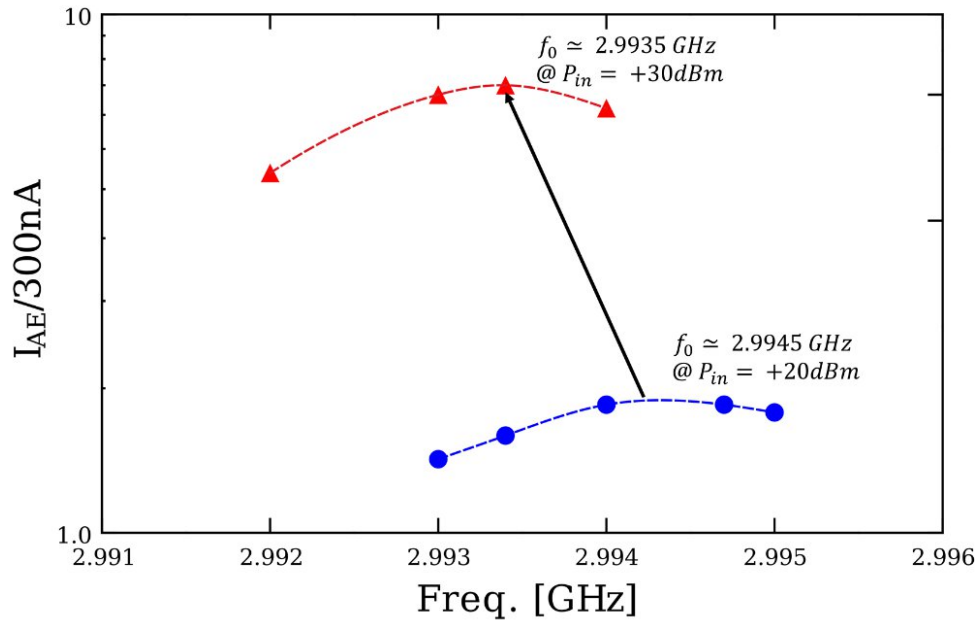


**Figure 5.17:** Analysis of the frequency shift for the same device from an input power of +20 dBm to +30 dBm (the dotted lines are the natural spline interpolation).

The most significant contribution seemed to be the temperature-related, in fact, by performing an analysis of the resonant frequency vs. input power, shown in Figure 5.17, a redshift of  $\sim 100$  MHz was estimated when shifting from +20 dBm (0.1 W) to +30 dBm (1 W), which is compatible with the hypothesis of thermal expansion.

Finally, some pictures of the damaged IDTs are shown in Figure 5.18 for further insight. The failures are concentrated and fairly large, but they could be compatible with either a melting of the metal or a local lack of adhesion with the substrate.

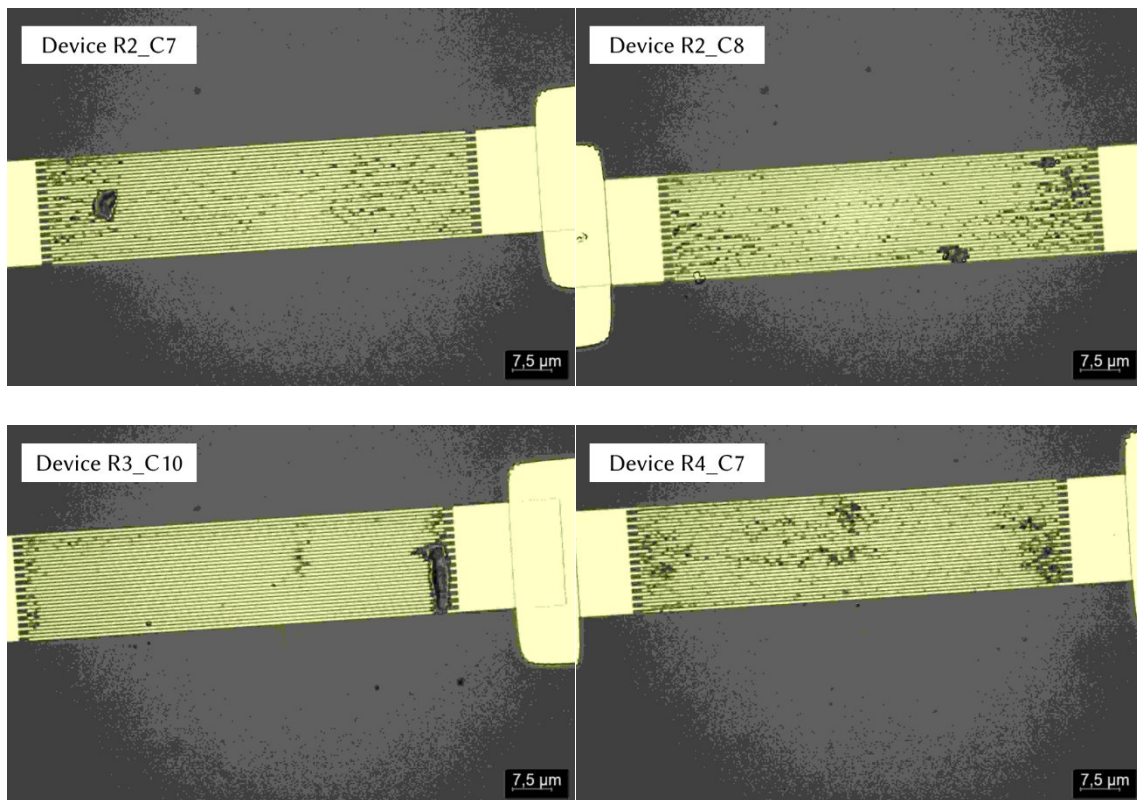


*Figure 5.18: Pictures of the broken IDTs after testing.*

### 5.3.3 Automation of the setup

A LabVIEW program (interface shown in Figure 5.19) was made to automate the setup of the AE coupling over a wide input frequency and power range, with a defined granularity.

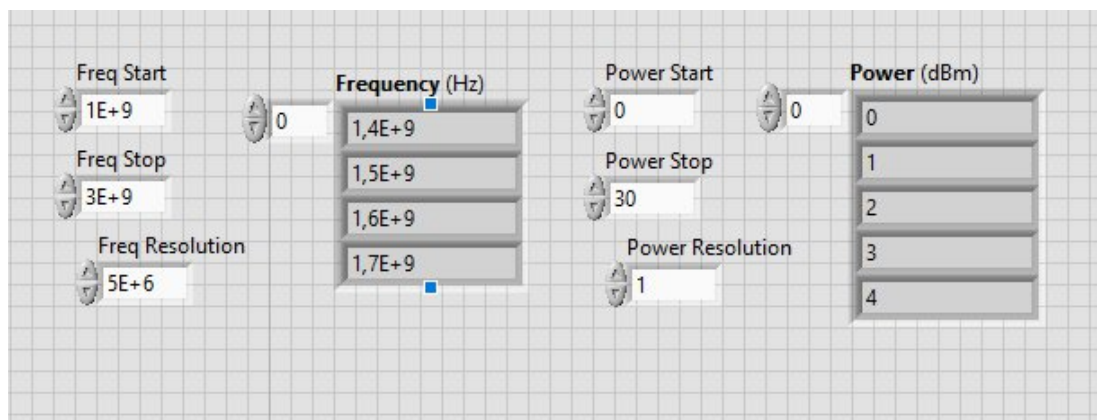


*Figure 5.19: The LabVIEW interface.*

The program was configured to:

1. Set a certain frequency;
2. Set the power;
3. Activate the generator;
4. Wait 30 s;
5. Measure the current;
6. Stop, wait 60 s.

The system would sweep all the power range and then increase frequency. The measurements were performed on the samples ‘R2\_C10’ and ‘R1\_C10’ and the results are shown in Figure 5.20 and Figure 5.21 respectively. **Interestingly, the data clearly shows a switch in sign for some frequencies, which was probably caused by a bulk wave propagation outside the IDTs resonance.** Like in Figure 5.10, some plots at certain frequencies display an elongation, interestingly, in some cases the data at an adjacent frequency does not. This seems to agree with the hypothesis of a frequency shift due to heating.

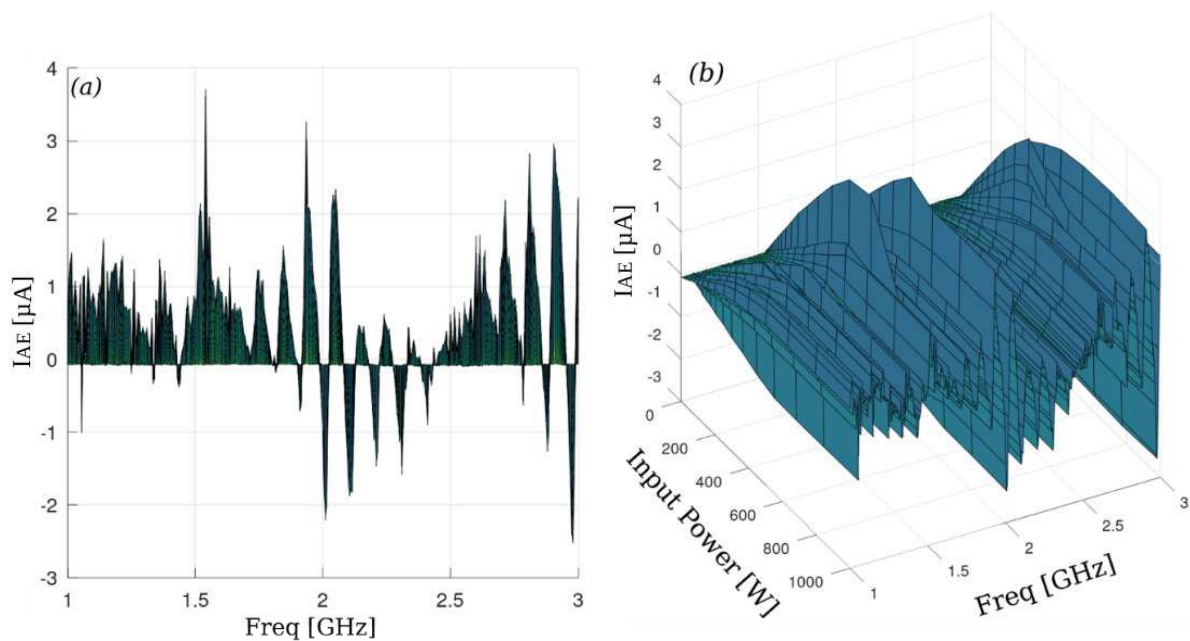


*Figure 5.20: Wide-band AE characterization of the device ‘R2\_C10’ (a) shows the peak  $I_{AE}$  for  $P_{in} = 0 \text{ W} - 0.5 \text{ W}$  and (b) shows the 3D plot of the full data set (black lines connect points for which  $P_{in} = \text{const.}$ , and frequency = const.). The frequency resolution is 5 MHz and the power resolution is 1 dB.*

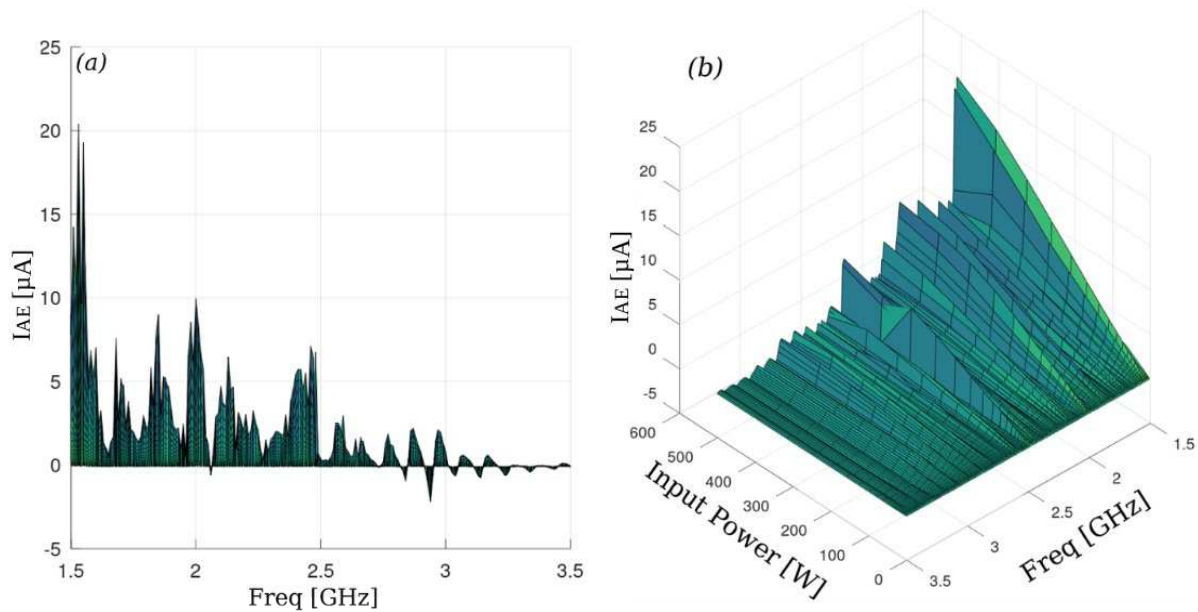


*Figure 5.21: Wide-band AE characterization of the device ‘R1\_C10’ (a) shows the peak  $I_{AE}$  for the measured range  $P_{in} = 0 \text{ W} - 0.5 \text{ W}$  and (b) shows the 3D plot of the full data set (black lines connect points for which  $P_{in} = \text{const.}$ , and frequency = const.). The frequency resolution is 10 MHz and the power resolution is 1 dB.*

## 5.4 Conclusion

In conclusion, the results show a **strong AE coupling for GoL** in the frequency range 2.0 GHz - 3.0 GHz. The data showed a **saturation effect around the input power of 0.4 W**, which was probably due to the heat up from the power dissipation. A breakdown of the IDTs was observed for sufficiently strong outputs and the possible causes have been explored. Finally, the setup used for an automatic wide-band AE characterization was described and the results for the wide-band AE characterization are shown and discussed.

## 5.5 References

- [1] Colin Campbell, *Surface Acoustic Wave Devices and Their Signal Processing Applications*. Academic Press Inc., 1989.
- [2] C. K. Campbell, ‘Applications of surface acoustic and shallow bulk acoustic wave devices’, *Proc. IEEE*, vol. 77, no. 10, pp. 1453–1484, Oct. 1989, doi: 10.1109/5.40664.

- [3] P. Das and M. N. Araghi, 'Surface Wave Signal Processor Using CdS-Fluid-LiNbO<sub>3</sub> Structure', in *1972 Ultrasonics Symposium*, IEEE, 1972, pp. 306–309. doi: 10.1109/ULTSYM.1972.196088.
- [4] A. R. Hutson, J. H. McFee, and D. L. White, 'Ultrasonic Amplification in CdS', *Phys. Rev. Lett.*, vol. 7, no. 6, pp. 237–239, Sep. 1961, doi: 10.1103/PhysRevLett.7.237.
- [5] A. R. Hutson, 'Piezoelectric Scattering and Phonon Drag in ZnO and CdS', *Journal of Applied Physics*, vol. 32, no. 10, pp. 2287–2292, Oct. 1961, doi: 10.1063/1.1777061.
- [6] V. J. Gokhale, Y. Shim, and M. Rais-Zadeh, 'Observation of the acoustoelectric effect in gallium nitride micromechanical bulk acoustic filters', in *2010 IEEE International Frequency Control Symposium*, Newport Beach, CA, USA: IEEE, Jun. 2010, pp. 524–529. doi: 10.1109/FREQ.2010.5556273.
- [7] A. Wixforth, J. Scriba, M. Wassermeier, J. P. Kotthaus, Weimann, G, and Schlapp, W, 'Surface acoustic waves on GaAs/Al<sub>x</sub>Ga<sub>1-x</sub>As heterostructures', *Physical Review B*, vol. 40, no. 11, p. 7874, 1989.
- [8] J. M. Shilton *et al.*, 'Experimental study of the acoustoelectric effects in GaAs-AlGaAs heterostructures', *J. Phys.: Condens. Matter*, vol. 7, no. 39, pp. 7675–7685, Sep. 1995, doi: 10.1088/0953-8984/7/39/010.
- [9] M. Rotter, A. Wixforth, W. Ruile, D. Bernklau, and H. Riechert, 'Giant acoustoelectric effect in GaAs/LiNbO<sub>3</sub> hybrids', *Appl. Phys. Lett.*, vol. 73, no. 15, pp. 2128–2130, Oct. 1998, doi: 10.1063/1.122400.
- [10] R. Adler, 'Simple theory of acoustic amplification', *IEEE Transactions on Sonics and Ultrasonics*, vol. 18, no. 3, pp. 115–118, 1971.
- [11] D. P. Morgan, *Surface acoustic wave filters: with applications to electronic communications and signal processing*, 2nd ed. Amsterdam ; London: Academic Press, 2007.
- [12] P. Defranould and C. Maerfeld, 'A SAW planar piezoelectric convolver', *Proc. IEEE*, vol. 64, no. 5, Art. no. 5, 1976, doi: 10.1109/PROC.1976.10203.
- [13] S. A. Reible, 'Acoustoelectric Convolver Technology for Spread-Spectrum Communications', *IEEE Transactions on Microwave Theory and Techniques*, vol. 29, no. 5, pp. 463–474, 1981.
- [14] V. Miseikis, J. E. Cunningham, K. Saeed, R. O'Rourke, and A. G. Davies, 'Acoustically induced current flow in graphene', *Appl. Phys. Lett.*, vol. 100, no. 13, Art. no. 13, Mar. 2012, doi: 10.1063/1.3697403.

- [15] L. Bandhu and G. R. Nash, ‘Controlling the properties of surface acoustic waves using graphene’, *Nano Research*, vol. 9, pp. 685–691, 2016.
- [16] L. Bandhu and G. R. Nash, ‘Temperature dependence of the acoustoelectric current in graphene’, *Appl. Phys. Lett.*, vol. 105, no. 26, Art. no. 26, Dec. 2014, doi: 10.1063/1.4905222.
- [17] L. Bandhu, L. M. Lawton, and G. R. Nash, ‘Macroscopic acoustoelectric charge transport in graphene’, *Appl. Phys. Lett.*, p. 5, 2014.
- [18] A. Hernández-Mínguez, A. Tahraoui, J. M. J. Lopes, and P. V. Santos, ‘Acoustoelectric transport at gigahertz frequencies in coated epitaxial graphene’, *Appl. Phys. Lett.*, vol. 108, no. 19, p. 193502, May 2016, doi: 10.1063/1.4949756.
- [19] T. Poole and G. R. Nash, ‘Acoustoelectric Current in Graphene Nanoribbons’, *Sci Rep*, vol. 7, no. 1, p. 1767, Dec. 2017, doi: 10.1038/s41598-017-01979-8.
- [20] O. A. C. Nunes, ‘Piezoelectric surface acoustical phonon amplification in graphene on a GaAs substrate’, *Journal of Applied Physics*, vol. 115, no. 23, p. 233715, Jun. 2014, doi: 10.1063/1.4883914.
- [21] S. Okuda *et al.*, ‘Acoustic carrier transportation induced by surface acoustic waves in graphene in solution’, *Appl. Phys. Express*, vol. 9, no. 4, p. 045104, Apr. 2016, doi: 10.7567/APEX.9.045104.
- [22] J. R. Lane, L. Zhang, M. A. Khasawneh, B. N. Zhou, E. A. Henriksen, and J. Pollanen, ‘Flip-chip gate-tunable acoustoelectric effect in graphene’, *Journal of Applied Physics*, vol. 124, no. 19, p. 194302, Nov. 2018, doi: 10.1063/1.5047211.
- [23] A. Hernández-Mínguez, Y.-T. Liou, and P. V. Santos, ‘Interaction of surface acoustic waves with electronic excitations in graphene’, *J. Phys. D: Appl. Phys.*, vol. 51, no. 38, Art. no. 38, Sep. 2018, doi: 10.1088/1361-6463/aad593.
- [24] F. Giubileo and A. Di Bartolomeo, ‘The role of contact resistance in graphene field-effect devices’, *Progress in Surface Science*, vol. 92, no. 3, pp. 143–175, Aug. 2017, doi: 10.1016/j.progsurf.2017.05.002.
- [25] D. C. Malocha, C. Carmichael, and A. Weeks, ‘Acoustoelectric Amplifier With 1.2-dB Insertion Gain Monolithic Graphene Construction and Continuous Wave Operation’, *IEEE Trans. Ultrason., Ferroelect., Freq. Contr.*, vol. 67, no. 9, Art. no. 9, Sep. 2020, doi: 10.1109/TUFFC.2020.2984176.
- [26] C. Carmichael, D. C. Malocha, and A. Weeks, ‘Asymmetric energy coupling through acoustoelectric effect using graphene on lithium niobite surface acoustic wave delay line

- in GHz Range’, in *2019 IEEE International Ultrasonics Symposium (IUS)*, Glasgow, United Kingdom: IEEE, Oct. 2019, pp. 702–705. doi: 10.1109/ULTSYM.2019.8925837.
- [27] Graphenea, Inc., ‘Graphenea Monolayer Graphene on Polymer Film Datasheet’. Accessed: Oct. 10, 2022. [Online]. Available: [https://cdn.shopify.com/s/files/1/0191/2296/files/Graphenea\\_Monolayer\\_Graphene\\_on\\_Polymer\\_Film\\_Datasheet\\_02-16-2022.pdf?v=1645025331](https://cdn.shopify.com/s/files/1/0191/2296/files/Graphenea_Monolayer_Graphene_on_Polymer_Film_Datasheet_02-16-2022.pdf?v=1645025331)
- [28] G. K. Reeves and H. B. Harrison, ‘Obtaining the specific contact resistance from transmission line model measurements’, *IEEE Electron Device Lett.*, vol. 3, no. 5, pp. 111–113, May 1982, doi: 10.1109/EDL.1982.25502.
- [29] V. Kumar, A. Kumar, D.-J. Lee, and S.-S. Park, ‘Estimation of Number of Graphene Layers Using Different Methods: A Focused Review’, *Materials*, vol. 14, no. 16, p. 4590, Aug. 2021, doi: 10.3390/ma14164590.
- [30] A. C. Ferrari and D. M. Basko, ‘Raman spectroscopy as a versatile tool for studying the properties of graphene’, *Nature Nanotech*, vol. 8, no. 4, pp. 235–246, Apr. 2013, doi: 10.1038/nnano.2013.46.
- [31] Z. H. Ni *et al.*, ‘The effect of vacuum annealing on graphene’, *Journal of Raman Spectroscopy*, vol. 41, no. 5, pp. 479–483, 2010, doi: 10.1002/jrs.2485.
- [32] A. Hsu, H. Wang, K. K. Kim, J. Kong, and T. Palacios, ‘Impact of Graphene Interface Quality on Contact Resistance and RF Device Performance’, *IEEE Electron Device Lett.*, vol. 32, no. 8, Art. no. 8, Aug. 2011, doi: 10.1109/LED.2011.2155024.
- [33] J. S. Moon *et al.*, ‘Ultra-low resistance ohmic contacts in graphene field effect transistors’, *Appl. Phys. Lett.*, vol. 100, no. 20, Art. no. 20, May 2012, doi: 10.1063/1.4719579.
- [34] H. Zhong *et al.*, ‘Realization of low contact resistance close to theoretical limit in graphene transistors’, *Nano Res.*, vol. 8, no. 5, Art. no. 5, May 2015, doi: 10.1007/s12274-014-0656-z.
- [35] K. Kurokawa, ‘Power Waves and the Scattering Matrix’, *IEEE Trans. Microwave Theory Techn.*, vol. 13, no. 2, pp. 194–202, Mar. 1965, doi: 10.1109/TMTT.1965.1125964.
- [36] Y. Zhang, L. Zhang, and C. Zhou, ‘Review of Chemical Vapor Deposition of Graphene and Related Applications’, *Acc. Chem. Res.*, vol. 46, no. 10, pp. 2329–2339, Oct. 2013, doi: 10.1021/ar300203n.
- [37] L.-W. Chang, M. Alexe, J. F. Scott, and J. M. Gregg, ‘Settling the “Dead Layer” Debate in Nanoscale Capacitors’, *Adv. Mater.*, vol. 21, no. 48, pp. 4911–4914, Dec. 2009, doi: 10.1002/adma.200901756.

- [38] D. De Fazio *et al.*, ‘High-Mobility, Wet-Transferred Graphene Grown by Chemical Vapor Deposition’, *ACS Nano*, vol. 13, no. 8, pp. 8926–8935, Aug. 2019, doi: 10.1021/acsnano.9b02621.
- [39] A. Venugopal *et al.*, ‘Effective mobility of single-layer graphene transistors as a function of channel dimensions’, *Journal of Applied Physics*, vol. 109, no. 10, p. 104511, May 2011, doi: 10.1063/1.3592338.



# Contents of the chapter:

- 6 Preliminary results on acoustoelectronic convolvers ..... 184
  - 6.1 Convolver.....184
  - 6.2 Numerical simulation of the devices.....186
    - 6.2.1 Description of the algorithm.....186
    - 6.2.2 Simulated results ..... 188
    - 6.2.3 Description of the experiments.....190
    - 6.2.4 Difference between batches variations..... 199
    - 6.2.5 Explanation of the optimized current ..... 200
  - 6.3 AE GoL SAW amplifiers.....201
  - 6.4 Conclusions.....202
  - 6.5 References.....203

## 6 Preliminary results on acoustoelectronic convolvers

This chapter displays the numerical analysis and experimental results to perform nonlinear Surface Acoustic Wave (SAW) acoustoelectronic convolver and amplifier devices produced using the GoL technology. The SAW signals are generated via Inter-Digital Transducers (IDT) and the nonlinearity is excited via an applied DC current, which also serves an amplification on the acoustic field.

### 6.1 Convolver

As stated in the introduction, SAW acoustoelectronic convolvers based on two contra-propagation waves exists in degenerated and non-degenerate versions. **The convolution is achieved through a nonlinear mixing of the acoustic waves in a nonlinear medium.** The nonlinearity can either be **mechanically** caused, in the case of metallic thin film convolvers, or **electrically** generated, in the case of semiconductive films.

Degenerate convolvers are well adapted for a thin metallic film technology, as their manufacture is relatively straightforward, however, they introduce considerable damping and scattering on the acoustic field. The semiconductive films can be coupled with an air gap, reducing mechanical losses and enabling more complex architectures [1], [2], however, they also possess a much more challenging and costly manufacture which usually overweighs the benefits [3], [4].

The convolver design implemented here overcomes the limitation of classical metallic-film and semiconductive-film designs, through the use of the nonlinear electrical coupling between a DC current in graphene and the electric field component in the SAW Rayleigh waves in piezoelectric substrates. This kind of convolver was first theorized by *Wang and Das* in 1972 [5] and physically manufactured and demonstrated by *Solie et al.* in 1973 for a thin CdS film on LiNbO<sub>3</sub> [6], [7]. This simple design uses a **DC current to both achieve bidirectional amplification and convolution**, revealing a very efficient and simple design.

The response of the device was modeled starting from the mathematical description of the phenomenon from *Wang and Das* [5]. Modeling the nonlinear electric conduction of

graphene on the piezoelectric LiNbO<sub>3</sub> during the SAW propagation, while also including the electron drift, channel modulation and secondary effects due to the metallic contacts is quite complex. Figure 6.1 gives a hint of the complexity of the problem to be solved in the case of acoustic propagating waves, with the radiated electric field and with charge accumulation/migration. Indeed, **the model proposed cannot take into account the effects caused by the metallic Au contacts**. Indeed, the mass loading and electrical loading of metal films tend to guide the wave underneath [4], which could also be used for more interesting designs.

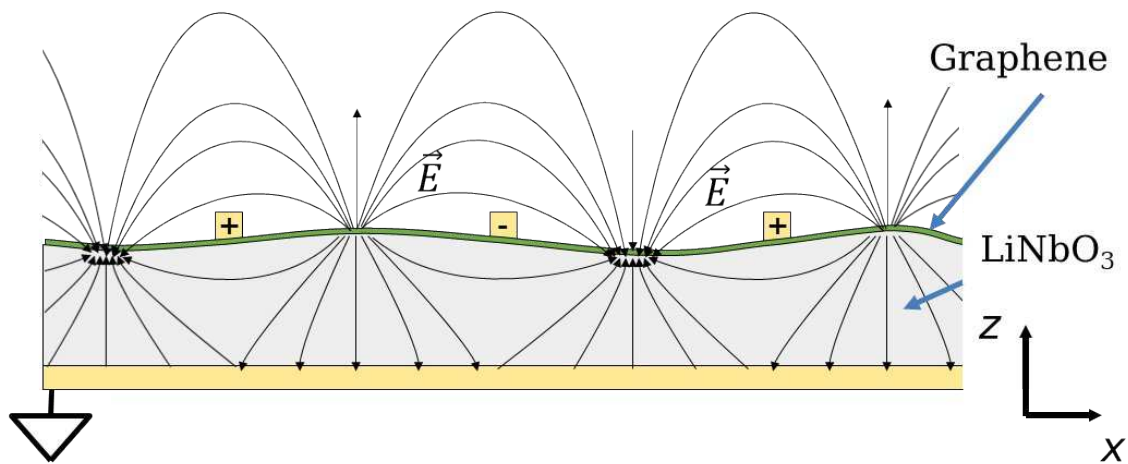


*Figure 6.1: Cross-section representation of the GoL convolver.*

The convolver considered is shown in Figure 6.2. On the left, there is port 1, which is used to generate the acoustic waves propagating to the right with  $\vec{k}_1 = \beta_1 \hat{x}$  and  $\omega_1$  through IDT 1, on the right, there is port 2, which, through IDT 2, is used to generate the contra-propagating waves to the left, with  $\vec{k}_2 = -\beta_2 \hat{x}$  and  $\omega_2$ , and finally, in between there is a **non-degenerated (Chapter 1.4.2.2) electrode pattern** lattice underneath of the graphene for collecting the charges to port 3. The convolver can be used in a degenerate mode, where a phase match is ensured by the same propagating velocity of  $\omega_1$  and  $\omega_2$ , so that  $\omega_1 + \omega_2 = \omega_3$  and  $\vec{k}_1 + \vec{k}_2 = \vec{k}_3 \cong 0$ . In Figure 6.2 the shiny surface is constituted by the gold electrodes. Graphene is only in the center part of port 3. For the ease of access, both the positive and negative electrodes of port 3 are carried outside of the IDT area via two microstrip waveguides, designed to possess wave impedance  $\sim 50 \Omega$ . On both sides of the device, a gold damping stop has been inserted to

both limits the backscattered acoustic waves and reliably identify the timing of scattering-related events.

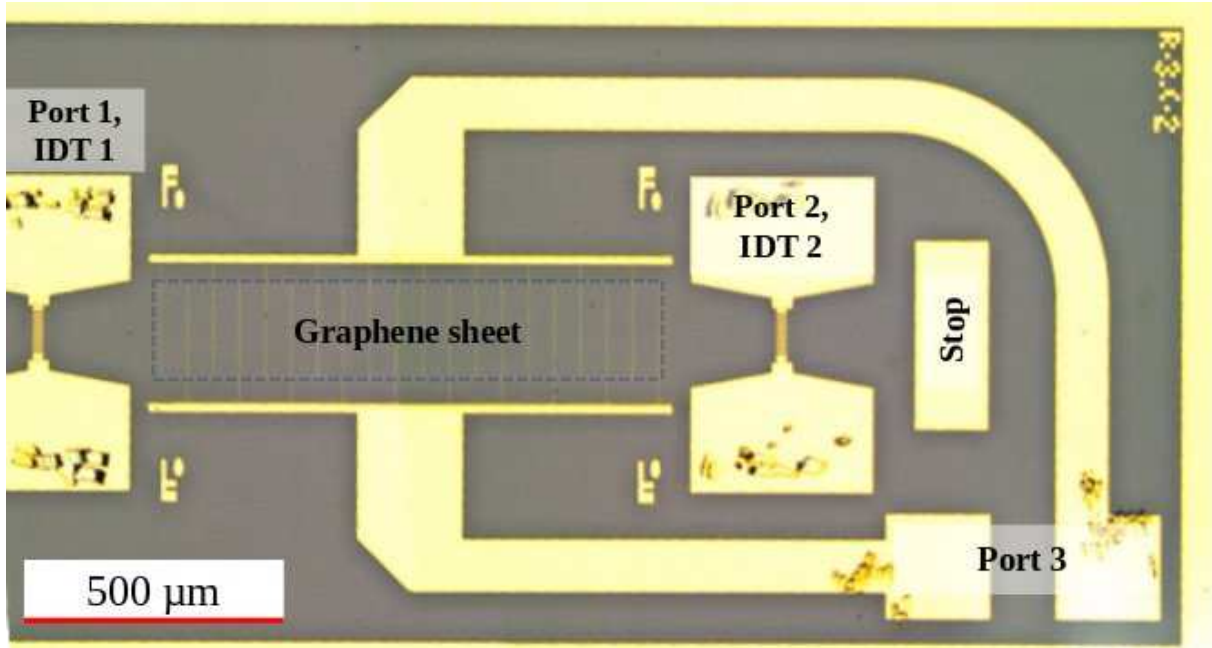


*Figure 6.2: Photo of a GoL SAW convolver device, the distance between the two IDTs is 1.4 mm and the convolver plate is 1 mm long.*

## 6.2 Numerical simulation of the devices

### 6.2.1 Description of the algorithm

As the output of the signal is expected to be distorted by the propagating losses of waves in GoL at **2.5 GHz**, the response of the device was simulated to understand exactly the shape and the timings of the signals to be expected. The complete response of the device (port 3) is represented mathematically as:

$$V_3(t) = k_0(t) + \int_0^L \sum_{i=1}^N k_i \cdot (V_1(\omega t - \gamma x) + V_2(\omega t + \gamma x))^i dx, \quad (6.1)$$

Where  $k_0(t)$  is a DC voltage given by the AE effect and is a function of the envelope of the signal  $V_1$  and  $V_2$  generated by port 1 and port 2,  $\gamma$  is the propagation constant of the waves and  $k_i$  are values which depend on:

1. The linear and the nonlinear response of the LiNbO<sub>3</sub> crystal;

2. The AE coupling;
3. The nonlinear coefficients of the signal generators and amplifiers.

Numerically simulating the response of the convolver means to solve the space-like integral for the two moving inputs at each time point. For the sake of simplicity and speed, only the frequency components of the carrier  $f_0$  and at  $2 \cdot f_0$ , are considered ( $N=2$ ). As represented in Figure 6.3, the mechanical waves are numerically treated as an array of  $M$  elements and the convolver plate is defined as an array of  $P$  elements, each element of the arrays correspond to a finite length  $dx$ , which is bound to a finite time resolution  $dt$  via the speed of the acoustic wave:

$$dt = dx/v_0. \quad (6.2)$$

It must be noted that, in order to reduce numerical errors, the value of  $dx$  is chosen to be an integer fraction of the acoustic wavelength  $\lambda$ :

$$dx = \frac{\lambda}{i}, \quad i \in \mathbb{N} - \{0\}. \quad (6.3)$$

The algorithm of the simulation is as follows:

1. Define the input waveforms  $V_1(t)$  and  $V_2(t)$ ,
2. Pre-multiply the inputs by the  $e^{-\alpha t/v_0}$  to take into account the propagation loss,
3. Convert  $V_1(t)$  and  $V_2(t)$  to their discrete  $M$ -long array  $V_1(i)$ ,  $V_2(i)$ ,
4. Define the convolver window function  $C_W$ ,
5. Compute the response at the instant  $i = 0$ ,
6. Shift  $V_1(i)$  and  $V_2(i)$ ,
7. Compute the response at the instant  $i = 1$ ,
8. Apply propagation loss ( $V_1(i) V_1(i) \cdot e^{-\alpha \cdot dt/v_0}$ ,  $V_2(i) V_2(i) \cdot e^{-\alpha \cdot dt/v_0}$ ),
9. ...
10. End after  $M+P$  steps.

The window function of the convolver is  $C_W$  is defined by the size of the convolver plate, its pattern, and the AE amplification/attenuation. The response at each time step  $i \cdot dt$  are multiplied through the linear and quadratic response weighted by  $C_W$ :

$$V_3(i \cdot dt) = \sum_{j=1}^{C_W} \left( k_1 \cdot (V_1(j) + V_2(j)) + k_2 \cdot (V_1(j) + V_2(j))^2 \right) \cdot C_W(j), \quad (6.4)$$

where  $\sum_{j=1}^{C_W}$  denotes the sum over the length of  $C_W$ .

Finally,  $C_W$  is built to include the contributes of a nonlinearly spaced convolver which will be used in the simulation of more complex designs.

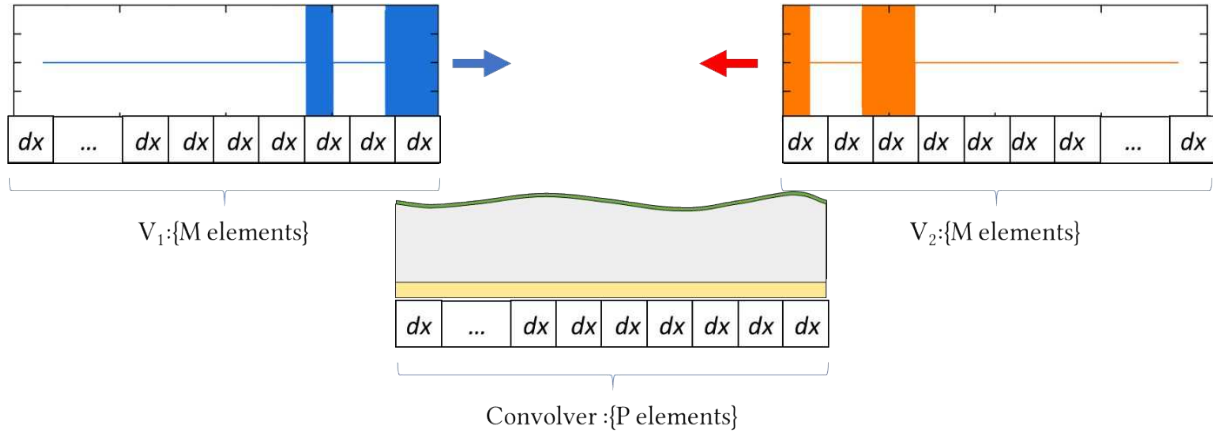


**Figure 6.3: Representation of the numerical simulation.**

## 6.2.2 Simulated results

As discussed more in detail in Section 6.2.3, the convolvers were tested via amplitude-modulated waveforms on a 2.55 GHz carrier. Before performing the experiments, the outputs of the waveforms used to have been simulated numerically assuming the standard propagation speed for x-propagating SAW waves on YX-128° LiNbO<sub>3</sub>  $v_0 = 3992$  m/s. Both the ideal case of null propagation velocity  $\alpha = 0$  m<sup>-1</sup>, and the case of the previously measured  $\alpha = 1550$  m<sup>-1</sup>, symmetrical for both directions of propagation, have been considered, and the results are confronted and discussed.

The self-correlation, equivalent to the self-convolution for the time-symmetric input of the 250 ns wide square pulse is shown in Figure 6.4. Considering a delay time between the trigger event at 0 ns and the arrival of the SAW at the convolver plate at  $\sim 240$  ns, the ideal response in Figure 6.4(a) displays a triangular wave peaking at  $\sim 490$  ns. However, when considering the mechanical propagation losses in the crystal, as shown in Figure 6.4(b), the amplitude of the output shrinks considerably and the shape gets slightly distorted and a small quadratic response from the single inputs  $V_1(t)$  and  $V_2(t)$  gets visible. **Most importantly, however, the peak position does not shift in time.**

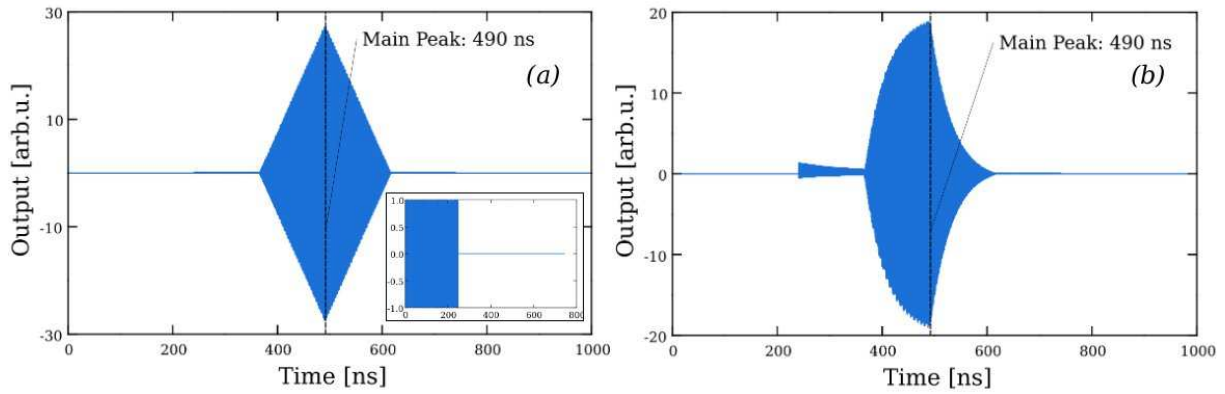


**Figure 6.4:** Simulated self-correlation output from a defined 250 ns pulsed input (insert in (a)). (a) Displays the ideal case of null propagation loss ( $\alpha = 0 \text{ m}^{-1}$ ) and (b) considers the measured propagation loss of  $\alpha = 1550 \text{ m}^{-1}$ .

The self-correlation of the Amplitude-Shift Keying (ASK) modulated input is displayed in Figure 6.5. The ideal response in Figure 6.5(a) displays three peaks; the main central peak is caused by the complete overlap of the waves, and is centered at  $\sim 490 \text{ ns}$ . The secondary peaks are at  $\sim 345 \text{ ns}$  and  $\sim 519 \text{ ns}$  respectively and represent a partial overlap of the inputs. When considering the mechanical propagation losses in the crystal, in the results in Figure 6.26(b), similarly as the previous case, the amplitude of the output shrinks considerably and each consecutive peak gets progressively smaller due to the propagation loss, as much as the first sidelobe gets bigger than the second, which was the opposite of the ideal case.

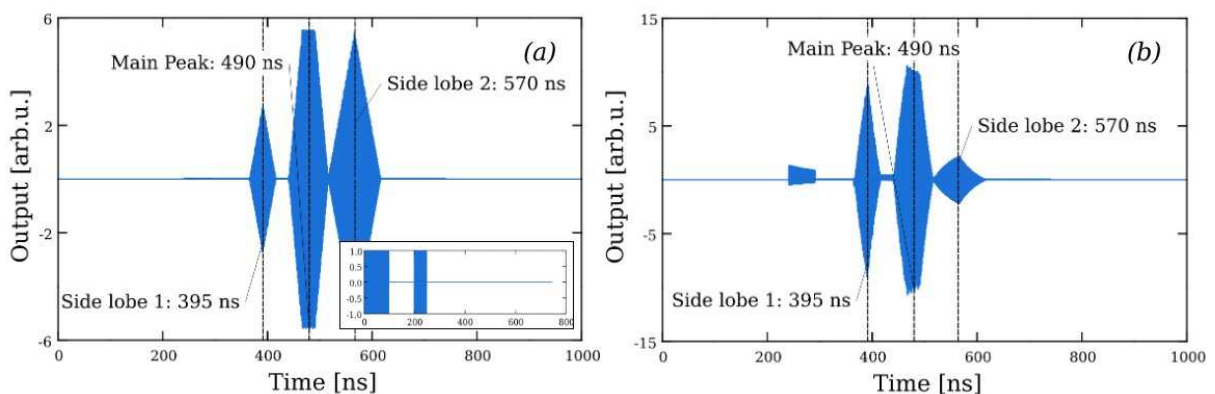


**Figure 6.5:** Simulated self-convolution output from the defined ASK waveform (insert in (a)). (a) Displays the ideal case of null propagation loss ( $\alpha = 0 \text{ m}^{-1}$ ) and (b) considers the measured propagation loss of  $\alpha = 1550 \text{ m}^{-1}$ .

### 6.2.3 Description of the experiments

The setup for exciting the convolver and collecting the results is explained in Figure 6.6 and pictured in Figure 6.7. The signals at the two inputs Port 1 and Port 2 were generated and synchronized via the same arbitrary waveform signal generator, the Tektronix AWG7122B [8], which was capable to drive two output channels with a sample rate of 12 GS/s, a 10-bit voltage resolution and a power available  $P_a$  of 3 dBm at of the each outputs. Both outputs from the generator were amplified via a Mini-Circuits ZX60-V62+ [9] and filtered via a Mini-Circuits VLFG-3500+ [10] 3.5 GHz low-pass filter, for a total gain of  $\sim 12$  dBm at 2.5 GHz. This was enough to cancel out spurious outputs from the generator, which otherwise were visible on the output.

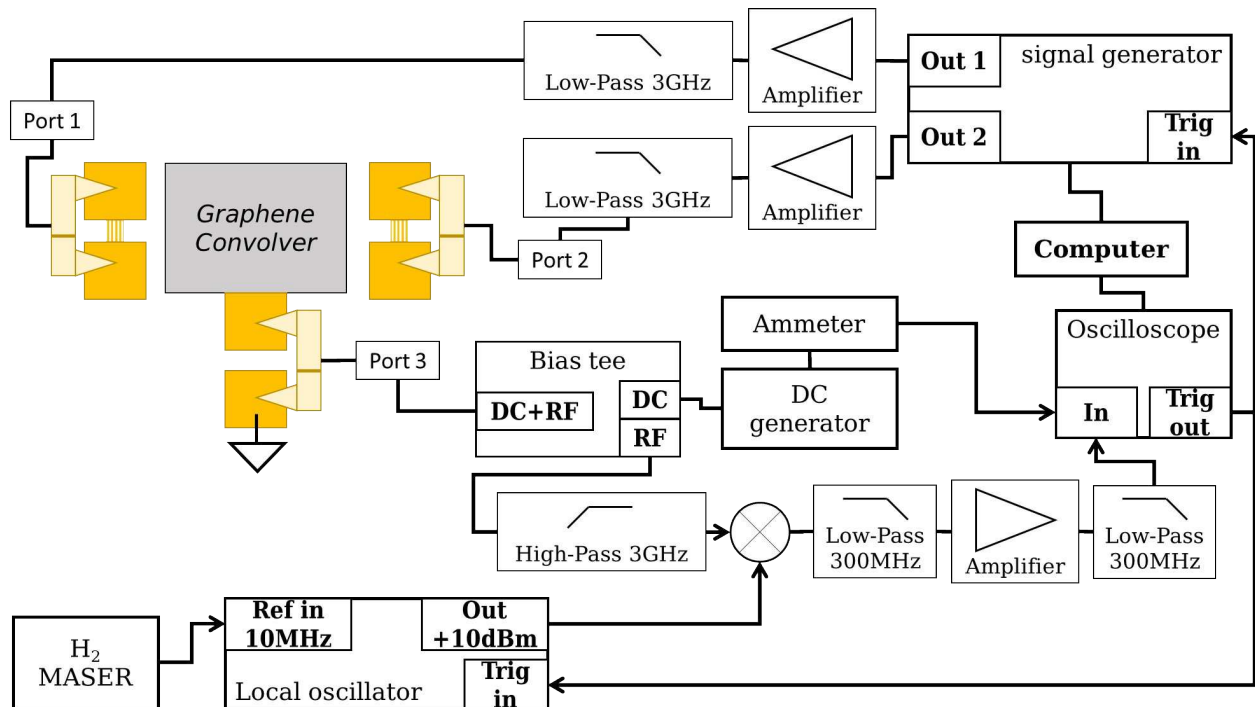


*Figure 6.6: Block diagram of the measurement setup.*

The splitting of the DC current  $I_{Gr}$  and the output signal was performed via a Bias-Tee which connected the 0 MHz – 50 MHz band with the “DC” port and the 50 MHz – 6000 MHz with the RF port. The detection of the output signal from the convolver was performed from the RF port via a **heterodyne system** composed of a VHF-3500+ [11] 4 GHz high-pass filter mixer, which had an insertion loss  $< 1$  dB at 5 GHz and 30 dB at 2.5 GHz, a double-balanced mixer (Mini-Circuit ZX05-63LH-S+ [12]) to lower the signal frequency to the a desired  $f_{IF}$

through mixing with the output of a sinusoidal signal generator, the Keysight N5181B [13], which was phase-stabilized through an H<sub>2</sub> MASER reference and was capable of generating a reference  $f_{LO}$  6 kHz - 6 GHz.

The converted output was then filtered with a 300 MHz low-pass filter (Crystek CLPFL-0300 [14]), fed to a low-noise amplifier (Mini-Circuit ZX60-P103LN [15]), filtered with a second 300 MHz low-pass filter (Crystek CLPFL-0300 [14]) and finally monitored via an oscilloscope [16]. **The total conversion gain from the heterodyne setup was estimated ~15 dB for  $f_{IF} = 20$  MHz.**



*Figure 6.7: Photo of the setup.*

Before starting performing the convolution tests, **the VNA (Keysight P5004) was calibrated via the Short-Open-Load-Through (SOLT) method at the Port 1 and Port 2 level and the crosstalk between the SG and GS probes was both tested by using the on-**

sample open circuit standard and leaving the probes floating at the same distance  $< 600 \mu\text{m}$ . The measured values were  $< -50 \text{ dB}$  over the frequency range  $0 \text{ GHz} - 2.7 \text{ GHz}$  and remained  $< -44 \text{ dB}$  until  $\sim 5.4 \text{ GHz}$ .

Afterwards, the  $\sim 1 \text{ mm}$  electrical length of the  $50 \Omega$  SG and GS probes were de-embedded via software through the characterization of a known an Open and Short a characterization of the scattering parameters  $S_{11}$ ,  $S_{21}$ ,  $S_{22}$ ,  $S_{12}$  of the delay line was performed (distance between probes  $\sim 1.7 \text{ mm}$ ), shown in Figure 6.8, which reveal a SAW propagation peak at  $\sim 2.55 \text{ GHz}$ , plus other secondary peaks, caused by bulk wave propagation and secondary modes from the IDTs. The SAW propagation peak was then confirmed via the AE current, finding  $\sim 1 \mu\text{A}$  for a  $2.547 \text{ GHz}$  input signal of amplitude  $17 \text{ dBm}$  at IDT 1.

Following a second calibration, the VNA was connected to the graphene convolver plate to measure the  $S_{11}$ , in order to find the impedance of convolver plate at the Port 3 level, shown in Figure 6.9, demonstrating an impedance of  $\sim 40 \Omega$  at the second harmonic ( $5.1 \text{ GHz}$ ) and  $52.545 + 18.78i \Omega$  at the carrier ( $2.55 \text{ GHz}$ ). The same procedure was repeated for a AZnLOF-process type sample (*sample B*) and a S1813-process variation sample (*sample F*). The main discussion is based on the results of the latter and the results of sample B are described in Section 6.2.4.

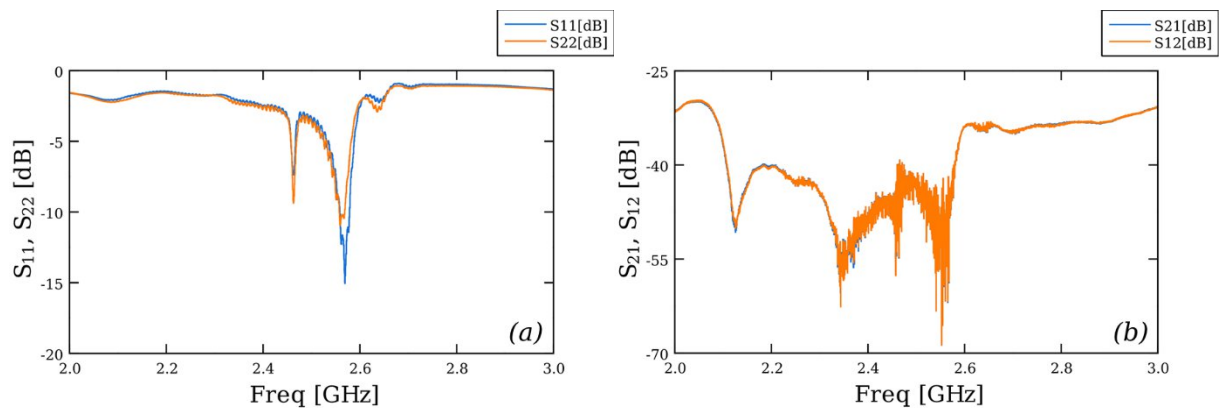


**Figure 6.8: Amplitude in dB of (a)  $S_{11}$ ,  $S_{22}$  and (b)  $S_{21}$ ,  $S_{12}$**

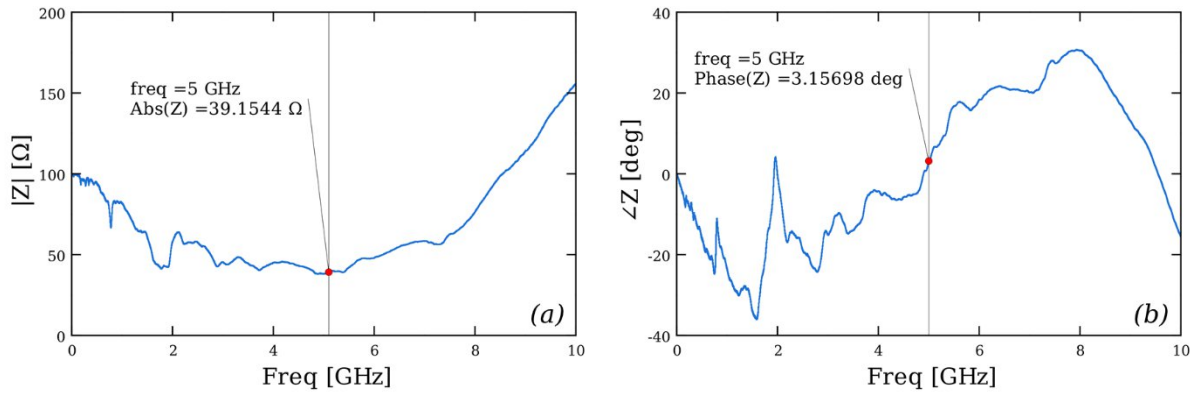


**Figure 6.9: Impedance of the graphene convolver plate at Port 3.**

The first convolution tests were performed in **self-correlation mode of a 250 ns-wide pulse**, which, considering a room-temperature propagation velocity of Rayleigh waves in YX-128° LiNbO<sub>3</sub> and a SAW velocity  $v_0 = 3992$  m/s, was equivalent to a  $\sim 1$  mm length, that was enough to cover the entire convolution plate, maximizing the output.

The testing of the device was divided in three phases:

1. Measurement of the linear averaging,
2. Measurement of the single-port nonlinear response,
3. Convolution and current optimization.

The measurement of the linear response, in Figure 6.10, was performed by tuning  $f_{LO} = f_{RF} - f_{IF}$ . The measured output enabled to confirm the compatibility of the timings with the theory, confirm the linear averaging of the samples and choose the optimal  $f_{IF}$  to maximize the output. First of all, the optimization of the local oscillator output found that the strongest output signal was for  $f_{IF} = 20$  MHz and  $f_{IF} = 80$  MHz and input power from the local oscillator +13 dBm (the maximum defined by the manufacturer).

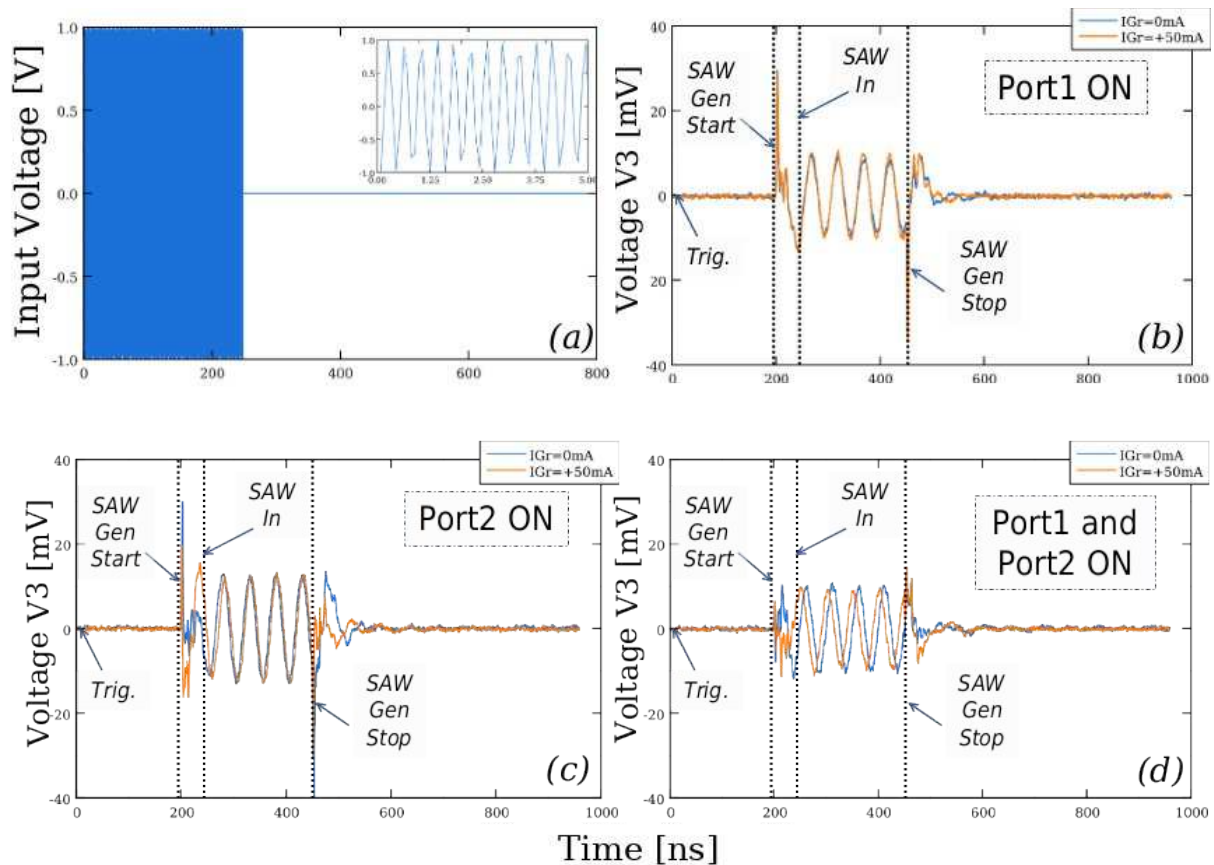


**Figure 6.10:** (a) The defined 250 ns pulsed input signal fed to the signal generator and the corresponding linear response on the graphene generated from input (b) IDT 1, (c) IDT 2 and (d) IDT 1 and IDT 2 with and without the current on graphene (sample F). The insert in (a) is a zoom showing the time resolution of the generator. The timings of the Trigger event, start and stop of the signal generation and time of arrival of the generated SAW at the convolver plate are indicated through the dashed lines.

The timings of the Trigger event, start and stop of the signal generation and time of arrival of the generated SAW at the convolver plate are highlighted. After a **delay of ~190 ns** following the trigger signal, caused by the amplifiers and the filters in the inputs, the sum of the propagation delay in the output waveguides, the cables, the mixer, the amplifier and the filters, and a certain **setup time of the generator**. This event is immediately visible in the output (Figure 6.10(b) and Figure 6.10(c)), likely because of an **electrical cross-talk between the input ports and the output port** caused by the short distance between the probes, which was lower than 300  $\mu\text{m}$ . Instead, the propagation of the SAW between the IDTs and the convolver plate causes an additional ~52 ns between before the acoustically-coupled signal starts to be visible on the output.

Interestingly, both the beginning and end of the electrical generation are accompanied by a sharp delta. As the filters in the input should not let pass frequencies  $> 4$  GHz, this could have been caused by a nonlinear response at the load level, or by the heterodyne amplifier. When activating both of the inputs (Figure 6.10(d)), the delta events for the input and output of the waves cancel out and the total amplitude of the signal decreases considerably, as they were chosen to interfere destructively.

The high propagation delay, together with the high losses in the acoustic field, makes difficult to see the signal exiting from the convolution plate.

When the current is activated, both the amplitude of the signal and its phase changes slightly, which was due to the AE amplification and the local heating-up of the sample.

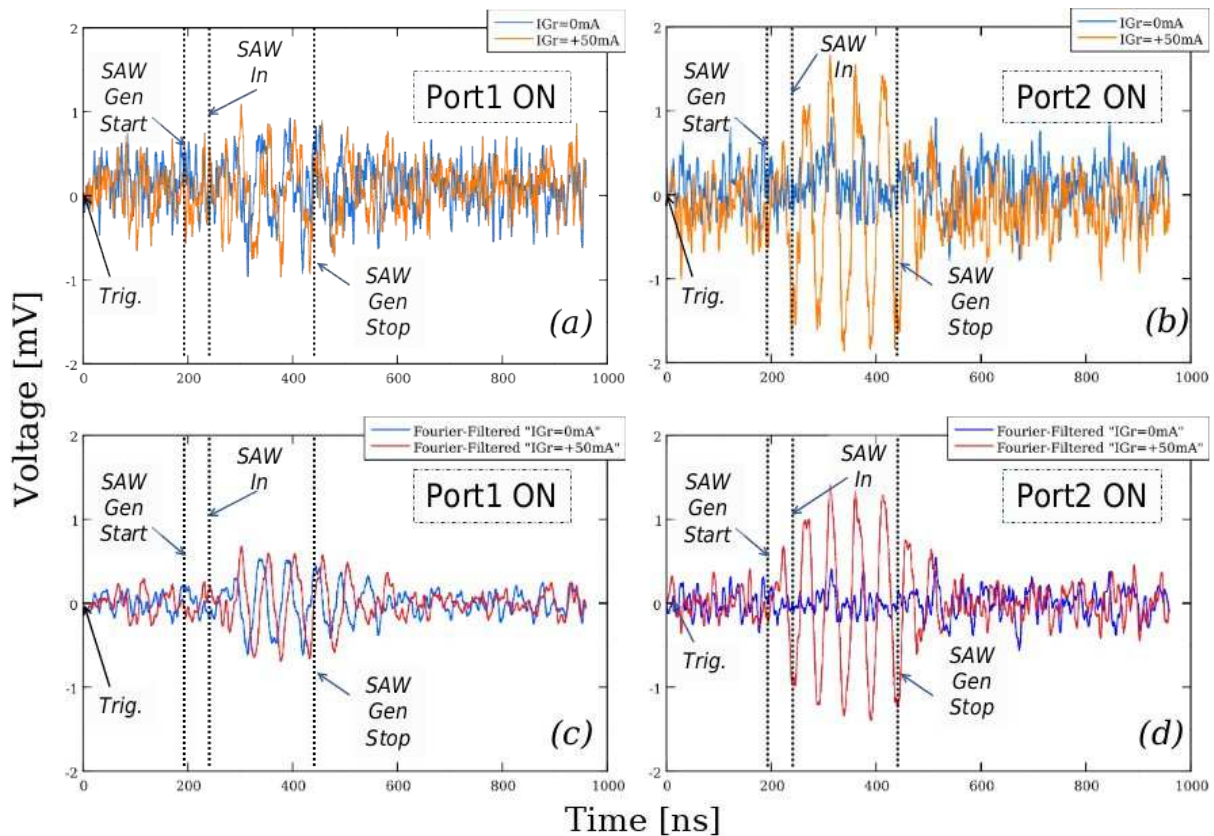


**Figure 6.11:** The 2<sup>nd</sup> harmonic output response on the graphene from the defined 250 ns input pulse on (a) IDT 1 and (b) IDT 2 (sample F). (c) and (d) are the numerically filtered output of (a) and (b) respectively (1st order Butterworth band-pass 10 MHz – 30 MHz). The timings of the Trigger event, start and stop of the signal generation and time of arrival of the generated SAW at the convolver plate are indicated through the dashed lines.

The monitoring of the second harmonic was performed by changing the  $f_{LO}$  to  $2 \cdot f_{RF} - f_{IF}$  and it was performed with and without the current on the graphene, as shown in Figure 6.11. The data demonstrates a strong nonlinear coefficient from the small current of 50 mA. Interestingly, the outputs of the signal from port 1 and port 2 are different. In particular, as shown in Figure 6.11(b) and Figure 6.11(d), when  $I_{Gr} = 50$  mA, the signal propagating from IDT 2 has a stronger nonlinear output than for IDT 1, which begins immediately at  $\sim 235$  ns. As demonstrated by Figure 6.11(a), and in the filtered Figure 6.11(c), the signal propagating from IDT 2, instead, is less intense, starts between 10 ns – 40 ns afterwards and is nonzero even when  $I_{Gr} = 0$  mA. The difference was probably caused by slightly different propagation properties of the SAW in the two directions, the different relative direction of the current in graphene, or other structural asymmetries.

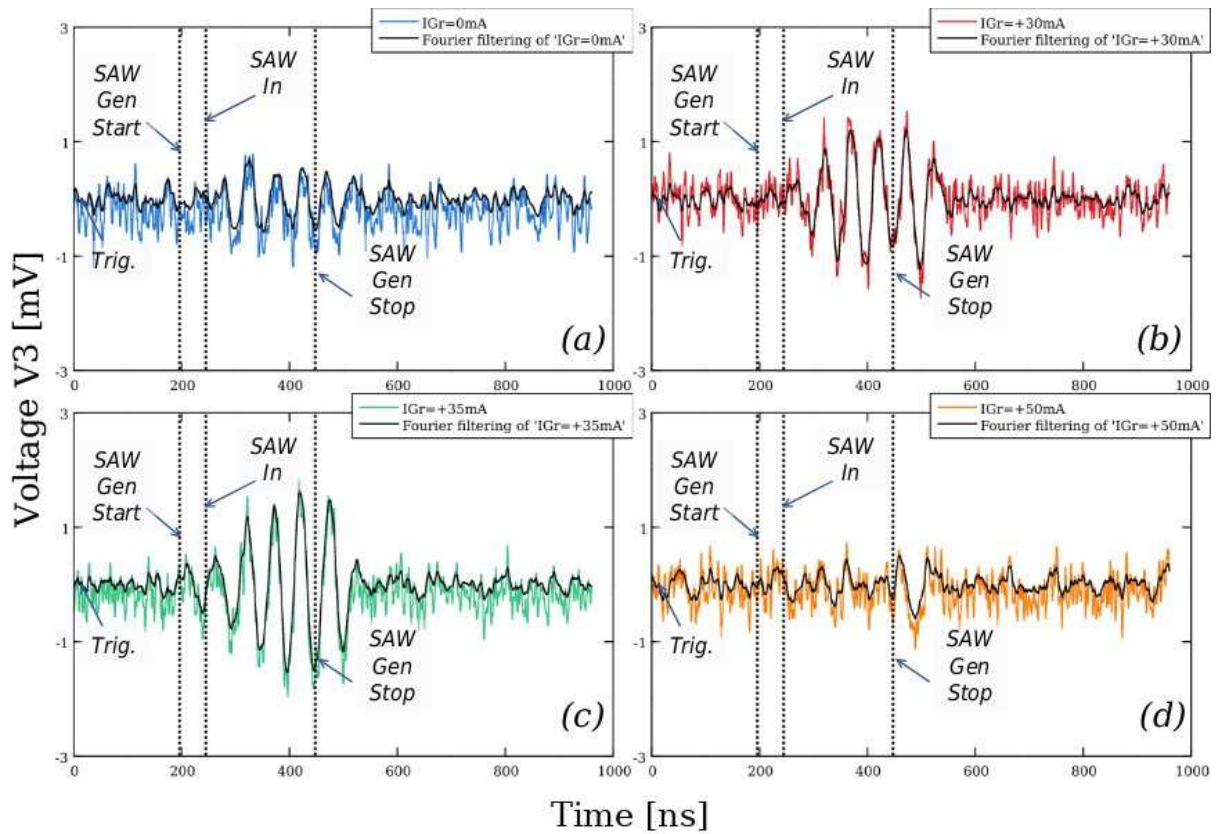


**Figure 6.12:** Raw and numerically filtered (1st order Butterworth band-pass 10 MHz – 30 MHz) self-correlation output from the defined 250 ns input pulse on the graphene when applying the DC current (a)  $I_{Gr} = 0$  mA, (b)  $I_{Gr} = 30$  mA, (c)  $I_{Gr} = 35$  mA and  $I_{Gr} = 50$  mA (sample F). The timings of the Trigger event, start and stop of the signal generation and time of arrival of the generated SAW at the convolver plate are indicated through the dashed lines.

Finally, the convolution output is shown in Figure 6.12, and the Figure 6.13, offers a confront between the measured data and the simulated semi-ideal output frequency-shifted to  $f_{IF}$ , following the configuration of the setup described in Section 6.2.3.

For  $I_{Gr} = 0$  A, the response is comparable to the nonlinear propagation for the signal from port 1 shown in Figure 6.11(a). When the current is set to 50 mA, a small convolution peak is already visible at  $\sim 490$  ns. However, when tuning the current to 30 mA – 35 mA, the response changes and is closer matches the simulated convolution peak shown in the simulations of Section 6.2. Switching the polarity of the DC bias on the graphene did not cause a significant variation on the convolution output.

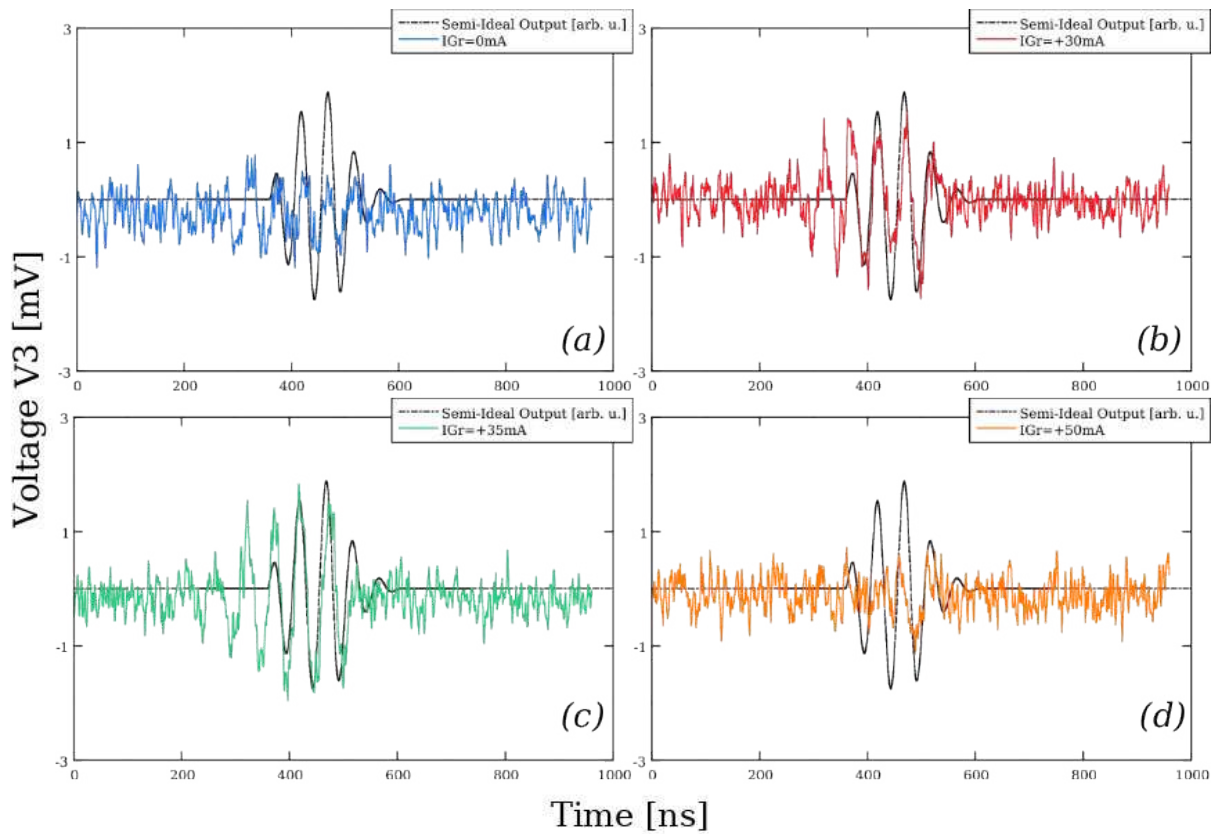


**Figure 6.13:** The semi-ideal simulated output and self-correlation output from the defined 250 ns input pulse on the graphene using the DC current (a)  $I_{Gr} = 0$  mA, (b)  $I_{Gr} = 30$  mA, (c)  $I_{Gr} = 35$  mA and  $I_{Gr} = 50$  mA (sample F).

After confirming the convolution peak, the next step was to test a more complicated **Amplitude-Shift Keying (ASK)** waveform. The ASK waveform was chosen to fill the entire

length of the convolution plate and is shown in Figure 6.14. The output shown in Figure 6.15(a), shows a convolution peak around 490 ns, however, the output at  $f_{IF} = 20$  MHz does not possess enough time resolution to visualize the two side lobes. Switching to  $f_{IF} = 80$  MHz (Figure 6.15(b)) does display a secondary peak at  $\sim 300$  ns, corresponding to the single-port quadratic responses, however, both the first convolution side-lobe at 395 ns is virtually undistinguishable from the primary peak, while the one at  $\sim 570$  ns is considerably less intense due to propagation loss and is under the noise floor.

From the result shown and considering the propagation loss  $\alpha = 1550 \text{ m}^{-1}$  for SAWs at 2.55 GHz, the convolution efficiency internal convolution efficiency of the convolver  $\eta_{cnv}$  was estimated to be  $\sim 34 \text{ dBm}$ . This is among the highest values ever reported for a SAW convolver [2]–[4], [6], [7].

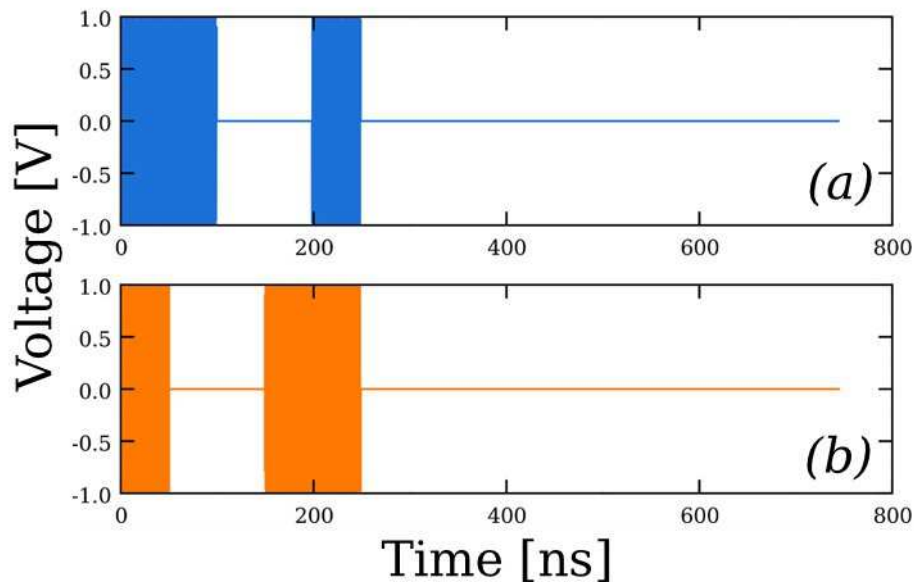


*Figure 6.14: The ASK input waveforms used (a) and its time reverse (b) (sample F).*

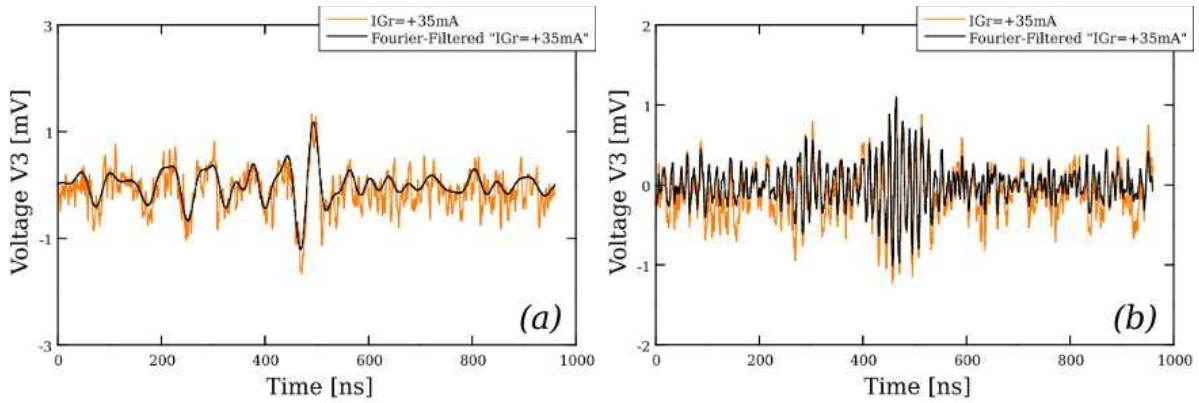


**Figure 6.15:** The raw and filtered data for the auto-convolution of an ASK waveform performed with (a)  $f_{IF} = 20$  MHz (1st order Butterworth band-pass 10 MHz – 30 MHz) and (b)  $f_{IF} = 80$  MHz (1st order Butterworth band-pass 70 MHz – 90 MHz) (sample F).

### 6.2.4 Difference between batches variations

The same was tested with an AZnLOF processed sample (sample B). The difference in resistivity and contact resistivity of the device caused a different electrical and AE response. In particular, the lower resistance displayed in Figure 6.16 allows for better matching, but also led to a lower output voltage and the optimal current was found to be  $\sim 65$  mA, as visible in Figure 6.17 and Figure 6.18.

However, most of the characterization was performed on the S1813 sample and the testing procedure for this sample was not as well optimized.

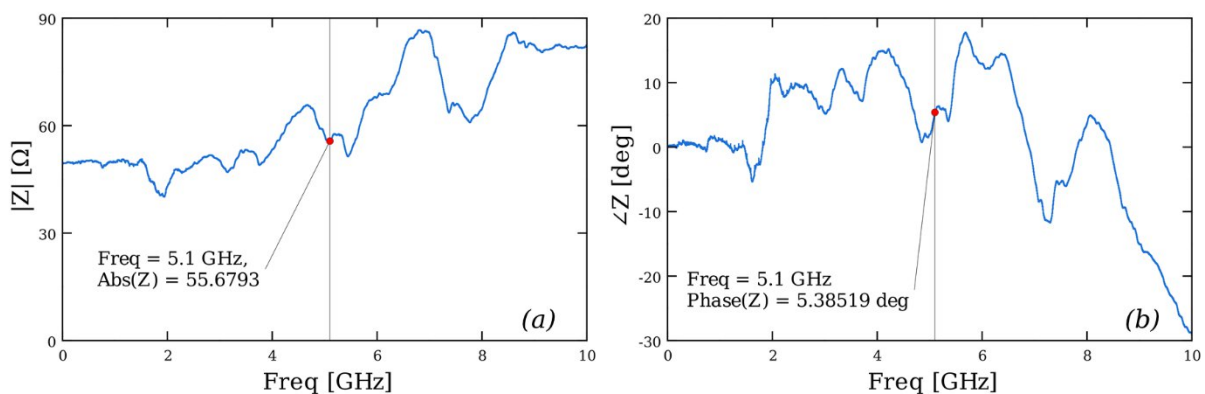


**Figure 6.16:** Impedance of the graphene convolver plate at Port 3 (sample B).

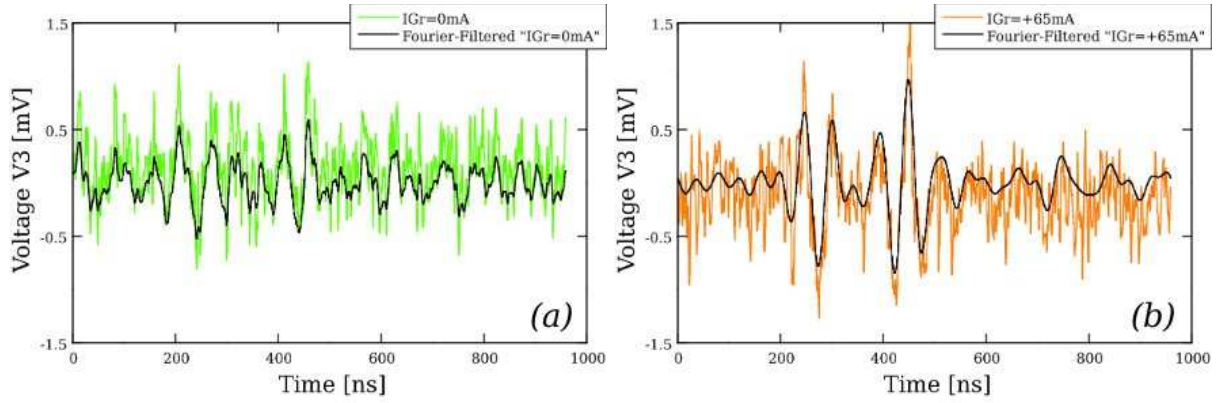


**Figure 6.17:** The auto-convolution of an ASK waveform performed with  $f_{IF} = 20$  MHz on sample B for (a)  $I_{Gr} = 0$  mA and (b)  $I_{Gr} = 65$  mA (band-pass 10 MHz – 30 MHz) (sample B).

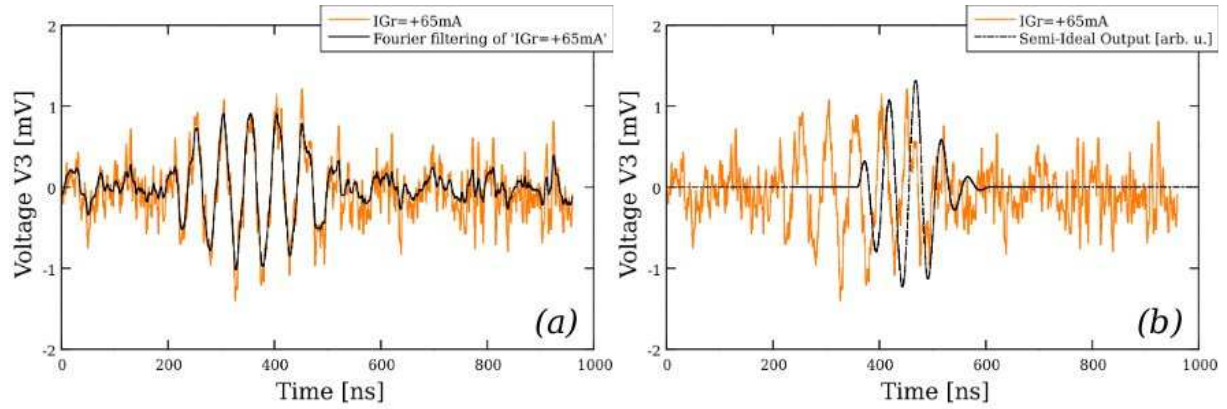


**Figure 6.18:** (a) Raw and numerically filtered (band-pass 10 MHz – 30 MHz) self-correlation output from the defined 250 ns pulsed input on the graphene using the DC current  $I_{Gr} = 65$  mA and (b) confront with the semi-ideal simulated output (sample B).

### 6.2.5 Explanation of the optimized current

The presence of an optimized current is explained via the mobility of the charges in graphene, which for the sample F is  $\mu \approx 1600 \text{ cm}^2/\text{Vs} = 0.16 \text{ m}^2/\text{Vs}$  (see Chapter 4.2), and the velocity of the SAW wave  $v_0 \approx 4000$  m/s. From this assumption, via the definition of mobility via the drift velocity  $v_d$  and electric field  $E$ :

$$v_d = \mu \cdot E. \quad (6.5)$$

If  $v_d = v_0$ , then  $E = v_0/\mu = 24.98$  V/mm. Considering that the interdigital distance of the structure was  $d = 50$   $\mu\text{m}$ , this corresponds to a DC electric potential drop over the graphene:

$$V_0 = E_0 \cdot d = 1.25 \text{ V.} \quad (6.6)$$

As  $v_d$  must be similar in value as  $v_0$  [6], the corresponding resistance is:

$$R_0 = V_0/I_0 = d \cdot (qW\mu \cdot n_s)^{-1}, \quad (6.7)$$

where  $I_0 = qW\mu E_0 n_s$ , and  $n_s$  is the surface charge carrier surface density,  $q$  is the electron's charge and  $W$  is the width of the convolver plate.

Finally, for a measured optimal current  $I_0$ , Equation (6.7) can be rewritten as:

$$I_0 = qWv_0n_s, \quad (6.8)$$

Experimentally, for the sample F, the optimized response was around 35 mA, therefore it is safe to assume  $I_0 \sim 35 \text{ mA}$ , meaning that  $R_0 = 35.68 \ \Omega$ .

Through a TLM analysis of nearby devices, it was estimated that the actual total DC resistance of the graphene sheet was  $70 \ \Omega$ , and that the total contribution of the contact resistance was 20, in part due to the narrow  $0.75 \ \mu\text{m}$ -wide Au contacts. This lines up very well with what observed experimentally.

As for the sample B, the resistivity is roughly half as much, which, by virtue of Equation (6.8), seems to indicate a higher doping.

### 6.3 AE GoL SAW amplifiers

The testing of the amplifiers has been performed in a modified three-port variation of the setup, where the third port could be connected to the second end of the delay line, allowing measuring the gain on the acoustic field from the DC current in graphene. In order to extract the gain, first a characterization of the scattering parameters  $S_{11}$ ,  $S_{21}$ ,  $S_{22}$  and  $S_{12}$  at  $I_{Gr} = 0$  was performed for a null  $I_{Gr}$ , to find the resonance of the IDTs and identify frequency range corresponding to the SAW propagation, where the amplification effect should be visible. The optimal frequency found from the scattering parameters was 2.553 GHz (Figure 6.19(a)), which was then re-tested through the AE coupling, confirming the latter hypothesis. Afterwards, several values of currents were tested and the changes in the scattering parameters were saved after the response was stabilized. Indeed, **the results shown in Figure 6.19(b) display a certain variation in respect to the current, however, the data demonstrate that the**

**amplification is overshadowed by a combination of thermal dissipation and reflected bulk waves.** Some possible solutions to improve the accuracy of the measurements could be:

- pulse the current of graphene,
- search for the most temperature-stable propagation peak in  $S_{21}$  and measure the amplitude of the acoustic wave through the IDTs in the time domain,
- use the direct AE effect to measure the amplitude of the wave before and/or after the distributed amplifier.

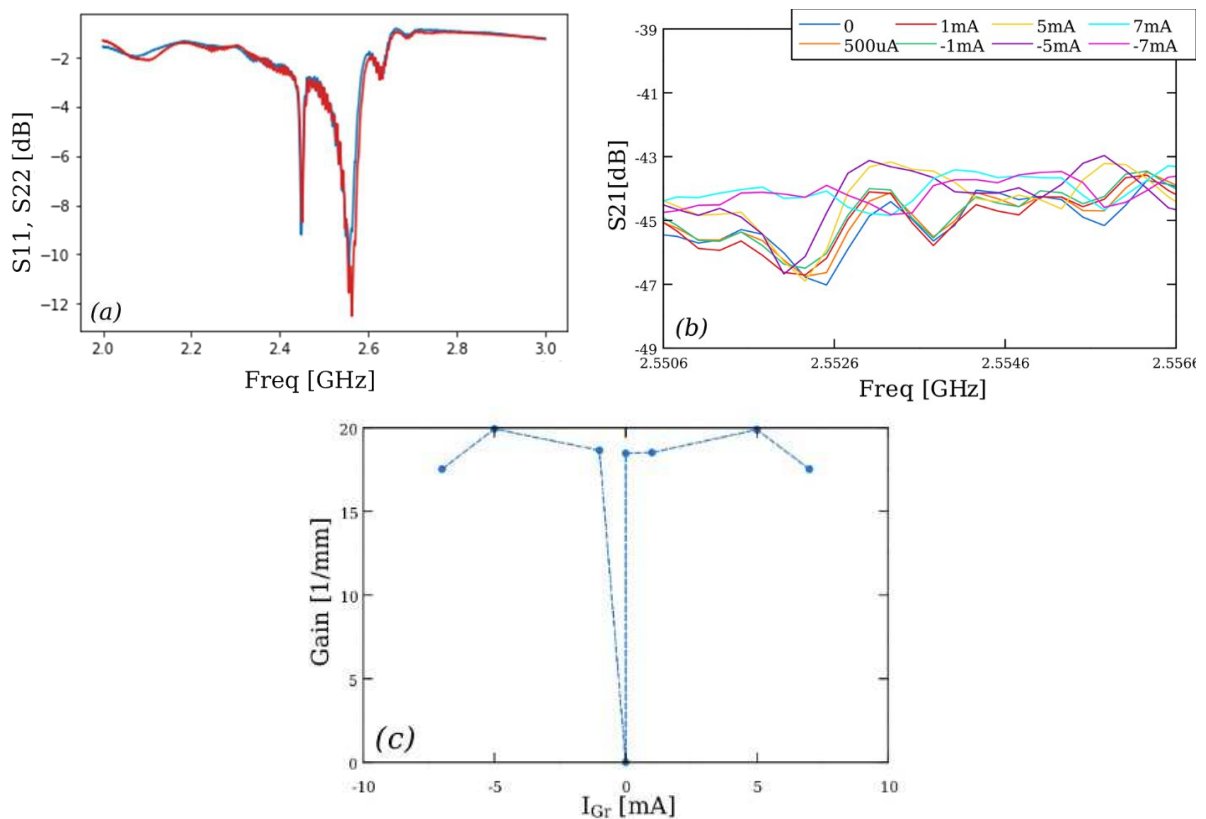


*Figure 6.19: The (a)  $S_{11}$  (blue) and  $S_{22}$  (red) parameters of the device ‘R2\_C1’.*

## 6.4 Conclusions

In conclusion, the first GoL SAW convolver was manufactured and demonstrated. The device exploited a GoL architecture which allowed for high performances and lower losses than for other thin film materials, achieving **one of the highest ever reported convolution efficiency at the highest ever reported operational frequency of 2.55 GHz**. A numerical model was proposed, and the simulated results are quite close to the experimental data. Finally,

AE amplifiers are also shown, however, the relatively low resistivity of the graphene film, plus the thermal deviation of the sample, did not allow to reliably extract the amplification data.

## 6.5 References

- [1] G. S. Kino, S. Ludvik, H. J. Shaw, W. R. Shreve, J. M. White, and D. K. Winslow, ‘Signal Processing by Parametric Interactions in Delay-Line Devices’, *IEEE Transactions on Microwave Theory and Techniques*, vol. 21, no. 4, pp. 244–255, Apr. 1973, doi: 10.1109/TMTT.1973.1127975.
- [2] D. P. Morgan, ‘Surface acoustic wave devices and applications: 5. Signal processing using programmable non-linear convolvers’, *Ultrasonics*, vol. 12, no. 2, pp. 74–83, 1974.
- [3] D. P. Morgan, *Surface acoustic wave filters: with applications to electronic communications and signal processing*, 2nd ed. Amsterdam; London: Academic Press, 2007.
- [4] C. Campbell, *Surface Acoustic Wave Devices and Their Signal Processing Applications*, vol. 89. 1991. Accessed: Aug. 17, 2023. [Online]. Available: <https://pubs.aip.org/jasa/article/89/3/1479/676393/Surface-Acoustic-Wave-Devices-and-Their-Signal>
- [5] W. C. Wang and P. Das, ‘Surface Wave Convolver Via Space Charge Nonlinearity’, in *1972 Ultrasonics Symposium*, IEEE, 1972, pp. 316–322. doi: 10.1109/ULTSYM.1972.196091.
- [6] L. P. Solie, ‘A new mode of operation for the surface-wave convolver’, *Proceedings of the IEEE*, vol. 64, no. 5, pp. 760–763, May 1976, doi: 10.1109/PROC.1976.10207.
- [7] L. P. Solie, ‘An integrated surface wave convolver/amplifier’, in *1973 Ultrasonics Symposium*, Nov. 1973, pp. 175–177. doi: 10.1109/ULTSYM.1973.196176.
- [8] Tektronix ltd., ‘Arbitrary Waveform Generators AWG7000 Series Datasheet’. Accessed: Sep. 30, 2023. [Online]. Available: <https://download.tek.com/datasheet/AWG7000-Arbitrary-Waveform-Generator-Datasheet-76W2225918.pdf>
- [9] Mini-Circuits, ‘Gain Block, 50 - 6000 MHz, 50Ω | ZX60-V62+’. Mini-Circuits.
- [10] Mini-Circuits, ‘LTCC Low Pass Filter, DC - 3500 MHz, 50Ω | VLFG-3500+’.

- [11] Mini-Circuits, 'LTCC High Pass Filter, 4000 - 8800 MHz | VHF-3500+'. Accessed: Sep. 30, 2023. [Online]. Available: <https://www.minicircuits.com/WebStore/dashboard.html?model=VHF-3500%2B>
- [12] Mini-Circuits, 'Level 10, Double Balanced Mixer, RF/LO Freq 750 - 6000 MHz | ZX05-63LH-S+'. Accessed: Sep. 30, 2023. [Online]. Available: <https://www.minicircuits.com/WebStore/dashboard.html?model=ZX05-63LH-S%2B>
- [13] Keysight, 'MXG X-Series Signal Generator N5181B Analog & N5182B Vector'.
- [14] Crystek, 'Crystek CLPFL-0300'. Accessed: Sep. 30, 2023. [Online]. Available: <https://www.crystek.com/specification/filter/CLPFL-0300.pdf>
- [15] Mini-Circuits, 'Low Noise Amplifier, 50 - 3000 MHz, 50Ω | ZX60-P103LN+'. Accessed: Sep. 30, 2023. [Online]. Available: <https://www.minicircuits.com/WebStore/dashboard.html?model=ZX60-P103LN%2B>
- [16] Rohde & Schwarz GmbH & Co KG, '© Rohde & Schwarz; R&S®RTB2000 Oscilloscope'. 2023. Accessed: Sep. 19, 2023. [Online]. Available: [https://scdn.rohde-schwarz.com/ur/pws/dl\\_downloads/pdm/cl\\_brochures\\_and\\_datasheets/specifications/3607\\_4270\\_22/RTB2000\\_dat-sw\\_en\\_3607-4270-22\\_v1700.pdf](https://scdn.rohde-schwarz.com/ur/pws/dl_downloads/pdm/cl_brochures_and_datasheets/specifications/3607_4270_22/RTB2000_dat-sw_en_3607-4270-22_v1700.pdf)

## 7 General conclusion

During the course of this work, I have been involved in numerous devices microfabrication and characterization to develop acoustoelectronic devices and convolvers. The main results can be grouped as:

- Graphene transfer and processing represent a crucial step to achieve good quality devices and I succeeded in the development of a robust microfabrication process. One of the major elements is that graphene-LiNbO<sub>3</sub> chemical interaction limits the annealing temperature as compared to silicon transfer technology. Still, the film presents state-of-the-art mobility and conductivity.
- The results of the Raman analysis of graphene on periodically-poled LiNbO<sub>3</sub> show that the physical properties of graphene have little to no variation from the different polarization of LiNbO<sub>3</sub>.
- Concerning the properties of GoL, we confirmed by Raman scattering, Hall mobility and acoustoelectronic effect that the graphene is hole-doped. There is likely a local change of the properties near the electrodes over small distance, that can be attributed to a localized strain from the step and charge transfer between graphene and the doping metal contact.
- Finally, I succeeded in making state-of-the-art Acousto-Electric current measurements in the 2.0 GHz – 3.0 GHz range. Our device presents a strong interaction for the charges in graphene and the phonons in the piezoelectric, as described in Chapter 5. A review and confront with other data in the literature show that acoustoelectronic coupling strongly depends on the quality of the devices. The results for graphene/piezoelectric are somewhat different from what defined in the theory, but I hope to have given the details of methodology for a rigorous evaluation of charge carriers interactions.
- The characterization performed on the GoL acoustoelectronic amplifiers were limited by thermal effects.
- The produced convolver designs show excellent nonlinear properties, it enables to achieve **one of the highest ever reported convolution efficiency of -34 dBm at the highest ever reported carrier frequency of 2.55 GHz**, for a relatively low-power **12 dBm input**. The results show that a higher signal could be extracted if using higher amplitudes of input signals.

In conclusion, the work of my thesis could be expanded upon in terms of testing methodology and manufacturing.

For testing, it would be very interesting to perform a test of the manufactured convolver devices in a proof-of-concept of real-time communication.

As for manufacturing, the geometries of the convolvers and the amplifiers could be further optimized. Moreover, one could consider using other 2D materials in combination with graphene, like hexagonal-Boron Nitride (hBN), or in substitute, like black phosphorous, 2D transition metal-dichalchogenids, etc. Also, a direct growth of 2D material on  $\text{LiNbO}_3$  would simplify the manipulation and the adhesion of graphene to the substrate.

## 8 Summary of my research and teaching activities

I defend my PhD on my personal work conducted at FEMTO-ST on the acousto-electronic of GoL. Meanwhile, I have been involved in numerous projects and collaborations on energy harvesting, modeling, RF measurements and IoT.

Below, you will find a list of my current publications, presentations and posters where I contributed during my PhD (2020-2023). I was also involved in numerous teaching activities at SUPMICROTECH, H-KA and FEMTO-ST.

### 8.1 List of presentations and publications

#### **On RF/microwave micro-acoustics and acousto-electronics:**

[Paper 1] **Mario Costanza**, Léa La Spina, Arthur De Sousa Lopes Moreira, Djaffar Belharet, Ausrine Bartasyte, and Samuel Margueron. “Acousto-Electric measurements at 2.5 GHz on graphene transferred onto YX128°-LiNbO<sub>3</sub>”. In: *Nanotechnology* 34.32 (2023), p. 325202.

[Oral] **Mario Costanza**, Lea La Spina, Ausrine Bartasyte, Samuel Margueron, Graphene-Based Surface Acoustic Wave autocorrelator on LiNbO<sub>3</sub>. IEEE Int. Ultrasonic Symposium 2023, Montreal, September 3-8.

[poster] **Mario Costanza**, Arthur De Sousa Lopes Moreira, Joseph Scola, Yves Dumont, Ausrine Bartasyte, Samuel Margueron “Electrical properties of Graphene Transferred on Lithium Niobate substrates”, HOWDI 2022, Low dimensional Van Der Waals heterostructures, May 9 - 13 2022.

[poster] **Mario Costanza**, Arthur De Sousa Lopes Moreira, Ausrine Bartasyte, Samuel Margueron “Graphene transferred on LiNbO<sub>3</sub> for high-frequency non-linear microacoustic devices”, JNTE 2022

[poster] **Mario Costanza**, Samuel Margueron, Djaffar Belharet, Laurent Robert, Arthur De SousaLopes Moreira, Ausrine Bartasyte, “Etude des proprietes du graphene transferé sur LiNbO<sub>3</sub>”, OPTIQUE Dijon 2021

[poster] **Mario Costanza**, Samuel Margueron, “Graphene for micro-acoustic high speed calculators”, General assembly femto-st 2020

[poster\*] 32.8°Y-LiNbO<sub>3</sub> Thin Film Grown by DLI-CVD for High-Frequency Bulk Acoustic Resonators Sondes Boujnah, Quentin Micard, Lilia Arapan, Mihaela Ivan, Valérie Soumann, **Mario Costanza**, Samuel Margueron, Vincent Astié, Jean-Manuel Decams, Ausrine Bartasyte . IEEE Int. Ultrasonic Symposium 2023, Montreal, September 3-8.

(\*poster where I helped on RF modeling)

### **On piezoelectric Energy Harvesting in piezoMEMS group at FEMTO-ST:**

[paper 2\*\*] Giacomo Clementi, **Mario Costanza**, Merieme Ouhabaz, Ausrine Bartasyte, Bernard Dulmet, Samuel Margueron 2D+1 degree of freedom equivalent circuit model for LiNbO<sub>3</sub>/metal/LiNbO<sub>3</sub> bimorph bending cantilever. In: Sensors and Actuators A: Physical (2023) 362, 1 114606.

(\*\*paper where I conducted equivalent circuit modeling with Micro-Cap 12)

**[paper 3\*\*\*]** Namanu Panayanthatta, Giacomo Clementi, Merieme Ouhabaz, **Mario Costanza**, Samuel Margueron, Ausrine Bartasyte, Skandar Basrour, Edwige Bano, Laurent Montes, Catherine Dehollain, et al. “A Self-Powered and Battery-Free Vibrational Energy to Time Converter for Wireless Vibration Monitoring”. In: Sensors 21.22 (2021), p. 7503.

(\*\*\*paper where I contributed to the programming of STM microcontroller for ultra-low power consumption)

[oral] Samuel Margueron, Giacomo Clementi, Merieme Ouhabaz, **Mario Costanza**, Ausrine Bartasyte, Namanu Panayanthatta, Skandar Basrour, Edwige Bano, Laurent Montes, Catherine Dehollain, et al. “Lead Free Piezoelectric Wireless Self-Powered Sensor Nodes”. In: EASS 2022; 11th GMM-Symposium. VDE. 2022, pp. 1–3.

[oral] Namanu Panayanthatta, Giacomo Clementi, Merieme Ouhabaz, **Mario Costanza**, Samuel Margueron, Ausrine Bartasyte, Skandar Basrour, Edwige Bano, Laurent Montes, Catherine Dehollain, et al. “A smart battery free system for wireless condition monitoring using piezoelectric energy harvester”. In: 2022 Smart Systems Integration (SSI). IEEE. 2022, pp. 1–4.

### **On IoT with STMICROELECTRONICS: (papers and conferences issued from my master trainee)**

**[paper 4]** Roberto La Rosa, Patrizia Livreri, Catherine Dehollain, **Mario Costanza**, and Carlo Trigona. “An energy autonomous and battery-free measurement system for ambient light power with time domain readout”. In: Measurement 186 (2021), p. 110158.

**[paper 5]** Roberto La Rosa, **Mario Costanza**, Andreas Burg, Catherine Dehollain, and Patrizia

Livrieri. “Intrinsically Self-powered, Battery-free, and Sensor-free Ambient Light Control System”. In: 2021 Ieee Sensors. IEEE. 2021, pp. 1–4.

**[paper 6]** Roberto La Rosa, Catherine Dehollain, Andreas Burg, **Mario Costanza**, and Patrizia Livrieri. “An energy-autonomous wireless sensor with simultaneous energy harvesting and ambient light sensing”. In: IEEE Sensors Journal 21.12 (2021), pp. 13744–13752.

**[proceeding 1]** Roberto La Rosa, **Mario Costanza**, Catherine Dehollain, Patrizia Livrieri, and Carlo Trigona. “A Self-powered Ambient Light Power Measurement Platform with Time domain Readout”. In: 2021 IEEE International Instrumentation and Measurement Technology Conference (I2MTC). IEEE. 2021, pp. 1–5.

**[proceeding 2]** Roberto La Rosa, Catherine Dehollain, **Mario Costanza**, Angelo Speciale, Fabio Viola, and Patrizia Livrieri. “A Battery-Free Wireless Smart Sensor platform with Bluetooth Low Energy Connectivity for Smart Agriculture”. In: 2022 IEEE 21st Mediterranean Electrotechnical Conference (MELECON). IEEE. 2022, pp. 554–558.

**[proceeding 3]** Roberto La Rosa, **Mario Costanza**, and Patrizia Livrieri. “Advanced techniques for powering wireless sensor nodes through energy harvesting and wireless power transfer”. In: 2020 AEIT International Conference of Electrical and Electronic Technologies for Automotive (AEIT AUTOMOTIVE). IEEE. 2020, pp. 1–6.

## 8.2 Teaching activities

Part of my classes have been recorded and are available on youtube (4h):

<https://youtube.com/playlist?list=PLqoB6gU-q5mQ5wYgPYPeKdvvMkiztu1Uj&feature=shared>

*Lectures given at Supmicrotech-ENSMM in Besançon:*

### **2021-2023 - Android Programming for IoT**

I held introductory classes to the Android Studio IDE. The lectures were divided into a brief theoretical section introducing the program and practical sessions. (36 h)

### **2021-2023 - STM32 Programming for IoT:**

I held the lab hours for the STM32 microcontroller programming classes. (48 h)

*Lectures given at H-KA (Karlsruhe):*

### **2022-2023 - Basics on STM32 & Low-Power programming**

I held lectures on ARM-based microcontrollers and the ST software suite. The lectures were divided into an introduction to the hardware inside a microcontroller, in the context of ultra-low-power optimization, introduction to STM32CubeIDE, followed by some practical sessions. (24 h)



**Titre :** Intégration du graphène sur composants micro-acoustiques radiofréquences

**Mots clés :** Graphène, convolveur, micro-acoustique, acoustoélectronique, microtechnologies, radiofréquences

**Résumé :** L'interaction acoustoélectronique des charges mobiles avec des ondes acoustiques est un phénomène au cœur des propriétés électroniques des matériaux. Depuis quelques années, cette interaction non linéaire est étudiée pour manipuler des dispositifs électroniques ou photoniques à l'aide d'ondes acoustiques. En particulier, les matériaux bidimensionnels, comme le graphène, ont le potentiel d'améliorer la réponse des dispositifs microacoustiques non linéaires du fait de leur forte mobilité et leur faible masse. L'objectif de cette thèse a ainsi été de démontrer qu'une architecture de graphène sur niobate de lithium pour des dispositifs à ondes acoustiques de surface permet de réaliser un dispositif fonctionnel de type convolveur opérant à plusieurs GHz. Pour cela, le transfert de graphène sur niobate de lithium a été optimisé en salle blanche. Les films transférés ont été caractérisés électriquement, par

des mesures Hall classique et quantique ainsi que par spectroscopie Raman. Les résultats ont montré que nous avons obtenu des films de graphène transférés dopés de type p. Les caractérisations du courant acoustoélectronique sur composants microacoustiques à ondes de surface à 2,5 GHz ont confirmé un fort couplage. Finalement, des amplificateurs et convolveurs non dégénérés basés sur l'effet acoustoélectronique ont été développés. Les résultats montrent une forte sensibilité des dispositifs avec l'échauffement induit à forte puissance acoustique dont les amplificateurs sont particulièrement sensibles. L'effet de convolution de signaux contrapropagatifs sur électrode en graphène est cependant clairement démontré. Ces résultats confirment la possibilité de réaliser des composants tout-analogique fonctionnant à plusieurs GHz pour le traitement de signaux spécifiques.

**Title :** Integration of graphene on micro-acoustic radiofrequency components

**Keywords :** Graphene, convolver, micro-acoustic, acoustoelectronic, microtechnologies, radiofrequencies

**Abstract:** The acoustoelectronic interaction of mobile carriers with acoustic waves is a phenomenon at the heart of the electronic properties of materials. For several years, this non-linear interaction has been at the heart of developments intended to manipulate the response of electronic or photonic devices with acoustic waves. In particular, two-dimensional materials, such as graphene, have the potential to improve the response of non-linear microacoustic devices due to their high mobility and low mass. The objective of this thesis was then to demonstrate that a graphene on lithium niobate architecture for surface acoustic wave devices makes it possible to produce a functional convolver device operating at several GHz. For this, the transfer of graphene onto lithium niobate was optimized in a clean room. The transferred films were characterized

electrically, by classical and quantum Hall measurements as well as by Raman spectroscopy. The results showed that we obtained p-type doped transferred graphene films. Characterizations of the acoustoelectronic current on micro-acoustic surface waves components at 2.5 GHz confirmed strong coupling. Finally, non-degenerate amplifiers and convolvers based on the acoustoelectronic effect were developed. The results show a high sensitivity of the devices with the heating induced at high acoustic power of which the amplifiers are particularly sensitive. The convolution effect of counterpropagative signals on a graphene electrode is clearly demonstrated. These results confirm the possibility of producing all-analog components operating at several GHz for the processing of specific signals.